Scattered radiation in projection X-ray mammography and digital breast tomosynthesis

O. Díaz Montesdeoca

Submitted for the Degree of
Doctor of Philosophy
from the
University of Surrey

Centre for Vision, Speech and Signal Processing
School of Electronics and Physical Sciences
University of Surrey
Guildford, Surrey GU2 7XH, U.K.

June 2013

Abstract

Breast cancer has a significant impact on the well-being of the female population both nationwide and worldwide. This has motivated the establishment of national breast screening programmes in most western countries, in order to reduce the mortality associated with this disease via early detection. X-ray mammography is considered the current gold standard technique for breast cancer detection in such screening programmes. However, this suffers from performance limitations due to tissue superposition which can either mimic or obscure malignant pathology. Therefore, alternative X-ray modalities, such as digital breast tomosynthesis (DBT), which employs a series of X-ray projections at different (but limited) angles, are being explored in order to improve breast cancer detection rates.

In all such X-ray based imaging methods, scattered photons produced deleterious effects on image quality to varying degrees. In order to model such scatter distribution, Monte Carlo (MC) simulations is often chosen as the default approach, and as such is used in this thesis to quantify its effects in X-ray mammography and DBT scenarios. Following validation on the use of the GEANT4 MC package for use in mammography, three commercially available full-field digital mammography (FFDM) systems were simulated with their corresponding anti-scatter grids using a CDMAM geometry. It was observed that, for the particular geometry studied, the scattered radiation recorded at the detector was 17% using a linear anti-scatter grid design. However, this figure was reduced by a factor of three when employing a cellular anti-scatter grid geometry.

In DBT geometries, scattered radiation is larger than in FFDM and, spatially, may vary more rapidly due to the absence of an anti-scatter grid. The excessively long times needed to run MC simulations (8-10 hours) for such analysis motivates the need for an alternative approach. A non-stationary kernel-based approach has thus been developed. It was found that using kernels based on breast thickness-only, can overestimate scatter radiation by more than 60% (compared to MC simulations) at the breast edge region. Simulation work presented here shows that this overestimation in scatter is largely due to the air gap between the lower curved breast edge and the image receptor. In this thesis, a more accurate scatter field estimator is proposed for use in DBT which not only considers the breast thickness and primary incidence angle, but also accounts for scatter exiting the breast edge region and traversing an air gap prior to absorption in the image receptor. This proposed approach has reduced such errors to an average error of 10% in scatter, and a maximum of 20% across the projected breast phantom, and has decreased the run-time ten-fold. Such an approach has potential applications in scatter correction methods in DBT, and as an efficient modelling tool in imaging system development and in evaluation of virtual clinical trials.

Key words: Monte Carlo simulations, GEANT4, scattered radiation, SPR, convolution, X-ray mammography, digital breast tomosynthesis.

Email: o.diaz@surrey.ac.uk / o.diaz.montesdeoca@gmail.com
WWW: http://www.ee.surrey.ac.uk/

Acknowledgements

First of all, I would like to thank to my supervisors Dr. Kevin Wells, Professor David R. Dance and Professor Kenneth C. Young for all the patient and the guidance to become a research scientist. Secondly, I would like to thank to Professor Nicholas Spyrou and Dr. John Kotre for agreeing to be involved in the examination of this thesis. In addition, I would like to thank Cancer Research UK, the Engineering and Physical Sciences Research Council Cancer Imaging Programme in Surrey, the Medical Research Council and the Department of Health (England) for the economic support of the project.

Also, many thanks to all current and former members of the CVSSP, especially to the Medical Imaging group as well as the National Co-ordinating Centre for the Physics of Mammography at the Royal Surrey County Hospital for all the useful discussions and great time I had in all these years. Special mention to Dr. Jorge Cabello for introducing me to the GEANT4 community, Dr. Mary Yip and Miss Michela Esposito for all the interesting discussions about the Physics world and proof-reading help, Dr. Premkumar Elangovan for adapting the ray tracing tool to the demands of my project and Dr. Predrag R. Bakic for providing with the breast phantom models used in the thesis.

Finally, I would like to thank my family and friends for all the warmth I received from the Canary Islands and also many many thanks to Maribel for all her kindness help and patient without which this work would not have been possible.

This work is part of the OPTIMAM project and is supported by Cancer Research UK and the Engineering and Physical Sciences Research Council Cancer Imaging Programme in Surrey, in association with the Medical Research Council and Department of Health (England).

En memoria de mi abuela Carmen.

Dedicado a mi madre Nieves y a mi padre Gabriel.

Contents

Chapter 1

Introduction

In 2008, approximately 7.6 million of people died from cancer worldwide (excluding non-melanoma skin cancer) [1]. Within the UK, the number of deaths from cancer was 157,000 in 2010 [2], corresponding to mortality rates of 204 per 100,000 males and 149 per 100,000 females [3]. The above figures illustrate the fact that cancer is a major cause of death.

Cancer is a group of diseases where cells grow abnormally without stopping [4]. This abnormal growth of the cells can produce benign or malignant tumours. A benign tumour is not considered hazardous because it grows slowly and does not spread to other parts of the body. On the contrary, malignant tumours can grow quickly and their cancer cells can leave the tumour and spread to other organs of the body (metastasis) using blood vessels and the lymphatic system, invading and damaging the surrounding tissue. They compete with normal tissue for space and nutrients, affecting the normal body functions and thus, eventually leading to death.

The incidence and mortality of the most common cancers observed worldwide in 2008 are shown in Figure 1.1, where breast cancer represents the second most common cancer and the fifth cause of cancer death.

1.1 Breast cancer

Abnormalities in the breast tissue structure (see breast anatomy in Appendix B), such as soft tissue masses, are found to be a sign of breast cancer. One of the most important features in any breast cancer is whether it is non-invasive ("in situ") or invasive, which also determines the associated treatment protocol.

The most important non-invasive cancers are *Ductal Carcinoma In Situ (DCIS)* and *Lobular Carcinoma In Situ (LCIS)* which do not grow further than lactiferous ducts or breast lobules respectively. However, in the case of invasive cancer, the cancerous cells pass through the breast tissue barrier and invade surrounding areas. *Invasive Ductal Carcinoma (IDC)* begins in the milk ducts before spreading beyond them and in *Invasive Lobular Carcinoma (ILC)*, the cancer starts in the milk-producing lobules.

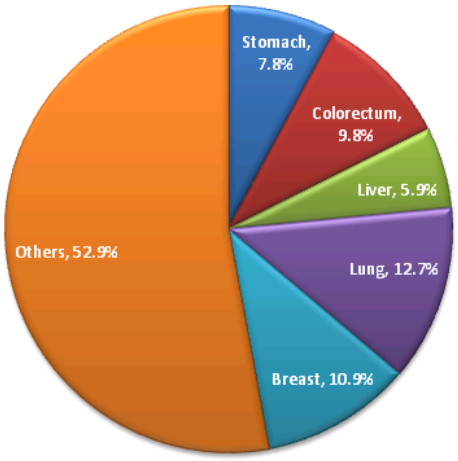

(e) Incidence

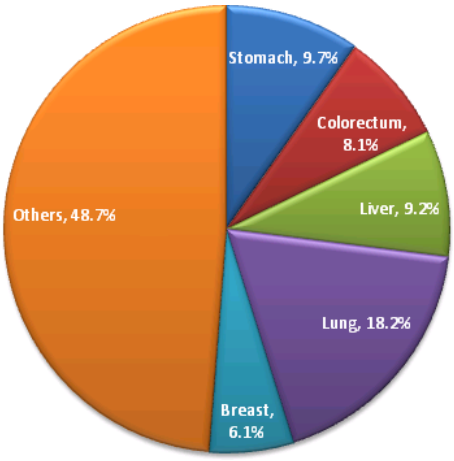

(f) Mortality

Figure 1.1: Cancer incidence and mortality worldwide for both sexes (2008) [1].

A diagram of invasive and non-invasive cancer which affect the lactiferous ducts is illustrated in Figure 1.2.

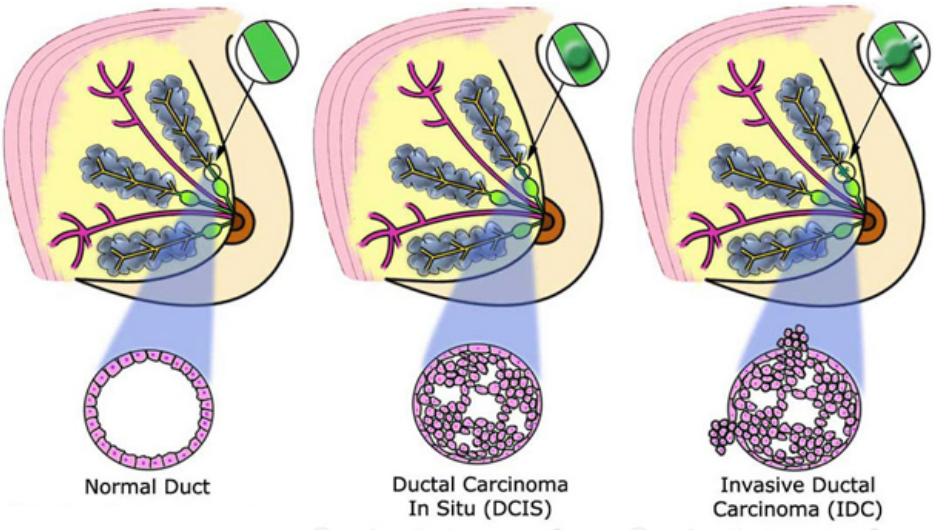

Figure 1.2: Diagram of a duct affected by non-invasive (DCIS) and Invasive (IDC) breast cancer. Image adapted from [5].

Examples of the mammographic appearance of breast cancer are illustrated in Figure 1.3. The breast cancer cases shown here are very obvious. However, the task performs by radiologist to detect breast cancer is very challenging.

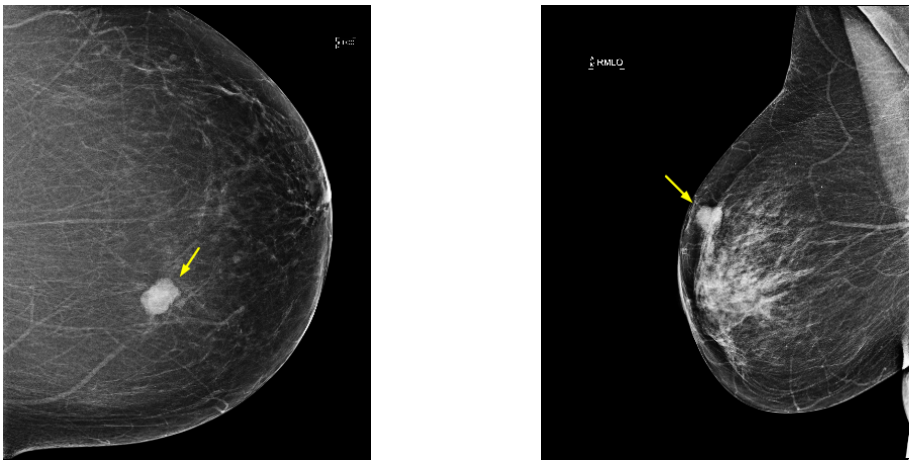

(a) (b)

Figure 1.3: Sample X-ray mammography images showing signs of breast cancer.

1.2 Impact of breast cancer in female population

In women, breast cancer is the most common cancer detected in both developed and developing countries [1]. Within the UK, approximately 49,500 women were diagnosed with breast cancer in 2010 [2], representing the highest incident rate of all cancers diagnosed in women [2, 3]. Figure 1.4 illustrates the breast cancer incidence rates in women within the UK for the last 35 years. It is observed how breast cancer has affected increasing numbers of women over this period. This could in part be explained by improvements in detection methods, as well as changes in life style [2].

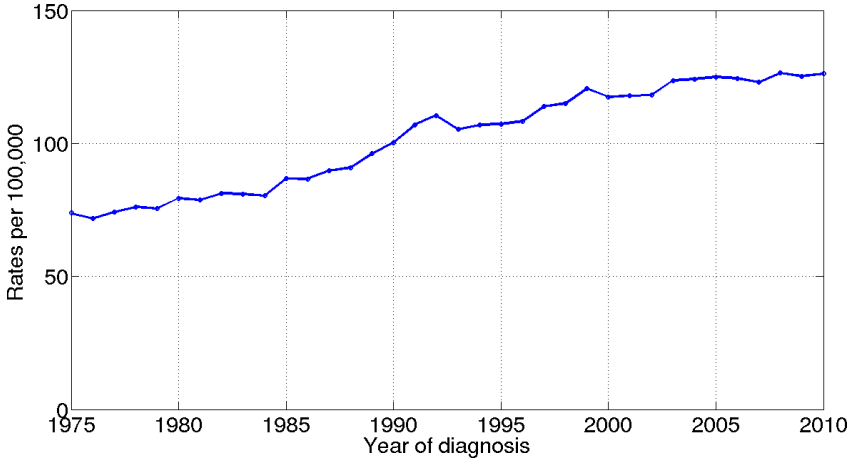

Figure 1.4: Breast cancer incidence rates per 100,000 female population within the UK from 1975 to 2010 [2].

In spite of UK breast cancer mortality rates having reduced by approximately 35% during the last 20 years (see Figure 1.5), in 2010 approximately 11,500 women lost

their lives in UK due to this disease [2]. This has placed breast cancer as the second higher cause of cancer mortality in women after lung cancer [2, 3]. The causes of the reduction in mortality are difficult to demonstrate but, according to Cancer Research UK (CRUK), the early detection of breast cancer due to the breast screening program and recent improvements in X-ray mammography systems have positively influenced this reduction. Furthermore, improvements in breast cancer treatments have also contributed to this trend. Note in Figure 1.5, how the breast cancer mortality rate has been reduced since the breast screening program was set up in the UK in 1988.

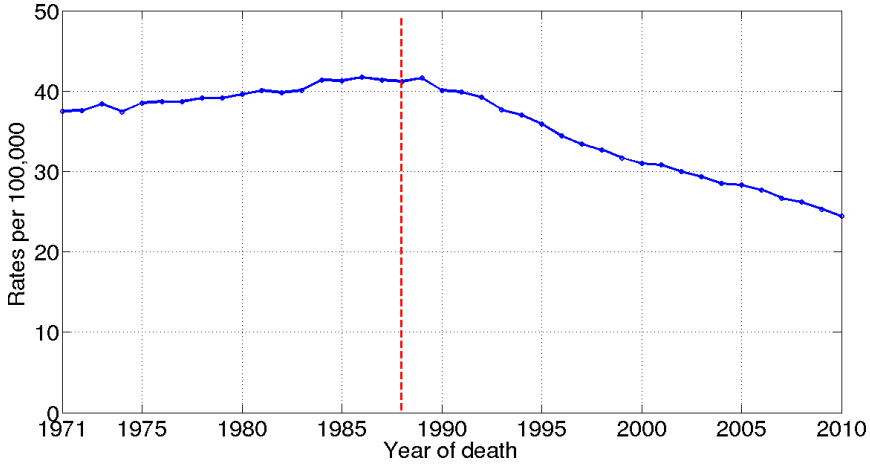

Figure 1.5: Breast cancer mortality rates per 100,000 female population within the UK from 1971 to 2010 [2]. Vertical dashed line represents the year the breast screening program was set up (1988).

As described at the beginning of the chapter, malignant tumours can grow very quickly and spread to other organs. In order to minimise the harm of such cancerous cells to normal tissue, tumour presence should be detected as soon as possible. For this reason, early detection of breast cancer can be translated into increasing the possibilities of a fast and successful recovery in the patient: the sooner the cancer is detected, the higher the probability of survival. This can also help to avoid traumatic treatments such as breast removal (mastectomy).

In order to detect breast cancer, X-ray mammography has been proven to be the gold standard technique and moreover, it is the standard radiological technique used in breast cancer screening [6].

1.3 National breast screening programme

In 1986, the Forrest report [7] concluded that regular screening mammography of women aged 50 and over may increase life expectancy as breast cancer can then be detected in an early stage and subsequently treated with enhanced results. Two years later (1988), the National Health Service (NHS) introduced the NHS Breast Screening Programme (NHSBSP) and women between 50 and 69 years of age were invited to have a mammogram every three years.

At the time, the UK was the first country in the world to undertake such as screening programme. Currently, around 1.5 million women accept the invitation to attend the NHSBSP and about 95% of women scanned are reported as normal after the first mammogram [8]. Women below 50 years old were not originally invited because the incidence rate of breast cancer was lower for that age group and because the X-ray mammography technology of the time, screen-film cassette, was not as effective for dense breast tissue observed in this younger cohort. However, as will be explained in Section 2.5.1, the arrival of digital detectors in X-ray mammography has shown an improvement in breast cancer detection for dense breasts [9, 10]. Therefore, the NHSBSP is currently extending the age range of women to ages 47 to 73 in order to detect breast cancer in a wider group of the female population.

A report by the Department of Health Advisory Committee, published in 1991, suggested that the NHSBSP would avoid 1,250 breast cancer deaths by 2010 [8]. In fact, the International Agency for Research in Cancer (IARC) also suggested that X-ray mammography screening reduces mortality for breast cancer, for every 500 women screened, one breast cancer death will be avoided.

However, an issue with the NHSBSP is the X-ray dose given to the asymptomatic breast screening population. It is well-known that using ionising radiation comes with it a risk of inducing cancer. Thus, women participating in the screening programme may be at slightly higher risk of inducing cancer for the years that the individual is included in the breast screening programme. This ionising radiation effect is very difficult to measure but the NHSBSP estimates that for every 14,000 women in the age range 50-70 years old screened three times over a 10 year period, the associated exposure to X-rays will induce about one fatal breast cancer [11]. Thus, the benefit in reduced overall mortality is thought to outweigh the risks of screening by X-ray mammography.

1.4 Motivation

When the NHSBSP was set up in 1988, X-ray mammography systems used screen-film cassettes as image receptors. Two of the limitations of screen-film cassettes are their limited contrast sensitivity and dynamic range [12], which can lead to missed breast tumours in dense tissue regions [13, 14]. In order to improve the performance of screen-film cassettes, digital detectors were introduced. These have demonstrated detection performance that can equal that of screen-film cassettes [9, 15, 16, 17] as well as delivering improved breast cancer detection in women with dense breast composition [9, 10].

Thus, it is seen that digital technology is playing an important role in the improvement of breast cancer detection. One particular advantage arising from the adoption of digital technology is that the various imaging processes involved (image acquisition, storage and image display) can be optimised independently. Computer simulations are key in this optimisation process. They facilitate study of the impact on image quality when varying key parameters in current X-ray mammography system (e.g. scatter reduction methods), as well as evaluation of new design options without requiring irradiation of human subjects. They can also be used to performance virtual clinical trials and

evaluate new technology provided by manufacturers much quicker than conventional clinical trials.

The aim of this work is to characterise the distribution of scattered radiation, using Monte Carlo (MC) and non MC methods, for different X-ray mammography geometries. Scattered radiation reduces the contrast in X-ray imaging, a metric which is key important for the detection of breast cancer in X-ray mammography images. Knowledge of scatter is essential, not only for use in image simulations studies, but also to develop methods to reduce its undesired effects in digital detectors, where post processing of the raw image is possible. Special attention has been paid to digital breast tomosynthesis (DBT) where the scatter magnitude is higher than conventional planar X-ray mammography. DBT is a developing technology which reduce the overlapping tissue problem found in conventional planar X-ray mammography by imaging the breast at limited angles. It is hoped that this study will lead to new insights of scattered radiation, and the relative sources of its deleterious effect on image quality.

This research forms part of a wider programme of work in developing simulation tools for optimising the use of digital technologies in X-ray mammography, known as the OPTIMAM project. This project aims to develop an overarching simulation framework to investigate the performance of two dimensional (2D) digital X-ray mammography systems, as well as exploring new technologies available for breast cancer detection such as DBT.

1.5 Structure of the thesis

As described in the previous section, computer simulations have been used in this work to study scattered radiation.

In order to design an accurate simulation of X-ray mammography systems, knowledge of all the physical interactions involved in X-ray mammography acquisition (e.g. scattering processes) is necessary. Furthermore, the geometry used in this type of X-ray technologies is also needed to reproduce accurately an X-ray system in a virtual environment. All this key information is described in **Chapter 2**.

Once the geometry and the physical interactions are known, a computer simulation can be built. However, before doing so, prior understanding of the effects of scattered radiation on image quality, can help to correctly interpret the subsequent results. Thus, **Chapter 3** describes how this undesirable signal component is measured as well as which parameters influence in its magnitude and spatial distribution. Furthermore, typical strategies currently used (anti-scatter grids, air gaps, etc.) to minimise its effects on image quality are also included.

At this point, the computer simulation to be used in this work can be designed. Due to the stochastic behaviour of the particle interactions, MC simulations have been used. The MC toolkit employed in this work (GEANT4) is described in detail in **Chapter 4**. Its performance in X-ray mammography is shown via careful validation with experimental and published data.

A feasibility study of MC simulation-based scatter in the generation of synthetic images is presented in **Chapter 5**. In this chapter, scatter-to-primary ratio (SPR) maps are inserted into an existing CDMAM image simulation framework.

During the work developed using MC simulations, it was found that this technique is extremely time consuming. Therefore, non-MC approaches to study scattered radiation are proposed in **Chapter 6** in particular for DBT geometries, where the scatter signal is more prominent due to the absence of anti-scatter devices. Using anthropomorphic breast phantoms, the limitations of conventional convolution-based methodologies for the calculation of scatter are explored. Using insight gained from simulations studies, several new strategies are proposed to improve the performance of kernel-based methods for scatter field modelling.

The conclusions of these findings are described in **Chapter 7**, where further work to improve on these new developments performance is also suggested.

1.6 Achievements and major contributions

The main achievements, including contributions to the field, contained in this thesis may be summarised as follow.

A detailed MC simulation has been developed and validated, and used to study scattered radiation fields for both 2D full-field digital mammography (FFDM) and DBT geometries.

SPR maps generated for three commercially available FFDM systems have been inserted into an existing CDMAM image simulation framework [18] in order to reduce the dependency on clinical measurement while maintaining similar performance. Previously, this CDMAM image simulation framework estimated the scatter signal based on clinical measurements. However, this framework has been modified in this work to introduce MC-based SPR maps for the first time. Furthermore, SPR values have been shown for the first time using the cellular anti-scatter grid currently employed by the Hologic Selenia system, demonstrating the larger scatter reduction when comparing with the linear anti-scatter grid found in the GE Essential system.

Investigation of the scatter field in DBT was initiated as scatter is substantially higher in DBT systems, compared to FFDM (due to the lack of anti-scatter grids). However the need for scatter fields for each angular projection motivated the development of non-MC alternatives. While doing so, it was found that the conventional convolution-based approach [19, 20, 21, 22, 23, 24, 25] (employing breast thickness dependent scatter kernels) was not sufficient to accurately estimate the scattered radiation in DBT, showing errors of more than 150% in the region of the image which corresponds to the edges of the realistic breast phantoms.

After rigorous examination of the imaging system and the physical process involved, it was discovered that the variable air gap distance between the lower surface of the breast phantom and the breast support significantly affects the magnitude of the scattered radiation recorded within the image receptor.

To address this previously unaccounted phenomena, a novel approach to model scatter due to the air gap distance is proposed. Moreover, the scattered radiation contribution from sources other than the breast (compression paddle, breast support,...), which is often neglected, has also been included in the new kernel-based approach suggested in this work.

By applying this new kernel-based approach to a range of breast phantoms and different projection angles, it was found that such an approach can produce good quality estimates of the scatter field, with error of less than 10% (compared to MC simulations) across almost all of the projection image.

A list of the publications produced during this work is found in Appendix D.

Chapter 2

X-ray mammography imaging systems

This chapter starts with an introduction of the physics involved in the process of X-ray generation and X-ray photon interactions within the mammographic energy range, which are key to understand future chapters. Then, the components found in a typical X-ray mammography system, which are included in simulations described in further chapters, are described. The last section of this chapter includes a discussion about the X-ray breast imaging technologies currently available.

2.1 X-rays

X-rays were discovered by Wilhelm Röntgen in 1895 and these have been used in medical imaging since then. X-rays are a type of high frequency electromagnetic radiation which have enough energy to traverse most objects, including human tissue. Due to the high energy carried, X-rays have the potential to strike and eventually liberate an electron of an atom, creating a vacancy. In other words, X-rays are forms of ionizing radiation which can create ion pairs, consisting of a negatively charged particle (electron) and a positive atom or molecule [12].

In X-ray medical imaging, X-rays are considered as a set of particles (photons or quanta) and they are produced as a consequence of high speed electrons interacting with the nuclei (Bremsstrahlung radiation) or the atomic electrons (characteristic radiation) of an atom as described below.

Bremsstrahlung radiation is emitted when a high speed electron travels close to the nucleus of an atom. Due to the positive charge of the nucleus, the high speed electron can be slowed down releasing a Bremsstrahlung X-ray photon with part of its kinetic energy. Furthermore, the high speed electron can collide directly with the nucleus of the atom, where all its kinetic energy is transformed into an X-ray photon. This process is observed in Figure 2.1(a), where the two cases explained are shown.

In the case of *Characteristic radiation*, the high speed electron ejects an atomic electron from its shell (K, L, M,...) producing a vacancy as illustrated in Figure 2.1(b). This

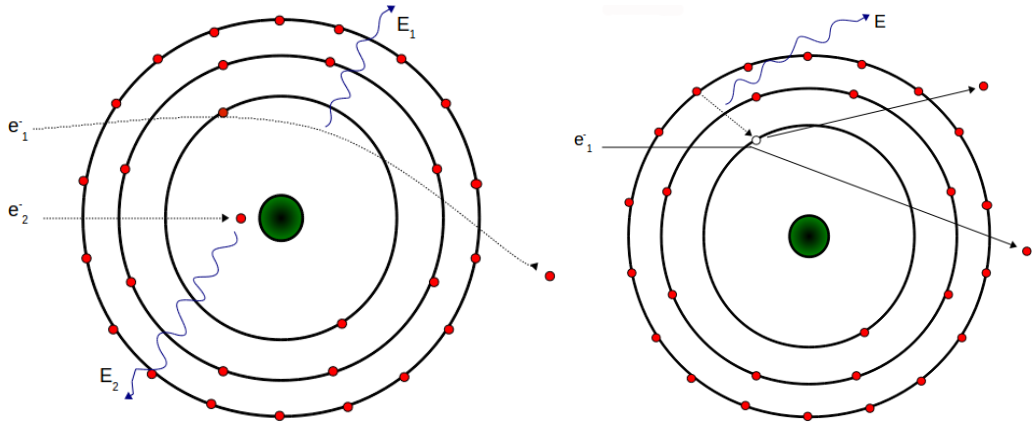

(a) Bremsstrahlung radiation (b) Characteristic radiation

Figure 2.1: Diagrams of the processes involved in the X-ray production. In Bremsstrahlung (a), a high speed electron interacts with the nucleus of an atom whereas in characteristic radiation (b), the high speed electron interacts with the electrons of an atom.

vacancy is filled with an electron from an outer shell producing a characteristic X-ray photon which energy is equal to the binding energy (E_{BE}) difference between the two shells. Each element has different E_{BE}, so the energy of the photon emitted during this process is characteristic for an element. Furthermore, this characteristic X-ray photon can interact and eject an electrons from the outer shells (Auger electrons). As will be discussed in Section 2.4, a common material to produce X-ray photons is tungsten (W). An example of the characteristic X-ray photons ($K_\alpha, K_\beta, L_\alpha, L_\beta$) produced when an electron jumps from one shell to another in a W atom is shown in Figure 2.2.

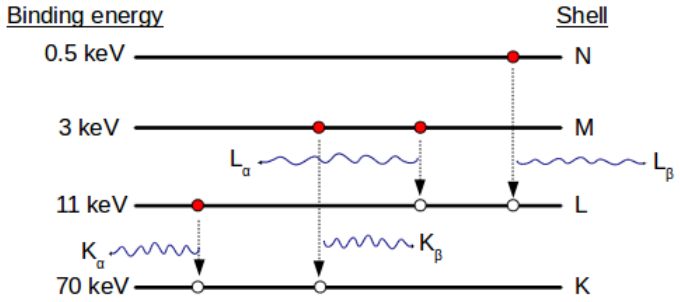

Figure 2.2: Diagram of characteristic X-ray photons ($K_\alpha, K_\beta, L_\alpha, L_\beta$) produced when a electron occupies a vacancy in an inner shell. Example of binding energies (E_{BE}) for tungsten are illustrated. Adapted from [12].

The X-ray photons are particles with energy, nevertheless they have not charge nor mass. This makes the X-ray photons immune to any electrical or magnetic field. However, they can be diffracted in a manner similar to light. As they pass through matter, they can be scattered, absorbed or they could travel without interaction as explained in the following section.

2.2 X-ray photon interactions

Consider an X-ray photon beam collimated towards a surface of area A of a given material. If that area contains n atoms, the probability for a single X-ray photon to interact with one of the n atoms is

$$\frac{n\sigma}{A}, \tag{2.1}$$

where σ is the total atomic cross section and represents the effective area for an interaction between an X-ray photon and an atom of a particular material.

Within the X-ray mammography energy range (0-50 keV), three particle interactions with matter are observed: the photoelectric effect, coherent and incoherent scattering.

Their cross sections depend on the energy and material composition as will be explained below. Figure 2.3 illustrates the cross section for adipose tissue, a main component found in breast tissue. Note that up to approximately 25keV, the photoelectric effect is dominant. After that energy, the most likely interaction is incoherent scattering.

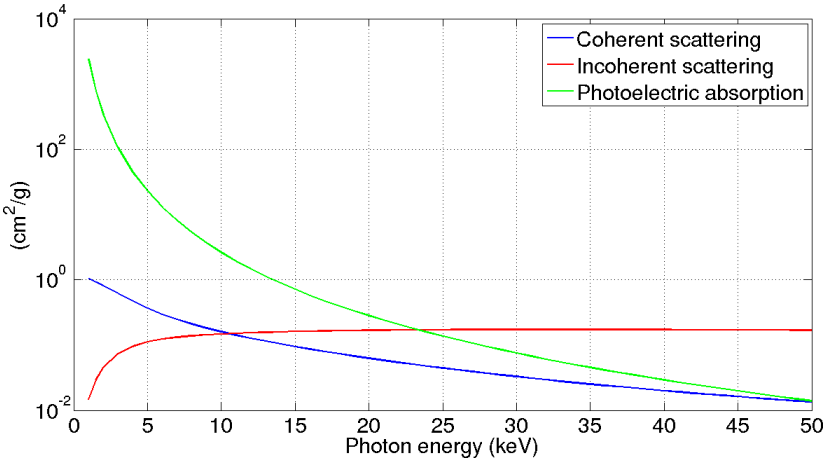

Figure 2.3: Photon cross sections for scattering and photoelectric absorption for adipose tissue [26]. Adipose tissue composition is described in Table 2.2.

2.2.1 Photoelectric effect

In the photoelectric mechanism, an X-ray photon with kinetic energy E_0 collides with an electron binded to an atom in the medium, transferring all its kinetic energy.

If the X-ray photon energy is smaller than the binding energy E_{BE}, the X-ray photon will not interact with the electron of that specific shell. However, the X-ray photon can interact with electrons in the outer shells where the E_{BE} is lower, making the interaction energetically possible. In case that E_0 is equal or greater than E_{BE}, the X-ray photon can eject the electron of the shell as illustrated in Figure 2.4, causing

ionization. This free electron is called photoelectron and its energy will be the difference between E_0 and E_{BE}. When the interaction occurs in breast tissue (mainly hydrogen (Z=1), carbon (Z=6), nitrogen (Z=7) and oxygen (Z=8)), the photoelectron is locally absorbed contributing to the patient dose [27]. This is observed in Figure 2.5, where the electron ranges are shown for soft tissues and CsI, being the latter a very common image receptor as discussed later. In both cases, the maximum distance travels by an electron within the mammography energy range is less than 50μm.

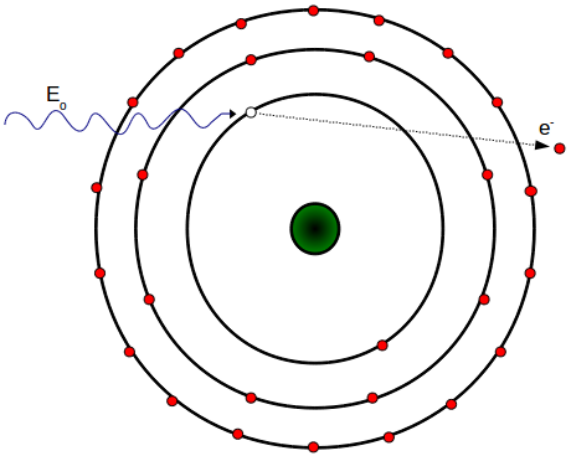

Figure 2.4: Diagram of the photoelectric effect. An X-ray photon interacts with an atomic electron, ejecting it from its shell. Characteristic X-rays photons are produced when electrons from outer shells are reorganized to fill in the vacancy left by the ejected electron.

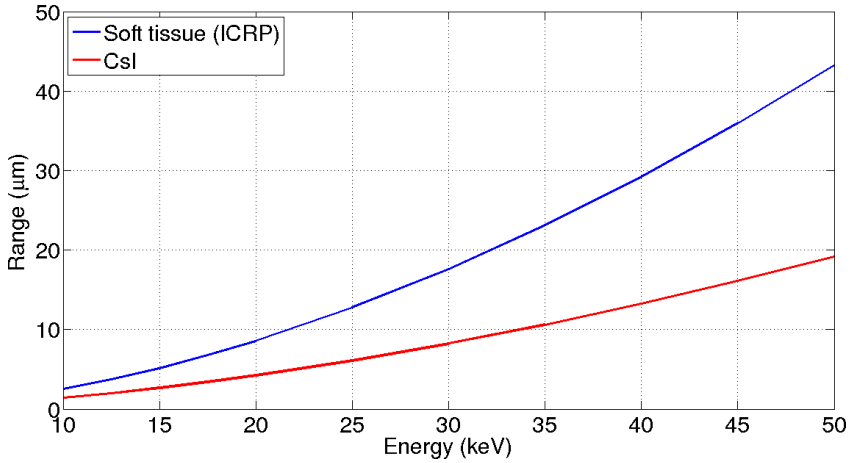

Figure 2.5: Electron range calculated for soft tissue (ICRP composition) and CsI within the mammography energy range [28].

The vacancy left in the atom is rapidly filled by electrons of the outer shells producing one or more characteristic X-rays (also known as fluorescent X-rays), following the process explained in section 2.1. The probability of producing characteristic X-ray photons is known as fluorescent yield ω. In the K shell, the fluorescent yield (ω_k) is

virtually zero for elements of atomic number (Z) less than 10 as shown in Figure 2.6. If energetically possible, these characteristic X-ray photons can interact with electrons in the outer shells producing new photoelectrons (Auger electrons). The probability of Auger electrons is 1-ω.

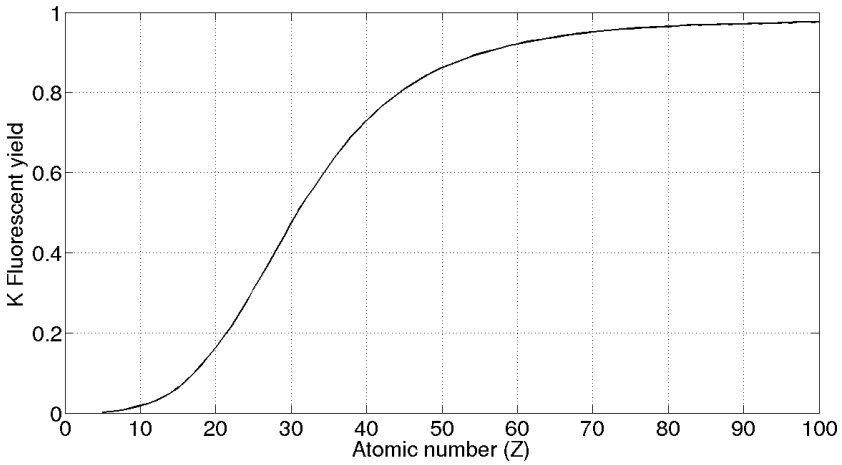

Figure 2.6: K fluorescent yield from a Z range between 5 to 100 [29].

In mammography scenarios, due to the low E_{BE} observed in the K edges of breast tissue (low Z materials), the energy of the characteristic X-ray photon is low, as well as ω. Therefore, it can be said that the characteristic X-rays produced do not travel far until they are re-absorbed by the medium [12, 30]. However, this might not be the case when photoelectric interactions occurs in image receptors materials (see Table 2.3), where the E_{BE} of K edges are larger, allowing the characteristic X-rays to travel further distances [12, 27]. For example, K_α X-ray photons have a mean free path [1] of 0.07, 0.21 and 0.60 mm for Se, I and Cs respectively, which represent typical detector's materials.

Within the mammography energy range, the cross section for photoelectric interaction (τ) of a photon with energy E_0 in a element of atomic number Z is

$$\tau = k\frac{Z^n}{E_0^m}, \tag{2.2}$$

where k is a constant and n and m represent values in the range 3.6-5.3 and 2.5-3.5 respectively depending on the element [31]. Typical n and m values in the diagnostic photon energy range illustrate that τ is inversely proportional to the cube of the X-ray photon energy and directly proportional to the fourth power of its atomic number.

$$\tau \propto \frac{Z^4}{E_0^3}. \tag{2.3}$$

Thus photoelectric interactions typically occur for low energy photons as observed in Figure 2.3. Thus, different photoelectric probabilities are obtained for materials, or

[1] Average distance a particle travels before interacting.

tissues, with small differences in atomic number. This leads to different absorption rates and consequently differences in contrast.

Furthermore, as the photon energy passes a shell binding energy for a given element, the photoelectric probability increases sharply. As will be explained below, this increase in photoelectric effect will also increase the attenuation coefficients for that particular element. This will provide greater contrast for particular elements. Because they typically occur in the mammography energy range, the increase in the K shell is the most important and it is called 'K edge effect'. An example of this increase in the photoelectric probabilities is shown in Figure 2.7 for I, a common contrast agent, where the effects of the L and K edges are shown.

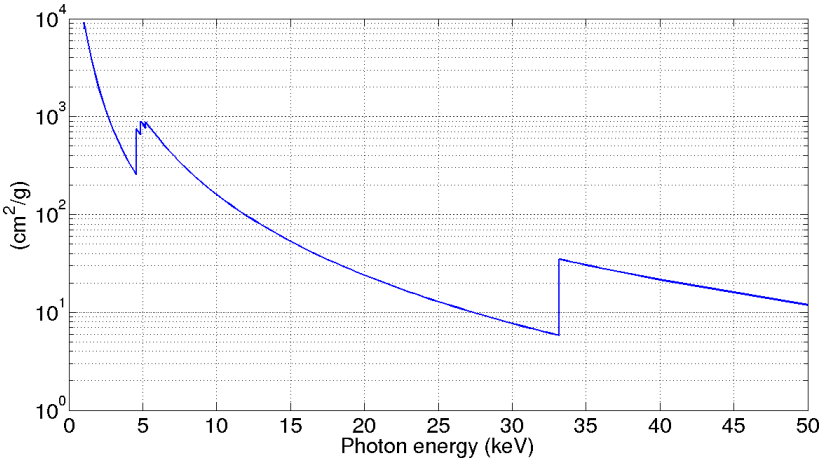

Figure 2.7: Photoelectric cross section for iodine [26]. The sharp increase of the cross section at 33.2keV correspond to the K edge effect while the increase at 4.6, 4.9 and 5.2 keV represent the contribution from the L edge [32].

2.2.2 Coherent scatter

Coherent scattering occurs when an X-ray photon is deflected after hitting an electron binded within an atom shell, leaving the atom neither ionized not excited. The X-ray photon loses a very small fraction of its energy which can be safely neglected [33]. Therefore, the incident X-ray photon is scattered with an angle θ with respect to its original trajectory and remains with its initial kinetic energy ($E' = E_0$) as shown in Figure 2.8.

J.J. Thomson described, at the beginning of last century, that the differential cross section[2] of an X-ray photon scattered by a free electron is

$$\frac{d\sigma_T}{d\Omega} = \frac{r_e^2}{2}(1 + cos^2\theta), \tag{2.4}$$

[2]Cross section in solid angle intervals $d\Omega$.

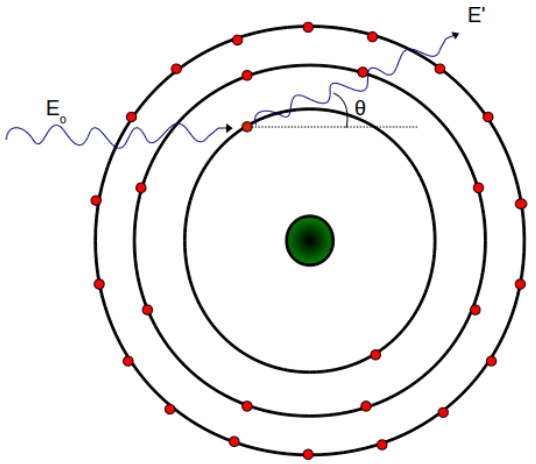

Figure 2.8: Diagram of the coherent scattering. An X-ray photon interacts with an atomic electron without energy exchange. The incident X-rays photons is scattered with angle θ and the same kinetic energy ($E' = E_0$).

where r_e corresponds to the classical electron radius ($2.8179380 \times 10^{-15} m$) [31, 34] and θ is the angle of the scattered X-ray photon with respect to its original trajectory as observed in Figure 2.8. If Equation 2.4 is integrated over the differential solid angle $d\Omega$, the total cross section for Thomson scattering σ_T becomes

$$\sigma_T = \frac{8\pi r_e^2}{3} = 6.652448 \times 10^{-29} m^2, \tag{2.5}$$

Note that according to equation 2.5, the Thomson cross section σ_T is constant.

The tissues investigated in medical imaging have electrons which are bound to an atom, so the σ_T is not truly correct for this case. The cross section for coherent scattering σ_{coh} is more representative in diagnostic images as it accounts for coherent interactions between X-ray photons and electrons attached to an atom. The differential cross section $d\sigma_{coh}/d\Omega$ is obtained from the product of $d\sigma_T/d\Omega$ (Equation 2.4) and the square atomic form factor $F^2(x, Z)$ [31, 34]:

$$\frac{d\sigma_{coh}}{d\Omega} = \frac{d\sigma_T}{d\Omega} \times F^2(x, Z), \tag{2.6}$$

where x is a measure of the momentum transfer and corresponds to $\frac{sin(\theta/2)}{\lambda}$, being λ the wavelength of the incident X-ray photon. The relationship between the energy of the photon E_0 and λ is

$$E_0 = \frac{hc}{\lambda}, \tag{2.7}$$

where h and c represents the Planck's constant and speed of light in vacuum respectively. The form factor $F(x, Z)$ introduces an energy dependency into the coherent scattering as well as the atomic structure (Z) that Thomson formula does not take into

account. This is translated into different scattering angular distributions for different energies and elements. However, $F(x, Z)$ assume that the atom is at rest and do not consider forces between atoms and molecules.

Figure 2.9 shows the distribution of scattering angles θ for adipose tissue and three photon energies. It is observed that coherent scattering produces mainly forward scattering, where $F(x, Z)$ is equal to the atomic number [31]. Then, as the scattering angle increases, the term $F(x, Z)$ decreases, making more difficult for a photon to scatter. Furthermore, as the photon energy is increased, the X-ray photon is more likely to scatter in smaller angles.

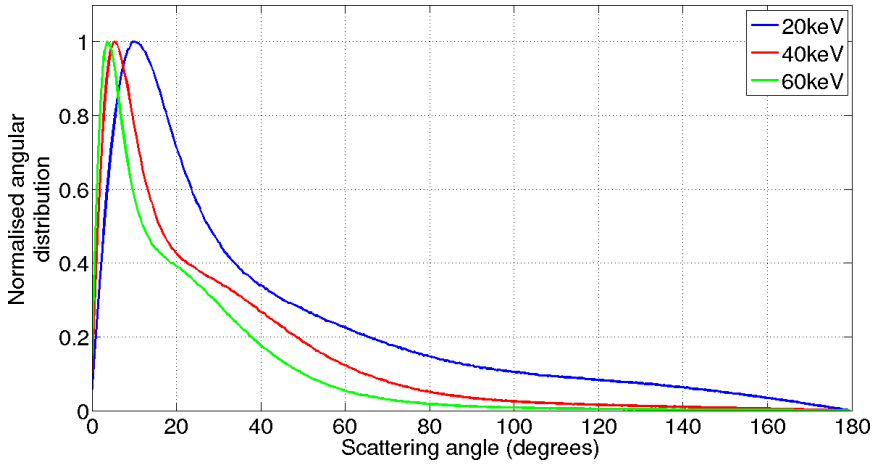

Figure 2.9: Shape of angular distributions for coherent scattering in adipose tissue calculated from Monte Carlo simulations. Results for three X-ray photon energies are shown, where each of them is normalised to a peak height of 1. Adipose tissue composition is described in Table 2.2.

2.2.3 Incoherent scatter

In incoherent scattering, the energy of the incident X-ray photon E_0 needs to be higher than the binding energy of the electron E_{BE}. The X-ray photon gives some of its energy to release the electron from its shell and it is scattered with energy E' and angle θ with respect to its original direction. The electron is ejected from its shell with an angle φ and energy T_e as illustrated in Figure 2.10. Thus after an incoherent interaction, an ionized atom, an electron and a scattered photon is produced.

Typically, incoherent scattering occurs where $E_0 >> E_{BE}$. Therefore, the outer shells of an atom are more likely to be affected by incoherent scattering [12].

The energy of the photon after the interaction E' can be approximated using the conservation of energy and momentum [31]:

$$E' = \frac{E_0}{1 + \alpha(1 + cos\theta)}, \tag{2.8}$$

where

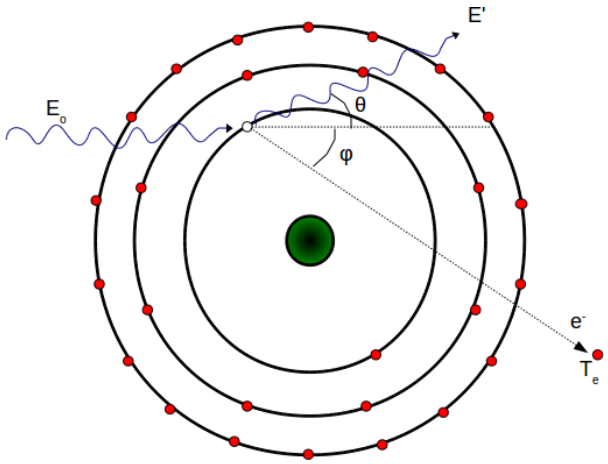

Figure 2.10: Diagram of the incoherent scattering. An X-ray photon interacts with an atomic electron. The incident X-ray photon is scattered with an angle θ with energy E' and the electron is ejected with angle φ from its shell carrying a kinetic energy of T_e.

$$\alpha = \frac{E_0}{m_o c^2}. \tag{2.9}$$

The term $m_o c^2$ corresponds to the rest-mass of an electron (511keV). Furthermore, the angle of the ejected electron φ corresponds to

$$cot\varphi = (1+\alpha)tan(\theta/2), \tag{2.10}$$

and its energy (T_e) can be calculated as the energy difference between the incident X-ray photon and the scattered X-ray photon ($T_e = E_0 - E'$), so the energy conservation is kept.

Compton scattering describes the interaction between an X-ray photon and a free electron at rest [31, 35]. The differential cross section for this scenario is described by the Klein-Nishina formula:

$$\frac{d\sigma_{KN}}{d\Omega} = \frac{r_e^2}{2}\Big(1+k(1-cos\theta)\Big)^{-2} \times \Big(1+cos^2\theta + \frac{k^2(1-cos\theta)^2}{1+k(1-cos\theta)}\Big), \tag{2.11}$$

where k corresponds to the photon energy in units of the electron rest-mass energy ($E(eV)/511003.4$). r_e is known as the classical electron radius.

To account for the fact that in practice, electrons are neither free nor at rest, the above equation is not truly correct in real scenarios. The incoherent scattering cross section σ_{inc} accounts for electrons binded to an atom, and corrects the above formula by multiplying it with the incoherent scattering function $S(x, Z)$. However, as described for $F(x, Z)$, $S(x, Z)$ has been assumed free atoms and the forces between atoms and molecules are not taken into account.

$$\frac{d\sigma_{inc}}{d\Omega} = \frac{d\sigma_{KN}}{d\Omega} \times S(x, Z). \tag{2.12}$$

$S(x, Z)$ is zero for the scattered photons in the forward direction. As the scattering angle increases, $S(x, Z)$ also increases towards the atomic number Z [31].

The cross section for incoherent scattering σ_{inc} is calculated by integrating Equation 2.12 over all angles from 0 to π. In many cases, σ_{inc} almost corresponds to the cross section for single electrons at rest times the atomic number of the atom [31]

$$\sigma_{inc} \approx Z\sigma_{KN}. \tag{2.13}$$

It is worth mentioning that the cross sections described here correspond to individual elements. In case of a compound or mixture, the total cross section corresponds to the weighted sum of the cross sections for each of the atomic elements found in the compound/mixture.

The distribution of scattering angles for the incoherent scattering interaction is shown in Figure 2.11, where larger scattering angles are observed compared to coherent scattering.

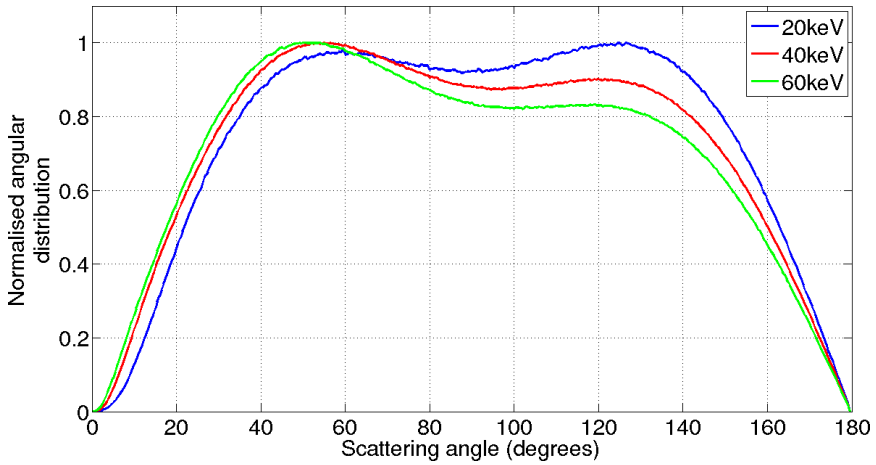

Figure 2.11: Shape of distribution of scattering angles for incoherent scattering in adipose tissue calculated from Monte Carlo simulations. Results for three X-ray photon energies are shown, where each of them is normalised to a peak height of 1. Adipose tissue composition is described in Table 2.2.

Low X-ray photon energies produce more backscatter (θ >90 ^{o}) while for higher X-ray photon energies, forward scatter is more likely. Because the scattered photons can travel over a wide angular range, these photons does not provide any information about the location of the interaction.

In this section, the X-ray photon interactions observed in the X-ray mammography energy range and their cross sections, which are proportional to their probability as shown in Equation 2.1, were described. These probabilities of interaction are combined to produce the total attenuation of an incident X-ray photon beam. The different total attenuation of separate tissues are used to create X-ray images as described below.

2.3 Principles of image formation

X-ray images are created using the different attenuation properties of the tissues or materials being imaged. The term attenuation refers to the removal of X-ray photons from an incident beam by absorption or scattering processes as they interact along a bulk.

Consider a single X-ray photon traversing normally a uniform material of thickness x as illustrated in Figure 2.12.

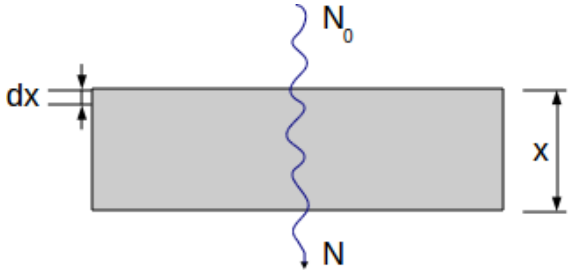

Figure 2.12: Diagram of a simple geometry where a photon traverses an object of thickness x.

It can be described, from Equation 2.1, that the probability of interaction of that photon in a thin section dx is

$$N_a \sigma dx, \tag{2.14}$$

where N_a is the number of atoms per unit volume and σ the total cross section. The product $N_a\sigma$ is known as the linear attenuation coefficient (μ) and has inverse unit to thickness dx, e.g. cm^{-1}. N_a for a given element or material can be calculated as

$$N_a = \frac{N_A \rho}{A_w}, \tag{2.15}$$

where ρ and A_w correspond to its density and atomic weight respectively and N_A is the Avogadro constant.

Using the same geometry as described in Figure 2.12, consider now that N_0 X-ray photons of the same energy, i.e. a mono-energetic beam, impinge normally onto a semi-infinite block of material of thickness x. Now, the probability for the N_0 X-ray photons to interact in dx would be $N_0\mu dx$. Therefore, the X-ray photon variation dN observed after traversing a thin slice, dx, is

$$dN = -N_0 \mu dx, \tag{2.16}$$

where the negative sign illustrates the reduction of X-ray photons. Integration of Equation 2.16 results in the exponential attenuation of an X-ray photon beam or Beer-Lambert law:

$$N = N_0 e^{-\mu x}. \tag{2.17}$$

This equation describes the number of primary photons, i.e. unscattered, after traversing a given material assuming parallel beam geometry. In the mammography energy range, μ corresponds to the combination of the the linear attenuation coefficients of all the X-ray photon interactions described in Section 2.2. Therefore,

$$\mu = \mu_{pho} + \mu_{coh} + \mu_{inc}, \tag{2.18}$$

where μ_{pho}, μ_{coh} ,μ_{inc} corresponds to the linear attenuation coefficients from photoelectric, coherent and incoherent scattering respectively. Each of these can be calculated as the product of the corresponding cross section (τ, σ_{coh} and σ_{inc}) and the N_a associated to a particular element as previously explained.

When a material is composed of a compound or mixture, the total linear attenuation coefficient is calculated as the summation of the linear attenuation coefficients of the ith elements (μ_i) which is properly weighted using the normalised weight fraction w_i of each of the elements or mixture components:

$$\mu = \sum_i w_i \mu_i. \tag{2.19}$$

Bear in mind that the example shown above corresponds to a mono-energetic X-ray beam. Thus no energy dependency has been shown. However, as previously explained in Section 2.2, the cross section for all individual mechanisms, and therefore μ, depends on the X-ray photon energy (see Figure 2.13).

The linear attenuation coefficient μ describes the attenuation properties for a given material. However, this attenuation depends on the density of the material (ρ). The denser the material, the greater the probability of interaction. In order to account for that, it is very common to illustrate the attenuation properties of a given material in terms of mass attenuation coefficient (μ/ρ), whose typical unit is cm^2/g. As in Equation 2.18, the total mass attenuation coefficient corresponds to the sum of the mass attenuation coefficient from individual interactions:

$$\frac{\mu}{\rho} = \frac{\mu_{pho}}{\rho} + \frac{\mu_{coh}}{\rho} + \frac{\mu_{inc}}{\rho}. \tag{2.20}$$

In a mammography scenario (see Section 2.4), X-ray photons travel from the X-ray tube until they are absorbed within any part of the system, including the image receptor, or as they leave the system. The X-ray photons reaching the image receptor can be primary or scattered photons, depending on their previous type of interaction as described in Section 2.2. The image receptor uses the energy deposited from primary and scattered photons to create the X-ray mammography image, also known as mammogram.

The distribution of primary X-ray photons in the mammogram contains useful information to visually separate the different tissue types in a X-ray mammography image, based on the different attenuation properties of these tissues. However, this task can be challenged for radiologist as glandular and tumour (carcinoma) tissues for example, have very similar attenuation properties (see Figure 2.13). They are typically differentiated due to differences in breast architecture [36].

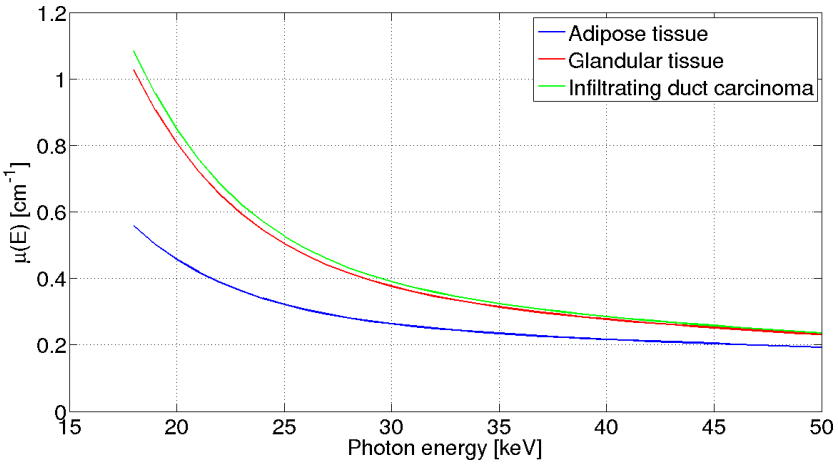

Figure 2.13: Linear attenuation coefficients for adipose, glandular and infiltrating duct carcinoma measured by Johns and Yaffe [37].

On the other hand, the scattered photons provides an offset signal which reduces the imaging performance of the system as will be explained in Chapter 3.

2.4 Geometry used in X-ray mammography scenarios

The main parts found in a typical X-ray mammography system are shown in Figure 2.14. They correspond, from top to bottom, to the X-ray tube where the X-ray photons are generated; a compression paddle, which is responsible for compressing the breast; the breast itself placed on a support plate; an anti-scatter grid whose main function is to geometrically reject scattered photons; and the detector where the X-ray radiation is absorbed.

Furthermore, an automatic exposure control (AEC) is typically found under the detector. This controls the amount of radiation that reaches the detector necessary to obtain good image quality. These main components are described below in more detail.

2.4.1 X-ray tube

An X-ray tube consists of a vacuum compartment wherein a filament in the cathode is heated by an electric current, then a narrow beam of electrons are accelerated by a potential difference between the cathode and the anode and finally high speed electrons strike the target material, or anode, producing X-ray photons as observed in Figure

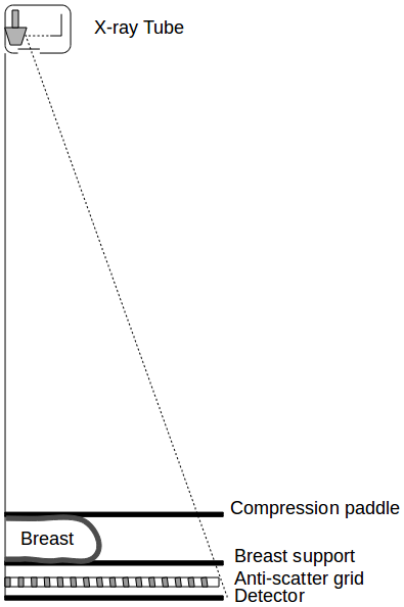

Figure 2.14: Diagram of a typical X-ray mammography system.

2.15(a). These X-ray photons are filtered and limited to the patient with the aid of a collimator.

As explained in Section 2.1, X-ray photons are produced as a consequence of these high speed electrons interacting with an atom or molecule, which corresponds to the anode, or target material in this case. For Bremsstrahlung radiation, X-ray photons of different energies are generated. The maximum photon energy is obtained when an electron interacts directly with the nucleus of an atom, where all the kinetic energy of the electron is transformed into an X-ray photon. In the X-ray tube, the kinetic energy of the electron is controlled by potential difference between the cathode and the anode and it represents the upper energy limit in the X-ray energy spectrum (kVp). Furthermore, characteristics radiation produces photon energies representative of the anode material. During the X-ray production, only 1% of the electrons hitting the anode produces X-ray photons, with the remaining energy dissipated as heat [30]. For this reason, target materials have a high melting point.

The anode material is key because it defines the shape of the resulting X-ray energy spectrum, which is mostly produced by Bremsstrahlung radiation. However, depending on the kVp selected, characteristics X-rays can be observed as illustrated in Figure 2.15(b). In X-ray mammography, molybdenum (Mo), W and rhodium (Rh) are the typical anode materials used due to their properties (e.g. high melting point) to generate a range of energy spectra from approximately 10 keV up to 50 keV.

The materials of both the target and filters as well as the tube voltage (kVp) are chosen according to the breast characteristics (composition and thickness) in order to obtain the lowest dose of radiation required to achieve acceptable image quality [38]. Dance et al. [39] studied the dose effects of a range of target/filter materials using MC simulations. They proposed optimal target/filter combinations for different breast thickness/compositions and detector technology (screen-film and digital detector).

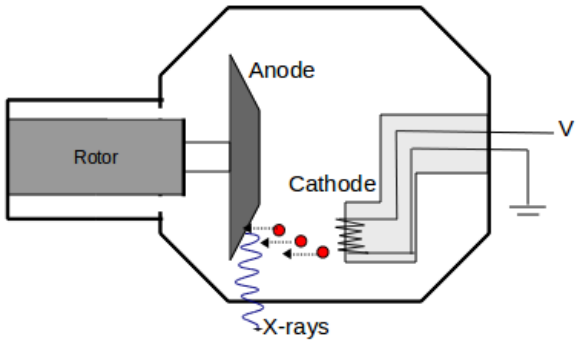

(a)

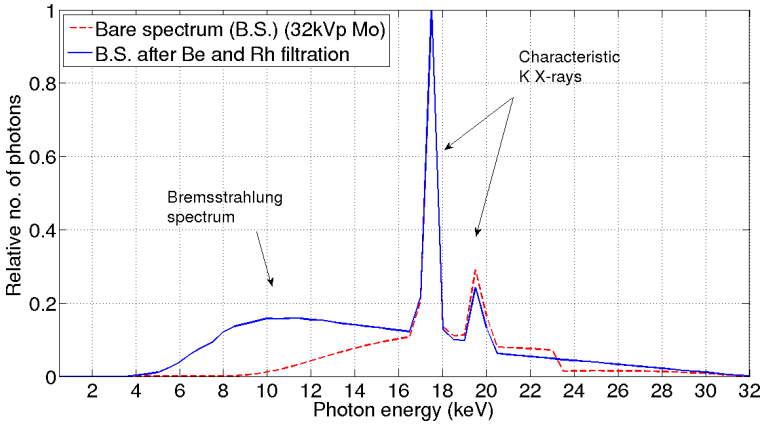

(b)

Figure 2.15: A diagram of a typical X-ray tube is illustrated in (a). The energy spectrum for 32 kVp Mo/Rh (target/filter) is shown in (b) before (blue) and after (red) being filtered.

When performing calculations analytically or using MC simulations, realistic X-ray energy spectra need to be used. Several authors have provided tabulated data to produce energy distribution of typical bare X-ray spectra [40, 41]. On the contrary, X-ray energy spectra can be generated after simulating the entire X-ray tube geometry in MC simulations [42]. However, this task can be very inefficient as only 1% of the electrons simulated are used to produce X-ray photons as previously stated. When simulating the X-ray spectrum of a given system, the half value layer (HVL) [3] also needs to be taken into account to match the exact X-ray spectrum.

Before leaving the X-ray tube, the X-ray photons are filtered in order to minimize lower and higher energies that are not useful for imaging purposes, reducing the dose imposed to the patient. This filtration can be applied mathematically using the aforementioned Beer-Lambert law (see Equation 2.17). A beryllium (Be) window is typically used to eliminate low energies while K edge filters of Mo, Rh, aluminium (Al) or silver (Ag) are employed to eliminate higher energies (above the K edge energy). Figure 2.15(b) shows a 32kVp Mo/Rh (target/filter) spectrum before and after filters are applied. Note how

[3] Thickness of aluminium required to reduce the exposure of the X-ray energy spectrum by half.

the spectrum is reduced for low energies due to the Be filter and, in this case, photons with energies above K edge of Rh (23.2keV) are strongly attenuated. The two peaks in the spectrum corresponds to the characteristic K X-rays for Mo: 17.4 and 19.7 keV.

The K edge energy and the characteristic X-ray energies for the most common target and filter materials used in mammographic X-ray tubes are described in Table 2.1.

Table 2.1: Characteristic X-ray and K edges energies for typical target and filter materials [32].

Z	Element	K_α (keV)	K_β (keV)	K edge (keV)
13	Al	1.5	1.6	1.6
42	Mo	17.4	19.7	20.0
45	Rh	20.1	22.9	23.2
47	Ag	22.0	25.1	25.5
74	W	58.7	67.8	69.5

2.4.2 Compression paddle

The compression paddle is typically a polycarbonate layer of thickness 2.4mm or more, which is responsible for compressing the breast. The main purposes of the compression of the breast are threefold. Firstly, it minimised the patient movement during the acquisition time which potentially blur the image. Secondly, the compression spreads the overlying tissues within the breast, so it helps to improve the visualisation of lesions. Finally, the effective thickness of the breast is reduced. The latter helps to reduce the scattered radiation, which degrades the image contrast, decreases the dose in the patient and improve the geometric unsharpness.

2.4.3 Breast (phantoms)

A mature breast is a mammary gland composed of variable portions of glandular and adipose tissue, surrounding by a thin layer of skin. Moreover, suspensory ligaments (Cooper's ligaments) support the breast between the skin and the chest wall.

Several physical anthropomorphic breast phantoms which mimic real breast morphology are found in the market (e.g. 'Rachel' (Gammex RMI, WI, USA) or CIRS (Norfolk, VA, USA)). Other breast phantoms, such as the Gammex-156 (Gammex RMI, WI, USA), have a shape different from a real breast (square), but they have several objects inserted to measure the ability to detect them. However, all of them have attenuation properties similar to real breast composition [43], which are obtained from a mixture of plastics. A common plastic used to mimic the breast attenuation properties is polymethyl methacrylate (PMMA). In fact, Dance et al. [44] described thicknesses of PMMA equivalent to a range of breast tissues from 2 to 11 cm.

When modelling the morphology of the breast mathematically, several authors have simulated the compressed breast using a cylinder of semicircular cross-section of certain thickness and glandularity, where a skin layer is often included [45, 46, 47]. Frequently,

a 'typical' breast is modelled using a composition of 50% adipose and 50% glandular tissue. However, Dance et al. [44] provided with the average breast composition for different breast thickness, associated to a particular women age range. Later on, Yaffe et al. [48] measured the glandularity in a 2,831 female cohort and found an average glandularity of approximately 20% (including skin), thus the assumption of a 50% adipose 50% glandular tissue might not be realistic in some studies.

More complex (and realistic) breast phantoms, which contain fine breast structures, have been developed by several authors [49, 50, 51, 52, 53]. In the work presented in this thesis, anthropomorphic breast phantoms developed by Bakic et al. [52] have been used. Examples of central slices of three of these Bakic phantoms are illustrated in Figure 2.16.

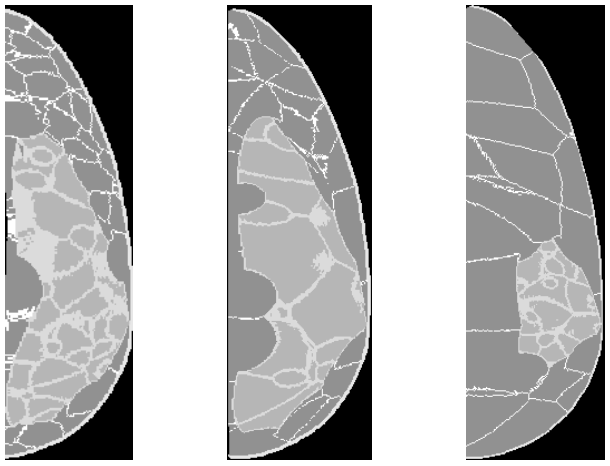

(a) 2.2cm (b) 5cm (c) 9.3cm

Figure 2.16: Central slices of anthropomorphic breast phantoms of different thicknesses and glandularities developed by Bakic et al. [52]. (a) corresponds to a 2.2cm thick breast phantom with glandularity of 30%, (b) represents a 5cm thick breast phantom with 20% glandularity and (c) illustrates a 9.3cm thick breast phantom whose glandularity corresponds to 9.6%.

As in all mathematical (breast) phantom models, it is necessary to assign a tissue to each of the voxels within the phantom to represent the attenuation properties of a real breast. In this work, the compositions of the adipose tissue, glandular tissue and skin within the anthropomorphic breast phantom observed in Figure 2.16 were taken from Hammerstein et al. [54], whereas the composition for Cooper's ligaments has been assumed to be that of adult skeletal muscle [55], as previously described by Ullman et al. [56]. Table 2.2 summaries the composition used in this work for the tissues found in the anthropomorphic breast phantoms shown in Figure 2.16.

Table 2.2: Breast tissue composition (in weight fractions) used for the tissues simulated within the anthropomorphic breast phantoms.

Tissue	Density(g/cm^3)	H	C	N	O	S	P	K	Ca	Na	Cl
Adipose [54]	0.93	0.112	0.619	0.0170	0.251	0.000250	0.000250	0.000250	0.000250	—	—
Glandular [54]	1.04	0.102	0.184	0.0320	0.677	0.00125	0.00125	0.00125	0.00125	—	—
Cooper Ligaments [55]	1.05	0.102	0.143	0.0340	0.710	0.00300	0.00200	0.00400	—	0.00100	0.00100
Skin [54]	1.09	0.098	0.178	0.0500	0.667	0.00175	0.00175	0.00175	0.00175	—	—

2.4.4 Breast support

In this work, the breast support, or Bucky table, is assumed to be 1.2-1.4mm thick polycarbonate table where the breast rests.

2.4.5 Anti-scatter grid

The main function of the anti-scatter grid is to permit passage of the primary (direct, or unscattered) X-rays photons to the image receptor and to geometrically reject scattered photons.

Anti-scatter grids are comprised of a septa material (lead or cooper) which is interlaced with a very low attenuation material (interspace), such as fibre, wood or air; also it contains a cover typically made of carbon fibre matching the detector size. Current anti-scatter grids are focused. This means that the septa material is aligned with the X-ray tube exit, thus the primary transmission through the grid is increased [45]. They also oscillate during the exposure time to avoid the visualisation pattern of the septa in the final image.

Grids are commonly specified in terms of their materials and geometrical parameters: lines per unit area, grid ratio (r), thickness (h) and width of the septa (d) and interspace (D). The grid radio r is defined as

$$r = \frac{h}{D}. \tag{2.21}$$

Two anti-scatter grid designs are found in X-ray mammography (linear and cellular) as illustrated in Figure 2.17. The linear design is more usually employed as this is simpler than cellular grids to manufacture.

In X-ray mammography, the typical strip densities observed for linear anti-scatter grids are 30 to 50 lines per cm whereas the most common r value rages from 3.5 to 5 [57]. For the cellular design, between 15 to 23 lines per cm and grid ratios from 3.8 to 4 are observed [58, 59]. Depending on the materials and physical dimensions, the anti-scatter grids absorb scattered radiation to different degrees.

As can be seen in Figure 2.17, most of the X-ray primary photons travel through the low attenuated interspace material whereas scattered X-ray photons (which have a different trajectory from the original primary photons) are absorbed by the septa material. However, as most of the scattered photons and some of the primaries are also absorbed by the septa material of the anti-scatter grid, an increase in the tube current

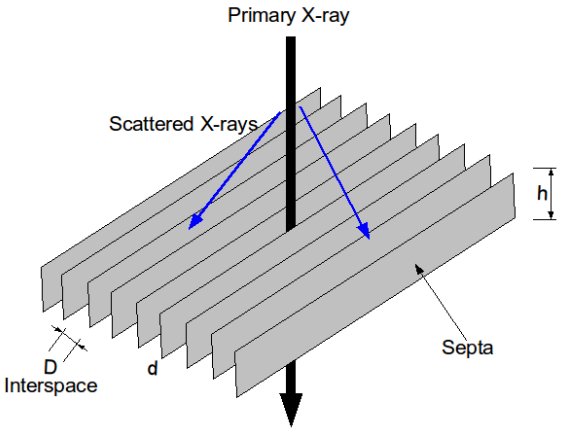

(a) Linear

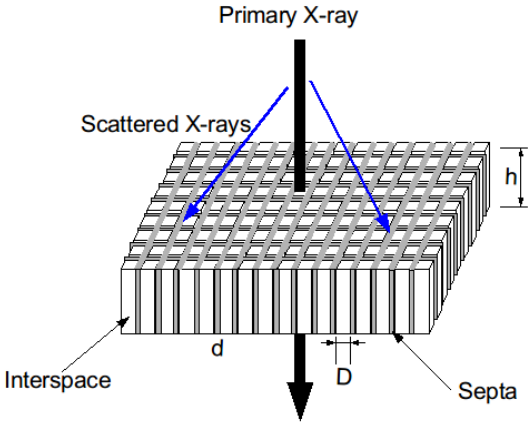

(b) Cellular

Figure 2.17: Diagram of different designs for anti-scatter grids: (a) linear and (b) cellular. The dimensions (h, d and D) are defined in the text.

of the X-ray tube is necessary to compensate for the loss of X-ray primary photons reaching the image receptor. This will inevitable increase the dose delivered to the patient [58], which could be up to three times in film-screen [60].

In order to study the performance of different anti-scatter grids, several assessment metrics are defined: contrast improvement factor (CIF), Bucky factor (BF), primary (T_p) and scatter (T_s) transmission.

T_p is the ratio of the primary signal observed in the image receptor with and without the anti-scatter grid and T_s the corresponding quantification for scattered radiation.

$$T_p = \frac{P}{P_0} \tag{2.22}$$

$$T_s = \frac{S}{S_0}, \tag{2.23}$$

where P_0 and S_0 corresponds to primary and scattered energy measured in the image receptor without an anti-scatter grid in place, whereas P and S are primary and scattered energy measure when the anti-scatter grid is employed. Ideally, all primary photons should travel across the anti-scatter grid without interaction (T_p=100%), whereas all the scattered photons should be absorbed by the septa material (T_s=0%).

The CIF measures the improvement in contrast (C) when the anti-scatter grid is used, thus high CIF values are desired. Bear in mind that, as previously explained, some of the primary photons are absorbed by the anti-scatter grid. This will harden the energy beam and produce changes in the contrast. The CIF is expressed as

$$CIF = \frac{C_g}{C_{ng}}, \tag{2.24}$$

where C_g and C_{ng} represent the contrast with and without anti-scatter grid respectively. Using the contrast definition described in Equation 3.1, Equation 2.24 can also be expressed as

$$CIF = \frac{1 + \frac{S_0}{P_0}}{1 + \frac{S}{P}}. \tag{2.25}$$

BF, defined as

$$BF = \frac{P_0 + S_0}{P + S}, \tag{2.26}$$

calculates the increase in dose resulting from using the anti-scatter grid while maintaining blackening on the film-screen. In digital detectors, BF is more conceptual, as the detector gain can be increased to account for the lost of radiation reaching the detector when using an anti-scatter grid [61]. Ideally, BF is desirable to be 1.

CIF and BF are often used to quantify the benefit and penalty of an anti-scatter grid respectively. They are related by the equation $CIF = Tp \times BF$. Further discussion on anti-scatter grids is found in Section 3.5, and an anti-scatter study on the two commercially available anti-scatter grid designs for mammography (linear and cellular) is shown in Section 5.7.

2.4.6 Digital detectors

The detector is the element of the X-ray mammography system where the X-ray photons energy is recorded after a photon interaction to generate the mammogram. As previously described, the two X-ray photon interaction processes which deposit energy within the X-ray mammography range are photoelectric absorption and incoherent

scattering. However, detectors are made of high atomic number (Z) materials, thus the main X-ray interaction is photoelectric absorption as the photoelectric cross section is proportional to Z^4 (see Equation 2.3).

Geometrically, detectors can be divided into flat panel detectors (FPD), where the entire detector covers the breast, or slot scanning detectors. In slot scanning detectors, the dimensions of the detector corresponds to a narrow rectangle, so this needs to be moved during the examination time in order to cover the entire breast geometry.

Regarding to the way the X-ray photons are absorbed, digital detectors can be described as *direct digital radiography (DR)* such as selenium-FPDs or *indirect digital radiography (ID)*, including phosphor-FPDs and computerised radiography system (CR). The difference between direct and indirect detectors is that the former records electrical charge directly from the interaction of the X-ray photons within the detector, while in indirect detectors, a phosphor transforms the X-ray energy into light which is detected using a photodetector.

In this section, only digital detectors are discussed. However, screen-film receptors (SFR), used in conventional X-mammography, are still used clinically. SFRs consist of a phosphor, typically gadolinium oxysulphide (Gd_2O_2S:Tb), and an emulsion film which is in contact with the phosphor. The impinging X-ray photons are absorbed by the phosphor and they are converted into light, which exposes the emulsion of the film. The film is then developed before being viewed.

The most common materials of the aforementioned X-ray detector types are illustrated in Table 2.3 along with their densities.

Table 2.3: Typical X-ray detector materials [12].

Composition	Density (g/cm^3)	Type
Gd_2O_2S:Tb	7.34	Film-screen
CsI:Tl	4.51	ID
Se	4.26	DR
BaFBr:Eu	4.56	CR
Si	2.33 [62]	Photon-counting

An important parameter to take into account when using a detector is its energy absorption efficiency (EAE). This metric represents the fraction between the energy absorbed within the detector and the incident energy. The EAE for some of the detectors materials described in Table 2.3 are shown in Figure 2.18. The detector thicknesses presented correspond to commercially available detectors. Note the increase of efficiency at the K edges.

Phosphor-FPD

In this system (see Figure 2.19(a)), X-ray photons are absorbed by a phosphor layer, such as thallium-activated cesium iodine (CsI:Tl). The phosphor is located on a large plate composed of amorphous silicon (a-Si) on which a matrix of photodiodes is found.

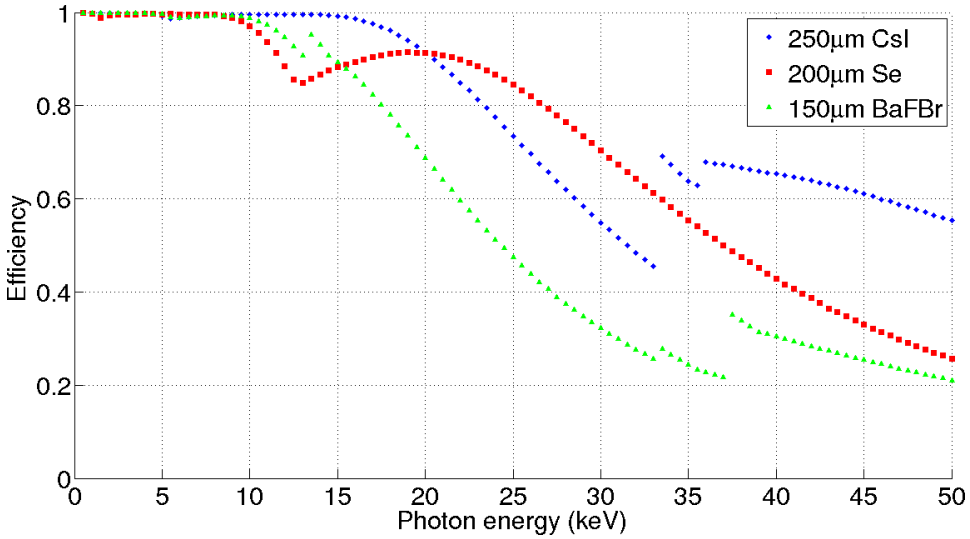

Figure 2.18: Energy absorption efficiency calculated from MC simulations for commercially available detectors.

The photodiodes collect the light emitted by the phosphor, after the interaction of X-rays, and the electronics below converts it to an electrical charge signal. Then the electric signal is transferred sequentially to the readout electronics using 'sample and hold' circuitry based on thin-film transistors (TFT) to create the final image. In order to reduce lateral light spread after X-ray absorption in the phosphor, the CsI crystal can be designed in needle-like shape. This design allows to increase the thickness of the phosphor, which improve the efficiency of the detector without much resolution lost [12, 63, 64].

The ability to perform rapid-sequence imaging is one of the major advantages of this detector [65]. This detector has a large pixel size because a relatively large area within the photodiode is occupied by a TFT transistor, e.g. GE produces phosphor-FPD detectors with pixel sizes of 100μm [63]. Other disadvantages of this detector are the high cost of the detector and the possibility of having residual signals from previous exposures (ghosting) [65].

Selenium-FPD

Instead of a phosphor, this (DR) X-ray detector employs a thin layer (100-200μm) of amorphous selenium (a-Se), a photo-conductor, to absorb the X-ray photon energy [64]. After the X-ray absorption, an electric charge is generated in the form of electron-hole pairs. This charge signal is then collected by a matrix of collection electrodes, which are placed on the upper and lower surfaces of the Se layer, with the aid of an electric field applied between the electrodes (Figure 2.19(b)). Finally, the charge signal is transmitted along the readout lines previous the image generation.

Like Phosphor-FPD, this X-ray detector also contains TFTs. However, the fill factor[4]

[4]Fraction of the area of each detector element that is sensitive to incoming radiation.

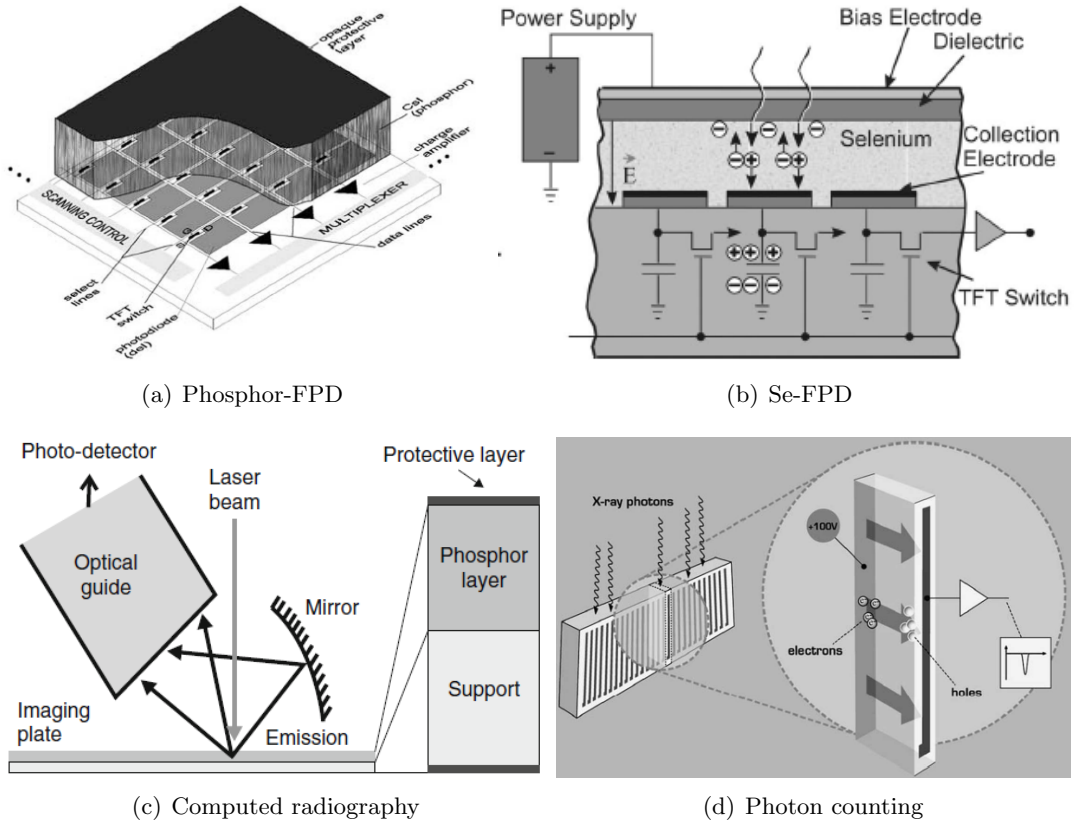

(a) Phosphor-FPD

(b) Se-FPD

(c) Computed radiography

(d) Photon counting

Figure 2.19: Common digital detectors for X-ray mammography: (a) phosphor-FPD [63], (b) Se-FPD [65], (c) computed radiography detector (single-side reader) [64] and (d) SECTRA photon counting detector [63].

is larger than Phosphor-FPD as the electric charge can be moved toward the collection electrode (active region) by controlling the electric field [63] as illustrated in Figure 2.20. This reduces the lateral spread of the signal and help to keep the detector thickness large enough to achieve a high efficiency [63]. Hologic produces Selenium-FPD with a pixel size of 70μm. On the other hand, Se-FPDs are very expensive and a high biasing voltage is needed [65]. This high voltage increases the energy consumption of the system as well as increases the temperature in the detector. They also require long time between exposures (50-70s) that can reduce throughput in a screening scenario [66].

Computed Radiography System

In this system, the process of data acquisition and read out are independent. In the acquisition stage, the X-ray absorber, which is embedded in a cassette, corresponds to a phosphor screen with photostimulable luminescence properties (typically BaFBr:Eu). Energy from X-ray absorption causes free electrons in the phosphor crystal. Some are recombine and emit light and others are captured and stored in traps within the crystal

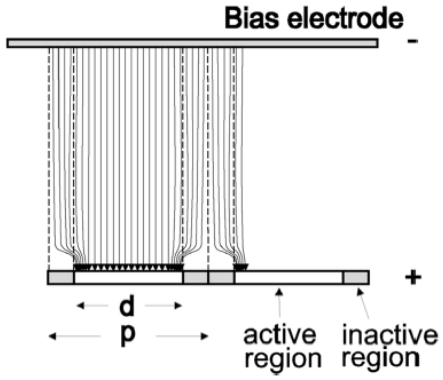

Figure 2.20: Diagram illustrating the high effective charge collection in Se detectors. An electric field moves the charge to the active region of the detector element. Image taken from [63].

lattice. In a particular location, the number of filled traps is proportional to the X-ray energy absorbed.

For the read out stage, the cassette is removed and placed in a separate reader, where it is scanned using a red laser beam. While scanning the cassette, electrons are reliberated from the traps and return to their original state in the crystal. As the crystal structure is doped by certain materials, the electron may pass between energy levels which are determined by these materials. Typically, the chosen dopped materials produce energy levels which correspond to blue light, which is proportional to the energy absorbed in the phosphor. Then, the blue light is measured by an optical collecting system using mirrors to avoid interference from the red laser beam. In order to increase the efficiency of the light collection, some manufacturers scan both top and bottom surfaces of the cassette (double-side reader).

This detector technology has allowed to reduce the pixel size down to 50μm [63, 65], thus small lesions might be visible. Furthermore, it can be manufactured in different dimensions at a relative low cost, so it can be employed as a detector in different systems [65]. Potential weaknesses are loss of spatial resolution and additional noise due to scattering of the laser light, difficulty of performing 'flat-field' corrections [5] and the extra time needed for processing the images [65].

Photon counting detector

The previous X-ray detector technologies described correspond to energy integrating detectors, where the energy deposited by X-ray photons within the detector, via photoelectric absorption or incoherent scattering, is used to create the X-ray mammography image. The signal recorded in the this type of detectors is approximately proportional to the absorbed photon energy [67]. Therefore, high energy photons will have a higher contribution (or weight) than low energy photons.

[5] Algorithm to correct for non-uniformities in the detector due to pixel's variations.

Figure 2.13 illustrates μ values of several tissues for a range of energies. It is observed that the largest difference in μ, and therefore contrast, occurs for low energy. However, in the previous paragraph is was described how high energy photons produce higher signal in the detector.

In photon counting detectors each X-ray photon interaction is counted independently of its energy, thus all interactions have a weight of one. Once an X-ray photon interacts in the detector, the corresponding detector element produce an electronic pulse. All the pulses are counted to create the final image.

The Sectra MicroDose mammography system [68] (now Philips Healthcare) is a currently available photon counting system which employs Si crystals (see Figure 2.19(d)). The Si absorbs the impinging X-ray photons and electronhole pairs are produced. These are collected as previously explained for Selenium-FPD systems. Then the electric signal is shaped in a pulse and finally threshold to produce a count.

This technology largely eliminates the electronic noise in the detector due to energy conversion [63]. This is because the X-ray interactions can be easily distinguish from the electronic noise by adjusting the threshold level [69]. Moreover, it can improve the contrast-to-noise ratio (CNR) for a given material if an optimal weight is applied to a given energy range (energy weighting) [70]. However, the largest disadvantage of photon counting detectors is their high cost. Furthermore, these detectors need to be able to account for the high X-ray interactions per second observed in mammography, which can be 10^6 photons in each pixel or higher for an unattenuated beam [63]. In fact, the Sectra MicroDose system described previously illustrates a frame rate of 5 MHz, allowing up to $5x10^6$ photons counts per second per pixel [69].

2.4.7 Automatic exposure control

An AEC consists of an X-ray sensor beneath the detector. Its main function is measuring the amount of X-ray radiation that reaches the X-ray imaging receptor. In conventional mammography, AEC is necessary in order to obtain a good contrast in the image avoiding overexposure and underexposure of the SFR. On the other hand, in FFDM the AEC sets the radiation level to determine a good signal-to-noise ratio (SNR).

2.5 Breast imaging modalities

In the previous section, the typical geometry found in X-ray mammography systems was described. However, different X-ray technologies are available to image the breast. This section illustrates an overview of the main technologies currently use or being explored for X-ray breast imaging.

2.5.1 Full-field digital mammography

X-ray mammography has been proven to be the gold standard technique for early breast cancer detection and it is the standard radiological technique used in breast cancer

screening [6]. There have been a large array of improvements achieved in breast cancer detection in the last few years, but arguably the most important was the introduction of digital detector technology [66], which permits the various imaging processes involved (image acquisition, storage and image display) to be optimised independently.

Full-Field Digital Mammography (FFDM) was approved for clinical use by the U.S. Food and Drug Administration (FDA) in 2000 and it has been found to perform as good as screen-film X-ray mammography (SFM) [15, 16, 17, 9]. However in the Digital Mammographic Imaging Screening Trial (DMIST) [9, 10], conducted by the American College of Radiology Imaging Network (ACRIN), it was found that FFDM detects breast cancer slightly better in women with dense breast composition. This finding represents a huge advantage of FFDM compared with SFM as breast cancer in dense breast are easily missed [13, 14].

Although two dimensional (2D) planar X-ray mammography is currently the widest accepted modality to detect breast cancer, it suffers from some limitations due to the superposition of three dimensional (3D) anatomical structures onto the 2D projected image [71]. This superposition effect may obscure real lesions (reducing sensitivity) or even simulate the appearance of pathology (reducing specificity), where none exists. Thus, other technologies such as digital breast tomosynthesis (DBT) and computed tomography (CT) breast imaging are being currently investigated as explained in the following sections.

2.5.2 Digital breast tomosynthesis

DBT [72, 73] is an emerging technology currently under investigation, which could overcome the aforementioned limitations found in 2D planar X-ray mammography. In 2011, the U.S. FDA approved a DBT system (Hologic Selenia Dimensions) to be used clinically, however several other systems are currently being used in Europe (e.g. Siemens Mammomat Inspiration) [74, 75]. Clinical results have shown the potential increase in sensitivity when using DBT technology [76] as lesions become clearer to radiologists [77].

DBT geometry differs slightly from manufacturer to manufacturer (e.g. static vs rotating detectors). However, it contains almost all the parts found in FFDM (see Section 2.4). In fact, some manufacturers integrate DBT technology into FFDM X-ray mammography devices, which is an advantage in economic terms.

Unlike FFDM, the X-ray tube is moved in DBT during the acquisition time with respect a rotation point (at or close to the detector) forming an arc as illustrated in Figure 2.21. While the X-ray tube is moved, the X-ray detector can be moved or it can remain static. This produces a series of 2D low-dose X-ray projections of the breast taken at different (but limited) angles, being the total dose similar to the dose observed in FFDM [78, 79]. The raw X-ray projection recorded within the detector for each projections are then processed using a reconstruction algorithm (e.g. filtered backprojection), creating a pseudo-3D image representation of the breast. This pseudo-3D image provides cross-sectional views of the breast at different depths, where a given plane (parallel to the detector surface) is shown in sharp focus while the obfuscating anatomical clutter from

other planes is displayed out of focus. DBT can achieve very high resolution in the planes parallel to the detector [80, 81], whereas lower resolution is observed in the planes perpendicular to the detector. However, this resolution is enough to reduce the tissue superposition [75] .

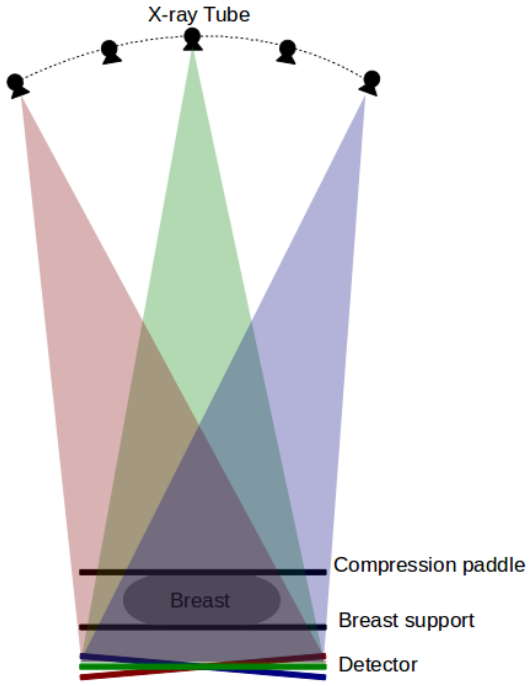

Figure 2.21: Diagram of a DBT system. The breast is imaged at different (but limited) angles. For some manufacturers, the detector remains static during the acquisition time, whereas others rotate the detector in synchrony with the X-ray tube.

One of the main disadvantages of using DBT is the significantly increased amount of scatter observed in the image receptor for each projection with respect to that encountered in planar X-ray mammography. This is due to the absence of an anti-scatter grid in most of the DBT commercial systems. Generally, the image receptor remains static while the X-ray tube is swept through a limited arc; a conventional fixed anti-scatter grid (see Section 2.4.5) would absorb much of the primary photons [82]. Thus relatively large scatter fields are present in the projection images which need to be estimated as part of any correction scheme to reduce the contrast-reducing effect of this undesirable component, and to minimise the associated error during reconstruction [83, 24].

As the tissue superposition problem encountered in FFDM is reduced in DBT, a reduction in the breast compression may be possible. This idea was studied by Saunders et al. [84] and Förnvik et al. [85]. They both agree that a breast compression reduction is possible in DBT while maintaining the same imaging performance. Furthermore, this will also mitigate the discomfort of the patient when having the breast compressed during the examination. However, this topic needs further investigation as the compression of the breast has further benefits as mentioned in Section 2.4.2.

Despite DBT being approved to be used clinically, there are several parameters that need to be optimised in order to improve breast cancer detection: the number of projections used during the data acquisition; maximum angle of the arc described by the X-ray tube, etc. Moreover, different algorithms can be applied in order to reconstruct the pseudo-3D breast image after the acquisition and need to be studied in depth.

It is still early to say that DBT will substitute FFDM in breast screening. The technology needs to be optimised as previously said. Furthermore, as discussed by Tingber [86], in spite of the examination time being similar for both FFDM and DBT, the time required for a radiologist to read a DBT image is approximately twice the time needed for FFDM as more data is generated.

2.5.3 Dedicated breast CT

In DBT, the limited angles used by the X-ray tube produces pseudo-3D images of the breast which reduce the aforementioned tissue superposition problem. However, some cancers can be well hidden in dense tissue background by DBT. In order to improve lesion detection, investigators are currently looking at breast CT technology [87, 88], where true 3D breast images are generated after imaging the breast over 360^o.

The examination procedure is quite different to both FFDM and DBT. In breast CT, the patient lies in prone position on a bed table introducing one breast in an aperture as observed in Figure 2.22. Under the bed table, the hanging or pendant breast is imaged using an X-ray tube and a detector which are rotated 360^o around the breast during the examination. A small pressure from the nipple to chest wall direction can be applied to minimise the movement of the breast as both X-ray tube and detector rotate, thus the patient discomfort from breast compression observed in FFDM and DBT is largely removed.

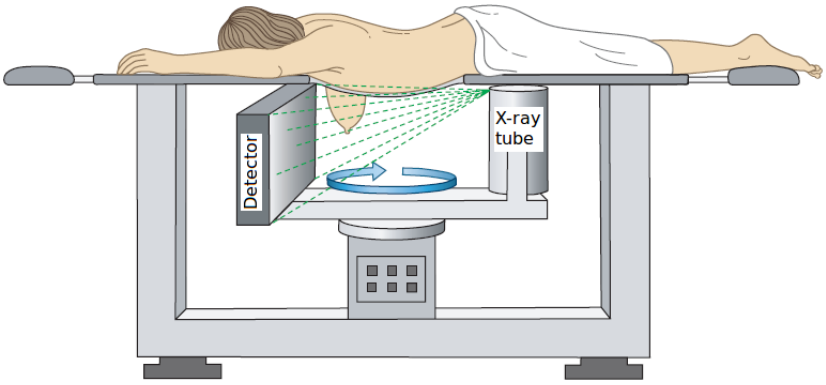

Figure 2.22: Diagram of a cone-beam breast CT scanner using a flat panel detector. The breast is inserted into an aperture on a bed table and it is scanned while hanging as observed. Image adapted from [89].

Like DBT, an image reconstruction stage is necessary to generate the final 3D volume of the breast, where transverse, coronal and sagittal slices of the breast can be displayed [89]. This provides further depth information for the breast which can be used

to increase the breast cancer detection [88, 89]. On the other hand, this 3D volume generates a lot of information which will increasing the time needed for the radiologist to examine the images, making difficult the use of breast CT in routine breast screening [90].

Scatter represents an important topic to study in flat panel breast CT, as it produces image artifacts after the reconstruction [89]. As the breast is not compressed in breast CT, the path lenght in the breast tissue is greater, thus the scattered radiation observe within the detector is also higher. In order to reduce scatter in dedicated breast CT, Kwan et al. [91] studied different approaches. They found that the dose penalty when using a conventional anti-scatter grids was high, so it is not recommended. They suggested to increase the air gap distance between the breast and the detector or collimate the field of view. The former might have problems associated with the magnifications, whereas the latter represents the approach taken by other authors when proposing slot scanning [67, 70] or spiral CT geometries [92].

Currently, there is only one dedicated breast CT scanner approved for clinical use in Europe (Koning Breast CT) [93]. However, several research groups have been working on the design of different prototypes [88, 92, 94, 95]. Preliminary results have shown the feasibility of detecting lesions and microcalcifications in breast CT while using doses comparable to two views FFDM [87, 92, 95]. However, further investigation is necessary to explore the optimal parameters to use in breast CT and the potential replacement of FFDM in diagnostic breast imaging and/or breast screening.

2.6 Summary and discussion

The physical processes more relevant in X-ray breast imaging have been described in this chapter as they represent a cornerstone to this thesis. Photoelectric effect is the predominant X-ray photon interaction at lower energies while incoherent scattering is more likely to occur at higher energies. The combination of both, together with coherent scattering, is responsible for the different tissue contrast displayed in the mammograms. As will be explained in the following chapter, both scattering processes cause an undesirable signal at the detector.

Photoelectric effect and incoherent scattering are the only two X-ray photon interactions which deposit energy within the mammography energy range (0-50keV). They are responsible for the image formation as the energy deposited for these processes is recorded within the image receptor. However, they can also deposit energy in the breast tissue, contributing to patient dose.

A typical X-ray mammography system has been characterised, where special emphasis has been put on the X-ray tube and X-ray energy spectrum generation, breast phantoms, anti-scatter grids and image detectors.

Several mathematical breast phantom models have been described, where the anthropomorphic breast phantoms used in this project were shown, together with the tissue composition employed. The use of these 3D breast phantom models is very important. Not only do they provide a realistic representation of a breast, but also simulated breast

lesions [96, 97] or microcalcifications [98] can be inserted in order to study the detection performance for a given system as described by Elangovan et al. [99].

Most of the FFDM systems include an anti-scatter grid to reduce the amount of scattered radiation that reaches the image receptor. A description of the geometries available (linear and cellular) as well as the typical assessment metrics (T_p, T_s, CIF and BF) are illustrated in this chapter. This information is essential to understand the scatter rejection performance for the commercially available anti-scatter grids shown in Chapter 5.

The different digital detector technologies are discussed in Section 2.4.6. The image generation for IR, DR and CR detectors are explained, together with their advantages and disadvantages. Furthermore, photon counting detectors are introduced.

In the penultimate section of this chapter, the most common X-ray breast imaging technologies are reviewed. It starts with the FFDM, which represents the gold standard technique for early breast cancer detection. Despite this technology being used for long time for breast cancer detection, it suffer from limitations due to breast tissue superposition. For this reason, researchers are investigating alternative technologies such as DBT and dedicated breast CT. They both have potential to overcome the limitations of FFDM and increase the breast cancer detection [100]. However, as emerging technologies, there are still a lot of parameters to be optimised if they want to be included as breast screening tools.

One of the major disadvantages of both DBT and breast CT is the relatively large amount of scattered radiation observed in the detector compared to FFDM. This is due to the absence of anti-scatter grids in most of their geometries. For that reason, scatter modelling techniques are necessary to reduce scattered radiation as part of a post-acquisition step. In the next chapter, the effect of scattered radiation in X-ray imaging as well as how is it quantified and reduced are described.

Chapter 3

Scatter and its effects on mammograpghy

The main topic of this thesis is the study and characterisation of the scattered radiation in X-ray mammography imaging. For this reason, a detailed study on X-ray photon scatter is necessary to understand its behaviour and the consequences of this behaviour.

In this chapter, the role of scattered radiation in X-ray mammography is described together with the typical techniques found in the literature for scatter estimation and scatter reduction. Furthermore, the effects of scattered radiation when changing parameters, such as breast thickness or glandularity, are discussed.

3.1 Effects of scattered radiation

It was explained in Section 2.3 that radiological images, such as mammograms, are created within the image receptor using the energy deposited from primary and scattered photons. The distribution of primary X-ray photons contains useful information to visually separate the different tissue types in a mammography image, based on the differing attenuation of these tissues. However, scattered X-ray photons acts as a background signal in screen-films image receptors that reduces contrast as demonstrated below, and therefore diagnostic effectiveness is reduced [24, 57]. With the arrival of digital image receptors, contrast can be adjusted to enhance the visualisation of the mammographic image. Consequently, in digital mammography systems, the scatter degradation is typically quantified using the differential signal-to-noise ratio (SNR_d) [101, 102, 103], which is very often called contrast-to-noise ratio (CNR). Fahrig et al. [104] quantified the reduction in contrast and SNR_d up to 50% and 55% respectively due to scattered radiation in both screen-film and digital detectors.

In order to demonstrate the relationship between the scattered radiation and the contrast, an example is discussed below. In Figure 3.1(a), a simple model of an object with linear attenuation coefficient μ_1 and thickness x_1 embedded in a larger object (background) with linear attenuation coefficient μ_2 and thickness x_2 is represented. It has been assumed that μ_2 is greater than μ_1. I_1 and I_2 represent, in this case, the

intensity (or energy deposited) of the X-ray photons after traversing both the object and background respectively as shown in Figure 3.1(b). Note that a parallel beam geometry and monoenergetic X-ray photons have been assumed in this example.

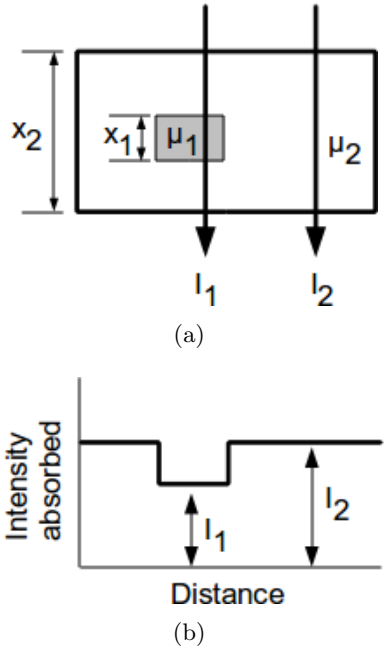

Figure 3.1: (a) shows a model used for the estimation of contrast assuming parallel beam geometry. x_1 represents the thickness of an object with linear attenuation coefficient μ_1, whereas x_2 is the thickness of the background, which linear attenuation coefficient is μ_2. Figure (b) represents a profile of the energy absorbed in the image receptor. I_1 and I_2 are the signal intensities recorded beneath the object and background respectively.

Using the signal intensities (i.e. energy deposited) under both the object and background, the contrast C can be defined as

$$C = \frac{I_2 - I_1}{I_2}, \tag{3.1}$$

where each signal intensity shown in Figure 3.1(b) is described as a combination of the primary (P) and scatter (S) signal (or energy deposited). Let assume that I_2 is described as

$$I_2 = P + S, \tag{3.2}$$

then, the signal intensity I_1 can be calculated using the well-known Beer-Lambert law through the energy beam. As the scatter is a low varying signal, it can be assume that S is the same beneath the object and background. Consequently, I_1 can be written as

$$I_1 = P \cdot e^{-(\mu_2 - \mu_1) \cdot x_1} + S. \tag{3.3}$$

Inserting Equation 3.2 and 3.3 into Equation 3.1, C can therefore be reformulated as

$$C = \frac{1 - e^{-\Delta\mu \cdot x_1}}{1 + \frac{S}{P}}, \tag{3.4}$$

where $\Delta\mu$ corresponds to $(\mu_2 - \mu_1)$. From Equation 3.4, it is observed that C not only depends on the object thickness (x_1) and attenuation properties along the the incident X-ray beam $(\Delta\mu)$, but, S also plays an important role, it being desirable to reduce S as much as possible.

By definition, the SNR_d illustrates the relation between the differential intensity between object and background $(I_2 - I_1)$ and the background noise (σ) [12]. The two major contributions of σ in the mammographic image are the quantum noise [1] and the noise generated within the image receptor and its electronics [27]. The SNR_d is represented as

$$SNR_d = \frac{I_2 - I_1}{\sigma}. \tag{3.5}$$

Using the contrast shown in Equation 3.1, the SNR_d can be rewritten as

$$SNR_d = \frac{C \cdot I_2}{\sigma}, \tag{3.6}$$

where it is observed the relationship between SNR_d and the contrast C. Therefore, scattered radiation needs to be reduced as much as possible to obtain the maximum contrast and SNR_d.

To sum up this section, it has been demonstrated that the scatter radiation produces an undesirable signal in X-ray imaging in general and mammography in particular, therefore low S is desired to improve lesion detection. For this reason scatter rejection devices and post-processing algorithms have been widely studied to reduce the effects of scatterer radiation in both 2D planar X-ray mammography and DBT.

3.2 Quantification of scatter

As described in the previous section, scatter is an unwanted radiation recorded within the image receptor of X-ray imaging technologies. In order to study its behaviour and so eventually minimise its deleterious effects on image quality, scatter intensity and its spatial distribution have been important topics of study in the literature for many years, e.g. [46, 47, 82, 105, 106, 107].

[1] Fluctuation in the number of photons per unit area.

3.2.1 Magnitude

The magnitude of the scattered radiation observed at the image receptor of a given system is normally quantified in terms of SPR or scatter fraction (SF):

$$SPR = \frac{S}{P}, \tag{3.7}$$

$$SF = \frac{S}{S+P}, \tag{3.8}$$

where S and P indicate the signal or integrated energy deposited within the imaging receptor from the scattered and primary radiation components respectively as explained above. SPR represents the amount of scatter with respect to the primary only signal, whereas the SF measures the quantity of scatter found in the total image recorded.

The values of both SPR and SF can vary depending on different parameters (energy, composition, imaging geometry, etc.) as will be discussed in Section 3.4. Table 3.1 illustrates examples of SPR and SF values described in the literature for a range of breast thicknesses [61, 108]. These specific values have been calculated experimentally for an X-ray mammography geometry without anti-scatter grid. PMMA phantoms of breast glandularity equivalent to 43% and an energy spectrum of 32kVp Mo/Mo target/filter combination have been used.

Table 3.1: Examples of SPR and SF values after imaging a PMMA phantom of breast glandularity equivalent of 43% and an energy spectrum of 32kVp Mo/Mo without anti-scatter grid [61, 108].

Thickness (mm)	SPR	SF
20	0.21	0.17
40	0.36	0.26
60	0.54	0.35
80	0.71	0.42

3.2.2 Spatial distribution

By definition, the point spread function (PSF) represents the spatial response of an imaging system to an input of a point source.

Consider that a narrow X-ray photon beam is introduced in the centre of an X-ray imaging system perpendicular to the image receptor. Then, the image recorded within the image receptor corresponds to the PSF of the system or $PSF_{sys}(r,\theta)$. Note that the PSF has been described in polar coordinates (r,θ) because it might not be radially symmetric as will be discussed below.

This $PSF_{sys}(r,\theta)$ corresponds to the energy contribution from the primary, $PSF_p(r,\theta)$, and scattered X-ray photons, $PSF_s(r,\theta)$), recorded within the image receptor:

$$PSF_{sys}(r,\theta) = PSF_p(r,\theta) + PSF_s(r,\theta). \tag{3.9}$$

The $PSF_s(r,\theta)$ component (or scatter PSF) gives the spatial distribution of the scattered radiation in the image domain. In other words, the $PSF_s(r,\theta)$ provides information about how far the scattered radiation is spread. An example of two scatter PSFs for a narrow pencil beam are shown in Figure 3.2, where a case of narrow and wide scatter spread are shown.

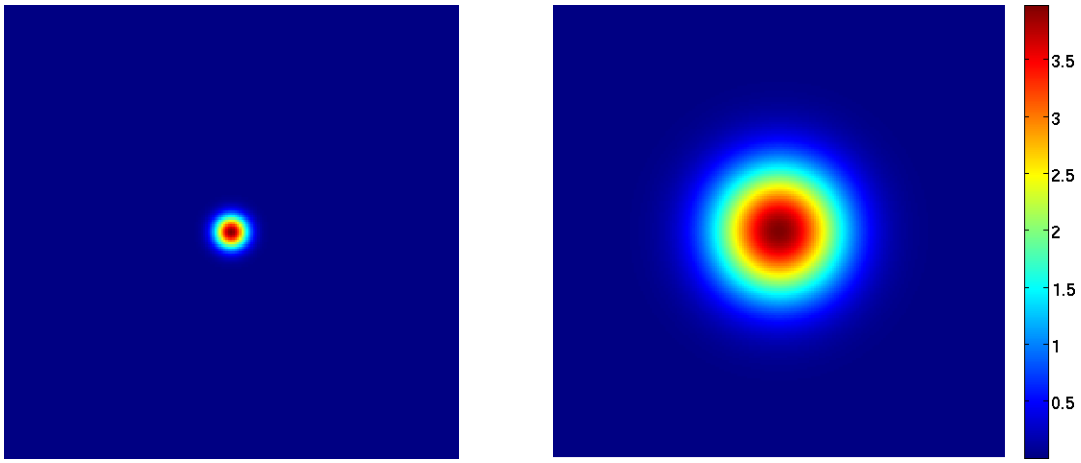

(a) Narrow scatter spread (b) Wide scatter spread

Figure 3.2: Example of the two scatter PSFs. The images correspond to the energy recorded within the detector (in keV) due to scattered X-ray photons.

The $PSF_s(r,\theta)$ is typically normalised to the total energy deposited by the primary X-ray photons.

$$PSF'_s(r,\theta) = \frac{PSF_s(r,\theta)}{\int_{\theta=0}^{2\pi}\int_{r=0}^{\infty} PSF_p(r,\theta)d\theta dr}. \tag{3.10}$$

Thus the area under the $PSF'_s(r,\theta)$ curve would correspond to the SPR value for a circular field of radius r_1 as illustrated in Equation 3.11.

$$SPR = \int_{\theta=0}^{2\pi}\int_{r=0}^{r_1} PSF'_s(r,\theta)d\theta dr. \tag{3.11}$$

In order to account for any pixel size observed in the image receptor, the $PSF'_s(r,\theta)$ shown in this work is expressed as a function of SPR per unit area (e.g. mm^{-2}). Therefore, the scatter distribution can be calculated for any detector pixel size by multiplying by the area of the detector's pixel.

In the literature, rectangular [20, 109], triangular [20], exponential [20, 23] and Gaussian [20, 21, 22, 108] distribution functions have been investigated in an attempt to accurately model the scatter PSF, the most commonly accepted being the exponential and Gaussian distributions. Both the intensity and the radial extent vary depending on various parameters as described in Section 3.4.

In all these aforementioned publications, the scatter distribution function has been considered to be radially symmetrical. However, it has been demonstrated that the scatter response function can suffer from asymmetry due to local variation in thickness [110, 111], primary beam angle [82, 112] or in presence of an anti-scatter grid [113] among others. For this reason, scatter PSFs have been calculated using polar coordinates in this work.

Figure 3.3 illustrates two examples of $PSF'_s(r,\theta)$ estimated for a $50mm$ thick circular phantom of glandularity 20% without an anti-scatter grid when using an ideal detector (100% efficiency). The $PSF'_s(r,\theta)$ has been calculated from MC simulations using a narrow X-ray beam hitting the centre of the circular phantom. The narrow beam is analogous to a delta function, thus the energy recorded within the image receptor, other than the primary photon beam, is due to scatter radiation. Two primary beam angles (ϕ), with respect to the detector plane, have been shown to illustrate the deformation of the scatter PSF when the primary incident angle is increased. Further discussion on this topic is found in Section 3.4.5.

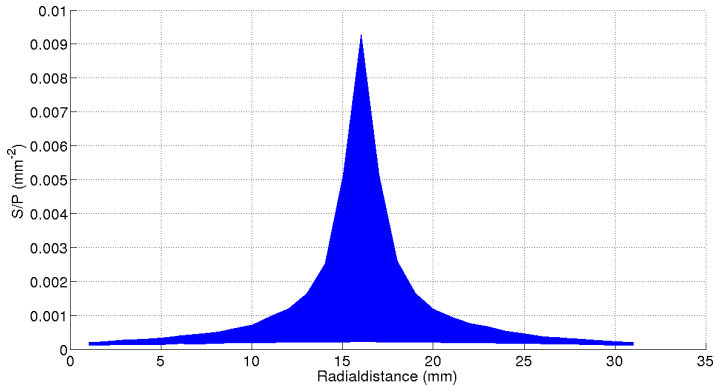

(a) ϕ=0^o

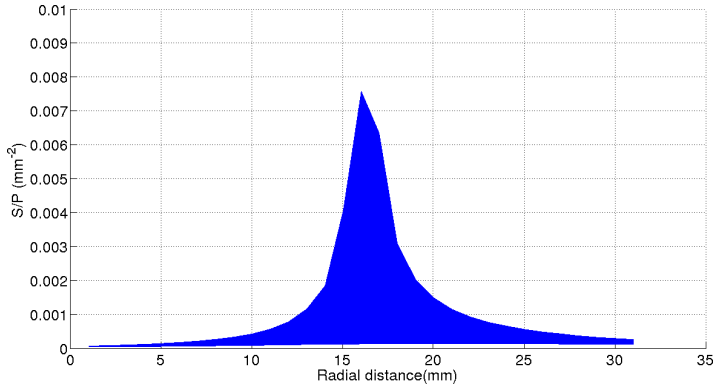

(b) ϕ=25^o

Figure 3.3: Examples of scatter PSFs recorded in an ideal image receptor (100% efficiency) for a circular phantom of thickness $50mm$ and glandularity 20%. The primary beam trajectory is perpendicular to the image receptor plane (ϕ=0^o) in (a) whereas in (b), the primary beam has an angle of 25^o with respect to the detector plane.

3.3 Techniques for scatter estimation

The benefits of scatter reduction in the image receptor have been demonstrated, as well as the different parameters used to quantify its effects on image quality. Several techniques described in the literature to estimate the magnitude and the spatial distribution of the scattered radiation are discussed below.

In this section, these techniques are classified in three groups: blocker-based experiments, MC calculations and mathematical modeling.

3.3.1 Blocker-based techniques

In the first study of scatter in mammography, Barnes and Brezovich [105] measured experimentally SPR values for different parameters. They used the conventional technique employed for scatter measurements in diagnostic radiography: the beam stop technique. Later on, this methodology was employed in X-ray mammography for a large number of authors to estimate both SPR and SF values [25, 104, 114, 115, 116].

The beam stop technique consists of imaging an object made of a high density material, typically lead (Pb), which absorbs the majority of the primary X-ray photons impinging from above. Normally, the beam stops are imaged with a breast tissue equivalent material, usually PMMA, to generate realistically scattered radiation within the image receptor.

Figure 3.4 illustrates the typical geometry of the beam stop where a lead disc, i.e. beam stop, is placed above the scattering material.

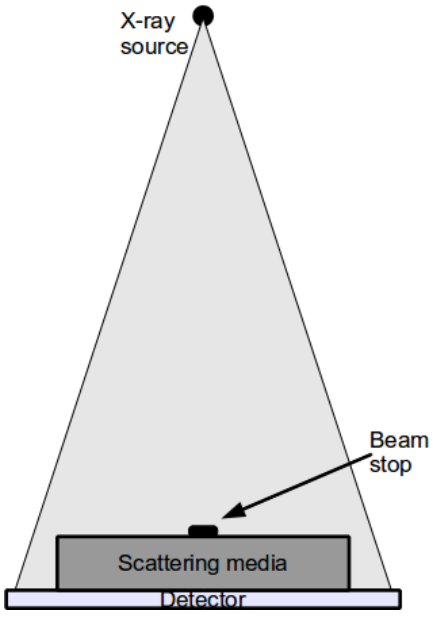

Figure 3.4: Typical diagram of a beam stop geometry.

As the beam stop is made of a high absorption material, most of primary radiation does not penetrate it, only the scatter signal S being observed beneath the beam stop.

In contrast, the energy recorded due to primary and scatter components $(P + S)$ are found elsewhere. As a results, both S and $(P + S)$ signals are combined to calculate the primary only image P and eventually, the SPR and SF for the studied geometry can be estimated as described in Equations 3.7 and 3.8 respectively.

Using this principle, the SPR and SF values are estimated using a series of lead discs of similar thickness but decreasing diameter. An example of this geometry used for scatter beam stop assessment is illustrated in Figure 3.5(a). SPR, or SF, under each disc is derived from the scatter signal (S) and primary and scatter $(P + S)$ measurements as explained above. Typical regions of interest (ROI) used to measure the signal inside (S) and outside $(P + S)$ the lead disc are shown in Figure 3.5(b). Note that to account for non-uniformities in the image, such as the heel effect [2], four ROIs are used to measure the signal in the background in different positions with respect to the disc.

To illustrate this, a $5cm$ thick PMMA slab was experimentally imaged in a Hologic Selenia X-ray system without an anti-scatter grid using an energy spectrum of 29kVp Mo/Rh. The scatter magnitude was calculated using the aforementioned beam stop methodology (See Figure 3.5(a)). The SPRs were measured for each disc, then, the SPR value of the system was finally calculated after extrapolating the individual SPR values to a zero diameter disc as illustrated in Figure 3.5(c). In this case shown, SPR values of 1.00 and 1.18 were obtained when extrapolating to zero diameter using linear and logarithmic methods respectively.

Boone and Cooper [19] found that linear extrapolation might underestimate (small discs) or overestimate (large discs) the SPR whereas logarithmic extrapolation overestimates the SPR in all the cases. So it is observed that the chosen method for extrapolation influences in the final SPR value, which represents a limitation of this method.

The above measurements using the beam stop method provide a single value to represent the scattered radiation for a given geometry. However, as discussed in the literature [19, 45, 46, 47] and in Section 3.4.6, the scatter magnitude depends on the spatial location where it is measured. In order to study the scatter distribution across the image, a phantom consisting of an 2D array of lead discs of uniform thickness equally distributed has been described in the literature [20, 117], and illustrated in Figure 3.6. The use of this phantom requires measurement of the SPR or SF values for each lead disc as previously described. Intermediate values can be interpolated assuming that the scatter is a slowly varying function.

The scattering due to light within the image receptor, i.e. veiling glare, is neglected in the MC simulations described in this work. However, as the beam stop images are acquired experimentally, the glare is intrinsic to the scatter measurements. It is worth pointing out that some authors have estimated the glare within the image receptor using the beam stop methodology [116, 118]. In this case, the scattering material is removed from the geometry and the lead disc is placed directly on the surface of the detector. Thus scatter produced within the detector is only recorded under the disc.

Despite the beam stop being is used very often to experimentally estimate scattered radiation, it suffers from some drawbacks. For example, it requires of a large number

[2] Non-uniform X-ray intensity across the image receptor.

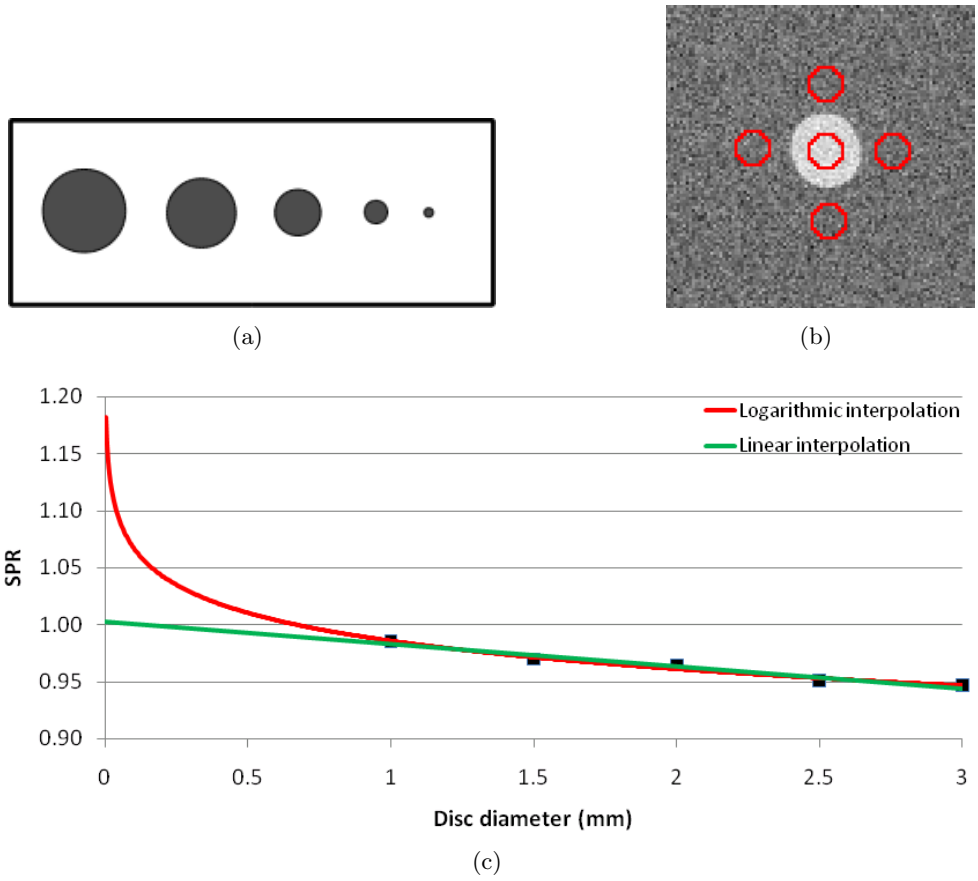

Figure 3.5: (a) shows a common beam stop geometry consisting of lead discs of equal thickness and decreasing diameter. Common ROIs used to measure the signals beneath and elsewhere the discs are illustrated in (b). An example of extrapolation to 0 diameter using linear and logarithmic approximation is presented in (c). For this case, a $5cm$ thick PMMA slab has been imaged in a Hologic Selenia mammographic system without anti-scatter grid using an energy spectrum of 29kVp Mo/Rh.

of exposures for the image acquisition process [106]. This is necessary to quantify the statistical fluctuations associated to each value measured. Moreover, if the lead disc is too small, this can fall across pixels and suffer from partial volume effects, so several measurements with the beam stop phantom shifted are needed to reduce this effect. Furthermore, as mentioned above, the method of extrapolation used to calculate the scatter at zero diameter disc may lead to inaccuracies in the results as different approximations can provide different results. This has been a controversial point widely discussed in the literature [106].

For this reason, Cooper et al. [106] and Nykanen and Siltanen [108] described a method, previously proposed for Chan and Doi [119] in diagnostic radiology, which not only estimates the scatter magnitude but also its spatial distribution by measuring the edge spread function (ESF).

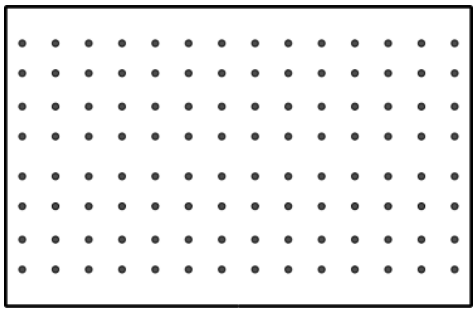

Figure 3.6: Typical beam stop array used to estimate the SPR and SF across the entire image receptor experimentally. The black dots represent lead discs of uniform thickness.

They showed that two images of an edge spread device (ESD), which is made of lead, are needed to estimate the scattered radiation. Thus, their proposed methodology reduces the large number of acquisitions needed for the beam stop method. In the first image, the geometry is setup as shown in Figure 3.7(a). For the second, the ESD is re-orientated 180^o, so a mirror image is generated.

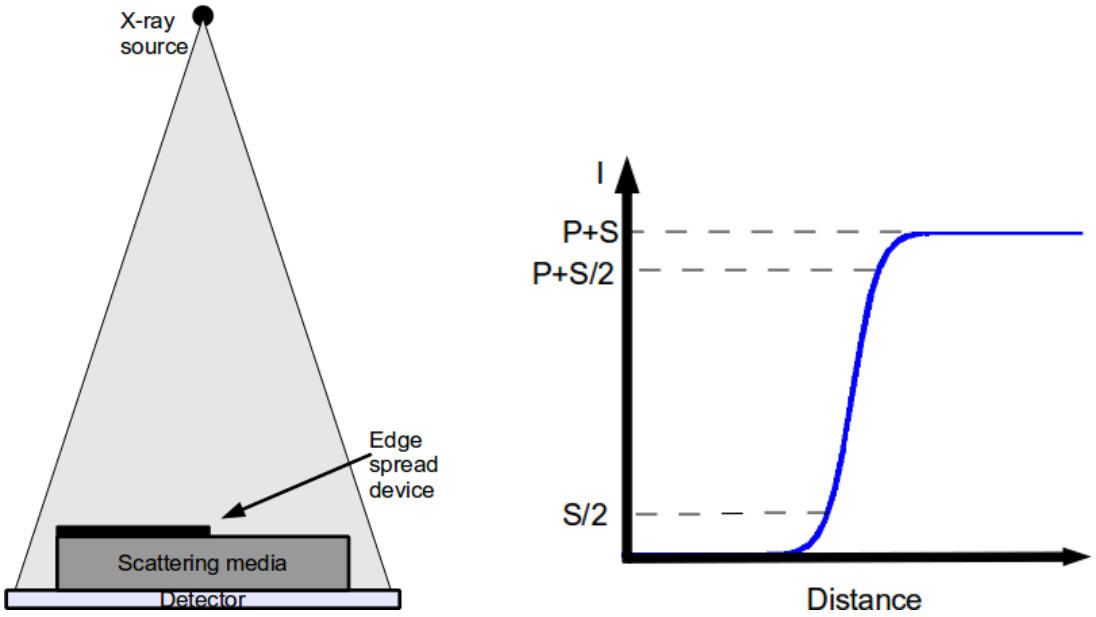

Figure 3.7: A diagram of the setup described by [106] to calculate the ESF is shown in (a). A representative intensity profile perpendicular to the edge of the ESD is illustrated in (b).

The ESF is calculated by taking a profile perpendicular to the edge of the ESD. A typical profile is shown in Figure 3.7(b). In this profile, the $(P + S)$ signal recorded outside the ESD is reduced as the ESD is penetrated, where the toe of the sigmoid corresponds to the scatter component. As mentioned before, two mirror images are generated, so

by subtracting the different parts of the profile, scatter and primary signals can be separated. Therefore, the scatter line spread function (LSF) for a particular direction is calculated as the derivative of the scatter ESF.

The scatter PSF is eventually calculated by deriving the scatter LSF. However, as the PSF provides spatial information in all directions, and the LSF in just one direction, the scatter PSF is assumed radially symmetric. Otherwise, the LSF in more directions are needed, which would increase the number of image acquisitions.

It has been seen that the number of acquisitions can be greatly reduced compared to the pencil beam experiment. However, this method has also some disadvantages. In order to reduce the number of acquired images, the scatter response was assumed symmetric, so it might fail in non-symmetric regions, such as close to the edge of an object. However, this can be taken into account by measuring the LSFs in more directions, which would increase the number of images required as previously described. Furthermore, the image acquisition of two geometries must be acquired under the same conditions. In other words, the ESD used to calculate the ESF have to be carefully placed in order to obtain a mirror profile.

3.3.2 Monte Carlo calculations

In the previous section, different techniques have been explained to estimate the scatter based on experimentally acquired images. The problem of these techniques is that the image acquisition process is tedious and very time consuming when calculating the scattered radiation for a wide range of conditions such as different scattered thicknesses, energy spectra or even different X-ray sets and image receptors.

MC simulations, which can be very time consuming too, represent an alternative option to estimate the scattered radiation. However, they provide direct access to scatter and the underlying physics which is impossible to access experimentally.

When using MC simulations, two main approaches can be followed: *indirect* and *direct* scatter field estimation. In the former approach, the aforementioned PSF_{sys} is calculated using the pencil beam experiment. A narrow X-ray beam represents a delta function entering a given geometry. Then, the response recorded in the image receptor corresponds to the PSF_p and PSF_s. A schematic diagram of this geometry is shown in Figure 3.8, where a representative PSF_s is highlighted in green.

The pencil beam geometry has been widely used in the literature [19, 24, 46, 82, 112, 120, 121, 122, 123]. As previously explained, the PSF_s provides information about both the magnitude (see Equation 3.11) and the spatial distribution of the scatter for a given geometry.

In order to calculate the energy deposited by scattered X-ray photons within the pixel (x, y) at the image receptor $S(x, y)$, the PSF'_s described in section 3.2.2 needs to be convolved with the primary X-ray field $P(x, y)$ recorded within the image receptor. As described before, PSF'_s is also normalised by area, so the pixel area A_p is also considered. The convolution integral is given in Equation 3.12.

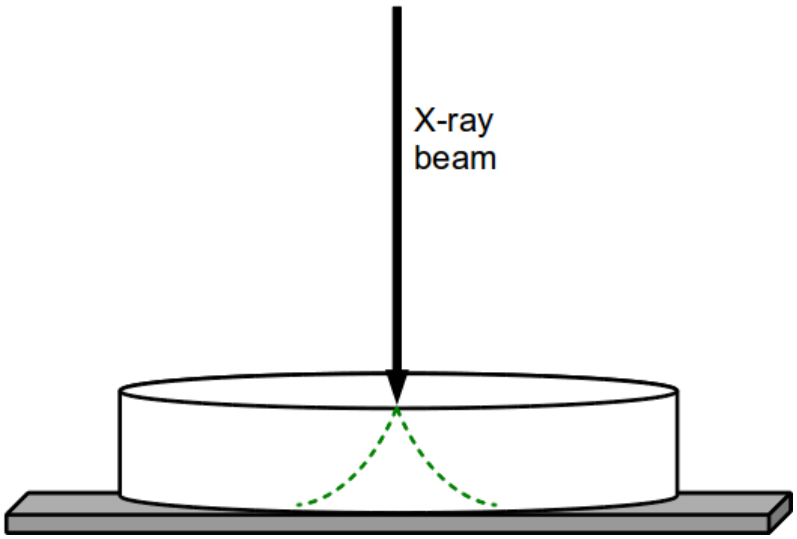

Figure 3.8: Simple diagram of the pencil beam geometry: a narrow X-ray beam hits the centre of a circular phantom and the energy is recorded in the image receptor (grey slab). A sample scatter distribution is shown in green dashed line.

$$S(x,y) = A_p \int_{\tau_1=-\infty}^{\infty} \int_{\tau_2=-\infty}^{\infty} P(\tau_1,\tau_2) \cdot PSF_s'(x-\tau_1, y-\tau_2) d\tau_1 d\tau_2. \tag{3.12}$$

Ideally $P(x,y)$ can be calculated analytically using Beer-Lambert law. However, in clinical scenarios, $P(x,y)$ cannot be calculated as the true geometry and composition of the breast are unknown. For this reason, $P(x,y)$ is often approximated to the total image recorded within the image receptor $I(x,y)$. As $I(x,y)$ represents the energy deposited due to both primary and scattered X-ray photons and they cannot be differentiated, the convolution method might be inaccurate [25, 109].

Due to the long time needed to generate the PSF_s' using MC simulations, these are generally calculated a priori for a range of parameters (thickness, glandularity, etc.) and stored in look-up tables for subsequent use [122, 123].

In the alternative *direct* method, the scatter field is calculated directly from the MC simulations by tagging X-ray photons as either primaries or scatter as these interact with matter along the geometry. Again, this technique has been widely used in the literature [19, 45, 46, 47, 82, 83, 107, 124, 125, 126, 127, 128, 129]. Using this approach, both SPR and SF can be calculated directly under any mammographic scenario from the primary and scattered X-ray photons recorded within the image receptor.

3.3.3 Mathematical modeling

It has been seen in the previous section that the PSF_s' can be calculated using pencil beam experiments in MC calculations, which can be very time consuming. However, some authors have calculated the PSF_s' based on the fundamental principles of particle

interactions. This might seem similar to the extensive calculations used by MC simulations, however, the mathematical models are typically faster as they make several simplifying assumptions.

For example, Boone and Siebert [130] developed an analytical model to derive scatter PSFs assuming only single scatter interactions. They have found good agreement of the scatter PSFs for thin phantoms when comparing their model with results from direct MC simulations, which account for both single and multiple scattering. However, as expected, this assumption could not be applied to thicker phantoms, where there is a higher probability of multiple scattering interactions.

In a recent paper, Tromans et al. [113] described a model which estimates the scattered radiation using fundamental physics relations as well. These authors employ sampling and interpolation methods which can dramatically reduce the large computation time observed in MC simulations.

3.4 Behaviour of scattered radiation

Section 3.2 described how the magnitude and spatial distribution of the scattered radiation are typically represented. Furthermore, different methods used to estimate the scatter field have been discussed. In this section, the variation of the magnitude and spatial distribution of the scatter with respect to certain physical parameters is studied. These include changes in X-ray energy spectrum, the breast thickness (T), glandularity of the breast tissue (G), the air gap AG (the distance between the breast/phantom and the image receptor), and the projection angles (ϕ) observed when moving the X-ray tube in DBT. Additionally, the effect of scattered photons from materials other than the breast or phantom are described.

A pencil beam geometry was simulated in MC to investigate the effects of these parameters on the recorded scattered radiation. This geometry is shown in Figure 3.9 and uses an ideal image receptor (100% efficiency) to record the PSF_p and PSF_s. The phantom corresponds to a cylinder of radius $116mm$ and lenght T. The SPR values calculated from MC results in this section illustrate a maximum statistical error of 0.1% after running 5 MC simulations using 10^9 photons each. As will be depicted in the next chapter, this geometry has been previously described by Boone and Cooper [19] and Sechopoulos et al. [82] and it was used as part of the validation of the MC toolkit used in this project.

The PSF_p and PSF_s were estimated when varying one parameter at a time while keeping all other parameters fixed. Unless it is said otherwise, the incident angle ϕ was equal to 0^o. The SPR value was also calculated for each of the shown examples after integrating the PSF'_s over a circular field of view (FOV) of radius $100mm$ as described in Equation 3.11. In order to keep the results generic, the scatter PSFs are expressed as a function of SPR per unit area (mm^{-2}).

Further information regarding each specific simulation is provided below. Note that all the results shown in this section exclude the use of anti-scatter grids as observed in most DBT systems. This will lead to larger variations in SPR magnitude than those found in 2D planar mammography, where an anti-scatter grid is routinely employed.

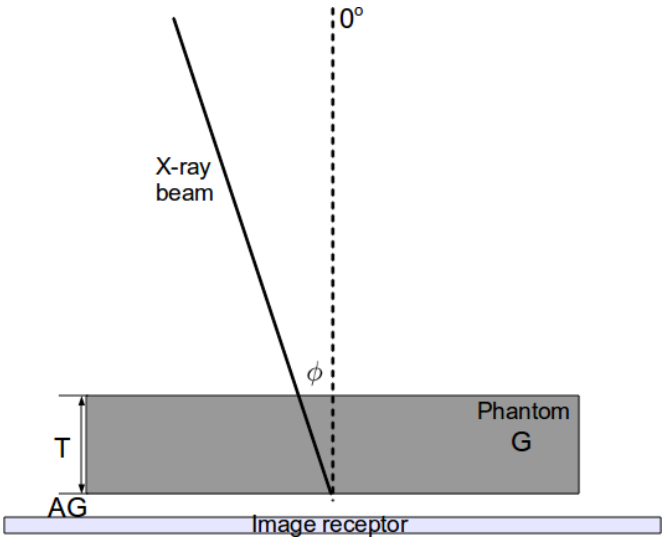

Figure 3.9: Pencil beam geometry used to study the variation of the scatter for certain parameters. A narrow beam of angle ϕ hitting a phantom of thickness T and glandularity G is simulated. An air gap AG between the bottom surface of the phantom and an ideal detector is also included.

3.4.1 X-ray energy spectrum

The first parameter studied here is the X-ray energy spectrum. Figure 3.10 corresponds to the PSF_s' from the pencil beam geometry using a phantom thickness of $50mm$ and a glandularity of 50%. An air gap of $10mm$ was included in the geometry as described by [19, 82]. Scatter PSFs for X-ray energy spectra of 26kVp Mo/Mo and 32kVp Rh/Rh have been plotted.

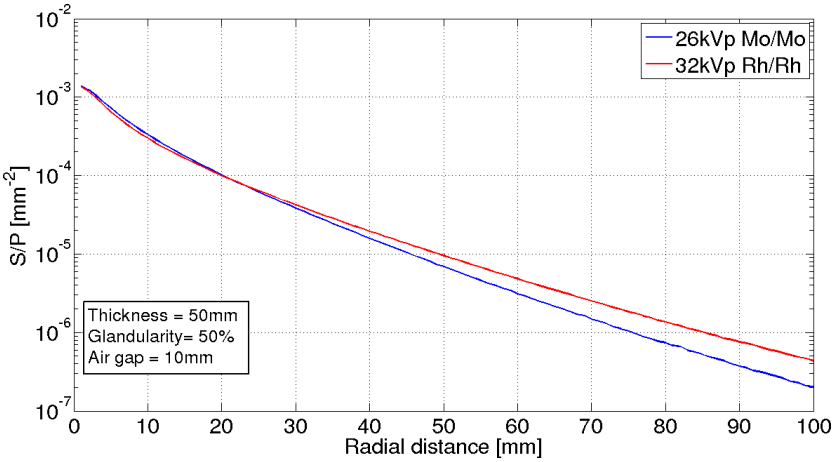

Figure 3.10: Scatter PSFs calculated for an ideal image receptor using the pencil beam experiment shown in Figure 3.9. Two X-ray energy spectra are illustrated.

It can be observed that the PSF_s' calculated for the 32kVp Rh/Rh energy spectrum

has a broader tail than the one observed for 26kVp Mo/Mo. Consequently, the SPR value for 32kVp Rh/Rh is expected to be larger. However, the difference between both $PSF_{s'}$ was less than 3% when comparing the area under each curve, i.e. SPR value, using a circular field size of radius $100mm$ as shown in Table 3.2.

Table 3.2: SPR values calculated for the PSF'_s curves shown in Figure 3.10 using a circular field size of radius $100mm$.

Energy spectrum	SPR
26kVp Mo/Mo	0.54
32kVp Rh/Rh	0.56

Although results for only two energy spectra have been shown here, the trend of the results illustrates that the SPR increases with energy as observed in the literature [46, 47, 82, 106, 121].

Despite the changes of SPR reported in the literature, the difference in magnitude is considered small, especially for thinner thicknesses, within the mammography energy range. Thus it is widely assume that the SPR values vary insignificantly with energy spectrum [46, 47, 82, 105, 106, 121].

3.4.2 Glandularity

Figure 3.11(a) illustrates the PSF'_s for an energy spectrum of 26kVp Mo/Mo recorded in an ideal image receptor, which is $10mm$ below the bottom surface of the phantom, i.e. air gap equals $10mm$. The phantom thickness is $50mm$ and three glandularities have been studied (0, 50 and 100%). The corresponding SPR values for each of the PSF'_s are shown in Figure 3.11(b).

It was found that PSF'_s changes slowly with glandularity as reported by other authors [46, 82, 106]. The scatter PSFs were found to be broader for smaller glandularities. This is because the scattered photon travels further in a less dense material as the probability of X-ray photons absorption decreases.

The largest SPR difference found between the extreme glandularities of 0% (SPR=0.52) and 100% (SPR=0.57) was just below 9% using a circular field size of radius $100mm$. Note that this difference can increase or decrease for a thicker or thinner phantom. In general, the SPR deviation due to breast composition is larger than the difference observed when varying the energy spectrum. However, the effects of glandularity on SPR are typically considered small in the literature and commonly neglected [46, 82, 106]. In this work, the average glandularity of the imaging object (breast phantom) is used in order to minimise this deviation in SPR values.

3.4.3 Thickness

Phantoms of several thicknesses (20, 40, 60 and $80mm$) with a fixed glandularity of 50% have been simulated using an energy spectrum of 26kVp Mo/Mo and an air gap of

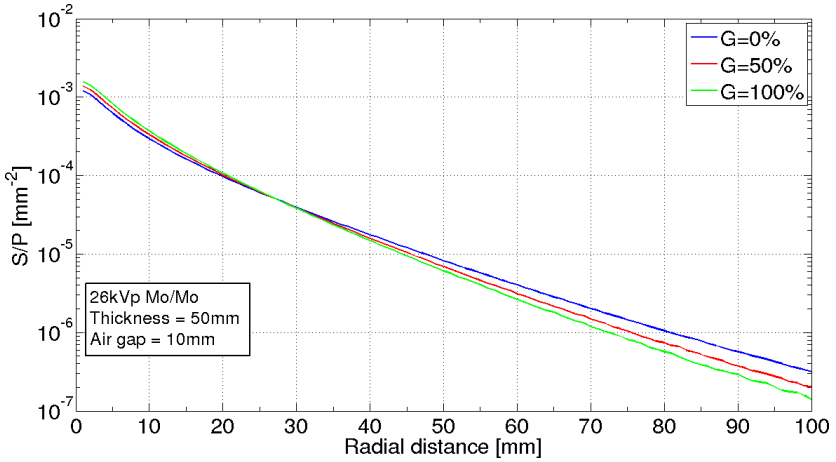

(a)

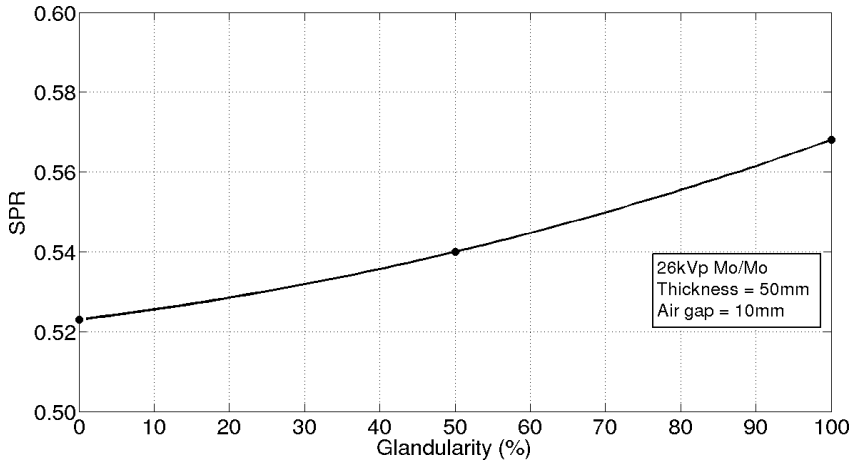

(b)

Figure 3.11: (a) Scatter PSFs for different glandularities (G) using the pencil beam experiment shown in Figure 3.9. (b) The SPR values corresponding for each of the studied cases calculated using a circular field size of radius $100mm$. Note that the y-axis shows in (b) only illustrates SPR values between 0.5 and 0.6.

$10mm$. The PSF_s' for each case studied and the corresponding SPR values are shown in Figure 3.12.

As expected, a significant increment in scattered radiation is observed when the phantom thickness is increased (note that Figure 3.12(a) is shown in a logarithmic scale). In other words, the PSF_s' becomes broader with increasing thickness. This is due to the scattered X-ray photons have to travel further forward, thus they also travel further sideways. This broadening effect is translated into a SPR increase when the thickness of the phantom increases.

In contrast to the behaviour seen with changes in the X-ray energy spectrum and glandularity, the SPR varies considerably with the breast thickness. For the study

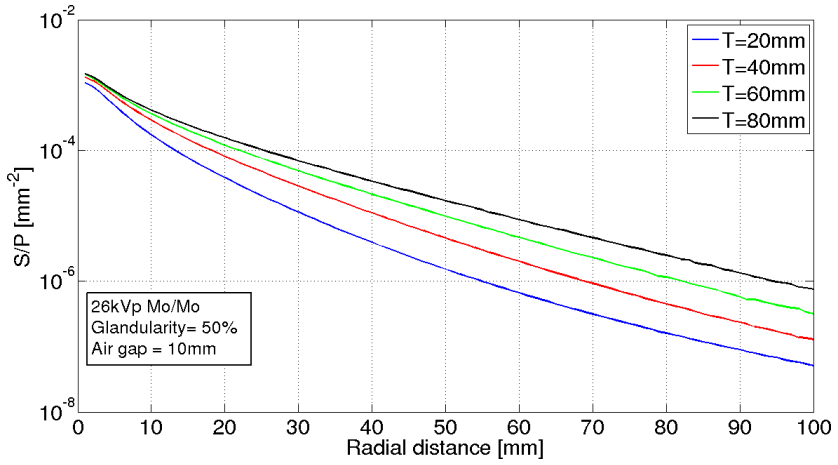

(a)

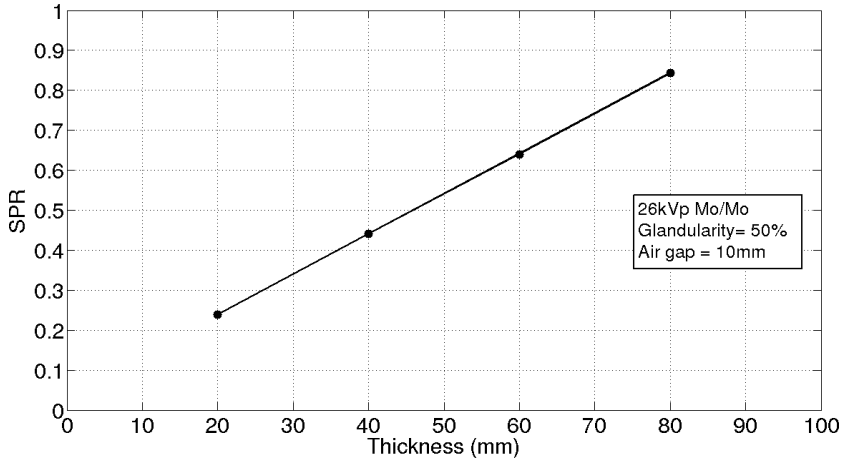

(b)

Figure 3.12: (a) Scatter PSFs for different phantom thicknesses (T) using the pencil beam experiment shown in Figure 3.9. (b) The SPR values corresponding for each of the studied cases calculated using a circular field size of radius $100mm$.

shown here, the SPR calculated for a thickness of $20mm$ was 0.24 for a circular field size of radius $100mm$, whereas that for a thickness of $80mm$ the SPR was 0.84. This makes a difference of over 70% in SPR when considering a thickness range of 20 to $80mm$. These findings are in line with those found in the literature, where the thickness is considered the parameter which has the greatest influence on SPR [46, 47, 82, 105, 107, 106, 121].

3.4.4 Air gap

The influence of the air gap on recorded scatter radiation is also pertinent. An air gap between the lower surface of the breast and the image detector is frequently found in mammography geometries.

Several authors have explored the air gap as a potential option for scatter reduction as described in Section 3.5. However, the effects of small air gaps (up to $30mm$) on the scatter radiation distribution are discussed here.

For this purpose, a $40mm$ phantom with 50% glandularity was inserted in the aforementioned pencil beam experiment using an X-ray energy spectrum of 26kVp Mo/Mo. The scatter response function was then studied for a range of air gaps between 0 and $30mm$ in steps of $10mm$.

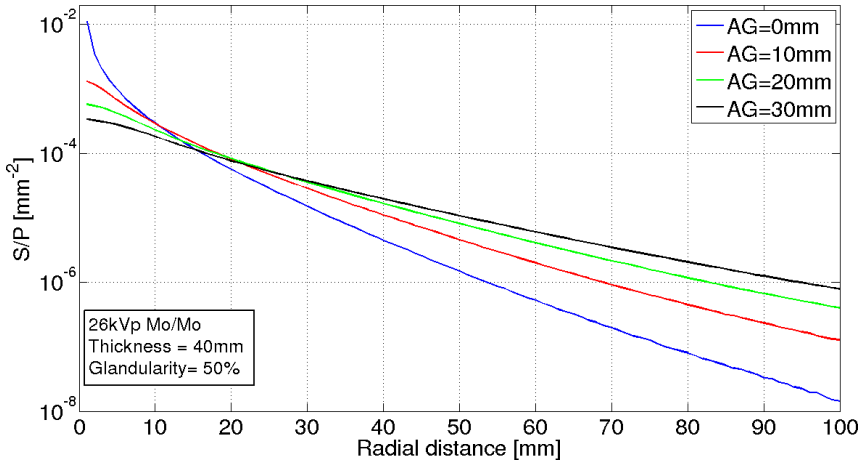

(a)

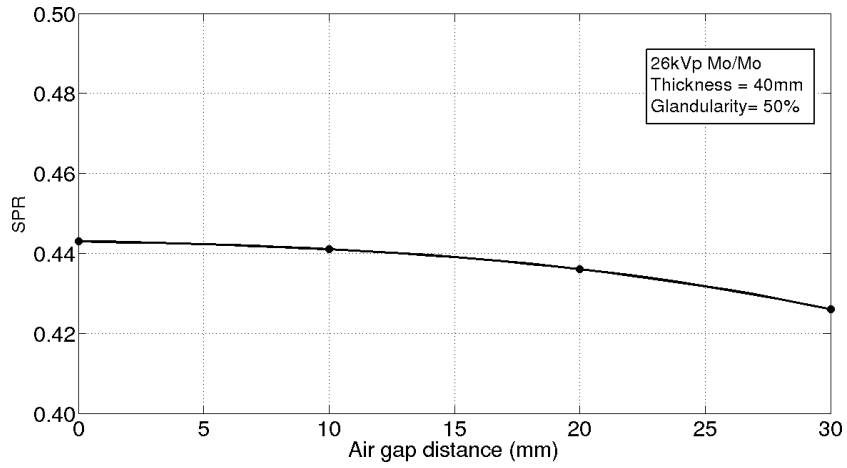

(b)

Figure 3.13: (a) Scatter PSFs for different air gap distance (AG) using the pencil beam experiment shown in Figure 3.9. (b) The SPR values corresponding for each of the studied cases calculated using a circular field size of radius $100mm$. Note that the y-axis shows in (b) only illustrates SPR values between 0.4 and 0.5.

The scatter PSFs shown in Figure 3.13(a) illustrate a change in spatial distribution of the scattered radiation when the air gap is increased. It is observed that the PSF_s' falls off more slowly as the air gap distance increases. This occurs because, as the air gap

increases, the scattered X-ray photons travel larger distances before impinging on the image receptor.

Despite the large changes in PSF'_s, a relatively small difference (4%) was found in terms of SPR values within the air gap range studied here as illustrated in Figure 3.13(b). This is because the FOV used to calculate the SPR was $100mm$. However, considerable variations of SPR with air gap distance might be found for a smaller FOV [46, 82].

3.4.5 Incident angle

An important parameter to take into account when simulating DBT systems is the incident angle ϕ. This represents the angle of an X-ray photon beam with respect to the normal to the image receptor plane as shown in Figure 3.9.

The immediate consequence of increasing ϕ is that the thickness of the phantom is virtually increased by $\frac{1}{cos\phi}$ as the photon's path length within the phantom is larger. As previously seen, the scattered radiation increases largely with breast thickness, thus it is expected that scattering processes also increase with ϕ.

Until this point, the pencil beam geometry employed in this section has used a ϕ equals to 0^o, thus a radially symmetric scatter PSF was expected. However, an increase in ϕ will also modify the spatial distribution of the scatter.

Figures 3.14(a) to 3.14(c) show the PSF'_s from a pencil beam for a thickness of $60mm$ and glandularity 50% at three incident angles (0, 7.5 and 25^o). An energy spectra of 29kVp W/Rh and a $0mm$ air gap distance have been used. The SPR values illustrated in Figure 3.14(d) were calculated for a circular field of radius $307mm$. Furthermore, SPR values for projection angles of 15 and 20^o were also included to have a better estimate of the SPR as the projection angle increases.

As previously suggested, the SPR was found to increase with ϕ. A difference of 1.6% was found between the SPR observed for 0^o and 7.5^o. Thus no significant variation is found in SPR values for small incident angles (ϕ <10^o) which accords with the previously published literature [19, 24, 82]. However, this difference was found to increase by up to 18% when comparing SPRs between 0^o and the largest simulated angle of 25^o. Thus, larger ϕ (>10^o) can significantly change the SPR magnitude, as well as the scatter kernel symmetry.

3.4.6 Scatter from the system

A simple setup has been employed in the pencil beam geometry previously described to study the behaviour of the scattered radiation under an ideal scenario. However, it is known that when using realistic geometries, scattered photons originating from materials other than the phantom or breast are recorded within the image receptor. These scattered photons are mainly generated in the breast support and compression paddle, and are described here as scatter from the system.

Dance et al. [107] and later Sechopoulos et al. [82] observed these effects produced in realistic geometries. They found that these scattered photons contribute significantly

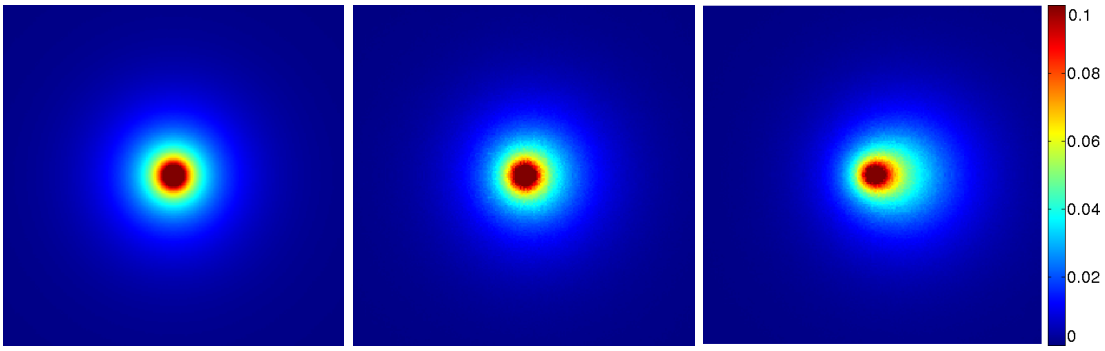

(a) $\phi = 0^o$ (b) $\phi = 7.5^o$ (c) $\phi = 25^o$

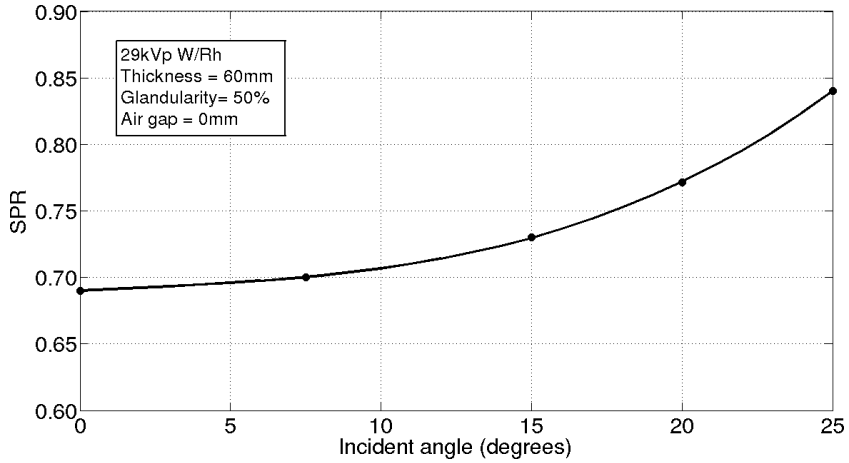

(d)

Figure 3.14: (a-c) illustrates the 2D projection of the scatter PSFs for three different angled pencil beams. The colour map illustrates the magnitude of the PSF'_s in mm^{-2}. Note the asymmetry as the X-ray source tilts towards the left edge of the page. Their corresponding SPR for a circular field of radius $307mm$ values are illustrated in (d). Moreover, SPR values corresponding to projection angles of 15 and 20^o were included. Note that the y-axis shows in (d) only illustrates SPR values between 0.6 and 0.9.

to the scatter field recorded within the image receptor, especially near the breast edges and at low energies. In fact, Sechopoulos et al. [82] quantified the increase on SPR up to 31% due to system scatter using a generic DBT geometry.

In contrast, this effect is not often noted in publications because either the compression paddle or breast support are excluded from the simulation for simplifying the simulation model [19, 45, 46], or because scatter profiles or scatter maps are not shown in scatter studies in spite of the compression paddle and breast support being simulated [24, 124].

The scattered radiation from the system has been explored here using a realistic geometry as shown in Figure 3.15(a). This new geometry consists of an cone beam emerging from an infinitesimal point source located at $660mm$ from a $250\mu m$ thick selenium image receptor, where all the detector size (240x300mm^2) is imaged. A detector with

a pixel size of 1mm^2 was used. The geometry also includes a 2.4mm thick polycarbonate compression paddle and a 1.2mm thick carbon fibre breast support. An air gap of 15mm between the breast support and the image receptor has also been taken into account. The breast phantom has been represented as a 90mm thick semicircular D-shape cross section of radius 80mm. The phantom comprises of an inner region of glandularity 4% surrounded by a 5mm thick adipose layer. The results presented here correspond to an energy spectrum of 40kVp W/Al, being the typical energy beam used in such as thick phantoms.

The planar view of the SPR map is shown in a colour map in Figure 3.15(b), where the highest SPR values are shown in red. The amount of SPR observed along the chest wall (CW) to nipple direction (shown as a solid white line in Figure 3.15(b)) is illustrated in Figure 3.15(c). The total SPR has been divided into the SPR contribution from the breast phantom, compression paddle and breast support. It is observed that the SPR values are not constant across the breast area, but varies with position.

As expected, the largest proportion of the total SPR comes from the breast phantom, as it represents the thickest object simulated in the geometry (90mm). Looking at the SPR profile, the scatter from the breast phantom changes from 0.5 at the CW to approximately 0.9 in the middle of the breast phantom and then drops again to almost 0.5 at the edge of the phantom. This is because near the edges of the breast phantom, including the CW region, there is less scattering material around than in the centre of the phantom. However, the total SPR illustrates constant SPR values after a distance of 50mm from CW (X-axis). This is because the drop of SPR from the phantom is compensated with the rise of scattered photons from the breast support and compression paddle. It can also be observed that the scatter from both the paddle and breast support are at a maximum near the edge of the phantom, but these contributions decrease towards the inner region of the breast phantom, where most of the system scattered photons are absorbed.

3.5 Scatter reduction techniques

In order to minimise the effects of scattered radiation on image quality, several techniques have been described in the literature for mammography systems. They are described here in two broad categories: geometrical scatter rejection and post-processing methods.

3.5.1 Geometrical rejection

This section describes the techniques which reduce the amount of scattered radiation that reach the detector using physical geometry.

Anti-scatter grids
Anti-scatter grids are the most common anti-scatter devices currently employed in both

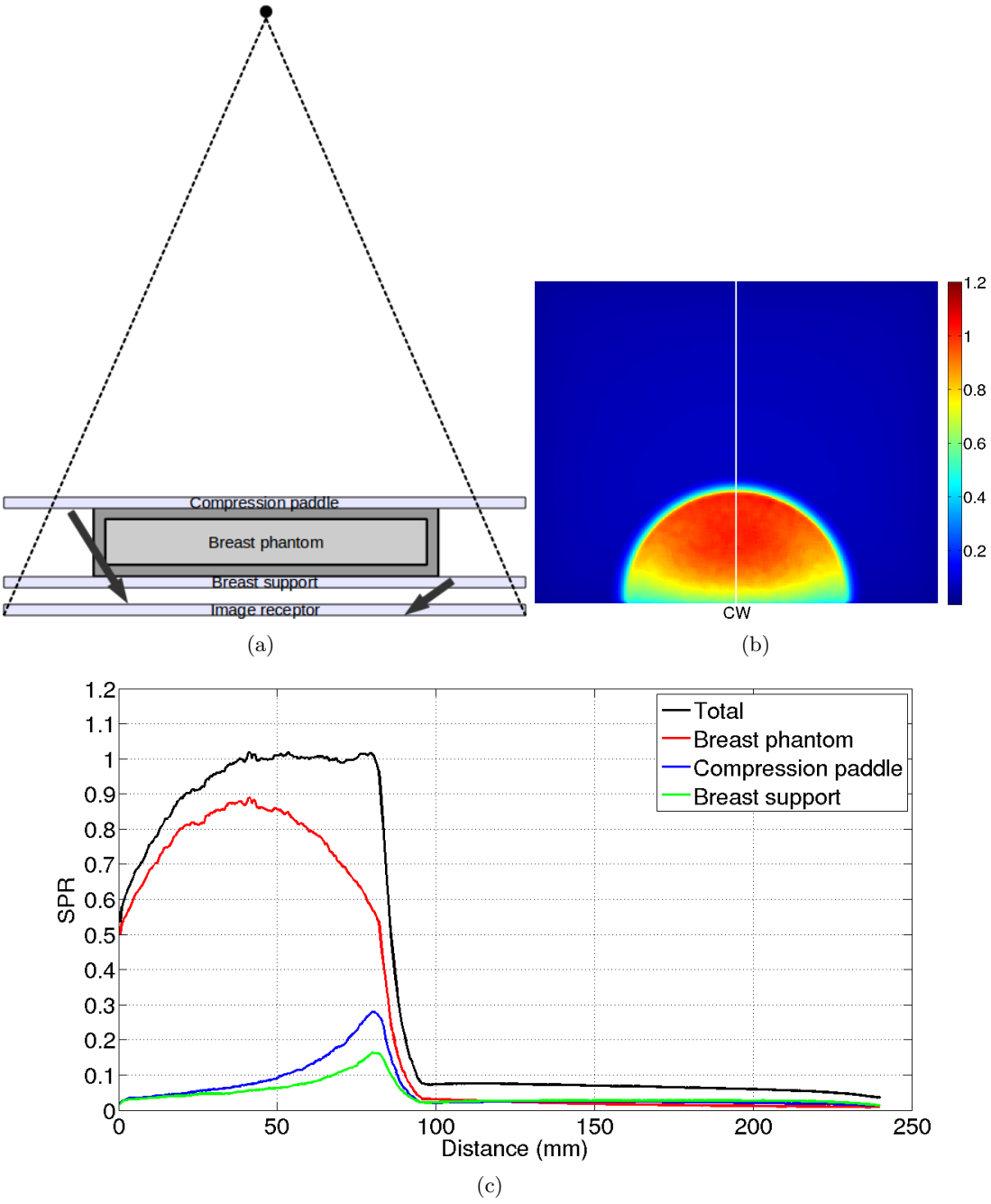

Figure 3.15: The geometry used to study the source of scatter in a realistic mammography scenario is shown in (a), where black arrows have been drawn to illustrate possible scattering paths from the compression paddle and breast support into the image receptor. (b) represents a 2D surface plot of the total SPR across the image receptor. Profiles of the SPR from the various layers included in the simulations along the vertical white line are shown in (c).

film-screen and FFDM. They were introduced in section 2.4.5 in conjunction with the typical parameters used to study their performance (BF, CIF, T_p and T_s).

The two anti-scatter grid designs available in mammography are linear and cellular. The linear grid is the preferred geometry employed by most of the manufacturers (e.g. Siemens, GE, etc.). However Hologic mammography systems use a cellular geometry [59].

Cellular anti-scatter grids, in general, have been found to outperform linear designs as they provide a higher CIF and lower BF than linear ones [47, 58, 61]. This increase in CIF is achieved by the larger scatter absorption from the cellular geometry of the grid. On the other hand, the reduction in BF can be due to the higher T_p associated to a less dense septa material, copper, and low grid ratios (r) of 3.8, which are lower in comparison with the usual ratio of 5 observed in linear anti-scatter grids. Furthermore, interspace material can play an important role, as the attenuation of primary photons is lower in air than in the materials employed by linear anti-scatter grids.

Table 3.3 illustrates data published by Boone et al. [61] to show the performance of two anti-scatter grids (linear and cellular). They have been calculated using a $60mm$ thick breast phantom representing 50% adipose 50% glandular tissue and an X-ray beams set at 28kVp Mo/Mo target/filter combination.

Table 3.3: Sample anti-scatter grid parameters calculated by Boone et al. [61] for a $60mm$ thick breast phantom of 50% glandularity using an X-ray energy spectrum of 28kVp Mo/Mo. The linear and cellular anti-scatter grids have been previously described by Rezentes et al. [58].

Anti-scatter design	Grid ratio r	Septa material	SPR	CIF	BF	T_p(%)
No Grid	—	—	0.69	—	—	100
Linear Grid	5	Lead	0.21	1.40	1.83	77
Cellular Grid	3.8	Cooper	0.10	1.54	1.70	91

It is observed that the cellular anti-scatter grid provides a better scatter rejection (i.e. lower SPR), which is translated into a higher CIF. The decrease of the BF is due to the higher T_p observed. Note that the T_p value is always less than 100% as the septa material, interspace material and grid covers absorb a small amount of the primary photons as they pass through the grid.

Air gap

It has been seen that the anti-scatter grid is the most common geometric scatter rejection technique. However, an alternative scatter rejection method is to resort to using a large air gap [60, 102]. These are found mainly in paediatric, magnification mammography and sometimes in chest radiography [102].

In section 3.4.4 it was described that the scattered radiation was slowly reduced by air gap distances up to $30mm$. However, large air gaps are required to achieve a considerable scatter reduction. With large air gaps, the scatter intensity is reduced following the inverse square law such that much of the scattered X-ray photon flux leaves the system without interacting within the detector.

However, the use of large air gaps has drawbacks. The magnified image obtained will suffer from larger focal spot geometric blurring, reduction of the FOV and the dose transfered to the breast is also increased [61, 131]. Large air gaps are used in mammography when the magnification of a specific region within the breast is required, and in this case a fine focal spot is used to reduce geometric unsharpness.

Other techniques
Several alternatives to anti-scatter grids and air gaps have been investigated in the literature.

Åslund and Cederström [114] studied scatter reduction when using multi slit digital mammography. A multi slit is comprised of two collimators. One is placed above the breast (pre-collimator), while the second one is located below the breast (post-collimator). If a perfect alignment of both collimators is achieved, the T_p is 100%. Moreover, results have suggested that this geometry produces the lowest SPR values, where the largest source of scattered X-ray photons is the image receptor [114].

In a slot-scan geometry, a collimator is placed near the X-ray tube to match the area of a narrow image receptor. Then the X-ray tube rotates, together with the narrow image receptor, thus the entire breast is scanned. Slot-scanning has a similar CIF than anti-scatter grids, however, the breast dose is lower [132] as T_p approaches to 100%. This was confirmed by Boone et al. [61], who found that slot-scan produces lower BF than cellular anti-scatter grids while maintaining the same CIF.

3.5.2 Post-processing

With the rise of digital detectors, X-ray mammography images can be manipulated after image acquisition. This post-processing property is used to enhance certain features of the image such as the skin line. Additionally, it can also be used to reduce the effects of scattered radiation on the resulting image.

Several techniques used for scatter estimation were described in section 3.3. Thus, based on the assumption that the scatter image $S(x, y)$ has been already estimated, the following methodologies can be applied to reduce the scattered field from digital mammograms.

Subtraction
It has previously seen that an image $I(x, y)$ recorded within an image receptor corresponds to its contribution of primary $P(x, y)$ and scattered photons $S(x, y)$:

$$I(x, y) = P(x, y) + S(x, y). \tag{3.13}$$

Ideally, the scatter component $S(x, y)$ needs to be removed from $I(x, y)$. Thus, the $P(x, y)$ or free scatter image, represents the desired image. Therefore, $P(x, y)$ can be estimated after subtracting $S(x, y)$ from $I(x, y)$ as employed by several authors [83, 129, 133].

An example of this methodology was carried out by Liu et al. [83]. They acquired images experimentally and using MC simulations. Then, the MC-based scatter image $S(x, y)$ was subtracted from the experimentally acquired total image $I(x, y)$. This approach is simple and easy to implement. However, it is not flexible as changes in the geometry (including the breast being imaged) require further MC simulations. Moreover, the use of direct MC simulations is a very time demanding task as already mentioned.

Deconvolution

The deconvolution methodology takes advantage of the properties associated to the Fourier domain.

Equation 3.12 described that $S(x, y)$ can be estimated by convolving $P(x, y)$ with the scatter kernel $PSF'_s(r, \theta)$. This convolution can be written in the Fourier domain as

$$\mathcal{F}\{S(x, y)\} = \mathcal{F}\{P(x, y) \star PSF'_s(r, \theta)\}, \tag{3.14}$$

where $\mathcal{F}\{\}$ and $\star$ represent the Fourier transform and convolution operators respectively.

Using the *convolution theorem* of Fourier, Equation 3.14 can be expressed as

$$\mathcal{F}\{S(x, y)\} = \mathcal{F}\{P(x, y)\}\mathcal{F}\{PSF'_s(r, \theta)\}. \tag{3.15}$$

Consequently, the scatter free image P(x,y) can be estimated as

$$P(x, y) = \mathcal{F}^{-1}\left\{\frac{\mathcal{F}\{S(x, y)\}}{\mathcal{F}\{PSF'_s(r, \theta)\}}\right\}, \tag{3.16}$$

where the operator $\mathcal{F}^{-1}\{\}$ corresponds to the inverse Fourier transform.

The scatter estimation by image deconvolution has been studied by several authors in the literature [22, 25, 108]. Operating in the frequency domain requires complex Fourier transforms which can be very time demanding. However, the difficulty of this calculations are extensively reduced with the aid of *fast Fourier transform* (FTT), which are extensively used [134, 135]. Once the FTT is performed, manipulation of images in the frequency domain is faster than calculations in the image domain.

However, as previously described, the scatter varies with position in the image. Thus this fact needs to be taken into account when applying the Fourier transform, which might lead to an increase in the computational time required for this method. Furthermore, real images have noise associated with them. Thus, this noise would introduce discrepancies in the calculated primary.

3.6 Summary and discussion

This chapter has illustrated a review of techniques for scatter estimation and reduction as well as the behaviour of scatter with various imaging and breast parameters. It has been demonstrated why the detecting scattered radiation is undesirable and how it reduces image contrast and SNR_d in both film-screen and FFDM. Before methods can be employed to mitigate the effects of scatter, the scatter field itself needs to be quantified and several techniques based on mathematical and physical models as well as experimentally acquired images have been described.

The most common methodologies found in the literature for scatter estimation are the beam stop method and MC simulations. They both have their advantages and disadvantages. For example, the typical beam stop method requires a large number of image acquisitions and its result depends on the type of extrapolation used [106]. MC simulations represent the alternative to experimentally acquired images. However, these simulations tend to be very time and resource heavy [123] and good knowledge of the geometry is necessary to realistically model the scatter in any such system. These two techniques have been compared, together with other methodologies, by Salvagnini et al. [116] for different imaging geometries. They have suggested to use MC simulations to estimate the scattered radiation when the anti-scatter grid is removed, i.e. in DBT, as will be pursued in further chapters in this thesis.

Before describing the available techniques to reduce the scattered radiation in the final X-ray image, the behaviour of the scatter field was discussed. In this section (3.4), both the magnitude and the spatial distribution have been studied while varying several parameters: X-ray energy spectrum, glandularity, breast thickness, air gap and incident angle. It was found that none or little difference in SPR is observed when varying the X-ray energy or glandularity, which is in line with the literature [46, 82, 106]. The air gap (up to $30mm$) showed no difference for a large FOV (circle of radius $100mm$). However, the spatial distribution suggested that a smaller FOV will generate large discrepancies in SPR values. Finally, the largest variation in SPR were found when modifying the breast thickness and when using large incident angles ($>10^o$). Both breast thickness and incident angle contribute to a rise in the photon's path traversing the breast/phantom, so the probability of scatter interactions increase. Other authors have also found that these parameters contribute most to the scattered radiation [19, 46, 82].

This study of the scatter behaviour has been calculated using a pencil beam experiment simulating an ideal geometry without an anti-scatter grid. This setup has been previously described by Boone and Cooper [19] and Sechopoulos et al. [82], and it has been used to validate the results produced here with those reported by Sechopoulos et al. [82] as will be described in Chapter 4.

When the anti-scatter grid is not used, a 2D plot of the scatter is needed instead of a single value as the scatter can vary significantly across the image receptor. However, when the anti-scatter grid is employed, the scatter varies slowly and a single scatter value can be used as a good approximation. Moreover, it was demonstrated that the scatter contribution from materials such as the compression paddle or breast support are significant, especially near the edges of the breast or phantom as previously ob-

served [25, 82, 107]. Thus, it is suggested to simulate the entire geometry when trying to model a real X-ray mammography scenario, in the absence of an anti-scatter grid.

In the final section of this chapter, scatter reduction techniques were discussed. Firstly, the geometrical rejection techniques were described. Anti-scatter grids, used in most commercially available X-ray systems, reduce greatly the scatter radiation. However, they are not employed in most of the DBT system, due to the difficulty of aligning the septa material of the anti-scatter grid with the X-ray tube exit. So alternative scatter reduction techniques explored in the literature such post processing were described. Furthermore, alternative methods to anti-scatter grids such as air gap, multi-slit or slot-scan geometric were also discussed. Secondly, with the arise of digital detector technology, image processing techniques are available after the image acquisition step. Therefore, the effects of scatter can be reduced after applying subtraction or deconvolution techniques. These techniques have been described assuming that the scattered field has been already estimated.

Accurate scatter estimation remains challenging in X-ray imaging. As already mentioned in this chapter, MC simulations provide direct access to all the physics involve in the scattering processes and represent the key tool for scatter characterisation used in this thesis. In the next chapter, the MC toolkit employed during this work is explained in detail.

Chapter 4

Monte Carlo simulations of X-ray mammography

4.1 Role of simulation in mammography

Mammography systems have always been under constant investigation and development in order to optimise their diagnostic performance. Due to the wide availability of relatively cheap computing power in the last decade, computer simulations have played an increasingly important role in mammography development.

Despite synthetic images requiring more time to be generated than clinical images, computer simulations represent a cheaper, more flexible and safer (with respect to radiation absorbed by the patient) method to evaluate current system configurations as well as to explore new setups in order to improve current systems [125, 136] .

Furthermore, various authors have used computer simulations within the mammography field to study complex physical processes individually that are impossible (or difficult) to study in physical experiments due to their random nature. Those processes include scattered radiation [82, 107], anti-scatter grid behaviour [45, 78], dose deposition [137] and detector performance [138].

MC simulations are often chosen to study the interaction of particles with matter due to the stochastic behaviour of the particle interactions. MC simulations can be defined as complex numerical integration methods which require random numbers to perform complicated calculations in pre-defined situation. In the case of simulating particle interactions, the probabilities of the different particles processes, i.e. cross sections, are fed into the MC simulation to calculate the particle's behaviour. The name of MC was coined during the World War II Manhattan Project because of the similarities with games probabilities and the location of a very famous casino in Monte Carlo [139].

Many authors have developed their own MC programs [107, 119, 121]. However, there exists several particle physics MC packages which are widely available to study particle interactions in medical physics. The most common MC packages are EGSx/EGSnrc [140], MCNP/MCNPX [141], Penelope [142], GEANT4 [143, 144] and FLUKA [145, 146].

EGS was one of the first robust MC codes to simulate electron-photon transportation for high energy physics and it is the most used MC package in medical physics [147]. MNCP is used primarily but not limited to simulate nuclear processes. It can simulate neutron, proton and electron transportation and it is maintained by Los Alamos National Laboratory. The small range of simulated particles in MCNP was widely increased with the development of MCNPX. The PENELOPE code includes very precise cross-sections for low energy particles interactions and a flexible geometry package. The Object-Oriented toolkit GEANT4 could simulate many different types of particles and it represents the base in the GEANT4 Application for Tomographic Emission (GATE) simulation toolkit for nuclear medicine applications. The FLUKA MC package can also simulate a large range of particle interactions. Moreover, it does not require programming from the end user for most of its applications.

4.2 Fundamentals of Monte Carlo

As previously described, MC simulations represent a tool to perform complex calculations. They rely on random samples of probability distributions to obtain values close to true values.

The most simple MC method is the direct (or inversion) sampling method. Consider a random number $\hat{r}$ which is used to draw a sample $\hat{x}$ with a probability density function (pdf) $f(x)$. Therefore, its cumulative distribution function (CDF), which describes the probability of a random variable is found at a value less or equal to x, is given by

$$F(x) = \int_{-\infty}^{x} f(u)\, du. \tag{4.1}$$

Then, it can be shown that if

$$\hat{r} = F(\hat{x}), \tag{4.2}$$

and the function $F(x)$ is monotonically increased, then $\hat{x}$ can be calculated as

$$\hat{x} = F^{-1}(\hat{r}). \tag{4.3}$$

So a sample $\hat{x}$ can be calculated as the inverse function F^{-1} at $\hat{r}$.

From the previously described Beer-Lambert's law, it was observed that the distance a photon travelling between interactions is governed by the exponential probability law. For a distance x, the pdf of a photon to travel without interaction in a medium with linear attenuation coefficient μ is $e^{-\mu x}$. Then, the pdf for a photon's interaction occurring in the distance x is given by $\mu\, e^{-\mu x} dx$. After inserting this pdf in equation 4.1, the CDF for a photon to travel a distance x somewhere in the range (0,x) is

$$F(x) = \int_{0}^{x} \mu\, e^{-\mu x} dx = 1 - e^{-\mu x}, \tag{4.4}$$

where $F(x)$ is normalised between 0 and 1. According to Equation 4.2, a random sample $\hat{x}$ from the distribution $F(x)$ can be obtained from a random number $\hat{r}$, where $0 < \hat{r} < 1$. Thus, after solving

$$\hat{r} = 1 - e^{-\mu\hat{x}}, \tag{4.5}$$

$\hat{x}$ can be calculated as follow

$$\hat{x} = -\frac{1}{\mu}\, ln(1 - \hat{r}). \tag{4.6}$$

Since $(1-\hat{r})$ is as random as $\hat{r}$ and $0 < (1-\hat{r}) < 1$, the term $(1-\hat{r})$ could be considered the initial random number $\hat{r}$. This represents the fundamental approach used in most MC simulations codes to calculate the particle transportation [140, 142, 148], where the the interaction points are directly sampling using random numbers.

However, it is not always possibly to apply direct MC methods of sampling to some distributions because of the difficulty of inverting equation 4.2. Thus, alternative sampling techniques, such as rejection sampling, are available. Rejection sampling is a common sampling technique used in MC simulations of physical process. It is used, for example, to calculate both the angle and energy of a scattered photon after an incoherent interaction [149]. Rejection sampling techniques involve evaluating a pdf of several variables using random variables for arguments, so

$$\hat{x} = f(\hat{r_1}, \hat{r_2}, ..., \hat{r_n}), \tag{4.7}$$

where the pdf is typically normalised to a maximum value of 1.

The method consists of generating the random numbers and evaluate the function f. If the value falls above the curve defined by the function f, the value is rejected. On the other hand, if the value falls somewhere on or below the curve, the value is accepted.

In MC methods, it is important to improve the speed and efficiency of the simulations. The efficiency ϵ of a MC experiment can be described as

$$\epsilon \propto \frac{1}{t\sigma^2}, \tag{4.8}$$

where t is the computing time required for the MC simulation and σ^2 the sampling variance associated with the estimated value [149]. In order to improve the efficiency of the simulation, t needs to be reduced to calculate the results for a given σ^2. There are methods in order to achieve that goal and they are called 'variance reduction techniques'.

In medical physics applications, some of the variance reduction techniques require physics biasing by distorting the interaction probabilities. The most common variance reduction techniques are control variates, antithetic variates, importance sampling and stratified sampling [149].

4.3 GEANT4 toolkit

Among the different MC programs described in the previous section, GEANT4 is the chosen MC software environment for this work because it is freely available and is supported for both Unix and Windows platforms. Furthermore, a worldwide community of physicists and software engineers, which is supported by the European Organization for Nuclear Research (CERN), provides active assistance for GEANT4.

The GEANT4 toolkit has been widely adopted by the scientific community to study particle interactions in different domains, e.g. astrophysics, medical physics or space engineering, as particle interactions within a wide range of energies (from 250 eV up to TeV) can be simulated.

4.3.1 Medical physics applications of GEANT4

GEANT4 was originally designed to simulate the interaction of particles with matter at high energies. However, the object-oriented structure of GEANT4 has allowed the development of physics models for a wide range of energies, thus it can be used in low-energy domains such as medical physics. Moreover, it provides flexibility to handle very complex geometries found in medical physics experiments including radioactive sources and patient anatomy (anthropomorphic phantoms).

The potential applications of GEANT4 in medical physics experiments have been widely described [150, 151, 152]. Its precise physics packages and modelling features to accurately design experimental geometries have been used extensively from radiology to radiotherapy studies, including mammography [153, 154], brachytherapy [155], hadron therapy [156] or dosimetry [157]. Furthermore, the GEANT4/GATE code is commonly used in positron emission tomography (PET) and single-photon emission computed tomography (SPECT) [158].

Several examples of the GEANT4 applications mentioned above are illustrated in Figure 4.1.

4.3.2 Modular architecture of GEANT4

The simulation software is structured in several modules implemented in the C++ programming language. The more relevant modules are described in this section.

4.3.2.1 Physics List

This is where the particles used in the simulations are defined (electrons, positrons, gamma rays, etc.) as well as the different physical processes to invoke during the simulation (photoelectric effect, coherent and incoherent scattering or Bremsstrahlung among others). Other processes such as Auger electrons can be activated or deactivated by the user, whereas X-ray fluorescence is activated by default in the low energy package used in this work. Finally, a user-defined threshold (range cut) to stop or "kill"

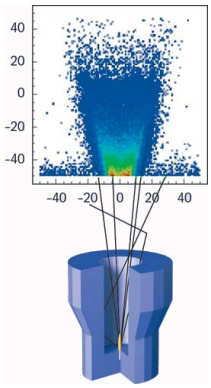

(a) Brachytherapy device

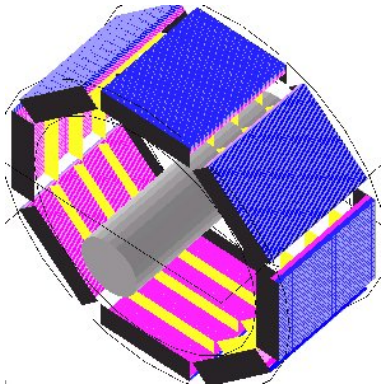

(b) PET scanner

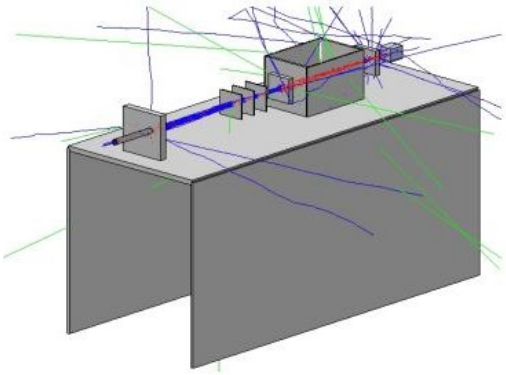

(c) Proton beam line

Figure 4.1: GEANT4 examples of medical physics applications: (a) represents a superficial brachytherapy device with its dose distribution [159], a PET scanner, adapted from [158], is shown in (b) whereas a proton therapy beam line described by [156] is illustrated in (c).

secondary particles is set in this module, where GEANT4 manages the conservation of energy. Further information about the physical processes are described in Section 4.3.6.

4.3.2.2 Detector Construction

In this module, the user specifies all the chemical elements (H, C, O, etc.) needed in order to describe the different materials used in the simulation, e.g. air, adipose tissue, CsI. Each material is defined using either its chemical formula or the fractional mass of its components, as well as its density. Examples of this are shown in table 2.2. Then the geometric shape for each element within the simulation (including anti-scatter grid, breast phantom, etc.) and its physical dimensions are created (box, tube, parallelepiped, etc.). In the case of a more complex design, a combination of simple shapes can be arranged or voxelised geometries (phantoms) can be loaded. Each geometric shape is converted into a logical volume, where it is filled in with the appropriate material. Finally, a physical volume is defined by locating the logical volume in the

desired spatial coordinates within the entire simulation space (world volume). Despite the fact that particle interactions can occur anywhere within the world volume during the simulation time, only the information of the interactions occurred on those volumes which have been marked as sensitive (defined in this module) is used in the subsequent analysis.

4.3.2.3 Stacking Action

Dealing with a large number of particles in the MC simulation could be a very time demanding task because new particle paths and probabilities of interaction need to be computed. Therefore different particles generated during the simulation can be "killed" at a certain point if this has been defined in this module. However, the user has to be careful because this action might break the conservation of energy. In most of the simulations produced for this work, secondary particles other than X-ray fluorescent have been killed, depositing their energy locally and reducing the computational time. This was previously discussed in Section 2.2. It was seen that in low Z materials, including breast tissue, both electrons and X-ray fluorescent photons do not travel far. On the other hand, X-ray fluorescent photons can travel further in materials found in typical image receptors (high Z materials).

4.3.2.4 Analysis Manager

This represents a key module of the simulation. Here all the information about the particle interactions (hits) occurring in the sensitive volumes are generated. Spatial position, distance travelled by the particle from previous hit, type of interaction, momentum, kinetic or deposited energy can be measured at any given hit. In order to create an image, a text file with the total energy deposited per pixel is generated in GEANT4. Then, this text file is analysed and visualised with the aid of MATLAB ® (The MathWorks Inc., MA, USA).

4.3.3 Input parameters

Once the simulation has been coded, all the necessary modules are compiled and linked before the program is ready to run. Some parameters which control several key inputs of the simulations such as number of the primary particles, momentum direction, source shape and position or energy distribution, need to be defined before running the program.

GEANT4 allows the user to define these key parameters by hard-coding in the simulation, interactive insertion by command lines or via macro files. Changes in the code require compilation of the entire simulation whereas the interactive command line needs the information to be manually inserted by the user every time the simulation is run.

In this work, these parameters have been inserted via a macro file using the GEANT4 General Particle Source (GPS) [160], where no compilation is needed and the information has been previously stored in a simple script file. Furthermore, the level of

verbosity is defined here, where the amount of information displayed on screen regarding particle hits can be fully controlled by the user. Finally, where the geometry of the simulation is generated, the visualisation drivers are also defined in this macro file.

4.3.4 Visualisation drivers

The typical problems in the geometry when designing a MC experiment are due to wrong positioning of a volume or objects overlapping, especially in complex geometries. For this reason, GEANT4 provides visualisation tools which help the user to ensure there are no errors in the code with respect to the geometry. Furthermore, these offer a quick response to study particle trajectories and hits using the zoom and camera angle features.

After running a simulation, geometry files can be saved in a variety of file formats. These files can be visualised with the aid of several graphics systems supported by GEANT4, each of which offers complementary advantages.

OpenGL: A popular software interface found in Windows and Linux platforms for volume visualisation in both 2D and 3D. It enables direct visualization from GEANT4, so it could be used in real time for demonstration.

DAWN: The Fukui Renderer DAWN (Drawer for Academic WritiNgs) allows rendering of 3D geometrical data for visualisation. It provides high drawing details for complex geometries and it allows re-visualisation of the geometry without running GEANT4. Furthermore, this visualisation driver serves as input for additional programs such as DAVID (DAWN-based Visual Volume Intersection Debugger), for detecting overlapping volumes or DAWNCUT, which allows a planar cut of the geometry for the visualisation of internal structure in complex geometries.

VRML: The Virtual Reality Modeling Language (VRML) is a modeling language for interactive graphics which allows visualisation of a geometry using an appropriate VRML viewer either at a local or a remote machine. Due to its high interactivity, a user could observe inside a volume or a particle shower making use of the zoom or by changing the camera angles.

RayTracer: The visualisation driver RayTracer executes ray tracing visualisation making use of the tracking routines of GEANT4. It is very useful as a debugging tool because the rendering process can be aborted in order to re-render the geometry from another angle of view.

In this work, DAWN and VRML drivers have been used to visualise the different geometries produced. Examples of each of the above visualisation drivers are illustrated in Figure 4.2.

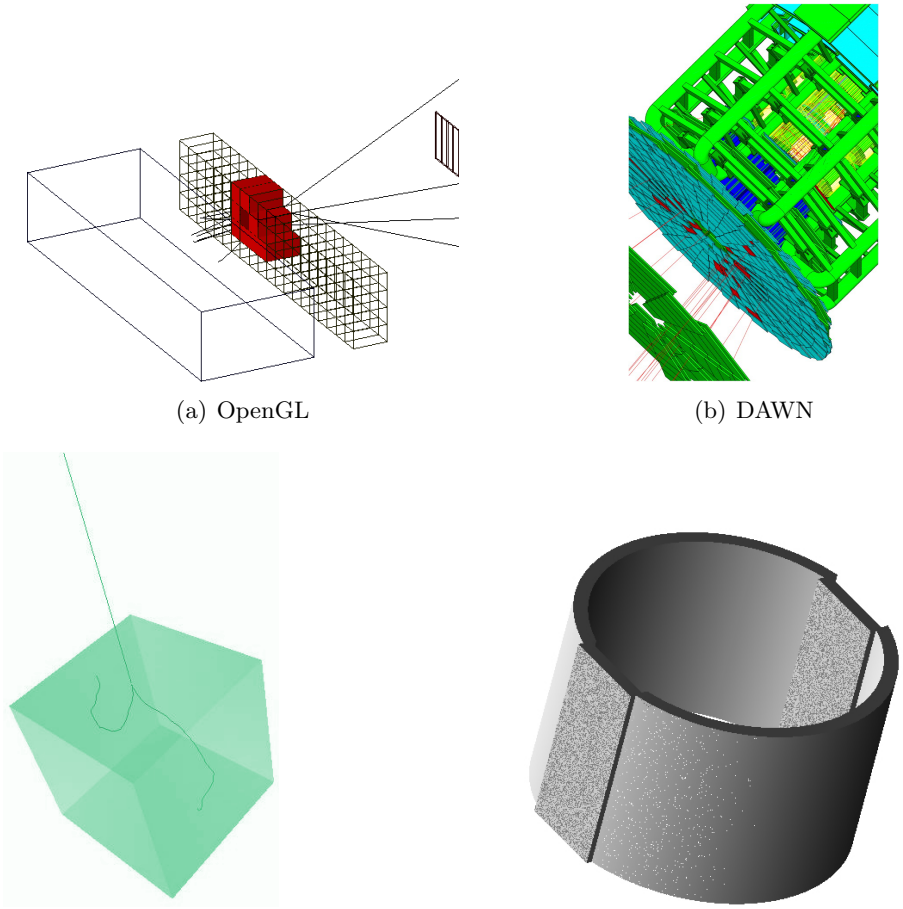

(a) OpenGL (b) DAWN

(c) VRML (d) RayTracer

Figure 4.2: Exemplar visualisations using the most common graphics drivers available in GEANT4. (a), (b), (c) and (d) have been taken from [161], [143], [159] and [162] respectively.

4.3.5 Pseudo-random number generators

By definition, a truly random number is an unpredictable number which must be produced by a random physical process, such as radioactive decay. Due to the difficulty to generate completely random numbers, pseudo-random numbers are commonly used in modern software packages for MC simulations in physics. Pseudo-random numbers are produced in a computer using a simple numerical algorithm, therefore they are not completely random.

The quality of the pseudo-random number generator (PRNG) used in MC simulations is pivotal in order to generate reliable representations of the physical imaging environment. It is not sufficient to only take into account the period of the PRNG cycle (after which the engine starts generating the same sequence of numbers) but also it needs to satisfy other properties such as the speed and the reproducibility [163].

GEANT4 takes advantage of the HepRandom module to produce pseudo-random num-

bers using commonly used pseudo-random engines, such as RANMAR, RANECU or Mersenne Twister. The periods and the speeds (random numbers generated per second) of these PRNGs are shown in Table 4.1.

Table 4.1: Specifications for different pseudo-random number generators taken from [163, 164].

Generator	Period (s)	Samples per second[1]
RANMAR	2×10^{43}	11×10^6
RANECU	2×10^{18}	7.9×10^6
Mersenne Twister (MT19937)	5×10^{182}	6.9×10^6

For the work presented here, the multiplicative linear congruential generator RANECU has been used. Given an index, the random initialization is carried out using a couple of seeds taken from a seed table. The initial index of the seed table is defined by an integer which is set by the time (in seconds) when the simulation is run.

The RANECU engine has a long period of 2×10^{18} particles [163], being sufficient for this work because the maximum number of particles anticipated for each MC experiment was 10^{10}. Furthermore, it provides reproducibility to the experiment, permitting easily to re-generate simulation data with knowledge of the initial seeds, while other PRNGs require a more complex representations of the initial state.

4.3.6 Physics processes in GEANT4

In the MC version used in this work (GEANT4.9.3), GEANT4 combines the standard electromagnetic physics with a low energy cross section package. The low energy package has higher accuracy in modeling physical interaction for low energies (below 1GeV). Furthermore, this package contains coherent scattering cross sections which are not included in the standard GEANT4 package of electromagnetic physics.

Two low energy packages are available for GEANT4.9.3: the electromagnetic Livermore physics cross sections [165, 166, 167], which has been used in this work, and the PENELOPE (PENetration and Energy LOss of Positrons and Electrons) physics model [168]. Both libraries have shown very good agreement with other databases [169, 170, 171]. However the PENELOPE model does not include atomic form factors at low energies for the coherent scattering [171]. This problem has been resolved from version GEANT4 9.4, where new set of PENELOPE models has been made available. These new models are based on the version 2008 of Penelope, rather than version 2001 previously available.

Once the geometry is defined and the physics list is built, particles are fired individually. The behaviour of an X-ray photon of energy E is simulated as follows.

Firstly, GEANT4 calculates the cross sections for each process independently (photoelectric, coherent scattering,...), $\sigma(E)$, based on the aforementioned physics models. These data are originally stored at a discrete number of energies. Intermediate values of the cross sections σ for energy E are interpolated using Equation 4.9:

[1] Intel Core 2 Quad CPU Q6600 at 2.40 GHz

$$log\big(\sigma(E)\big) = \frac{log(\sigma_1)log(\frac{E_2}{E}) + log(\sigma_2)log(\frac{E}{E_1})}{log(\frac{E_2}{E_1})}, \tag{4.9}$$

where E_1 and E_2 represent the closest lower and higher energies to E. The corresponding cross sections for the lower and higher energies are denoted as σ_1 and σ_2 respectively. For the absorption edges (K, L, etc.), the upper and lower values are calculated.

Then, the interaction point is determined. Equation 2.15 illustrates the number of atoms per unit volume (N_a) for an element. In case of a compound material, the number of atoms per unit volume for the i^{th} element of the compound is given by:

$$N_i = \frac{N_A\ \rho\ w_i}{A_i}, \tag{4.10}$$

where N_A is the Avogadro's number, ρ is the density of the material, and w_i and Ai represent the mass fraction and atomic weight of the i^{th} element respectively.

The distance travels by a photon is characterised by the mean free path λ, or interaction length. For a given process (photoelectric, coherent or incoherent scattering), λ can be calculated for all the elements of the material, i, as follows:

$$\lambda(E) = \frac{1}{\sum_i N_i\ \sigma(Z_i, E)}, \tag{4.11}$$

where $\sigma(Z, E)$ corresponds to the cross section per atom of the process. Then, the probability of a photon to survive a distance l is

$$P(l) = e^{-n_\lambda}, \tag{4.12}$$

where n_λ corresponds to:

$$n_\lambda = \int_0^l \frac{dl}{\lambda(l)}. \tag{4.13}$$

If $\hat{n_\lambda}$ is a random variable illustrating the number of mean free paths which a photon travels from a given point until the next interaction, the CDF of $\hat{n_\lambda}$ is $1 - e^{-n_\lambda}$ for $n_\lambda > 0$. Using the 'direct sampling method' previously described and the fact that $(1 - \hat{r})$ is as random as the random number $\hat{r}$ in the range (0,1), then n_λ can be sampled as:

$$n_\lambda = -ln\ \hat{r}, \tag{4.14}$$

which represents the equation used in GEANT4 to calculate the point of interaction in a given material. Once this is calculated for all the possible processes, the type of

interaction to occur at this point (photoelectric, coherent or incoherent scattering) is sampled based of their probabilities, which are proportional to the cross sections.

After having calculated the interaction point and the type of interaction, the parameters of the final product (new energy, scattering angle, secondary particles, etc.) are calculated according to the physical properties of that specific interaction as explained in Section 2.2.

For example, in coherent scattering, $cos\theta$ is sampled from the product of the differential cross section for Rayleigh scattering and the squared form factors developed by Hubbell [172, 173] as described in Equation 2.6. In the case of incoherent scattering, the scattering angle θ is sampled using the rejection sampling from the product of the Klein-Nishina formula and the scatter functions from Hubbell [35] as explained in Equation 2.12, whereas the scattered photon energy is calculated from Equation 2.8. Figure 2.9 and 2.11 illustrate samples of scattering angles for coherent and incoherent scattering calculated from MC simulations.

After the final state of a process is sampled, new steps are calculated as previously described: interaction point, type of interaction, final product parameters. This process is repeated until the particle loses all its energy (or reaches the user-defined threshold) or it leaves the system.

4.3.7 X-ray photon generation and tracking

In the MC simulations performed in this work, both monoenergetic and polyenergetic X-ray beams have been used depending on the purpose of the MC experiment. The polyenergetic X-ray energy spectra have been generated using the probability distribution of the photons from the raw energy spectra developed by Boone et al. [40]. Then, this is attenuated mathematically by the different filters and windows observed in the X-ray tube (Section 2.4.1) using Beer-Lambert's law. Furthermore, in order to simulate the energy spectrum more accurately for a given commercial mammography unit, HVL has been matched by attenuating the X-ray energy spectrum with aluminium until the required HVL is matched.

Once the X-ray energy spectrum is created, this is loaded in GEANT4, one bin at a time, where the upper limit of each bin and its weight are defined. The energy of a given photon is selected randomly within a bin, whereas the bin is chosen using the previously defined weights. The energy spectrum is inserted in the geometry depending on the shape of the beam to be simulated. Photon showers, pencil beams and cone beams have been used. The latter was most frequently used in this work, where the X-ray photons emerge from an infinitesimal point located at a specified distance above the chest wall side of the image receptor. The beam is collimated to cover the image receptor entirely as found in real systems. GEANT4 makes use of the random numbers generated to sample the momentum vector of each of the particles generated, ensuring that the X-ray photon flux is uniformly distributed in the beam. The pencil beam corresponds to a narrow photon beam whereas for the photon shower, parallel beams are generated to cover the entire image receptor area. Furthermore, instead of a infinitesimal point source, GEANT4 allows insertion of the energy spectra in the simulation using finite

focal spots such as a sphere or a square to realistically simulate the aperture found in physical X-ray tubes. However, this has not been included in this work. Moreover, as the interactions of the electrons with the anode within the X-ray tube are not modelled, the heel effect is not simulated.

In mammographic units, the distance from the X-ray source to the detector can vary from manufacturer to manufacturer. However, typical values go from $650mm$ to $700mm$. Examples of energy spectra used in this work are 28kV Mo/Mo, 40kV W/Al or 29kV Mo/Rh anode/filter combinations.

Different configurations have been used in the set-up according to the system and purpose of study as will be explained in the following chapters. Figure 4.3 illustrates two simulations in GEANT4. Figure 4.3(a) presents a square phantom in blue with an object of of higher density in red. In Figure 4.3(b), a semicircular breast phantom is shown in blue. In both cases, a set of X-ray photons travelling in the media can be observed in green.

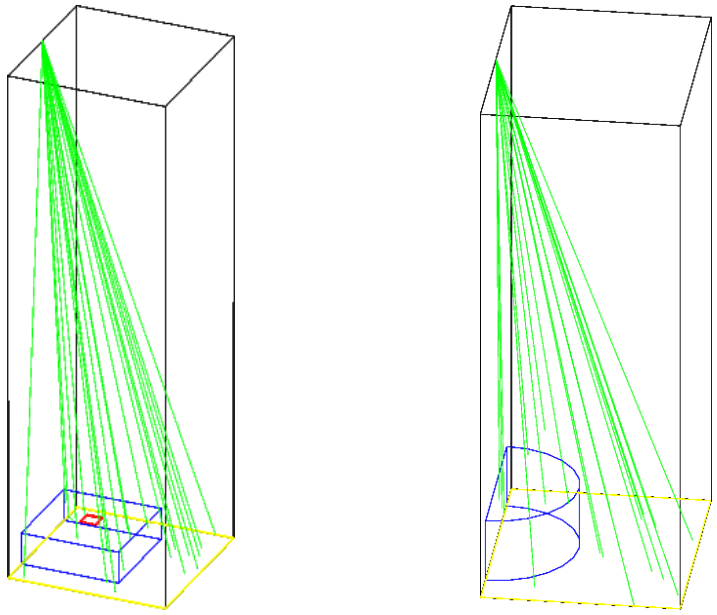

(a) (b)

Figure 4.3: Snapshots of simple GEANT4 simulations. In (a), a square phantom with a high density target (in red) is imaged and a semicircular breast phantom is used in (b).

Figure 4.4 shows the flowchart during the X-ray photon life. Once an X-ray photon is inserted from X-ray tube, this is tracked until it is completely absorbed or it leaves the system. During its passage through the geometry, a photon is considered part of the primary beam (indicated as Flg=0 in Figure 4.4) unless it undergoes a (coherent or incoherent) scatter interaction in any of the layers above the detector, in which case the photon is tagged as scatter (illustrated in Figure 4.4 as Flg=1).

When a photon reaches the image receptor, only incoherent and photoelectric absorption within the detector deposited energy. This energy deposited in the detector and

its spatial location are stored and used to create the accumulated primary and scatter image after the simulation. If an X-ray fluorescent photon is generated after an interaction, the process starts again, but in this case, 'Flg' is not initialised to 0.

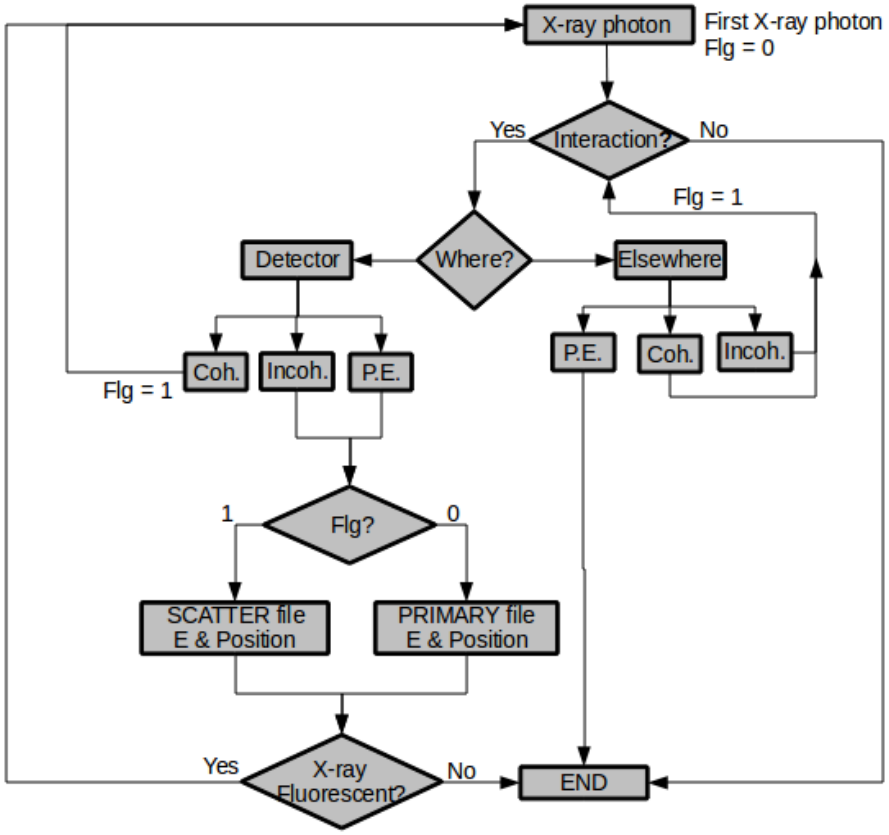

Figure 4.4: Flowchart of the photon's tracking during the simulations. Three different interactions are taken into account: P.E.(photoelectric effect), coherent and incoherent scattering. The entire process is explained in the text. Note that Flg is set to 0 only when an X-ray photon leaves the focal spot.

4.4 Uncertainties associated with Monte Carlo results

An important parameter to bear in mind when running MC simulations is the statistical uncertainty associated with the results. The MC uncertainties refer to the precision of the results, not to their accuracy. In other words, the uncertainties estimate the deviation of the MC results from their average value but not from the true value. The true value of the simulation is achieved by good modelling of the physics interactions and the experiment geometry.

The calculation of this MC error is crucial to initially design an experiment because it helps, for example, to optimize the number of particles to be simulated. If ignored, then a larger than needed number of simulated particles leads to a lengthy simulation

time. For this reason, the statistical fluctuations associated with the MC simulations have been calculated for the different experiments studied along this work.

In order to fully understand this section, it is necessary to clarify the relation between experiments, simulations and number of particles used in this work. A MC experiment represents a given scenario where N separate MC simulations are used often in parallel processing on different machines. Each of the N simulation is run using n particles, hence the total number of particles simulated for a MC experiment are $N \times n$. For example, an experiment could correspond to the scatter study for a given breast phantom using the geometry and technical specifications from a commercial mammography unit. In general, the number of MC simulations used for each experiment is ten ($N = 10$), each of which contains 10^9 X-ray photons. Consequently, the total number of particles simulated is 10^{10}.

Due to the random behaviour of the X-ray photon interactions and their independence between them, the uncertainties associated with the MC results are controlled by a Poisson distribution. However, this distribution will be approximated to a Gaussian as the number of photons get larger.

For this work, the standard error of the mean (SEM) between the different simulations results has used to specify the statistical uncertainty. After running N simulations, an estimate of the standard deviation $\sigma(x, y)$ of the energy deposited $g_i(x, y)$ within the image receptor is calculated for each pixel (x, y) as shown in Equation 4.15:

$$\sigma(x,y) = \sqrt{\frac{1}{N-1}\sum_{i=1}^{N}\Big(g_i(x,y) - \bar{g}(x,y)\Big)^2}, \tag{4.15}$$

where the mean energy deposited $\bar{g}(x, y)$ is represented as

$$\bar{g}(x,y) = \frac{1}{N}\sum_{i=1}^{N} g_i(x,y). \tag{4.16}$$

$\sigma(x, y)$ is computed independently for the primary and scattered X-ray photons as well as for the SPR. Once the standard deviation $\sigma(x, y)$ is known, the SEM of the primary, scatter and SPR images are calculated using

$$SEM(x,y) = \frac{\sigma(x,y)}{\sqrt{N}}. \tag{4.17}$$

The principal aim of this work is to accurately predict scattered radiation as part of a larger mammography simulation framework, where real mammography systems will be simulated. An acceptable mammographic image (primary plus scatter) contains a maximum relative noise of approximately 2.5% per pixel size of 100μm (DR system) for a typical exposure level using an uniform phantom [174]. Thus the statistical uncertainties associated with the MC simulations should be small enough compared to the aforementioned noise. Therefore, the maximum uncertainty associated with MC simulations observed in the main experiments of this work (Chapter 6) should not be greater than 0.25% when replicating a realistic mammographic system.

4.4.1 Simple uncertainty reduction techniques for MC results

In order to reduce the statistical uncertainties associated to the results from the MC simulations, several techniques have been studied. The uncertainty reduction techniques studied include (a) increasing the number of simulations N, and thus total number of particles n, (b) using a large pixel size in the image receptor, and (c) smoothing the image using a spatial filter. The aforementioned techniques cannot only be applied independently but also combined for optimal performance.

Increment of number of simulated particles: An increase in the number of particles, or MC simulations N, is expected to smooth the distribution of the estimates from the true result. Figure 4.5 illustrates the reduction of σ in scattered energy deposited as the number of particles simulated increases. As observed, this reduction is in line with the theory, where the error is reduced by $1/\sqrt{n}$, where n is the number of particles simulated.

The setup of this experiment is explained in [175]. The system geometry corresponds to Hologic Selenia, where a D-shape breast phantom, similar to the one shown in Figure 4.3(b), was inserted in the simulations. The semi-circular phantom has a radius of 80mm and a height 60mm. Its glandularity was 20.8% and it was imaged using an energy spectrum of 34kVp W/Al (HVL = 0.655mm).

The σ was calculated within a 10mm^2 region of interest (ROI) located at 40mm from the chest wall. The number of simulations was fixed to 10 (N=10), whereas the number of photons used per simulation was 10^6, 10^7, 10^8 and 10^9.

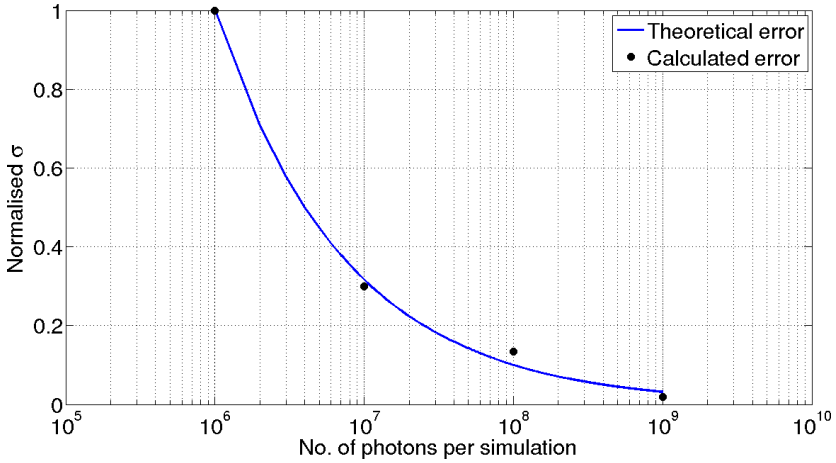

Figure 4.5: Black dots illustrate the calculated normalised standard deviation (σ) as the number of photons per simulation is increased. This is compared with the theoretical reduction (blue curve): $1/\sqrt{n}$.

Increase of pixel size: An increase of the pixel size at the image receptor will increase the number of particles hits per pixel. This will lead to a decrease in the in the standard deviation (at the expense of spatial resolution), which reduces the SEM

at the same time as illustrated in Equation 4.17. However, as the scattered radiation varies slowly with position, this can be average using a large pixel size.

Smoothing spatial filters: Linear and non-linear smoothing filters represent very common techniques in image processing for noise reduction [135].

Although the linear averaging filters reduce the sharp transition in the pixels corresponding to the random noise, the median filter is superior in preserving the features in the image [135]. Furthermore, the non-linear median filter is very effective in the presence of impulse noise, also known as *salt and pepper* noise. For these reasons, the latter filter has been used here to reduce the statistical fluctuations produced from MC simulations while preserving the principal characteristics of the image.

The median filter calculates, for each pixel, the median pixel value of the pixel itself and the $\big((k \times k)\text{-}1\big)$ neighborhood pixels, where the index k corresponds to the size of the median filter kernel. Then, the evaluated pixel value is substituted by this new value. For optimal performance, the index k of the median filter should be an odd number.

4.4.2 Example of statistical error reduction

To fully comprehend the MC statistical errors as well as observe the variance reduction properties of the aforementioned techniques, results from a set of exemplar MC simulations using a realistic mammography geometry have been analysed in this section. For this experiment, a 9.3cm thick anthropomorphic breast phantom (see Figure 2.16(c)) with a glandularity of 9.6% has been imaged from an angle of 25^o as illustrated in Figure 4.6(a). Each experiment has been simulated N times using 10^9 particles each. This specific phantom has been chosen because it represents the thickest breast phantom which has been used in this work and therefore, it will produce the noisiest images. Furthermore, the angle 25^o angle will increase the path traverses by the X-ray photons, which increases the photon path through the phantom even more.

The SEM has been calculated as explained on Equation 4.17 in a pixel by pixel basis as illustrated in Figure 4.6(b). This represents the SEM for ten simulations ($N = 10$) of the scatter (SEM_S) using the aforementioned breast phantom at 25^o. In this case, error reduction techniques have not been applied yet.

Table 4.2 illustrates the average SEM_S for the 20x20 pixels ROI within the breast phantom shadow illustrated in Figure 4.6(b) after making several changes (pixel size or number of simulated particles) in the MC experiments.

When increasing the number of particles, or number of simulations N, the SEM is reduced as described previously in Section 4.4.1. As it can be observed in the first and second row of Table 4.2, the error decreases by $\frac{1}{\sqrt{2}}$ when the number of particles is doubled.

The last two rows in the table represent the SEMs when increasing the pixel size. Thus comparing rows 1, 3 and 4, it is observed that the SEM is reduced by half every time the pixel size is doubled.

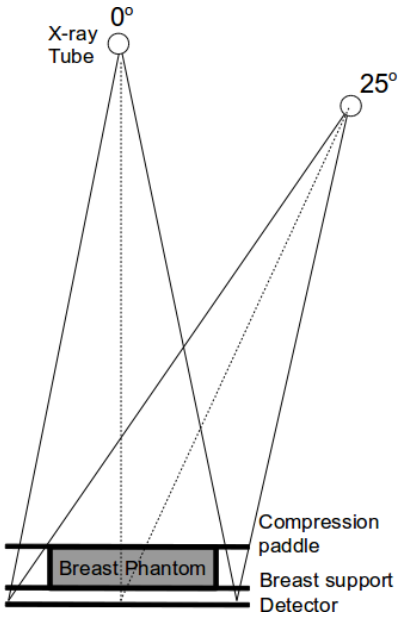

(a) Geometry

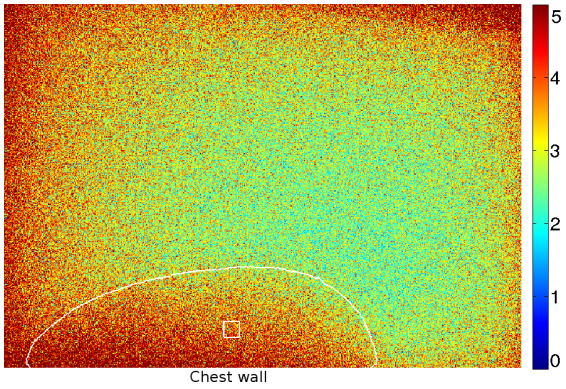

(b) SEM_S for 25^o

Figure 4.6: (a) represents the diagram of the MC simulations used for calculating the MC statistical errors. Despite only results for ϕ=25^o are shown here, the 0^o projection angle is shown for reference. In (b), the SEM map (in %) of the scatter have been calculated pixel by pixel using a $0.5mm^2$ pixel area for 25^o. The white square represents the ROI within the breast phantom used to calculate the average SEM value given in table 4.2, whereas the white contour corresponds to the outline of the projected breast phantom.

Table 4.2: Geometry used to study the statistical error associated to MC simulations.

Pixel size (mm)	Image dimension (pixels)	ϕ (degree)	N	SEM_S(%)
0.5	480 x 681	25	10	4.0
		25	20	2.8
1	240 x 340	25	10	2.0
2	120 x 170	25	10	1.0

Despite increasing both the pixel size and number of particles, the SEM_S is greater than the 0.25% target. Thus the influence of median filter's size has also been studied.

Figure 4.7 illustrates the SEM_S maps for the aforementioned geometry using ϕ=25^o, pixel size of $1mm^2$ and ten runs (N=10).

The average SEM values within each of the ROIs defined in Figure 4.7 are shown in Table 4.3. It is observed that the SEM is reduced when increasing the size of the $k \times k$ median filters. A kernel size of 7x7 pixels produces a mean SEM of 0.4%, which represents the proposed median filter size for smoothing the results from MC simulations. Bear in mind, that these errors represent the largest errors to be found

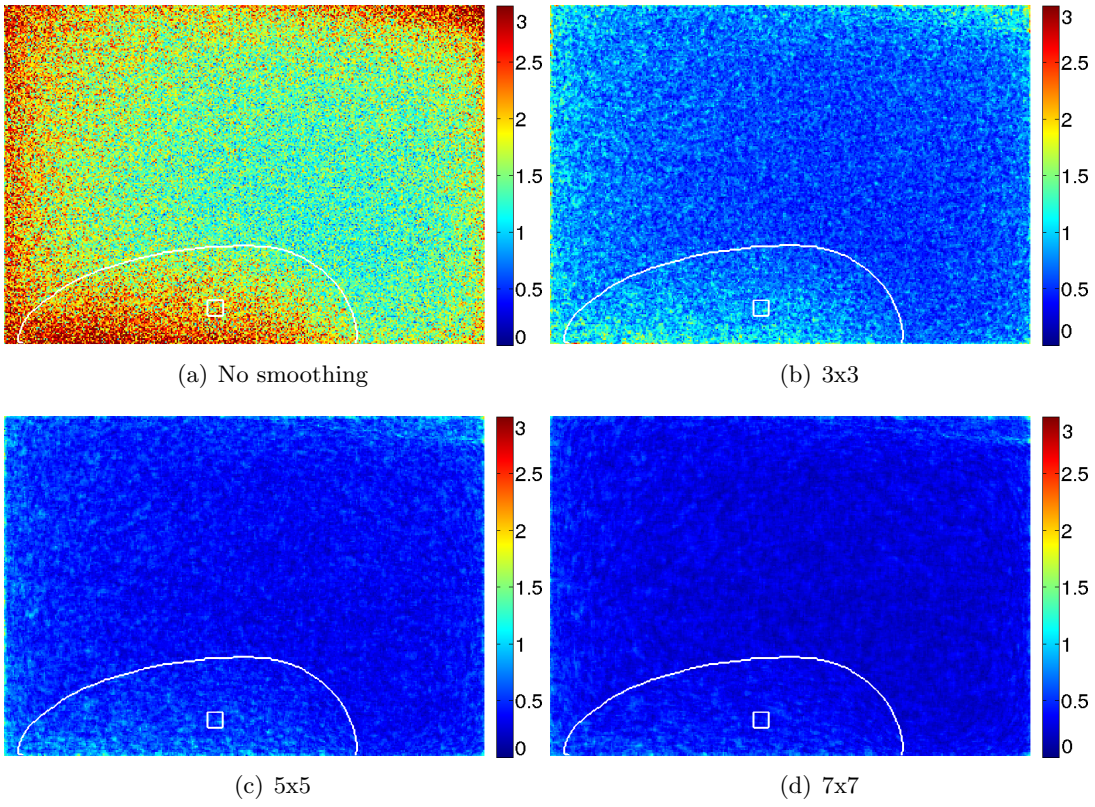

(a) No smoothing (b) 3x3

(c) 5x5 (d) 7x7

Figure 4.7: SEM_S maps (in %) for a projection angle ϕ of 25^o, pixel size of $1mm^2$ and ten runs (N=10). Several $k \times k$ median filters have been analysed. The white square represents the ROI used to calculate the mean SEM value illustrated in Table 4.3, whereas the white contour corresponds to the outline of the projected breast phantom.

in this study, as the rest of the simulations use thinner breast phantoms and different X-ray spectra, where errors are smaller than the SEMs illustrated here.

Table 4.3: Mean SEM values for scatter within the ROI defined in Figure 4.7 for different kernel sizes.

Kernel size (pixels)	SEM_S(%)
1x1	2.0
3x3	0.9
5x5	0.5
7x7	0.4

Another option has been explored to achieve a larger statistical noise reduction, which is to apply the median filter several times. In order to avoid fluctuations in the image due to tissue structure, the above experiments have been repeated using the same breast phantom but it has been filled in with adipose tissue only. Thus only statistical noise from MC simulations is observed. For this configuration, the average SEMs observed

for the scatter images within the ROI (see Figure 4.7) are shown in Figure 4.8, where a 7x7 median filter has been applied to the images several times using a pixel size of $1mm^2$.

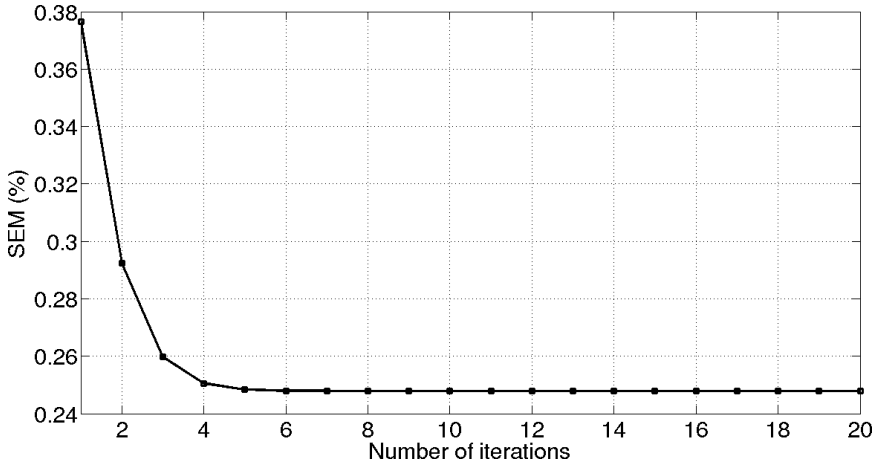

Figure 4.8: Average SEMs measured within a 10x10mm^2 ROI in the middle of a 93mm thick homogeneous breast phantom for different median filter iterations.

The SEM is reduced when increasing the number of iterations. However after approximately five iterations, the reduction in SEM is insignificant.

Finally, in order to make sure that the multiple applications of median filters are not over-filtering the image and crucial information is not lost, several profiles along the scatter image have been plotted as illustrated in Figure 4.9.

Noisy profiles corresponding to the non-smooth scatter image are observed in Figure 4.9. Those fluctuations are significantly reduced when applying the 7x7 median filter once. After median filtering twenty times, the resulted scatter image shows very smooth profiles which keep the original shape reducing the noise largely. Regarding the primary image, the median filter is not applied to make sure that internal breast structures are not lost. Moreover, this can be calculated analytically.

4.5 Validation of simulations

Although GEANT4 has been widely validated in the literature [169, 171, 176] and it has been used elsewhere in the mammography field [78, 82, 129], an in-house validation against published and clinical data has been performed in order to provide confidence in the subsequent results.

4.5.1 Cross-sections validation

The first validation exercise was to compare the total cross sections of GEANT4 and NIST-XCOM [26] for selected elements which are commonly found in breast tissue (see Table 2.2) and image receptors (see Table 2.3).

(a) Scatter image

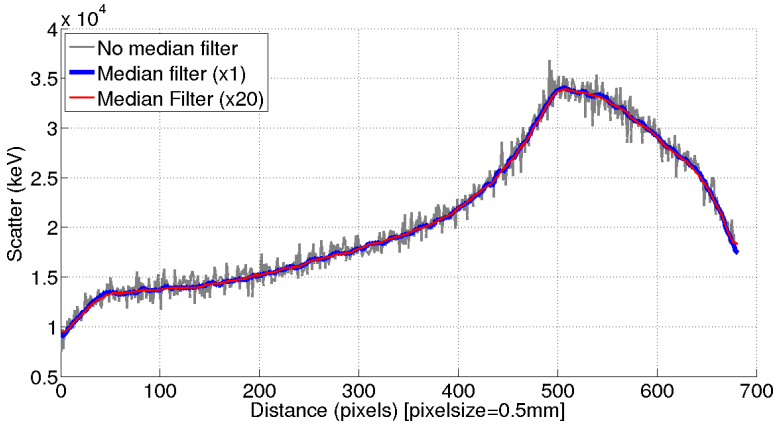

(b) Horizontal profile

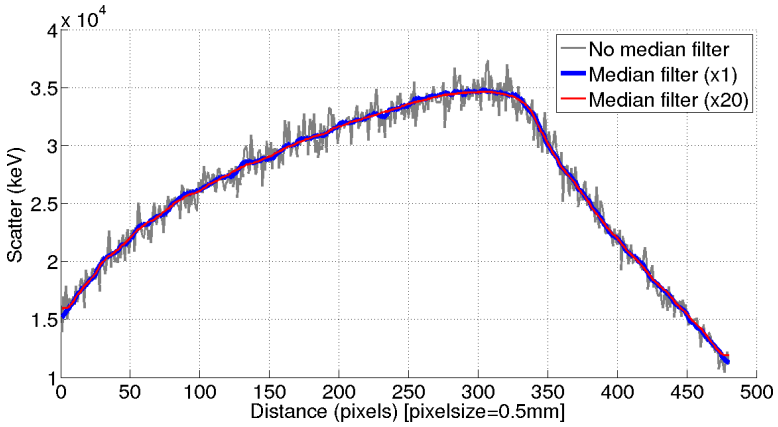

(c) Vertical profile

Figure 4.9: (a) illustrates the scatter image (in keV) of the 93mm thick breast phantom using a pixel size of 0.5mm^2. The horizontal and vertical profiles highlighted in solid white lines are shown in (b) and (c) respectively for no median filter, one and twenty iterations using a 7x7 median filter.

Both cross section libraries have been compared for discrete energies below 50keV, which corresponds to the maximum energy used in mammography. The cross section values from NIST-XCOM have been obtained from the online database whereas the GEANT4 cross section has been calculated using the Livermore package described in Section 4.3.6. The intermediate values have been interpolated as explained in Equation 4.9.

The average difference between both cross section libraries for the different elements studied was 0.06%. However, larger errors were observed for energies below 10keV or near the absorption edges, where the cross sections change rapidly. Furthermore, as described by several other authors [169, 171, 176], there exists large discrepancies in the coherent scattering for low energies between NIST and the low energy package used here (Livermore data). Cirrone et al. [171] describes that the discrepancies for coherent scattering between the libraries are due to the use of different form factors. NIST uses relativistic Hartree-Fock atomic form factors whereas GEANT4 employs Hubbel's form factors [172].

A first example of the cross section validation process undertaken in this work is illustrated in Figure 4.10. The total photoelectric, incoherent and coherent scattering cross sections are shown for carbon (C) when using the data from GEANT4 and NIST-XCOM. Note that for energies below 20keV there is higher probability of a photoelectric interaction for particles, while energies above 20keV, incoherent interactions are more likely to happen.

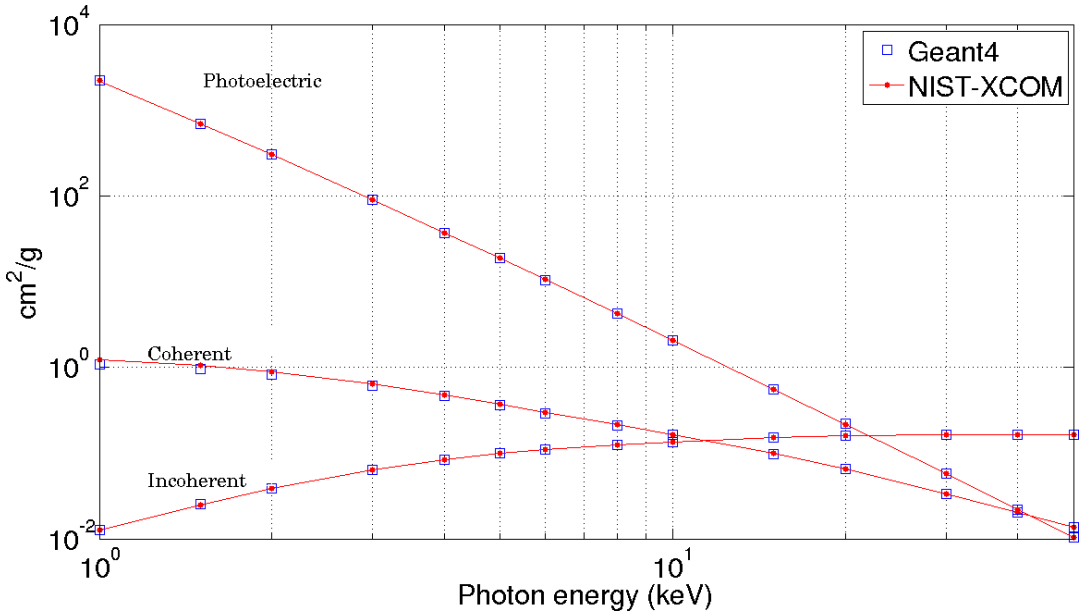

Figure 4.10: Comparison between GEANT4 cross sections (blue squares) and NIST-XCOM cross sections (red circles) for carbon. Incoherent, coherent and photoelectric physical interactions are shown for an energy range from 1keV to 50 keV.

For a more quantitative analysis of the data, the cross sections for C are tabulated in Table 4.4, where less than 1.5% of difference is observed within the mammography energy

range (10-50keV). Note that for lower energies, the discrepancies in coherent scattering are larger as already mentioned. However, coherent scattering is not important for the energies below 10keV where the interactions are dominated by the photoelectric effect.

Table 4.4: Quantitative comparison between incoherent, coherent and photoelectric cross sections for carbon measured from GEANT4 and NIST-XCOM for an energy range between 1keV to 50keV. Note that the largest discrepancies are highlighted in red.

	Incoherent			Coherent			Photoelectric		
Energy (keV)	GEANT4 (cm^2/g)	NIST-XCOM (cm^2/g)	Difference (%)	GEANT4 (cm^2/g)	NIST-XCOM (cm^2/g)	Difference (%)	GEANT4 (cm^2/g)	NIST-XCOM (cm^2/g)	Difference (%)
1	$1.26x10^{-2}$	$1.26x10^{-2}$	0.4	$1.23x10^{0}$	$1.08x10^{0}$	14.0	$2.21x10^{3}$	$2.21x10^{3}$	0.1
1.5	$2.50x10^{-2}$	$2.51x10^{-2}$	0.2	$1.05x10^{0}$	$9.59x10^{-1}$	10.0	$6.99x10^{2}$	$6.99x10^{2}$	0.0
2	$3.87x10^{-2}$	$3.86x10^{-2}$	0.3	$8.94x10^{-1}$	$8.32x10^{-1}$	7.4	$3.01x10^{2}$	$3.02x10^{2}$	0.2
3	$6.40x10^{-2}$	$6.41x10^{-2}$	0.1	$6.43x10^{-1}$	$6.13x10^{-1}$	5.0	$8.95x10^{1}$	$8.96x10^{1}$	0.1
4	$8.46x10^{-2}$	$8.45x10^{-2}$	0.2	$4.77x10^{-1}$	$4.60x10^{-1}$	3.8	$3.72x10^{1}$	$3.72x10^{1}$	0.0
5	$9.97x10^{-2}$	$9.95x10^{-2}$	0.2	$3.70x10^{-1}$	$3.59x10^{-1}$	3.1	$1.86x10^{1}$	$1.87x10^{1}$	0.3
6	$11.0x10^{-2}$	$11.04x10^{-2}$	0.3	$2.99x10^{-1}$	$2.92x10^{-1}$	2.5	$1.05x10^{1}$	$1.05x10^{1}$	0.3
8	$12.5x10^{-2}$	$12.52x10^{-2}$	0.4	$2.14x10^{-1}$	$2.10x10^{-1}$	1.8	$4.24x10^{0}$	$4.24x10^{0}$	0.0
10	$13.6x10^{-2}$	$13.52x10^{-2}$	0.4	$1.64x10^{-1}$	$1.62x10^{-1}$	1.4	$2.08x10^{0}$	$2.08x10^{0}$	0.2
15	$15.1x10^{-2}$	$15.10x10^{-2}$	0.1	$9.87x10^{-2}$	$9.79x10^{-2}$	0.9	$5.58x10^{-1}$	$5.59x10^{-1}$	0.2
20	$16.0x10^{-2}$	$15.95x10^{-2}$	0.0	$6.51x10^{-2}$	$6.48x10^{-2}$	0.5	$2.17x10^{-1}$	$2.18x10^{-1}$	0.3
30	$16.5x10^{-2}$	$16.55x10^{-2}$	0.3	$3.38x10^{-2}$	$3.36x10^{-2}$	0.5	$5.70x10^{-2}$	$5.71x10^{-2}$	0.2
40	$16.5x10^{-2}$	$16.53x10^{-2}$	0.2	$2.05x10^{-2}$	$2.05x10^{-2}$	0.1	$2.19x10^{-2}$	$2.19x10^{-2}$	0.0
50	$16.3x10^{-2}$	$16.30x10^{-2}$	0.0	$1.37x10^{-2}$	$1.37x10^{-2}$	0.2	$1.04x10^{-2}$	$1.04x10^{-2}$	0.1

A second example of cross section comparison is shown in Table 4.5 for Cs which has higher Z number than the previously calculated C. In this case, large discrepancies were found in all energies studied for coherent scattering as the discrepancies in the form factors are larger for higher Z materials. Furthermore, large errors are also observed for photoelectric effect near the absorption edges as previously discussed.

Apart from the above issues, which have been explained at the beginning of this section, the agreement between both cross sections was good. It is concluded then, that the MC toolkit used in this study can reliably reproduce the most common physics interactions in the mammography energy with sufficient accuracy.

4.5.2 Validation with published data

Further to the cross section validation, the MC code has been macroscopically validated using mammography geometries described in prior published work. Three different experiments published by Boone et al. [61], using a cellular anti-scatter grid described by Rezentes et al. [58], have been simulated.

The cellular anti-scatter grid has been simulated in GEANT4 using the appropriate dimensions for each experiment. Its design consists of a rectangular box filled in with the septa material (e.g. copper). Then, a series of parallelepipeds (aligned with the focal spot) filled with the appropriate material (e.g. air) are placed within the rectangular box, simulating the interspace.

These publications were chosen because they shows results for a cellular anti-scatter grid design (Lorad M-III) and it will validate the methodology used to implement the

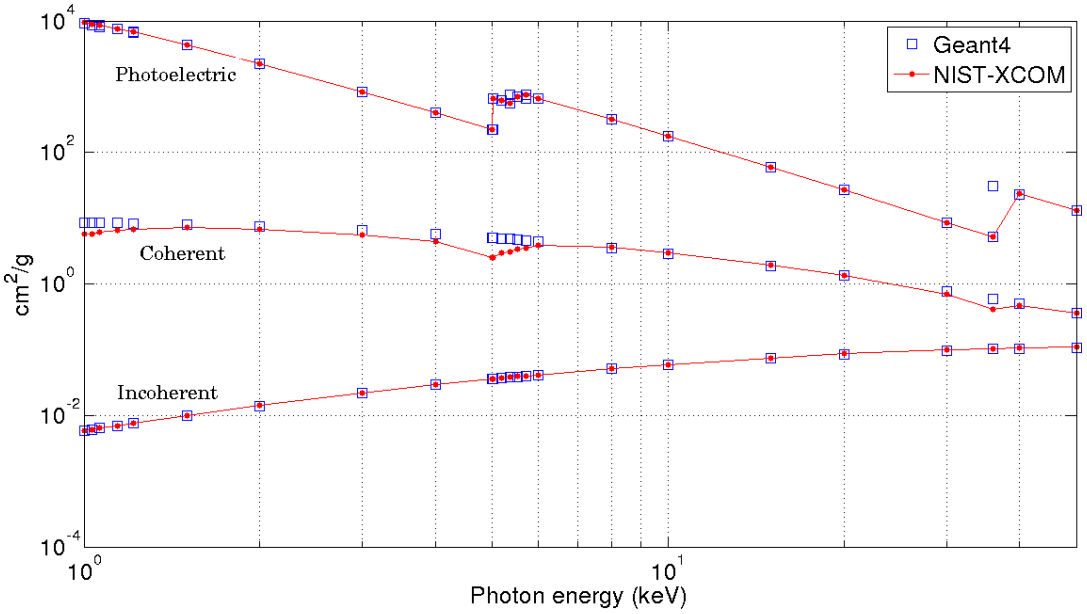

Figure 4.11: Comparison between GEANT4 cross sections (blue squares) and NIST-XCOM cross sections (red circles) for cesium. Incoherent, coherent and photoelectric physical interactions are shown for an energy range from 1keV to 50 keV.

Hologic Selenia Dimensions anti-scatter grid (also cellular) in future simulations. The dimensions and material of this grid are shown in Table 4.6.

For each experiment, five simulations using 10^9 photons were used. The resulting images were median filtered using a 11x11 kernel and a pixel size of $1mm^2$ was used. The SEM associated to each of the calculated metrics is shown in the results below. The MC setup used in these experiments is shown in Figure 4.3(b). A semicircular breast phantom with 10cm radius was used. The phantom composition was 50% adipose 50% glandular breast tissue and neither compression paddle nor breast support were included in the simulations described by Boone et al. [61]. The specific configurations used for each experiment are summarised in Table 4.7.

For all the experiments, the CIF and BF were calculated using methodology explained in Section 2.4.5. The primary plus scatter image (P+S) and the SPR were calculated with (G) and without (NG) the anti-scatter grid in a 50x90 pixels ROI (see red square in Figure 4.12(a)) using a pixel size of $1mm^2$.

The primary, scatter and SPR images recorded for Experiment I with and without the anti-scatter grid are shown in Figure 4.12.

The results from experiments I, II and III are shown in Tables 4.8, 4.9 and 4.10 respectively. Overall, it has been found less than 3% discrepancy in CIF and BF with Boone et al. data [61], the error being attributed to different HVL values employed as the author (J.M. Boone) did not specified them in his paper. Furthermore, both the statistical uncertainties and cross sections of his MC results are not described in the paper. Results from experiment II shows a discrepancy of up to approximately 8%

Table 4.5: Quantitative comparison between incoherent, coherent and photoelectric cross sections for cesium measured from GEANT4 and NIST-XCOM for an energy range between 1keV to 50keV. Note that the largest discrepancies are highlighted in red.

	Incoherent			Coherent			Photoelectric		
Energy (keV)	GEANT4 (cm^2/g)	NIST-XCOM (cm^2/g)	Difference (%)	GEANT4 (cm^2/g)	NIST-XCOM (cm^2/g)	Difference (%)	GEANT4 (cm^2/g)	NIST-XCOM (cm^2/g)	Difference (%)
1	$5.89x10^{-3}$	$5.88x10^{-3}$	0.1	$5.73x10^{0}$	$8.55x10^{0}$	33.0	$9.45x10^{3}$	$9.36x10^{3}$	1.0
1.032	$6.13x10^{-3}$	$6.13x10^{-3}$	0.0	$5.76x10^{0}$	$8.52x10^{0}$	32.5	$8.83x10^{3}$	$8.76x10^{3}$	0.8
1.065	$6.39x10^{-3}$	$6.39x10^{-3}$	0.1	$6.07x10^{0}$	$8.49x10^{0}$	28.5	$8.51x10^{3}$	$8.21x10^{3}$	3.7
1.065	$6.39x10^{-3}$	$6.39x10^{-3}$	0.1	$6.07x10^{0}$	$8.49x10^{0}$	28.5	$8.51x10^{3}$	$8.68x10^{3}$	2.0
1.139	$6.97x10^{-3}$	$6.93x10^{-3}$	0.1	$6.44x10^{0}$	$8.42x10^{0}$	23.5	$7.59x10^{3}$	$7.56x10^{3}$	0.5
1.217	$7.59x10^{-3}$	$7.59x10^{-3}$	0.1	$6.71x10^{0}$	$8.35x10^{0}$	19.6	$6.87x10^{3}$	$6.58x10^{3}$	4.5
1.217	$7.59x10^{-3}$	$7.59x10^{-3}$	0.1	$5.71x10^{0}$	$8.35x10^{0}$	19.6	$6.87x10^{3}$	$6.88x10^{3}$	0.1
1.5	$9.88x10^{-3}$	$9.86x10^{-3}$	0.1	$7.11x10^{0}$	$8.07x10^{0}$	11.9	$4.33x10^{3}$	$4.33x10^{3}$	0.1
2	$1.40x10^{-2}$	$1.40x10^{-2}$	0.2	$6.78x10^{0}$	$7.58x10^{0}$	10.5	$2.22x10^{3}$	$2.22x10^{3}$	0.0
3	$2.21x10^{-2}$	$2.20x10^{-2}$	0.2	$5.59x10^{0}$	$6.59x10^{0}$	15.2	$8.25x10^{2}$	$8.25x10^{2}$	0.0
4	$2.95x10^{-2}$	$2.94x10^{-2}$	0.3	$4.40x10^{0}$	$5.75x10^{0}$	23.5	$3.99x10^{2}$	$4.00x10^{2}$	0.1
5	$3.60x10^{-2}$	$3.58x10^{-2}$	0.4	$2.48x10^{0}$	$5.04x10^{0}$	50.8	$2.25x10^{2}$	$2.25x10^{2}$	0.1
5.012	$3.60x10^{-2}$	$3.59x10^{-2}$	0.4	$2.50x10^{0}$	$5.03x10^{0}$	50.4	$6.66x10^{2}$	$2.24x10^{2}$	197.5
5.012	$3.60x10^{-2}$	$3.59x10^{-2}$	0.4	$2.50x10^{0}$	$5.03x10^{0}$	50.4	$6.66x10^{2}$	$6.63x10^{2}$	0.6
5.183	$3.70x10^{-2}$	$3.69x10^{-2}$	0.3	$2.99x10^{0}$	$4.92x10^{0}$	39.1	$6.14x10^{2}$	$6.09x10^{2}$	0.8
5.359	$3.80x10^{-2}$	$3.79x10^{-2}$	0.2	$3.02x10^{0}$	$4.82x10^{0}$	37.4	$5.63x10^{2}$	$5.60x10^{2}$	0.6
5.359	$3.80x10^{-2}$	$3.79x10^{-2}$	0.2	$3.02x10^{0}$	$4.82x10^{0}$	37.4	$5.63x10^{2}$	$7.64x10^{2}$	26.4
5.534	$3.89x10^{-2}$	$3.89x10^{-2}$	0.2	$3.39x10^{0}$	$4.72x10^{0}$	28.2	$7.09x10^{2}$	$7.05x10^{2}$	0.6
5.714	$3.99x10^{-2}$	$3.99x10^{-2}$	0.2	$3.54x10^{0}$	$4.62x10^{0}$	23.4	$7.52x10^{2}$	$6.51x10^{2}$	15.5
5.714	$3.99x10^{-2}$	$3.99x10^{-2}$	0.2	$3.54x10^{0}$	$4.62x10^{0}$	23.4	$7.52x10^{2}$	$7.50x10^{2}$	0.3
6	$4.15x10^{-2}$	$4.14x10^{-2}$	0.3	$3.88x10^{0}$	$4.46x10^{0}$	13.0	$6.66x10^{2}$	$6.67x10^{2}$	0.1
8	$5.11x10^{-2}$	$5.08x10^{-2}$	0.6	$3.60x10^{0}$	$3.55x10^{0}$	1.5	$3.17x10^{2}$	$3.18x10^{2}$	0.2
10	$5.93x10^{-2}$	$5.89x10^{-2}$	0.6	$2.97x10^{0}$	$2.89x10^{0}$	3.0	$1.76x10^{2}$	$1.76x10^{2}$	0.1
15	$7.51x10^{-2}$	$7.46x10^{-2}$	0.6	$1.91x10^{0}$	$1.90x10^{0}$	0.8	$5.90x10^{1}$	$5.91x10^{1}$	0.1
20	$8.59x10^{-2}$	$8.52x10^{-2}$	0.8	$1.32x10^{0}$	$1.36x10^{0}$	2.6	$2.67x10^{1}$	$2.68x10^{1}$	0.1
30	$9.83x10^{-2}$	$9.76x10^{-2}$	0.8	$6.95x10^{-1}$	$7.79x10^{-1}$	10.8	$8.62x10^{0}$	$8.63x10^{0}$	0.1
35.98	$1.03x10^{-1}$	$1.02x10^{-1}$	0.7	$4.17x10^{-1}$	$5.95x10^{-1}$	29.9	$5.16x10^{0}$	$5.17x10^{0}$	0.1
35.98	$1.03x10^{-1}$	$1.02x10^{-1}$	0.7	$4.17x10^{-1}$	$5.95x10^{-1}$	29.9	$5.16x10^{0}$	$3.07x10^{1}$	83.2
40	$1.05x10^{-1}$	$1.04x10^{-1}$	0.9	$4.65x10^{-1}$	$5.07x10^{-1}$	8.3	$2.33x10^{1}$	$2.32x10^{1}$	0.6
50	$1.09x10^{-1}$	$1.08x10^{-1}$	1.0	$3.58x10^{-1}$	$3.61x10^{-1}$	0.8	$1.29x10^{1}$	$1.29x10^{1}$	0.2

Table 4.6: Specifications of Lorad M-III cellular grid described by Rezentes et al. [58].

Grid type	Grid ratio(h/D)	Interspace material	Septa material	Septa height (h)	Septa thickness (d)	Interspace thickness (D)
Cellular	3.8	Air	Copper	2.4mm	0.03mm	0.64mm

Table 4.7: Configuration used for each experiment described by Boone et al. [61].

Experiment	X-ray spectrum	Breast thickness	Detector (thickness/composition)
I	28kVp Mo/Mo	6cm	Kodak Min-R (46μm Gd_2O_2S)
II	40kVp W/Al	6cm	Ideal detector
III	30kVp Mo/Mo	8cm	Kodak Min-R (46μm Gd_2O_2S)

in SPR values. It is not stated in the paper, but in the past, it has been found that this author (J.M. Boone) uses slightly different glandular and adipose tissue composition. This might show larger discrepancies for this case, where the maximum energy simulated was 40kVp.

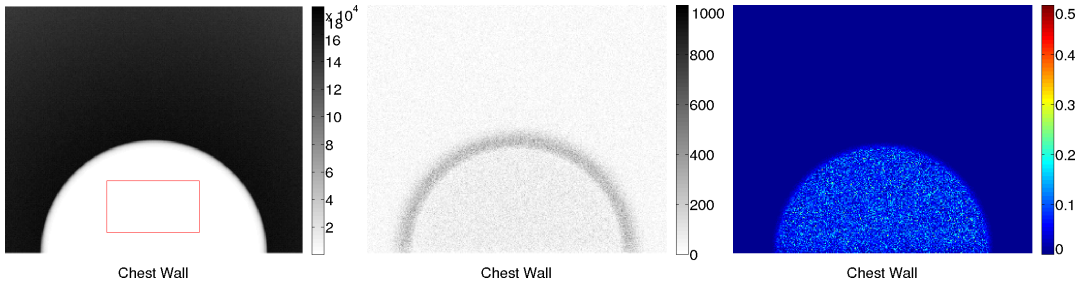

(a) Primary image (b) Scatter image (c) SPR

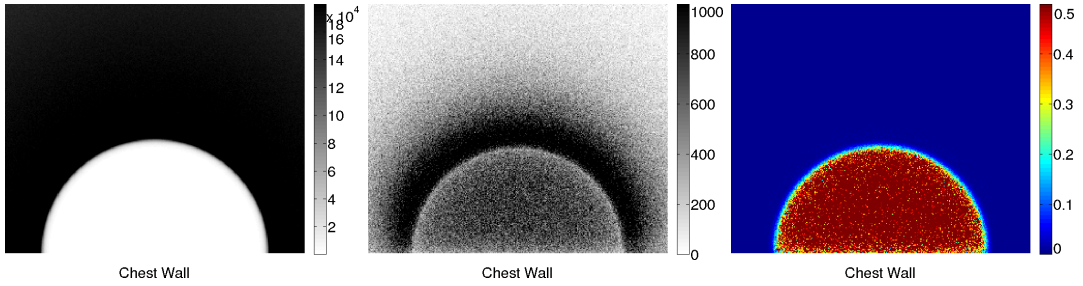

(d) Primary image (e) Scatter image (f) SPR

Figure 4.12: Images recorded within the image receptor for Experiment I. The first row corresponds to images with anti-scatter grid present, and the second row illustrates images without the anti-scatter grid. The red square shown in (a) represents the location of the ROI used to calculate CIF and BF.

The ROI used in this work to calculate the SPR is shown in Figure 4.12(a) (red square). It is unknown, where Boone et al. measured the SPR. This could also lead to discrepancies, as SPR changes across the detector when the anti-scatter grid is not employed. Moreover, Boone et al. has not included the scatter originated in the anti-scatter grid, whereas in this work, scatter from all elements in the geometry (including anti-scatter grid) is simulated.

Table 4.8: Experiment I: SPR, CIF and BF values calculated from this work and Boone et al.(2002) [61]. SEM associated to each calculation of this work is shown in brackets.

	Boone et al.(2002)		This work		Difference	
	Grid	No Grid	Grid	No Grid	Grid	No Grid
SPR	—	0.690	0.0749 (0.2%)	0.689 (0.1%)	—	0.1%
CIF	1.54		1.57 (0.0%)		2.0%	
BF	1.70		1.75 (0.1%)		3.0%	

Table 4.9: Experiment II: SPR, CIF and BF values calculated from this work and Boone et al.(2002) [61]. SEM associated to each calculation of this work is shown in brackets.

	Boone et al.(2002)		This work		Difference	
	Grid	No Grid	Grid	No Grid	Grid	No Grid
SPR	—	0.660	0.135 (0.1%)	0.610 (0.0%)	—	7.6%
CIF		1.44	1.42 (0.0%)			1.4%
BF		1.60	1.57 (0.0%)			2.0%

Table 4.10: Experiment III: SPR, CIF and BF values calculated from this work and Boone et al.(2002) [61]. SEM associated to each calculation of this work is shown in brackets.

	Boone et al.(2002)		This work		Difference	
	Grid	No Grid	Grid	No Grid	Grid	No Grid
SPR	—	0.970	0.120 (0.4%)	0.920 (0.3%)	—	5.2%
CIF		1.75	1.71 (0.2%)			2.3%
BF		1.95	1.93 (0.3%)			1.0%

4.5.3 Validation with clinical data

The MC simulation code has also been validated with raw images acquired experimentally in a commercial X-ray mammography systems.

A $4.5\times5.5cm^2$ copper (Cu) sheet of $1mm$ thickness was placed on top of a $5cm$ thick block of PMMA as shown in Figure 4.13(a). This was then imaged using a Hologic Selenia Dimensions system, which contains a High Transmission Cellular (HTC) anti-scatter grid. This is the first assessment of the Hologic Selenia Dimensions HTC anti-scatter grid to the authors knowledge. A snapshot of this experiment is illustrated in Figure 4.3(a).

The validation task consisted of comparing the contrast of the Cu sheet between the simulated and experimentally acquired raw images. The mean pixel values of an ROI within the Cu sheet image (I_{Cu}) and four ROIs in the the background (I_b) as illustrated in Figure 4.13(b) were used to calculate the contrast (C) using Equation 4.18.

$$C = \frac{I_b - I_{Cu}}{I_b}. \tag{4.18}$$

Ten simulations using 10^9 photons each were used and the energy spectrum was set to 37kVp Mo/Rh with and without the cellular anti-scatter grid included in this system. Clinical images were taken using Hologic Selenia Dimensions mammography system [177], thus the appropriate geometry information provided by the manufacturer was replicated in the simulations. The MC simulations recorded energy deposited in the detector. Despite the pixel values measured experimentally are proportional to the energy deposited, they have an offset value associated. This offset value was measured for this particular system to be 43.7 [178]. Therefore, a value of 43.7 was subtracted

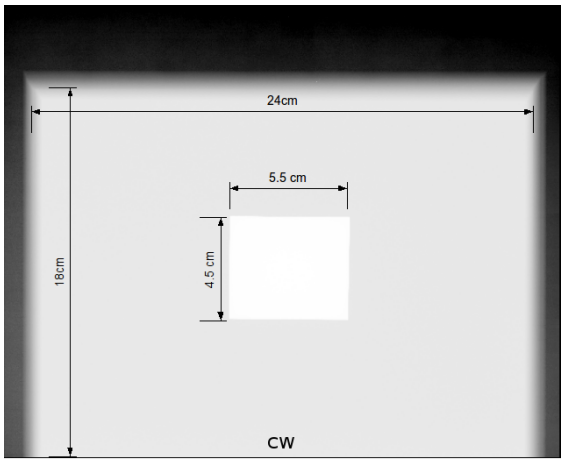

(a)

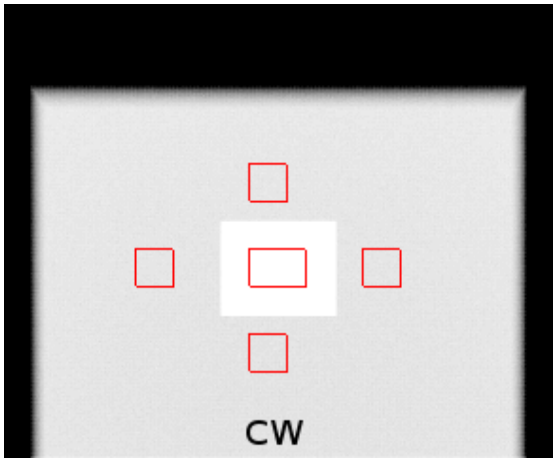

(b)

Figure 4.13: The raw image acquired experimentally for a 1mm thick Cu sheet op top of a 50mm thick PMMA is shown in (a) with their dimensions. The corresponding simulated image is illustrated in (b). The red squares shown in (b) represent the ROIs used inside and outside of the Cu sheet to calculate the contrast. The chest wall (CW) is located at the bottom of the images.

from the the pixel values measured in the images before calculating the contrast in the experimental image. Due to the large ROIs used, the SEM associated to the contrast calculations were found to be less than 0.1%.

Table 4.11 shows the results comparing the contrast of the Cu sheet in experimental (C_{exp}) and simulated (C_{sim}) images for grid and no grid imaging. 0.1% and 1.5% differences were found between the contrast calculated for the experimental acquired and simulated images for the grid and no grid geometry respectively. These discrepancies may arise from thicknesses irregularities or impurities in the Cu sheet or variation in the PMMA density. However, a larger effect can come from the fact that the heel effect was

not simulated in the MC simulations as the X-ray tube exit was a infinitesimal point source, which might affect the contrast value. Furthermore, scatter interactions within the image receptor have not been included within the simulations. This fact might has underestimated the scattered radiation in the MC simulation and would have increased the contrast value in the simulated images.

Table 4.11: Contrast calculated for a Cu sheet acquired experimentally (C_{exp}) and the contrast calculated in the corresponding simulated image (C_{sim}).

Energy Spectra	Config.	C_{exp}	C_{sim}	Difference
37MoRh	Grid	0.992	0.991	0.1%
	No Grid	0.757	0.769	1.5%

As described above, only one setup using a 1mm Cu sheet was used to validate the MC simulations. However, it met the purpose of this experiment to compare experimental and simulated data under the same circumstances.

Although small discrepancies have been found when comparing results from this work against published and experimental data, it has been demonstrated the good performance of the GEANT4 toolkit in mammographic experiments. Moreover, the cellular anti-scatter grid designed in GEANT4 has been shown good agreement with the real cellular anti-scatter grid. Therefore, it represents a suitable tool to use in this work.

4.6 Summary and discussion

In this chapter, the importance of computer simulations in mammography, in particular MC simulations, has been discussed. They represent an invaluable tool to investigate physical parameters in depth, such as scattered radiation, which are difficult to measure using real physical systems.

The main features of the MC package used for this work, GEANT4, have been described in Section 4.3 where special emphasis has been placed on the physics processes and pseudo-number random generations: key parameters for producing realistic results. Despite of accounting for all type of particle interactions, the kinetic energy of secondary particles, different to fluorescence photons, were locally absorbed. This was demonstrated in Chapter 2, where it was observed that electrons do not travel long distances in soft tissue or detector's materials (see Figure 2.5), thus their energy is deposited locally in the MC simulations. This has enormously increased the efficiency of the simulations as no computational time is spent on calculating the probabilities for interactions and path lengths of these secondary particles.

The X-ray photon tracking along the simulation was also explained in this section for real systems, where only energy deposited within the image receptor due to incoherent scattering and photoelectric effect are considered. This, however, is different when simulating an ideal detector, where all X-ray photons that reach the image receptor deposit all their kinetic energy at the point of entry.

A procedure to discriminate between scattered and primary photons along the simulation was also described. In general, the total scatter observed in the system is calculated by tagging an X-ray photon as scatter when coherent or incoherent scattering occurs. However, the contribution of scatter from individual volumes within the system, such as compression paddle or breast support, can be calculated if necessary. This represents one of the most powerful features for scatter calculation in MC simulations, where the source of scatter can be traced.

Regarding the X-ray photon generation, it was described that the X-ray beams are collimated attending to the purpose of the experiment. This can be inserted in the system using photon shower, pencil beam or cone beam geometries. Being the latter the most frequently used in this work. In this case, the X-ray photons can emerge from an infinitesimal point or from a finite focal spot (sphere or square). However, in this work, only infinitesimal points sources have been used.

The statistical errors associated to MC simulations were described. Different simple techniques (increase number of particles, median filters,...) were proposed to reduce those uncertainties. Furthermore, in Section 4.4.2 the error reduction was quantified for a given MC experiment.

In order to provide credibility to the results obtained from MC simulations, it is extremely important to validate the simulations with results from different sources. In this case, the validation started from the basic level of the cross-sections. Despite this stage having already been already validated in the literature, it provided a useful exercise to investigate the cross sections of different elements found in mammography scenarios as well as their X-ray absorption edges.

In addition, results from the MC simulations were compared with those produced by Boone et al. [61]. This particular publication was chosen for two reasons: firstly, to validate the primary and scatter images recorded within the image receptor and secondly, to verify the design of a cellular anti-scatter grid employed in the MC simulations. The overall MC results agree with those found by Boone et al. [61]. However, small deviation in the results were found in some cases as discussed above. In addition, pencil beam geometry used in MC simulations was validated against Sechopoulos et al. [82] as will be described in Section 6.1.1.1.

Boone et al. [61] uses cellular grid parameters available from a Lorad M-III system. As will be explained in the next chapter, cellular anti-scatter grid from Hologic Selenia will be modelled. Although this model employs a cellular grid as well, the dimensions are different. As published data regarding this specific model of anti-scatter grid was not found, MC results were validated with experimental data from a Hologic Selenia system, where images of a Cu sheet were acquired with and without an anti-scatter grid.

From the validation section, it was observed that the GEANT4 toolkit was suitable to model X-ray mammography systems. In the following chapter, MC simulations are used to estimate the scatter in X-ray mammography geometries using CDMAM phantoms.

Chapter 5

Scatter calculations for CDMAM phantoms

The motive behind the work presented in this thesis is the accurate estimation of scatter fields in mammography and their use in image simulation frameworks. Image quality metrics, such as the SPR, noise or modulation transfer function (MTF) among others, must be known to realistically model X-ray mammography systems when imaging breast phantoms or test objects.

Therefore, this chapter presents an example of application where MC simulation-based scattered radiation is used to generate a synthetic image of a CDMAM phantom. It reports on a study of a CDMAM image simulation framework previously developed by Yip et al. [18], and in particular, the inclusion of contrast degradation across an image using SPR values calculated from MC simulation. The MC technique has been implemented to model the scatter conditions when imaging the CDMAM phantom with several digital X-ray mammography systems which are commercially available.

Contrast-detail (CD) curves from experimentally acquired CDMAM images at different doses have been compared with simulated CDMAM images using uniform and MC-based scatter. Furthermore, the simulation of X-ray mammography systems with linear and cellular anti-scatter grids has also provided useful information to understand grid performance as well as the effects of scattered radiation in conventional 2D planar imaging.

The chapter starts with a brief description of the CDMAM image simulation framework. Then, the experimental (and MC) geometry of each of the studied X-ray mammography systems is specified as well as the SPR maps generated from MC simulations. The procedure for calculation of the contrast of the discs in the simulated CDMAM images is explained before the CD curves are shown. Finally, SPR profiles are compared for both linear and cellular anti-scatter grids.

5.1 CDMAM phantom

The CDMAM (Contrast Detail MAMmography) phantom is a CD test object widely used throughout Europe to assess the small lesion detection performance of both film-screen and digital mammography systems [179]. Furthermore, it is also recommended for use in the European Protocol for quality assurance in digital mammography. The CDMAM phantom is comprised of a matrix of cells within an aluminium base attached to a PMMA cover (see Figure 5.1). Each cell contains two identical gold discs; one is placed in the middle of the cell and the other is randomly located in one of the four quadrants of the cell as shown in Figure 5.2. The gold thickness and diameter of the discs decrease logarithmically with the rows and columns of the matrix from 2 to $0.03\mu m$ and from 2 to $0.06mm$ respectively.

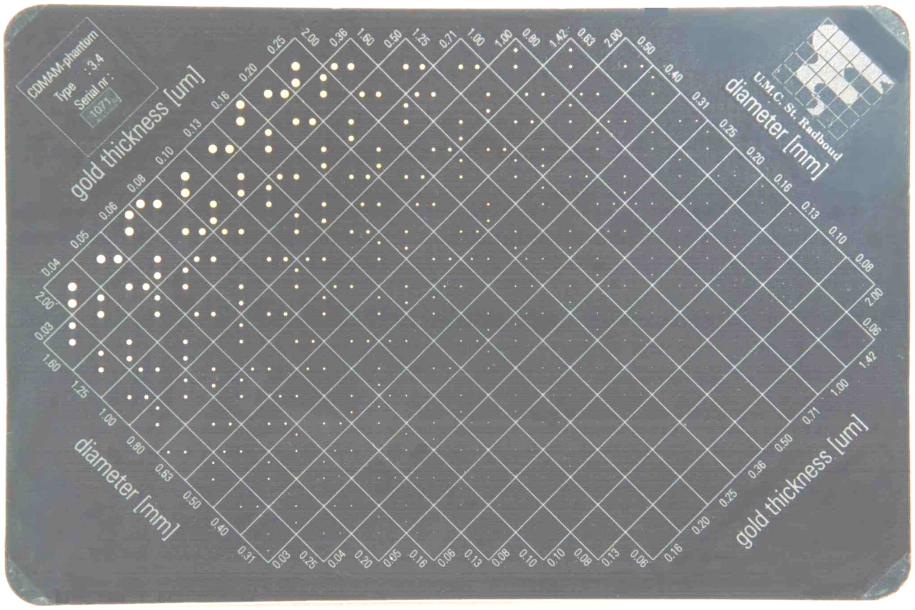

Figure 5.1: Photograph of a CDMAM phantom v3.4.

After imaging the CDMAM phantom for a given system and parameters, i.e. energy spectrum or dose, the evaluation task requires an observer to read the CDMAM image. The reader has to locate the disc placed in one of the four quadrants of each cell row by row, starting from the cell with thickest gold disc and moving along the row towards the thinner discs [180]. Then, a score is given based on the threshold where the discs are not visible, i.e. wrong decision quadrant, providing a quantitative measure of the observer performance in detecting small calcifications for the given imaging parameters.

As discussed below, results from human observers suffer inter-observer variability, which might hide differences in the image quality between different systems [181, 182]. For this reason, automatic scoring of CDMAM is recommended [182, 183] using the CDCOM framework [184].

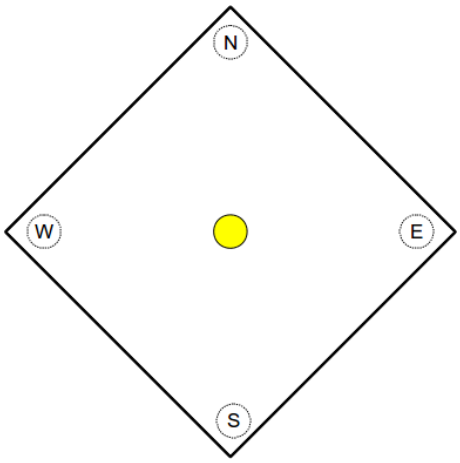

Figure 5.2: Diagram of a CDMAM phantom's cell. A disc is located in the middle of the cell (yellow disc), whereas an identical one is placed randomly in one of the four quadrants of the cell (N, S, E or W).

5.2 CDMAM image simulation framework

As mentioned above, the CDMAM phantom is used to assess the performance of a specific system and imaging conditions. However, undertaking CDMAM analysis in the wide variety of X-ray mammography systems available represents an expensive and very time-consuming task.

For this reason, realistic computer modelling of CDMAM images provides a substantial advantage. Yip et al. [18, 185] proposed an image simulation framework to calculate synthetic images as acquired under different imaging parameters. This is achieved by modelling the different image quality metrics (heel effect, noise, MTF, etc.). To validate their framework, they developed a CDMAM image simulation tool which produces synthetic CDMAM images.

In their previous work, Yip et al. [18] estimated the SPR using the contrast measured for the largest discs of each thickness disc (primary and scatter signal) and the contrast for the same discs calculated for only primary X-ray photons, using the Beer-Lambert's law. Then, the SPR was averaged and assumed to be uniform across the entire CDMAM phantom.

However, their work has been modified here to build a more robust image simulation tool. In this work, SPR maps generated from MC simulations have been introduced in order to determine the contrast of each gold disc based on its position in the CDMAM phantom. Figure 5.3 shows the different steps of the CDMAM image framework used in this work, where modification to the original image simulation framework proposed in [18] is highlighted in gray. This new approach should provide a more accurate representation of the scatter image degradation process compared to the simple uniform offset approach which was assumed previously.

As observed in Figure 5.3, the CDMAM image simulation chain contains two main arms. First, a noise free image is generated. Pixels values are assigned to a high

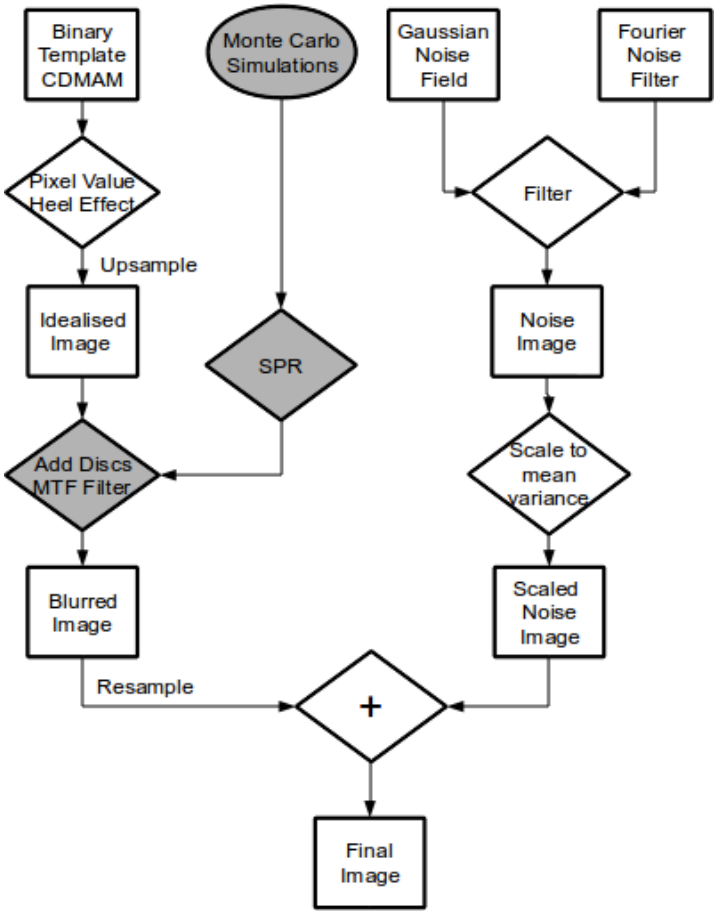

Figure 5.3: Flowchart of the CDMAM image simulation tool. Modifications with respect to previous work [18] are highlighted in gray.

resolution binary CDMAM template according to the exposure to be simulated and a heel effect mask is applied. Discs are added to the CDMAM template using the SPR calculated from MC simulation in order to calculate the contrast for each disc as will be explained below. The image is then blurred with an MTF filter and resampled to the original pixel size of the system studied [186].

In the second part, a noise image is simulated using a Gaussian noise field and a noise filter calculated from the relevant Normalised Noise Power Spectrum (NNPS). This image is scaled according to an a-priori mean variance relationship for the detector on a pixel-by-pixel basis to the blurred image. The final image is obtained after adding the blurred image and the scaled noise image. Further information regarding this process can be found in [18, 185].

5.3 Geometries of the experiment

In this section, the geometries used to generate both the simulated and clinically acquired CDMAM images are described. The same setup has been used in both cases,

thus results from the simulated CDMAM images were compared with the experimentally acquired CDMAM images for different doses as explained below.

5.3.1 Monte Carlo simulations

For the MC calculations, the typical experimental setup used for CDMAM imaging has been simulated, where three different commercial mammography systems have been modeled: Hologic Selenia Dimensions, GE Essential and a Siemens Mammomat 3000. For the Siemens system, the detector has been replaced with an Agfa computerised radiography (CR) plate.

The following components, from top to bottom, have been included in the MC setup according to the dimensions and materials provided from the manufacturer's specifications: (i) compression paddle, (ii) CDMAM phantom with blocks of PMMA on top and bottom, (iii) breast support, (iv) anti-scatter grid with its cover on top and bottom and (v) image receptor with its top cover as well. The image receptor materials used in the simulations were selenium (Se), cesium iodine (CsI) and cesium bromide (CsBr) when simulating the Hologic, GE and Agfa image receptors respectively.

The CDMAM test object has been simulated using a $3mm$ thick PMMA layer and $0.5mm$ thick aluminium layer according to the manufacturer's specifications. However, the gold discs have not been explicitly included in the scatter simulations as their contribution to total scattered radiation is considered negligible. As in the physical clinical setup, two PMMA blocks of thickness $20mm$ each ($40mm$ in total) were placed above and below of CDMAM, representing a total equivalent breast thickness of $45mm$ and 40% glandularity [44]. The X-ray tube was considered as an infinitesimal point source located $650mm$ above the centre of the chest wall edge of the detector.

A sagittal view of the GE Essential geometry is illustrated in Figure 5.4. The other systems have similar geometry but different dimensions as discussed below.

Plan view diagrams of the setups used for the three mammographic systems modelled are shown in Figure 5.5(a). The chest wall (CW) is located at position O and the outer area (1) represents the external dimensions of the system (detector, grid, breast support and compression paddle). (2) illustrates the position of the PMMA blocks placed above and below of CDMAM, whereas (3) and (4) shows the location of the PMMA and aluminium layers respectively used to simulate CDMAM phantom.

Note that GE Essential incorporates the largest detector (24x31cm^2). For the Siemens Mammomat 3000, the detector dimensions are 18x24cm^2, matching the dimensions of the PMMA blocks placed above and below the CDMAM phantom. Finally, the Hologic Selenia Dimensions has a detector size of 24x29cm^2.

The energy spectra used for each of the X-ray mammography systems simulated are shown in Table 5.1. These have been simulated in MC using data calculated from Boone et al. [40] and adjusted mathematically with a specific aluminium filter thickness to match the HVL, which has been previously measured for each of the manufacturers. 3×10^{10} X-ray photons have been used for each of the simulated systems.

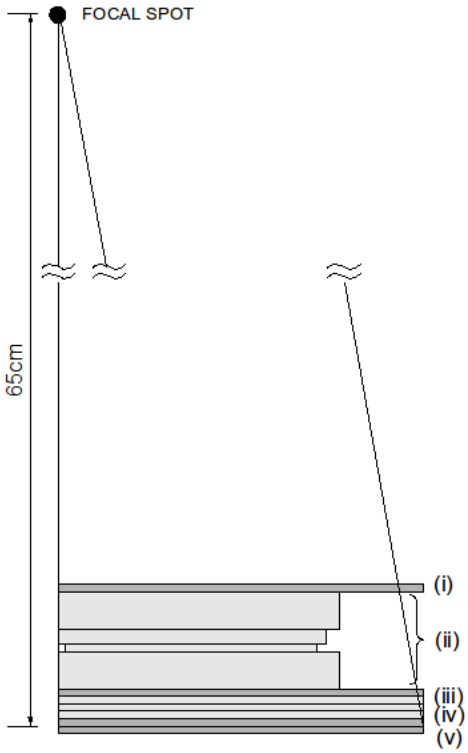

Figure 5.4: Cross-section of the set-up used in MC simulations for the GE Essential X-ray system with a compression paddle (i), CDMAM phantom (PMMA and aluminium layer) with two slabs of PMMA (ii), breast support (iii), anti-scatter grid (iv) and detector (v).

Table 5.1: Imaging setting used in the CDMAM experiments.

System	Spectrum (Target/Filter)	HVL (mm) Al	Tube current (mAs)	MGD [44] (mGy)
GE Essential	Rh/Rh @ 29kVp	0.42	14	0.26
			28	0.52
			57	1.06
Hologic Selenia Dimensions	W/Rh @ 30kVp	0.45	61	0.84
			122	1.68
			245	3.37
Siemens Mammomat 3000/Agfa	Mo/Rh @ 28kVp	0.41	40	0.84
			80	1.68
			160	3.35

5.3.2 Clinical setup

Images acquired experimentally have been used as a ground truth to compare the synthetic CDMAM images from the aforementioned framework. The setup used in the clinical systems corresponds with the geometry described in the previous section for MC simulation. For each of the combinations studied, sixteen CDMAM images have been taken as suggested by Young et al. [182].

In addition, for each of the mammographic systems, CDMAM images have been ac-

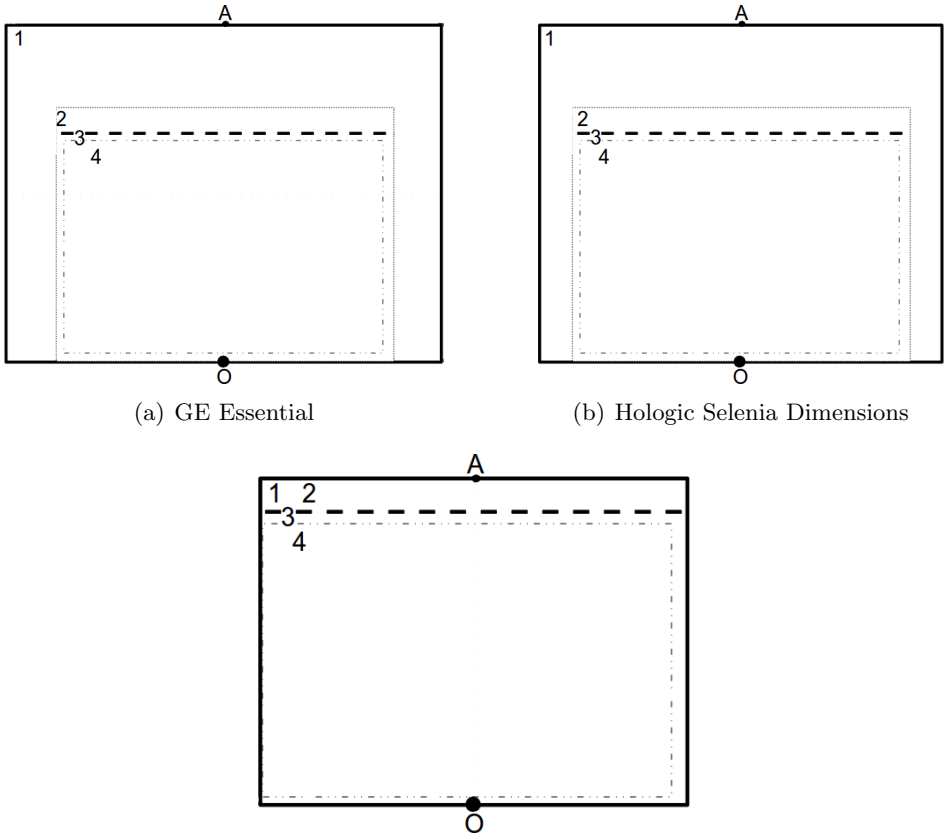

(a) GE Essential

(b) Hologic Selenia Dimensions

(c) Siemens Mammomat 3000

Figure 5.5: Top diagram of the (a) GE, (b) Hologic and (c) Siemens system showing the dimension of each system (1), slab of PMMA above and below of CDMAM (2) and, (3) and (4) represents the PMMA and Aluminium layers that contains the CDMAM itself. The chest wall edge is located at position O. OA represents the profile perpendicular to the chest wall edge.

quired using three values of the mean glandular dose (MGD)[1] [44] as listed in Table 5.1. The different doses have been acquired/simulated because the original aim of the CDMAM image simulation framework was to create a reliable tool to study the effects of dose reduction on the system performance. However, in this work, this effects will not be discussed as the main purpose was to validate the use of MC scatter in the CDMAM framework.

5.4 SPR map calculation

The SPR image was generated using an image receptor comprising $1mm^2$ pixels under the assumption that the scatter distribution does not contain fine structures. Then, using this assumption that the scatter distribution is a slowly varying function, the

[1]The MGD was calculated for a breast thickness of $6cm$ with 50:50 adipose/glandular tissue.

SPR image was median-filtered by an 11x11 pixel kernel, providing a smoother, less statistically noisy representation of the SPR distribution. The average MC statistical error associated to the SPR values was 0.5%.

After each simulation, scatter and primary photons have been recorded independently to estimate the SPR. Exemplar primary and scatter images recorded for the GE Essential geometry are shown in Figure 5.6. For better understanding of the results, the outlines of the components of the CDMAM phantom, observed in Figure 5.5(a), have also been included within the images.

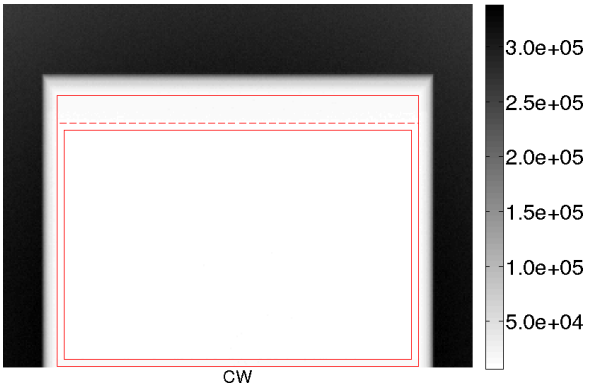

(a) Primary image

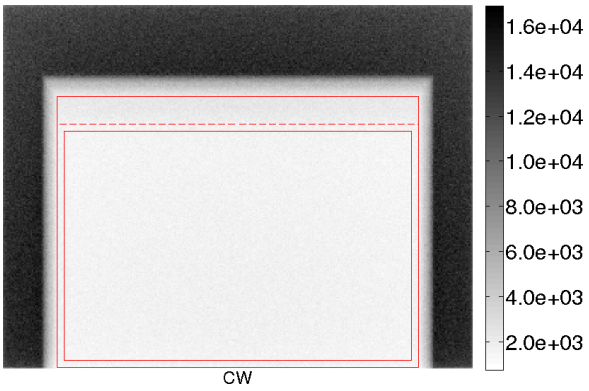

(b) Scatter image

Figure 5.6: Exemplar images of the energy deposited by (a) primary and (b) scattered photons. Note that boundaries of the layers described in Figure 5.5(a) are outlined in red in all the images. CW corresponds to the chest wall. In both images, the energy deposited corresponds to keV.

The SPR map corresponding to the primary and scatter images using the GE geometry shown in Figure 5.6, is plotted in Figure 5.7 using a 2D and 3D surface plot. The latter view provides a clearer spatial distribution view of the SPR values across the entire detector's area. Note that for this case, the SPR remains constant across most of the CDMAM area. However, an increase in SPR value is observed at the edges of the phantom. This phenomenon is discussed in more detail in Section 5.7.

Following similar procedures as explained for the GE Essential above, SPR maps for

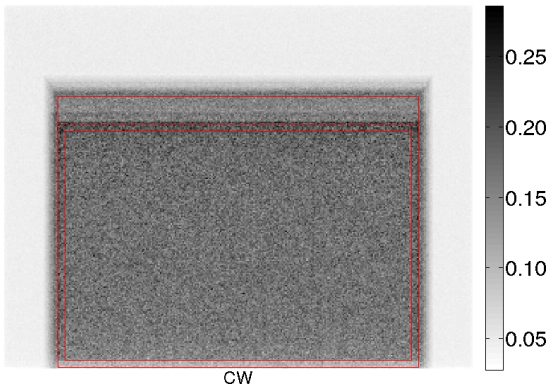

(a) 2D SPR

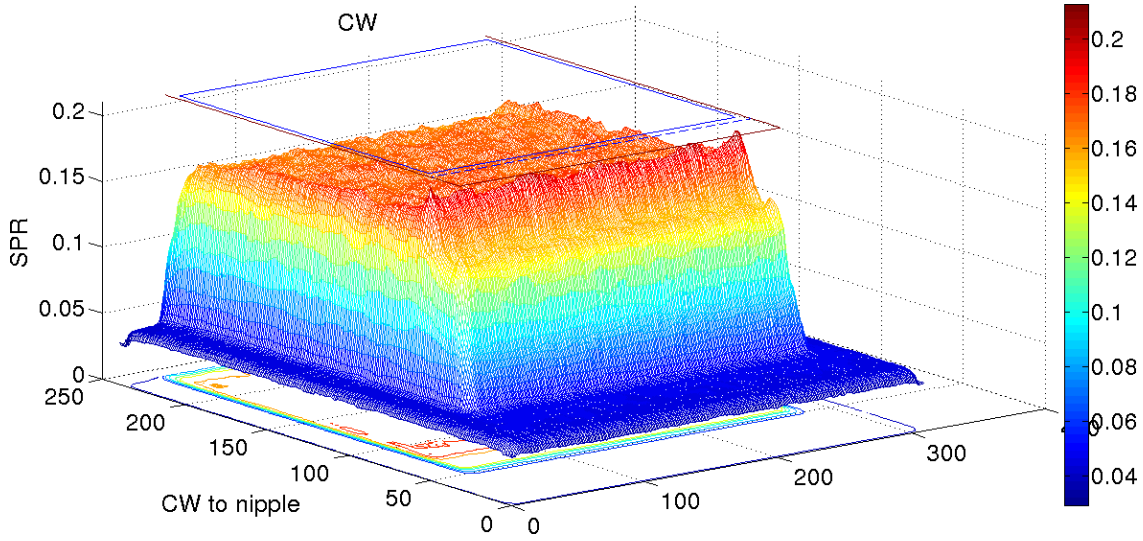

(b) 3D SPR

Figure 5.7: SPR map for the GE Essential system is shown for a 2D image (a) and a 3D surface plot (b), where the outline of the CDMAM phantom has been superimposed.

the Hologic Selenia Dimensions and Siemens Mammomat 3000 systems have been generated. For these systems, only the 3D surface plots of the SPR maps have been illustrated as shown in Figure 5.8(a) and Figure 5.8(b) for Hologic and Siemens systems respectively. In Section 5.7, where the performance of anti-scatter grids is studied, profiles of the SPR parallel to the CW edge to nipple axis (0A profile in Figure 5.5) for the GE and Hologic systems are shown (Figure 5.16).

The average SPR values from MC calculated for each of the X-ray mammography systems simulated in this work are shown in Table 5.2. A region of interest (ROI) of 100x100 pixels in the centre of the CDMAM phantom has been used for this purpose. The SPR values assumed in the previous CDMAM image simulation tool [185] are also given.

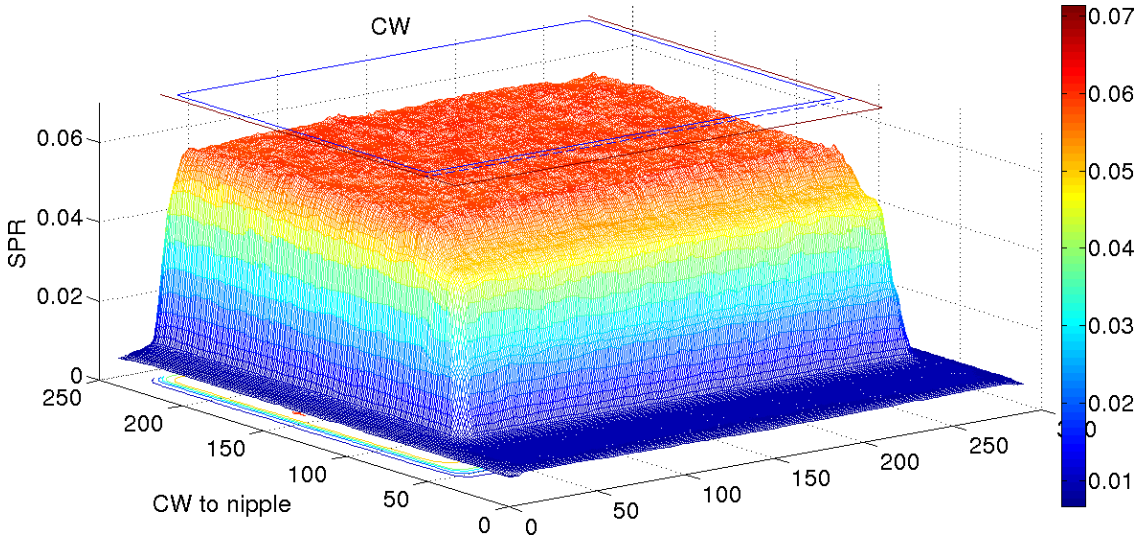

(a) Hologic

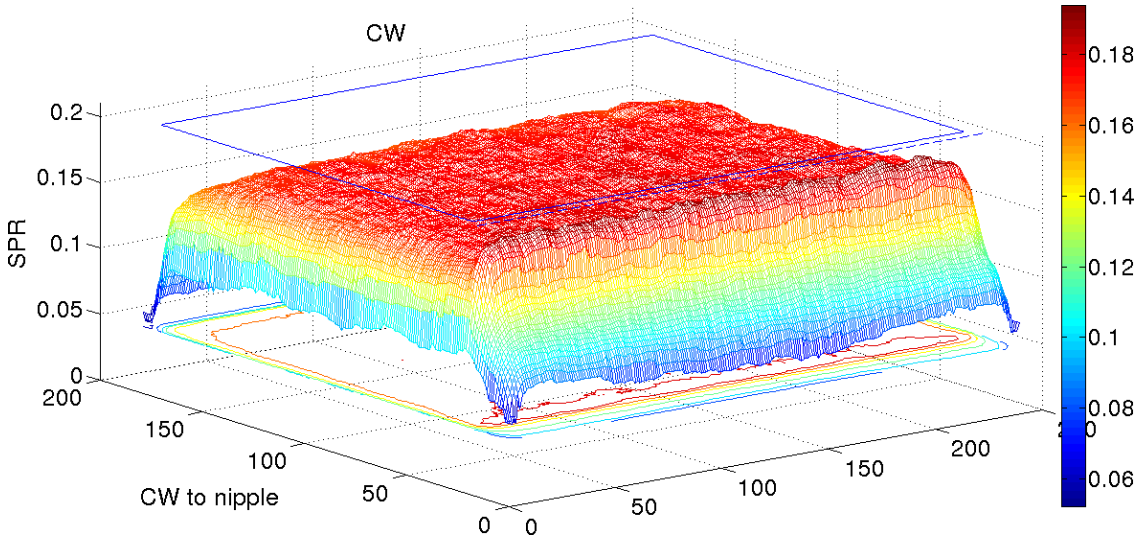

(b) Siemens/Agfa

Figure 5.8: SPR maps for the Hologic Selenia Dimensions and Siemens Mammomat 3000 with a CR Afga plate are illustrated in (a) and (b) respectively. The outline of the CDMAM phantom has been superimposed in the images.

Table 5.2: Average and standard deviation of SPR from MC simulation and empirical measurements from previous work [185] .

System	SPR from MC (average±standard deviation)	SPR used by Yip et al. [185] (average±standard deviation)
GE Essential	0.17±0.01	0.11±0.01
Hologic Selenia Dimensions	0.06±0.01	0.05±0.01
Siemens Mammomat 3000/Agfa	0.18±0.01	0.22±0.03

5.5 Contrast disc calculation

Once the SPR maps were generated for each of the mammographic systems studied here, they were inserted in the CDMAM image simulation framework (see Figure 5.3) to calculate the contrast of the gold discs within the synthetic CDMAM image as described in Section 5.2.

In the methodology used in this work, the contrast of each disc within the synthetic CDMAM image was calculated using Equation 5.1, where $C_{obs}(x, y)$ represents the contrast of a given disc observed at some particular location. $C_p(x, y)$ is the relative contrast of this disc considering only primary X-ray photons passing through the CDMAM phantom and PMMA blocks. This is calculated with and without the gold disc of specific thickness using the well know Beer-Lambert's law. The $\frac{S}{P}(x, y)$ represents the SPR value from MC simulations observed for the specific spatial coordinates where the disc is located within the CDMAM image.

$$C_{obs}(x, y) = \frac{C_p(x, y)}{1 + \frac{S}{P}(x, y)} \tag{5.1}$$

5.6 Contrast-detail analysis

Once the experimental CDMAM images had been acquired and the synthetic CDMAM images modelled, a CD analysis was undertaken.

The CD curves represent a common technique to evaluate the spatial and contrast resolution of an imaging system after irradiating a CD phantom [187]. Figure 5.9 illustrates a schematic example of a CD curve, where different sizes of an object (x-axis) are plotted against the contrast of the object (y-axis). The black line represents the minimum contrast, i.e. threshold, where the objects are visible for each of the sizes studied.

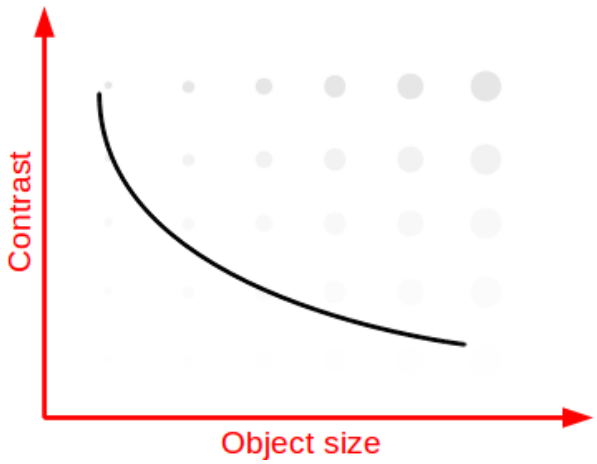

Figure 5.9: Example of a contrast-detail curve.

In the case of the CD curves created for the CDMAM phantom, the minimum visible contrast of the gold discs was evaluated for the range of disc diameters contained within the phantom. Results have been evaluated for a series of MGD values as previously explained in Table 5.1. The average standard MGD value measured for every single clinical oblique views of 50-60mm thick breast is approximately 1.5 and 2.1mGy within the UK for direct digital radiography (DR) and CR systems respectively[2] [188]. Thus combinations of similar, half, quarter or double standard doses have been studied for each of the mammography systems used here.

CDMAM images were originally scored by human observers. However, this task is very time consuming as several images have to be read and also, the results can vary from one reader to another. For this reason, automated scoring can reduce the subjectivity of the reader and it has been object of study in the last two decades [181, 189, 183, 190].

In this work, automated scoring software for CDMAM images using the CDCOM framework [184] has been used in both the simulated and experimentally acquired CDMAM images.

CDCOM (Department of Radiology, University Medical Center Nijmegen,The Netherlands) is a piece of software which reads CDMAM images and, based on a model of a synthetic observer, uses maximum contrast and minimum signal for detecting each disc position, and then estimates the sensitivity for disc detection (observation) within the CDMAM image over a range of disc diameters and thicknesses. The results from CDCOM are adapted to simulate the performance of a human observer as described by Young et al. [189]. For each of the configurations described here, sixteen real/simulated CDMAM images have been recorded/simulated for analysis using the CDCOM software [182].

Automated scoring of sets of simulated images of the CDMAM phantom were compared to the scoring of real CDMAM images to validate the image simulation tool including scattered radiation derived from MC simulations.

A comparison of the CD curves from the experimentally acquired data, previous simulation data using globally uniform SPR and results from this work are shown in Figure 5.10 using the GE Essential system for 0.26, 0.52 and 1.06 mGy MGD, representing a standard dose, half and a quarter of the standard dose.

Due to the difficulty to visualise the difference between the different curves in a logarithmic scale, the ratios of the values for each disc diameter are illustrated in Figure 5.11.

The CD curves corresponding to the Hologic Selenia system are illustrated in Figure 5.12 for three different doses. In this case, 0.84, 1.68 and 3.37 mGy MGD corresponds to half dose, standard dose and twice the standard dose.

As shown for the GE system, ratios of the CD values have also been calculated for the Hologic system (Figure 5.13).

Finally, the resultant CD curves observed when simulating the Siemens Mammomat 3000 using a CR Agfa plate for 0.84, 1.68 and 3.35 mGy MGD are presented in Figure 5.14.

[2]Note that the MGD values varies with imaging systems. These represent the average MGD values for a range of X-ray mammography systems.

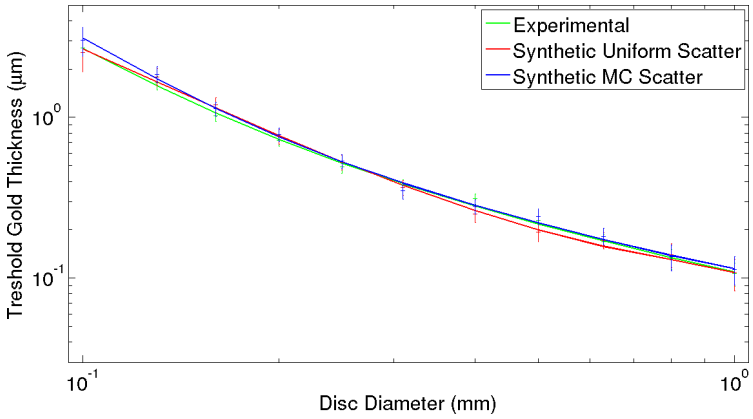

(a) 0.26 mGy MGD

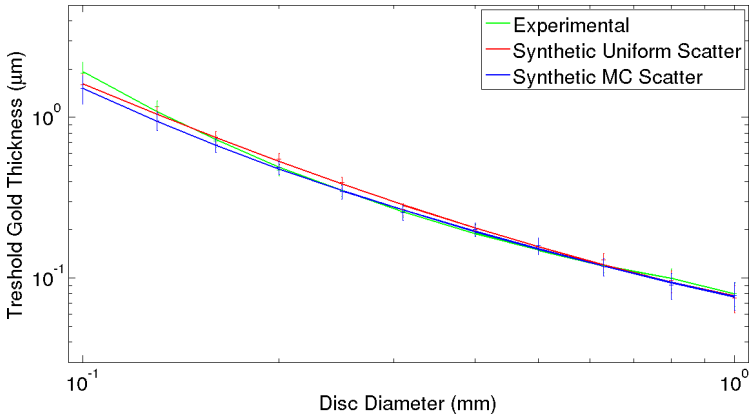

(b) 0.52 mGy MGD

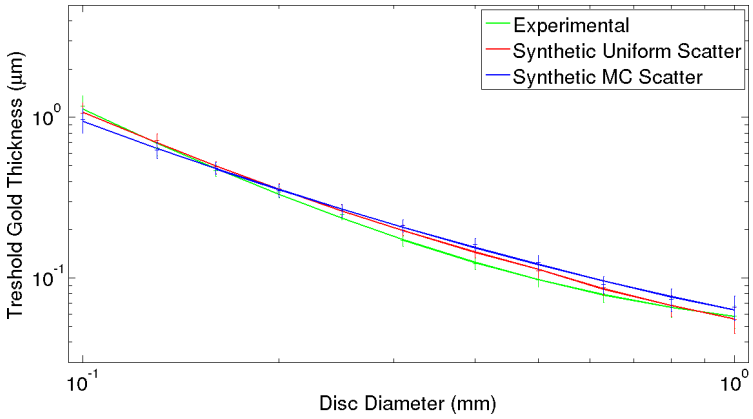

(c) 1.06 mGy MGD

Figure 5.10: Contrast detail curves for the GE system for (a) 0.26, (b) 0.52 and (c) 1.06 mGy MGD. Green solid lines illustrate contrast detail measured from experimental data. Red and blue lines represent contrast detail curves considering uniform scatter [18] and calculating SPR from MC simulations respectively. Error bars indicate 2 standard errors of the mean.

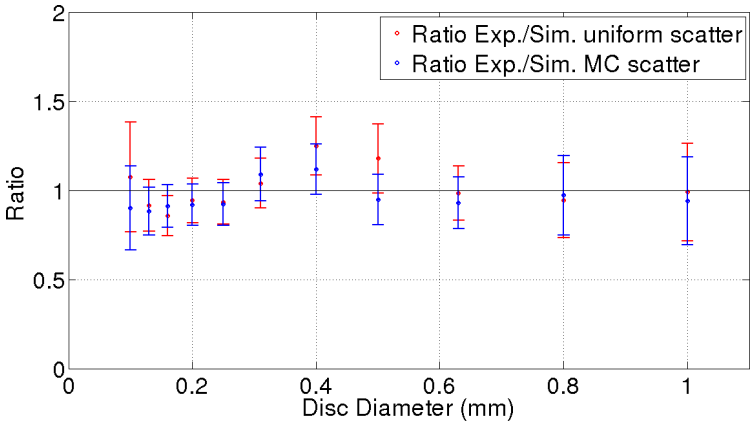

(a) 0.26 mGy MGD

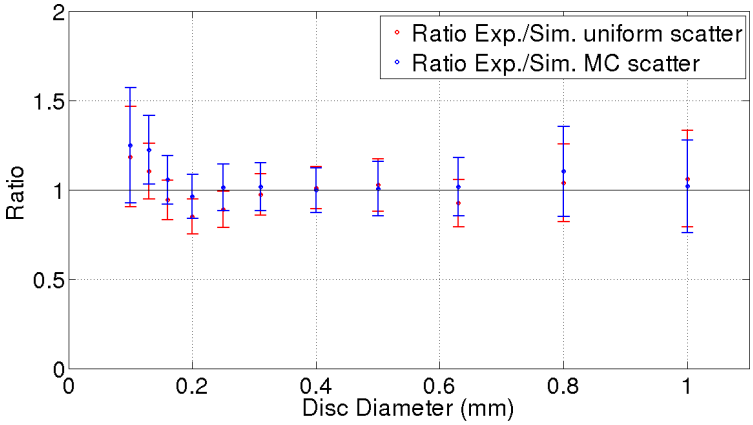

(b) 0.52 mGy MGD

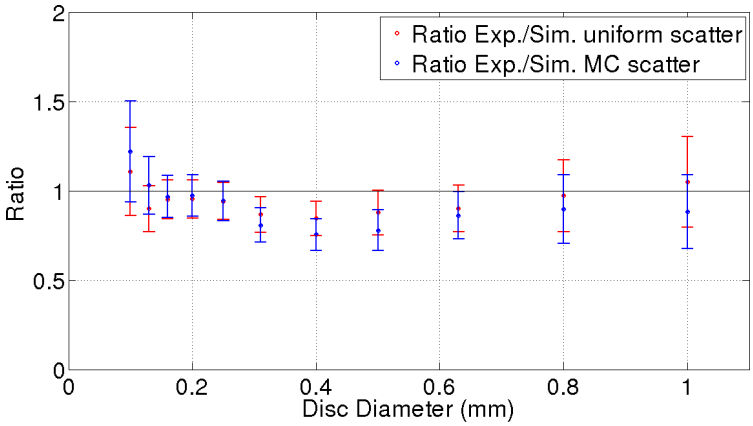

(c) 1.06 mGy MGD

Figure 5.11: Ratios of CD curves for the GE system shown in Figure 5.10. For each dose, the ratio between experimental and simulated using uniform scatter and experimental and simulated using MC scatter is illustrated. Error bars indicate 2 standard errors of the mean.

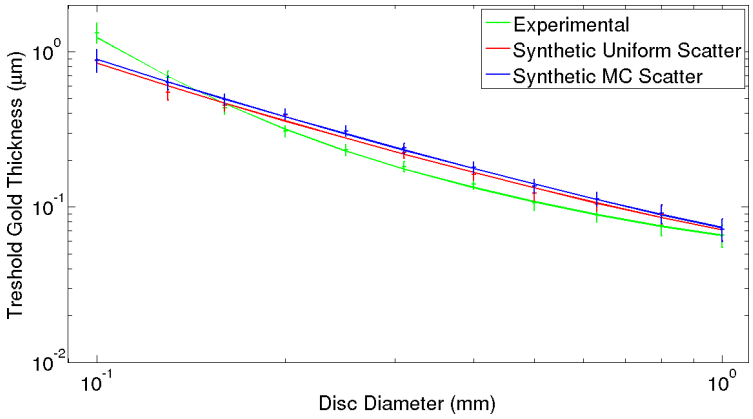

(a) 0.84 mGy MGD

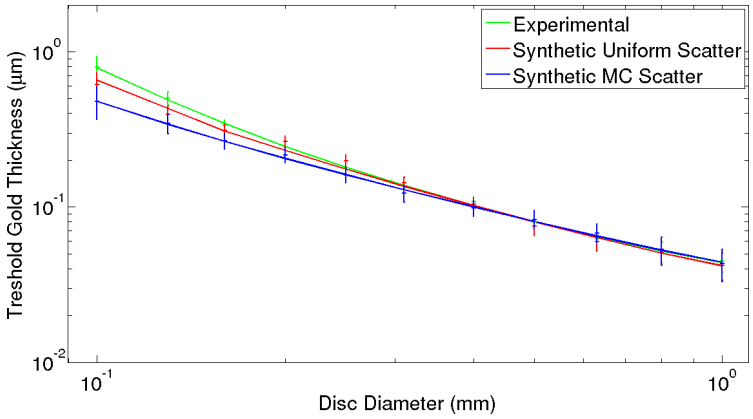

(b) 1.68 mGy MGD

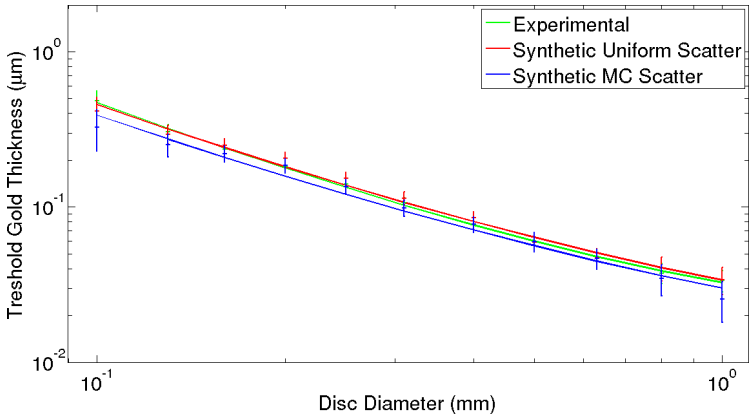

(c) 3.37 mGy MGD

Figure 5.12: Contrast detail curves for the Hologic system for (a) 0.84, (b) 1.68 and (c) 3.37 mGy MGD. Green solid lines illustrate contrast detail measured from experimental data. Red and blue lines represent contrast detail curves considering uniform scatter [18] and calculating SPR from MC simulations respectively. Error bars indicate 2 standard errors of the mean.

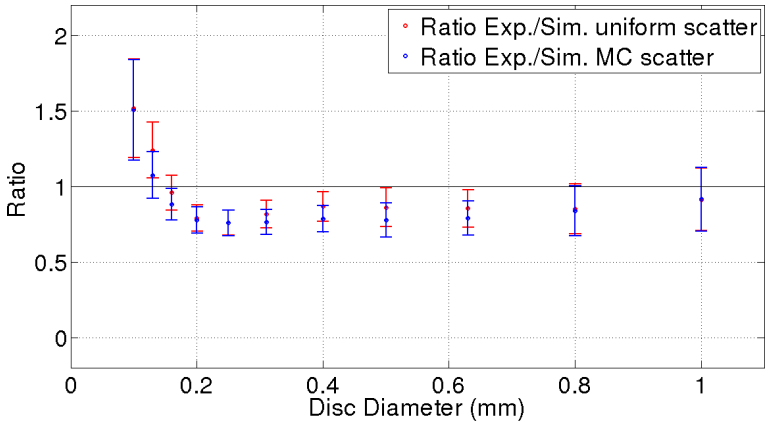

(a) 0.84 mGy MGD

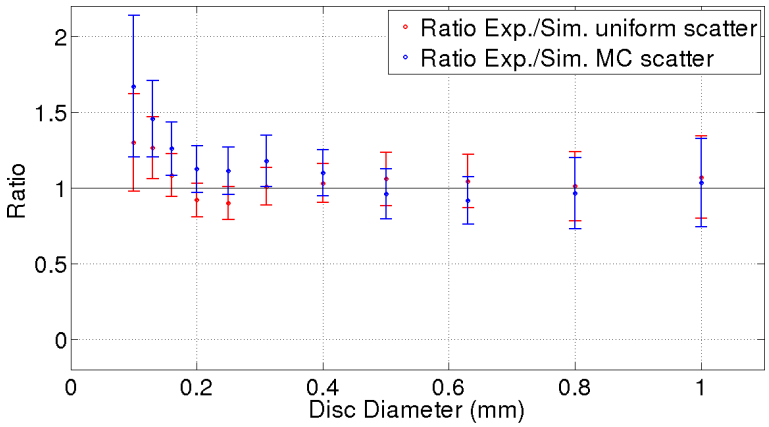

(b) 1.68 mGy MGD

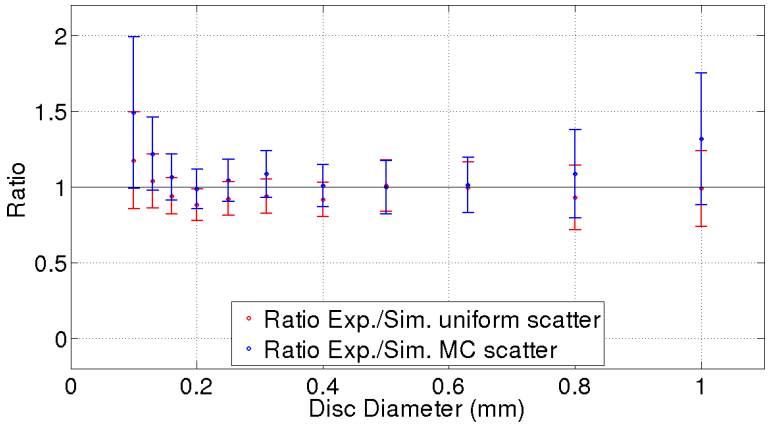

(c) 3.37 mGy MGD

Figure 5.13: Ratios of CD curves for the Hologic system shown in Figure 5.12. For each dose, the ratio between experimental and simulated using uniform scatter and experimental and simulated using MC scatter is illustrated. Error bars indicate 2 standard errors of the mean.

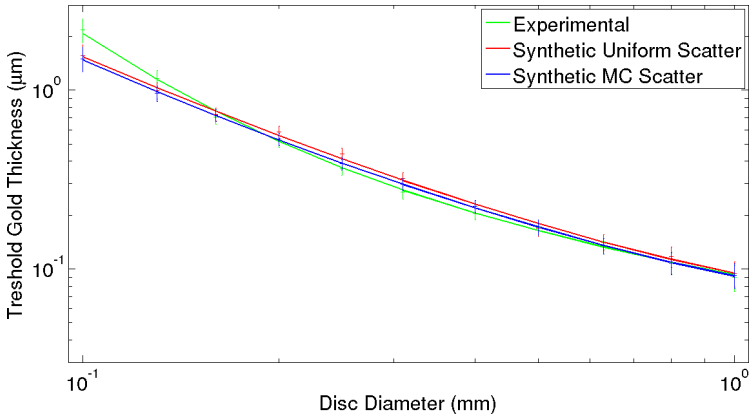

(a) 0.84 mGy MGD

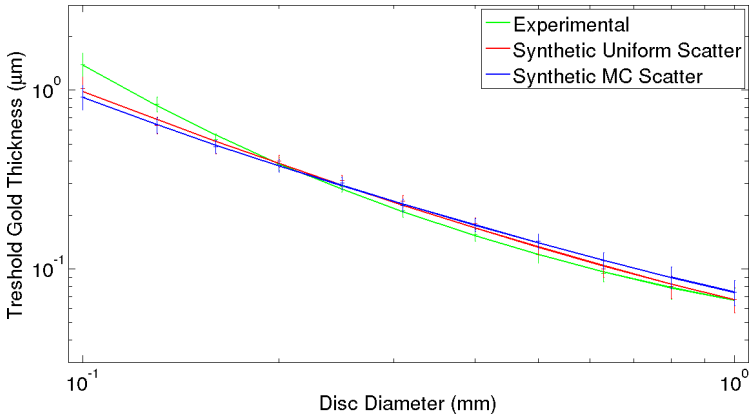

(b) 1.68 mGy MGD

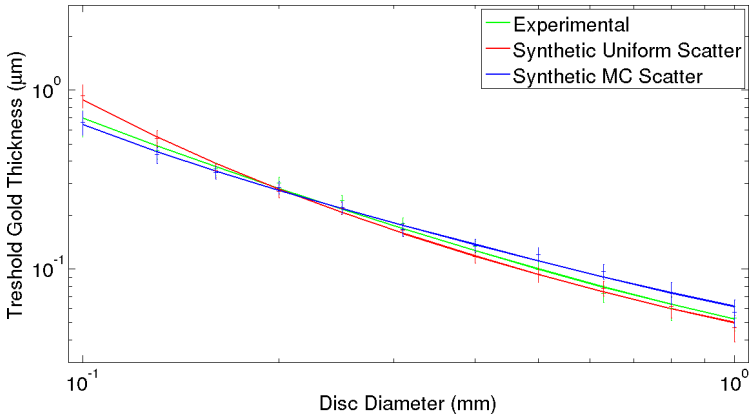

(c) 3.35 mGy MGD

Figure 5.14: Contrast detail curves for the Siemens system for (a) 0.84, (b) 1.68 and (c) 3.35 mGy MGD. Green solid lines illustrate contrast detail measured from experimental data. Red and blue lines represent contrast detail curves considering uniform scatter [18] and calculating SPR from MC simulations respectively. Error bars indicate 2 standard errors of the mean.

Figure 5.15 shows the ratios calculated for the Siemens results.

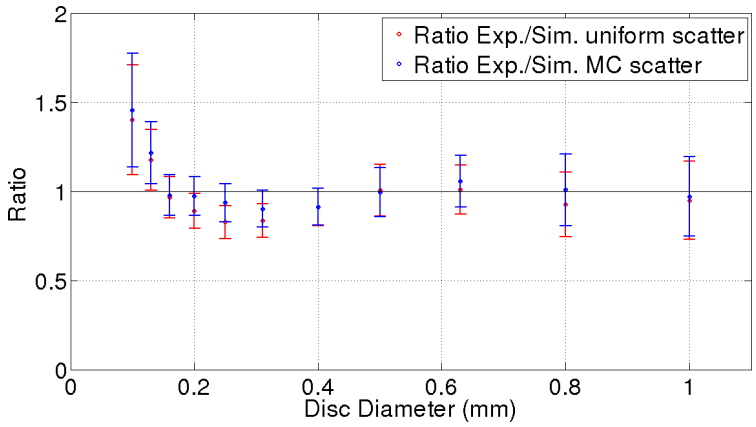

(a) 0.84 mGy MGD

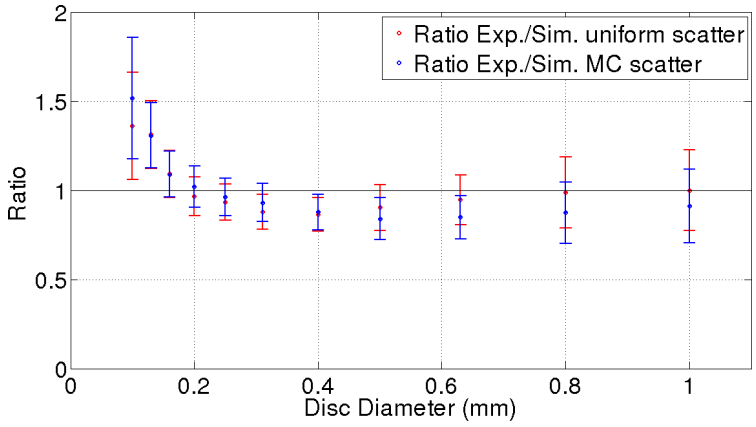

(b) 1.68 mGy MGD

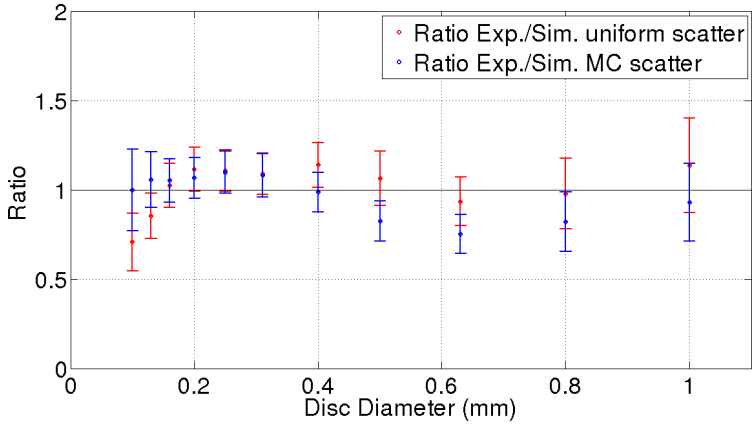

(c) 3.35 mGy MGD

Figure 5.15: Ratios of CD curves for the Siemens system shown in Figure 5.14. For each dose, the ratio between experimental and simulated using uniform scatter and experimental and simulated using MC scatter is illustrated. Error bars indicate 2 standard errors of the mean.

For each of the combinations of system and dose explored in this work, the average ratio has been calculated for all the disc diameters and it is illustrated in Table 5.15.

Table 5.3: Average and standard deviation values of the ratios for each of the system and dose combination shown in Figure 5.11, 5.13 and 5.15.

System	MGD (mGy)	MC scatter (aver.±st.dev.)	Uniform scatter [18] (aver.±st.dev.)
GE Essential	0.26	0.96±0.08	1.00±0.12
	0.52	1.06±0.09	1.00±0.10
	1.06	0.92±0.13	0.94±0.08
Hologic Selenia Dimensions	0.84	0.90±0.22	0.94±0.23
	1.68	1.16±0.23	1.06±0.12
	3.37	1.12±0.15	0.97±0.08
Siemens Mammomat 3000/Agfa	0.84	1.04±0.16	0.99±0.17
	1.68	1.02±0.21	1.02±0.17
	3.35	0.97±0.12	1.01±0.14

Results from previous work [18] which assumes uniform SPR value and from this work [128], where the SPR is calculated from direct MC simulations, show an overall similar performance, where both of them are within the error bars of experimental data in most of the cases studied. Nevertheless, in some cases, large discrepancies are observed for the smallest disc diameters where the CDMAM image simulation framework fails to accurately calculate the contrast. This experiments have illustrated two things: (1) SPR calculations from MC simulations can be used to model scattered distribution realistically in synthetic images and, (2) a constant value of SPR can be assumed in geometries similar to the ones studied here where anti-scatter grids are employed.

5.7 Anti-scatter grids performance

While analysing the CDMAM experiment, special attention has been paid to implementing the design of the moving focused anti-scatter grids to match the specifications of particular manufacturer's systems.

In order to model a moving anti-scatter grid during the MC simulations, this has been shifted several times along one axis for the case of linear grids or two axes in the case of the cellular grid, to cover a complete anti-scatter grid unit cell (septa width + interspace width). Moreover, the simulated anti-scatter grid was sufficiently large to cover the entire detector area after every shift.

The septa were positioned and perfectly angled so as to simulate a focused grid with the focal spot at a distance of $65cm$ from the edge of the detector. The cover layers situated above and below the anti-scatter grid have also been included in the MC geometry, simulating the scenario found in real systems. Note that when modelling the anti-scatter grid, this is perfectly aligned with the X-ray tube exit. However, this is not the case in real systems, as misalignment associated with the manufacturing process could be found, increasing the number of X-ray primary photons absorbed by the septa material within the anti-scatter grid.

For the commercial manufacturers chosen for this work, both GE and Siemens use a linear anti-scatter grid with lead septa. Thus only GE has been analysed to study the behaviour of a typical linear anti-scatter grid. On the other hand, a High Transmission Cellular (HTC) grid is implemented within the Hologic system.

The main characteristics of the anti-scatter grids implemented for the GE, Siemens and Hologic systems are shown in Table 5.4.

Table 5.4: Anti-scatter grid configuration for Hologic Selenia Dimensions [59], GE Essential and Siemens Mammomat 3000.

System	Grid type	Grid ratio (r)	Septa material
Hologic Selenia	Cellular	4:1	Copper
GE Essential	Linear	5:1	Lead
Siemens Mammomat 3000	Linear	4:1	Lead

As described in Section 2.4.5, the grid ratio r provides an idea of the reduction of scattered radiation from the anti-scatter grid. A large ratio implies greater scatter reduction, however, in screen-film, the dose applied to the patient increases in order to maintain blackening in the film.

This effect of scatter reduction can be observed when comparing the previously calculated SPR between the GE and Siemens system. GE's (linear) anti-scatter grid has a larger grid ratio, so the resultant SPR average value (0.17) was lower than the average SPR value observed for Siemens (0.18), which has also a linear grid. However, it is difficult to define the performance of a given anti-scatter grid based on the results shown here, as they have been calculated using different energy spectra. On the other hand, it is not possible to directly compare the linear and cellular anti-scatter grids based on the grid ratio as they have different designs.

As mentioned in Section 3.5, cellular anti-scatter grids provide better scatter reduction compared to linear designs. To investigate and quantify this notion, SPR profiles, CIF and BF values have been compared for the linear (GE) and HTC (Hologic) anti-scatter grid designs studied in the CDMAM geometry described in this chapter. As a reminder, the CDMAM phantom has been imaged using a $40mm$ thick PMMA block and the energy spectrum used for each system was described previously in Table 5.1.

Figure 5.16(a) shows the central profiles, parallel to the chest wall (CW) to nipple axis, of the SPR images corresponding to GE Essential and Hologic Selenia X-ray mammography systems when the anti-scatter grid has been removed from the geometry. Note that in both cases, the values of SPR are very similar. However, when the corresponding anti-scatter grid is used, the SPR plot (see Figure 5.16(b)) shows smoother and reduced values when the HTC grid design is employed as expected.

CIF and BF, which have been previously described in Section 2.4.5, are two common metrics used to evaluate the performance of anti-scatter grids. They have been calculated in this section, as previously mentioned, to quantify the benefit (CIF) and penalty (BF) of each of the anti-scatter grid designs described here.

Results illustrated in Table 5.5 shows that the HTC anti-scatter grid (Hologic Selenia) has higher CIF than the linear grid (GE Essential). In other words, an improvement

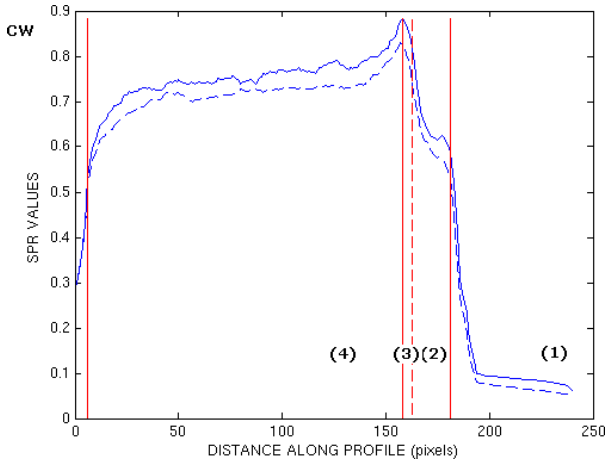

(a) No anti-scatter grid

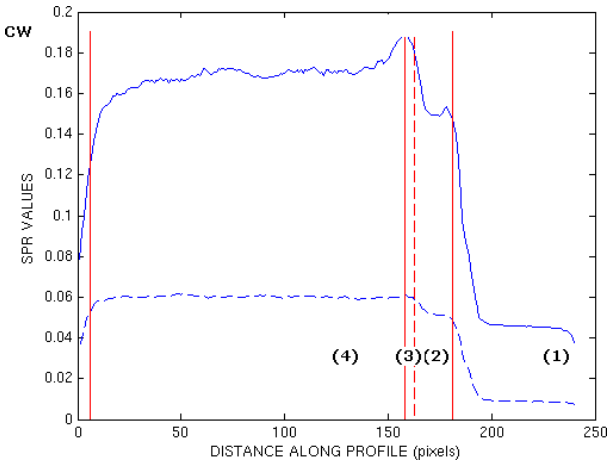

(b) Anti-scatter grid

Figure 5.16: In both figures, solid lines represent the SPR from the GE system (linear grid) and dashed lines from the Hologic system (HTC grid). (a) and (b) show the central SPR profiles along the CW to nipple axis with and without anti-scatter grid. Vertical lines represents changes in dimension along the vertical OA profiles shown in Figure 5.5. Numerical labels corresponds to the detector area (1), slabs of PMMA on top and bottom of CDMAM (2), PMMA of CDMAM (3) and Aluminium layer of CDMAM (4) as shown in Figure 5.5.

in contrast is achieved, as expected, as the scattered radiation is reduced more in comparison with the linear anti-scatter grid. The higher BF value observed in the HTC grid would indicate an increase in the dose required to blackening in screen-film. However, as described in Section 2.4.5, the digital detectors found in FFDM can modify their gains to account for the reduction of radiation when employing an anti-scatter grid.

Analysing the SPR profiles of above systems (Figure 5.16), an increase of scatter is

Table 5.5: CIF and BF calculated for GE Essential (linear grid) and Hologic Selenia Dimension (HTC grid).

System	*CIF*	*BF*
GE Essential	1.50	1.85
Hologic Selenia Dimensions	1.60	1.94

observed at the edge of the phantom (vertical dashed line). This increment, which is more obvious when using a linear anti-scatter grid, is mainly due to the scattered X-ray photons mainly introduced from the compression paddle and breast support plate as described by other authors in the literature [82, 107]. Thus, components of the system such as the compression paddle or breast support may increase somewhat the scattering on the edge of phantoms and will be taken into account for a more accurate scatter field estimation in future experiments.

5.8 Summary and discussion

Image simulation frameworks represent an important tool to model realistically clinical images without ionising radiation. In particular, the work developed in this thesis has been used to support the OPTIMAM project in the generation of several types of synthetic images (CDMAM, breast phantom, microcalcifications and masses' insertion) in different conditions.

In a first attempt to use MC-based results in the project and illustrate one of the many possibilities of their applications, scattered radiation has been estimated and inserted in a previously developed CDMAM image simulation framework [18], where detection performance for different mammography systems and several doses have been investigated.

SPR maps have been generated using the typical CDMAM geometry for each of the three systems studied (GE Essential, Hologic Selenia Dimension and Siemens Mammomat 3000 with a CR Afga plate) across the entire image receptor. These have shown a relatively constant SPR values within the CDMAM area, which varies from one system to other based on the anti-scatter grid geometry used. However, as discussed along the chapter, an increment in SPR values was observed near the edges of the phantom. This increase has been found to be more obvious for linear anti-scatter grids designs, where SPR values have risen up to 10% in some cases.

In the initial work published regarding the CDMAM framework [18], it was described that scatter was empirically measured on the edge of the CDMAM phantom, where the gold discs with largest diameters are located. Then the calculated SPR was assumed to be constant across the image. However, as explained in the previous paragraph, the SPR values near the edge of the CDMAM show large variation on SPR and therefore, discrepancies have been found between the previously calculated and the SPR values estimated in this work.

The comparison of the CD-curves between the two scatter approaches, i.e. uniform and MC-based scatter, proposed for simulating CDMAM images, show a very similar

performance when simulating the contrast of the gold discs. Both approaches are found within the the error bars. However, the great advantage of the new approach proposed here is that the clinical measurements needed in the previous work to calculate the contrast of the discs within the CDMAM, are not necessary because this could be calculated from MC simulations. This reduces the dependence on clinical measurements.

In general, the CDMAM image simulation framework modeled the experimentally acquired CDMAM images well as illustrated in Table 5.3, where average ratios close to one were found. However, when analysing the performance for each disc diameter individually, it is observed that the largest discrepancies occur for very low doses and small disc diameters. For this reason, a refinement of the CDMAM image simulation chain is required.

A further study of the scattered radiation and anti-scatter grid performance was undertaking for the two anti-scatter geometries used (linear and cellular). In that study, it was found that the SPR increment on the edges could be attributed to scattered X-photons contribution principally from the breast support and compression paddle. Scattered X-ray photons penetrate a few millimeters within the phantom penumbra, increasing the scattered energy and therefore SPR values in that region. On the other hand, the scatter from these layers are not observed in the inner part of the phantom as they have been absorbed by the phantom itself. These findings are in line with results reported by other publications in the literature [82, 107]. However, to the author's knowledge, this effect has been often neglected in the literature for scatter estimation and correction, where simplistic geometries or phantoms are commonly used in MC simulations [19, 191, 192, 193]. Furthermore, this phenomenon will be magnified in DBT where no anti-scatter grid is typically implemented. Thus scattered radiation from the system should be considered in future experiments.

One of the greatest advantages of the MC simulations with respect to clinical systems is the ability to separate primary and scattered photons. As most of the manufacturers of the systems modeled in this work have provided the technical information about the geometry of their X-ray systems, a realistic comparison of the scatter fields for each of them in a clinical scenario has been possible. Although most of the manufacturers have provided suitable technical information, there have been some assumptions used regarding the thickness and composition of materials such as carbon fibre, which is a common material used for the breast support. Thus the composition and thickness of certain elements used in the simulations have been assumed and might be different from those found in the real system.

Chapter 6

Convolution-based scatter prediction for DBT

As explained in Chapter 2, one of the main disadvantages of DBT is the large amount of scattered radiation observed in the image receptor. This is due to the absence of an anti-scatter grid in most commercially-available DBT systems. Therefore accurate scatter field knowledge for each projection is necessary to properly understand the undesirable effects on image quality described in Chapter 3. This can be used to model the appropriate scatter signal when simulating DBT images. Furthermore, it can be employed clinically to remove the scattered radiation component from DBT projections prior to reconstruction.

It has also been seen that although MC simulation represents a common technique to directly estimate the scatter field in X-ray mammography [19, 47, 82, 107], this approach is extremely time consuming [123]. For this reason, a fast convolution-based method using appropriate scatter kernels represents an attractive option to efficiently estimate the distribution of scattered radiation [19, 20, 21, 22, 23, 24, 25] in DBT imaging.

6.1 Idealised DBT geometry

In a first approach to explore the scattered radiation in DBT projections, an idealised DBT setup was studied. Figure 6.1 shows the idealised geometry used to simulate the full field irradiation of the breast, where only an anthropomorphic breast phantom and an ideal image receptor (100% efficiency) were considered.

Two anthropomorphic breast phantoms developed by Bakic et al. [52] were imaged at 0° and sample projection angles of 7.5° and 25°. The breast phantoms had compressed thicknesses of $5cm$ and $7.5cm$ with an average glandularity of 12% and 40% respectively. The composition of the tissues found in the breast phantoms is described in Table 2.2.

In this section, results only corresponding to the $5cm$ thick breast phantom and projection angles of 0° and 25° are shown as representative extremes of the angles analysed.

The results regarding the 7.5cm thick breast phantom for 0°, 7.5° and 25° projection angles and 5cm thick breast phantom for a projection angle of 7.5° can be found Appendix C.

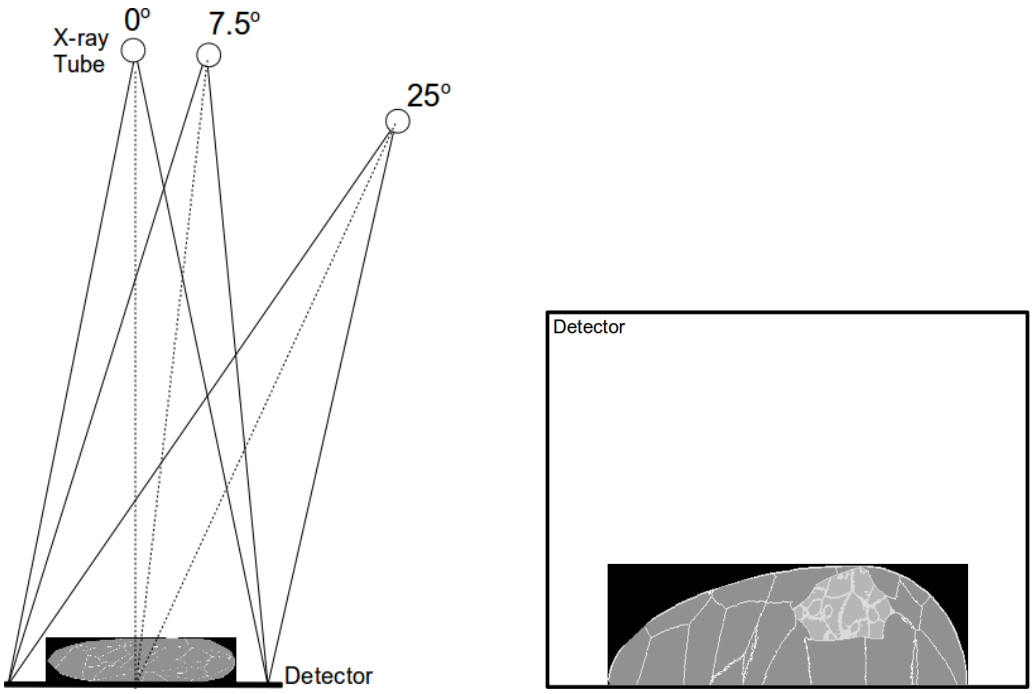

(a) Side View (b) Top View

Figure 6.1: Ideal DBT geometry used in this study. Side and top view are illustrated in (a) and (b) respectively.

In contrast to much of the prior work involving phantoms with perpendicular edges, the edges of these breast phantoms mimic the curvature seen at the edge of real breasts, wherein an air gap exists between the lower skin surface of the breast phantom and the detector (see Figure 6.2). This projected air gap and breast thickness along the X-ray's path, from the X-ray source, were calculated for each detector pixel using the ray tracing methodology described by Siddon [194].

MC simulations were run implementing the geometry shown in Figure 6.1 to calculate the ground truth scattered radiation for each of the breast phantoms and projection angles. Ten MC simulations of 10^9 photons each was used. The simulated X-ray spectrum was representative of a W/Rh target/filter combination at 29kVp (HVL=0.57mm Al). The source-to-detector distance (SDD) was 66cm and the rotation centre for the DBT projections was placed 4cm above an ideal image receptor with a pixel size of 0.5x0.5mm^2 . The SEM calculated in the MC simulations when using the 5cm thick anthropomorphic breast phantom was 1.6 and 2.1% for the primary and scattered radiation respectively.

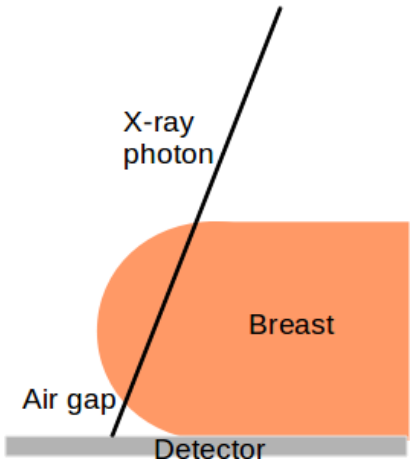

Figure 6.2: A diagram of the air gap between the curved edge region of the breast and the detector.

6.1.1 Scatter response function

The scatter point spread function (SPSF) was calculated for a series of uniform phantoms in a thickness range (0.1 to 10cm) and glandularities of 0% and 100% using a narrow pencil beam geometry as shown in Figure 6.3(a), which illustrates the position for three different projection angles. As described in the literature, MC simulation represents a flexible option to determine SPSFs [24, 46, 82, 122], hence the GEANT4 toolkit was used in this work to calculate the scatter response functions.

As described by Sechopoulos et al. [82], the SPSF is distributed symmetrically for a 0° projection angle. However, it becomes more asymmetric as the projection angle ϕ (perpendicular to the detector surface) increases. This phenomenon is illustrated in Figures 6.3(b) and 6.3(c), where the thick black curved lines represent regions with the same energy. For this reason, the spatial distributions of the $SPSF$s were recorded using polar coordinates (r, θ) for different radii r and angles θ in steps of 0.05mm (Δr) and 3°($\Delta\theta$) respectively. The intermediate values were calculated by simple linear interpolation due to the low spatial frequency composition of the scatter distribution in mammography images [46].

6.1.1.1 Validation of SPSFs with literature

A set of SPSFs was validated against SPSF results calculated by Sechopoulos et al. [82] and Boone and Cooper [19]. As described by these authors, the SPSFs were calculated using an X-ray pencil beam experiment (see Section 3.3.2). In this setup, a narrow beam hits a geometry which is made up of a circular shape phantom (radius 116mm) of different compositions, an air gap (between the bottom of the circular phantom and the image receptor) and an ideal image receptor for photon scoring. Five MC simulations of 10^9 photons each was used.

In order to calculate the SPSFs for this work, all the energy within the image receptor was recorded in annuli in steps of 1mm radii (see Figure 6.3(b)). For each annulus, the

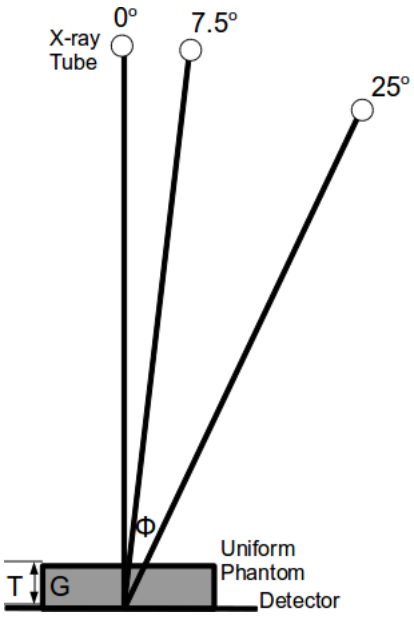

(a) Pencil beams diagram

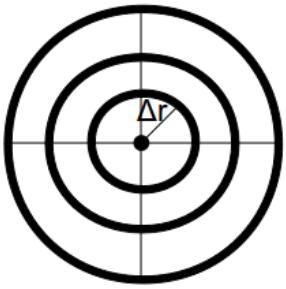

(b) SPSF $\phi = 0°$

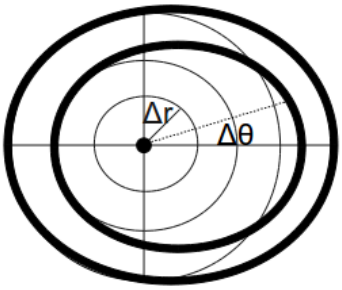

(c) SPSF $\phi > 0°$

Figure 6.3: (a) represents the side-views of three pencil beam experiments for a uniform slab phantom of thickness T and glandularity G. Top-view diagrams of scatter response for $\phi = 0°$ and $\phi > 0°$ are shown in (b) and (c) respectively. Each curve represents the distribution of a given energy. Note the isotropic scatter response for $\phi = 0°$ and the loss of circular symmetry for $\phi > 0°$ as the X-ray source tilts towards the left edge of the page.

total energy deposited by the scattered X-ray photons was normalized by the area of the ring (A). For example, the area of the n^{th} ring (A_n) would correspond to

$$A_n = (\pi r_n^2) - (\pi r_{n-1}^2), \tag{6.1}$$

where r_n and r_{n-1} are the radii of an the n and $n-1$ rings respectively.

Then, the results from the above area normalisation was divided by the total energy deposited by primary X-ray photons recorded within the image receptor. Thus, the SPSF has units of mm^{-2}.

The setup of the different validations described by [19, 82] used in this work is shown in Table 6.1.

Table 6.1: Configuration of the experiments used to validate the SPSF with Sechopoulos et al. [82] and Boone and Cooper [19].

Exp	Energy Spectrum(kVp)	Breast Thickness (cm)	Glandularity (%)	Air gap (mm)
A	26 Mo/Mo	5	0, 50, 100 & H_2O	10
B	26 Mo/Mo, 32 Rh/Rh	5	50	10
C	26 Mo/Mo	4	50	0, 10, 20 & 30
D	26 Mo/Mo	2, 4, 6 & 8	50	10

Sample comparisons of SPSF with the literature are illustrated in Figure 6.4. These results correspond to experiment D described in Table 6.1 using breast thicknesses of 2 and 8cm. The error bars for each of the points calculated in this work were also illustrated. However, they are too small as the y-axis is presented in a logarithmic scale. Therefore, the SEM of the SPSF is illustrated as a function of distance in the top right corner of each of the graphs. Note how the errors increase with distance as less number of photons reach the detector due to the larger absorption.

A quantitative comparison between the SPSF results from this work (Diaz) and Sechopoulos et al. [82] is presented in Table 6.2, where the SPR values were calculated after integrating the area under each SPSF curve using a circular field of view of radius 100mm. The average SEMs (in %) associated to the results for this work are shown in brackets. Sechopoulos et al. described their SEM errors as 0.4% and 1.6% for the 5cm and 8cm phantoms respectively (50% glandularity and energy beam of 27 kVp).

Table 6.2: Comparison of SPR values for Sechopoulos and results from this work using a circular field of view of radius 100mm. SEMs (in %) of this work are shown in brackets. Maximum and minimum differences are highlighted in red.

Exp. label		Area under the curve (SPR)		Difference (%)
		Sechopoulos	Diaz (SEM,%)	
A	G=0 %	5.33×10^{-1}	5.23×10^{-1} (0.2)	1.9
	G=50 %	5.57×10^{-1}	5.40×10^{-1} (0.4)	3.0
	G=100 %	5.92×10^{-1}	5.68×10^{-1} (0.9)	4.0
	H_2O	5.91×10^{-1}	5.89×10^{-1} (0.6)	0.3
B	26MoMo	5.57×10^{-1}	5.40×10^{-1} (0.4)	3.0
	32RhRh	5.70×10^{-1}	5.55×10^{-1} (0.2)	2.6
C	AG=0mm	4.57×10^{-1}	4.43×10^{-1} (0.8)	3.0
	AG=10mm	4.55×10^{-1}	4.41×10^{-1} (0.3)	3.0
	AG=20mm	4.48×10^{-1}	4.36×10^{-1} (0.2)	2.7
	AG=30mm	4.37×10^{-1}	4.26×10^{-1} (0.2)	2.5
D	T=2cm	2.44×10^{-1}	2.39×10^{-1} (0.2)	2.2
	T=4cm	4.55×10^{-1}	4.41×10^{-1} (0.4)	3.0
	T=6cm	6.63×10^{-1}	6.40×10^{-1} (0.5)	3.5
	T=8cm	8.72×10^{-1}	8.43×10^{-1} (0.8)	3.3

It was observed that the largest discrepancy found was 4.0% for 100% glandular breast tissue and, on the other hand, the minimum difference observed was 0.3% for a breast phantom filled in with water. In this work, the breast composition from Hammerstein [54] was employed. However, Sechopoulos et al. did not mentioned the adipose and glandular compositions they used. It is suspected that the discrepancies come

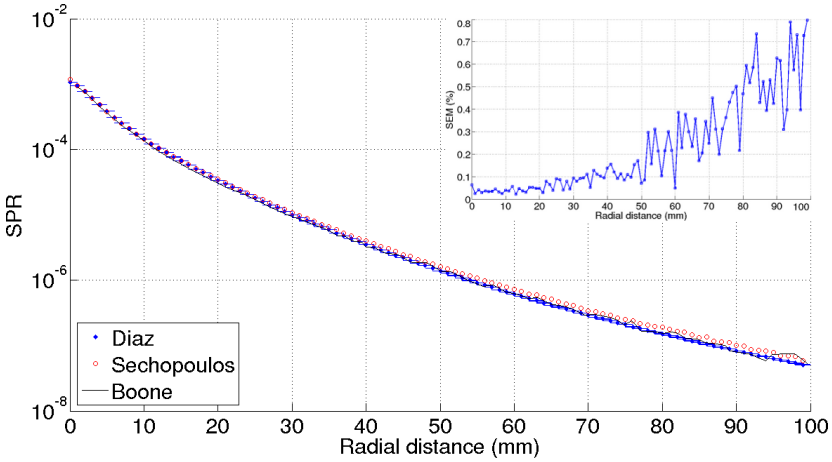

(a)

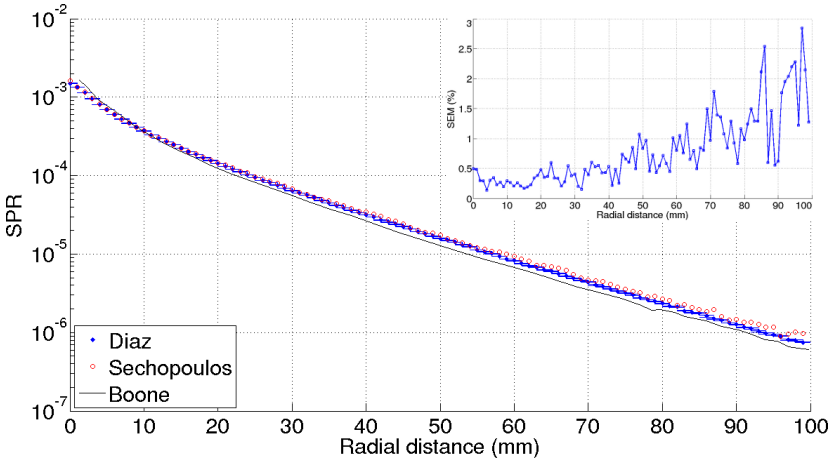

(b)

Figure 6.4: (a) and (b) illustrate the SPSFs using a D configuration (see Table 6.1) using a breast thickness of 2 and 8cm respectively. In each one, the SEM associated to the MC simulations of this work as a function of distance is shown in the top right corner. Results from this work, Sechopoulos et al. [82] and Boone and Cooper [19] are plotted as Diaz, Sechopoulos and Boone respectively.

from differences in the breast tissue composition as good agreement was found when simulating water.

The close agreement of the results with the literature suggested that the SPSF generated in this work can be used with confidence in the aforementioned convolution-based scatter calculations.

6.1.2 Scatter estimation: breast thickness consideration

The convolution method suggested in the literature [19, 20, 22, 24, 25] estimates the scatter image S by convolving an analytically calculated primary image P of size MxN with an appropriate scatter kernel K of size mxn. Mathematically, this 2D convolution can be expressed as:

$$S(x,y) = \sum_{k_1=-a}^{a} \sum_{k_2=-b}^{b} P(k_1,k_2)K(x-k_1, y-k_2) \qquad [eV], \tag{6.2}$$

where a and b corresponds to $(M-1)/2$ and $(N-1)/2$ respectively.

The primary image P can be calculated analytically using Beer-Lambert's law as will be explained in Section 6.2.1, using results derived from ray tracing. However, in order to compare directly the convolution-based calculations with the direct MC results, the primary image from the direct MC simulation was used as P in this section of idealised DBT geometry.

In order to construct the scatter kernel K, the appropriate $SPSF(r,\theta)$ described in Section 6.1.1, which has units of mm^{-2}, is multiplied by the area of the pixel (mm^2), which is $0.25mm^2$ in this case ($0.5mm$x$0.5mm$). Therefore, the scatter kernel is dimensionless.

Many authors have demonstrated that there is little effect on scatter distribution due to variations in overall breast composition and breast size [46, 82, 106]. Furthermore, no appreciable effects were found for different X-ray spectra as previously discussed in Chapter 3. Scattered radiation is principally influenced by breast thickness and projection angle. Thus spatially invariant scatter kernels, which only account for breast thickness t and projection angle ϕ, have been suggested in the literature [82] and therefore, Equation 6.2 was modified as follows:

$$S_\phi(x,y) = \sum_{k_1=-a}^{a} \sum_{k_2=-b}^{b} P(k_1,k_2)K_{\phi,t,G}(x-k_1, y-k_2) \qquad [eV], \tag{6.3}$$

where the $K_{\phi,t,G}$ corresponds to the new 2D scatter kernel which takes into account the thickness of the breast t and projection angle ϕ. As mentioned above, breast glandularity has a small effect on scatter, therefore G represents the average glandularity of the breast phantom.

This methodology assumes that all incident X-ray photons have an incidence angle ϕ (perpendicular to the image receptor plane). In other words, the scatter kernel calculated for a projection angle ϕ was used across the entire breast phantom.

6.1.2.1 Relative scatter error map

In order to validate the convolution-based methodology, scatter images from the convolution method S_ϕ were compared with scatter images from direct MC simulations

S_{MC}, which represents the ground truth. Maps of scatter relative error for each pixel ϵ_S, were created as described in Equation 6.4.

$$\epsilon_S(x,y) = \frac{S_{MC}(x,y) - S_{\phi}(x,y)}{S_{MC}(x,y)} \times 100 \qquad [\%] \tag{6.4}$$

6.1.2.2 Results for breast phantom

Results for $\epsilon_S(x,y)$ obtained when imaging the aforementioned $5cm$ thick breast phantom using a projection angle of 0^o are shown in Figure 6.5, where the relative errors are shown in a colourmap. Furthermore, the discrepancies outside the breast phantom region have been ignored and represented in dark red colour as they are not part of the scope of this work. As a reminder, the SEM calculated in the direct MC simulations when using the $5cm$ thick anthropomorphic breast phantom was 1.6 and 2.1% for the primary and scattered radiation respectively and the pixel size used was 0.5x0.5mm^2. On the other hand, it was observed that the maximum averaged SEM observed in the MC pencil beam experiment was less than 0.1% for projection angles of 0^o.

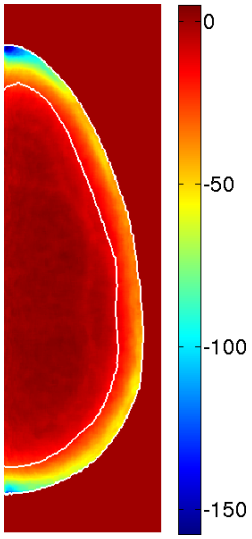

Figure 6.5: Relative error scatter map $\epsilon_S(x,y)$, in %, observed within a $5cm$ thick breast phantom and ϕ=0^o for estimated scatter using the thickness-dependent scatter kernels. Edges where the air gap starts as well as the edge region of the breast phantom are highlighted in white.

The above colourmap illustrates the overall magnitude of the discrepancies, which can go up to 150% (minus value means overestimation). In order to have a closer look at those discrepancies, the colourmap was modified. The same relative error map is shown in Figure 6.6(a), where a bipolar colourmap is used. The very low discrepancies are shown in grey colour, while difference greater than 20% or lower than -20% are displayed as dark red and dark blue respectively. Note that the sign in the errors illustrates overestimation (negative values) or underestimation (positive values) of the convolution-based scattered radiation when compared to MC-based scatter field. The

profile along the vertical white line shown in the relative error map is illustrated in Figure 6.6(b).

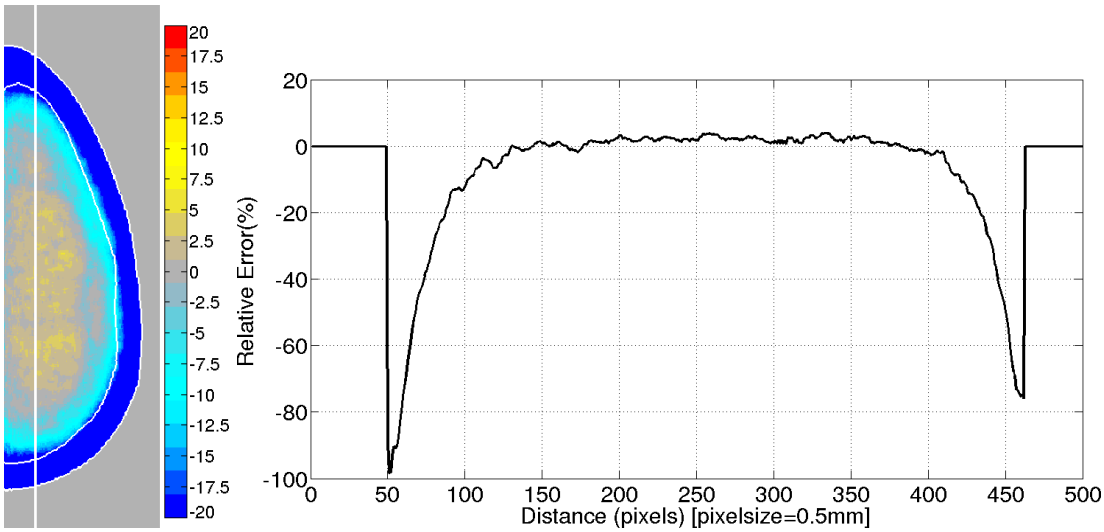

(a) Error map (%) (b) Vertical profile

Figure 6.6: (a) Relative error scatter map $\epsilon_S(x, y)$ observed within a $5cm$ thick breast phantom and ϕ=0^o for estimated scatter using the thickness-dependent scatter kernels. Note that errors are illustrated using a bipolar colourmap, in %, showing errors between lower than -20% and greater than 20%. Edges where the air gap starts as well as the edge region of the breast phantom are highlighted in white. The profile along the vertical white line is shown in (b).

As described previously in Equation 6.3, a thickness-dependent (Th.) scatter kernel was used to estimate the convolution-based scattered radiation, where only the breast phantom thickness and projection angles were considered. Analysing the profile shown in Figure 6.6(b), low discrepancies were shown in the central region of the breast phantom. However, large relative errors (up to 100% in the profile shown) were observed near the edges of the breast phantom, where scatter calculated from the convolution-based methodology $S_\phi(x, y)$ overestimates (negative values) the ground truth scatter from MC simulations $S_{MC}(x, y)$.

When imaging the same $5cm$ thick breast phantom using a wider projection angle of 25^o, good agreement was found once more in the central region of the breast phantom. In contrast, the discrepancies between the convolution-based method and MC became larger at the edges of the breast phantom as shown in Figure 6.7. It was observed that $S_\phi(x, y)$ overestimates (negative value) MC calculations up to 160% at the top edge of the breast phantom (dark blue). On the other hand, the dark blue region was reduced at the bottom edge of the breast phantom when compared with the results for 0^o. Bear in mind that the X-ray source tilts towards the bottom of the page.

Although the scatter calculation using thickness-dependent scatter kernels have demonstrated good agreement in the central area of the breast phantom, large discrepancies

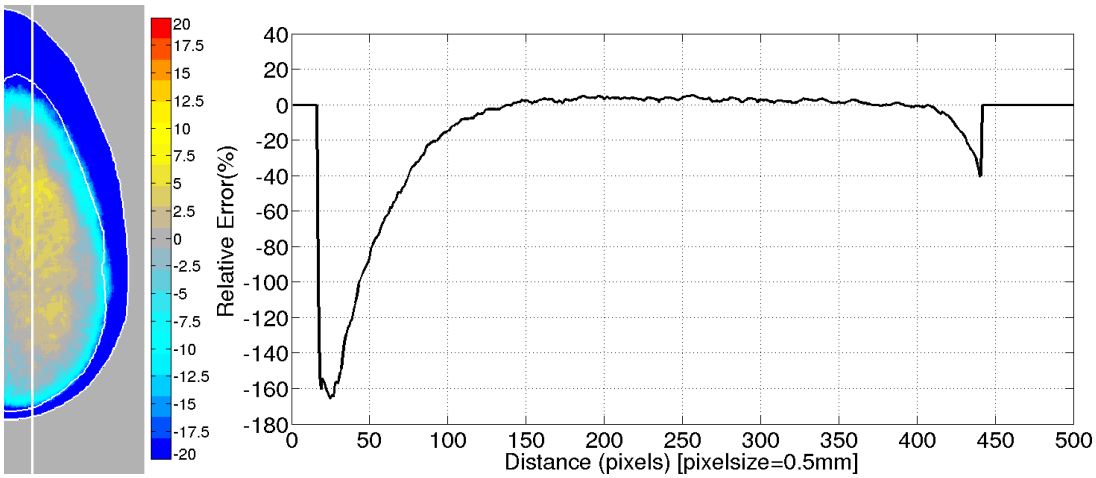

(a) Error map (%) (b) Vertical profile

Figure 6.7: (a) Relative error scatter map $\epsilon_S(x, y)$ observed within a $5cm$ thick breast phantom and ϕ=25^o for estimated scatter using the thickness-dependent scatter kernels. Note that errors are illustrated using a bipolar colourmap, in %, showing errors between lower than -20% and greater than 20%. Edges where the air gap starts as well as the edge region of the breast phantom are highlighted in white. The profile along the vertical white line is shown in (b).

were observed in the region near the edges of the breast phantom, especially for large projection angles. These early results then motivated a more exhaustive analysis of the use of thickness-dependent scatter kernels as described in the following section.

6.1.2.3 Scatter investigation using simple test objects

In this section, the scatter estimation using thickness-dependent scatter kernels is more fully explored using several simple geometrical test objects. SPR results from direct MC simulations were compared with the SPR derived from the convolution-based scatter (see Equation 6.3).

Unless otherwise stated, the experiments in this section used 6×10^9 X-ray photons in GEANT4 to image a given geometry using a parallel energy beam (26kVp Mo/Mo). The recorded scattered radiation in an idealised image receptor (100% efficiency) was median filtered using a kernel of 5x5 pixels (1mm^2 pixel size). The statistical error associated with each direct MC result is described below.

Uniform phantom: Firstly, a $2cm$ thick uniform phantom with glandularity 25% was used. The average SEM associated with the SPR was 0.7%. The side and top views of the geometry are shown in Figure 6.8(a) and 6.8(b) respectively.

A profile across the middle of the image receptor is illustrated in Figure 6.8(c) for the SPR calculated from the convolution-based methodology and direct MC simulations.

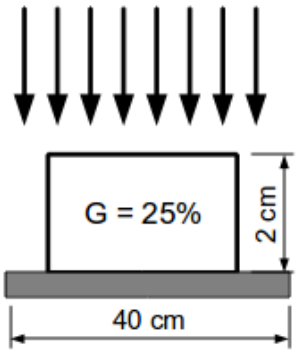

(a) Side View

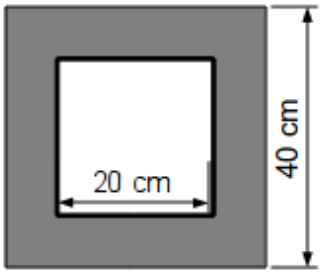

(b) Top View

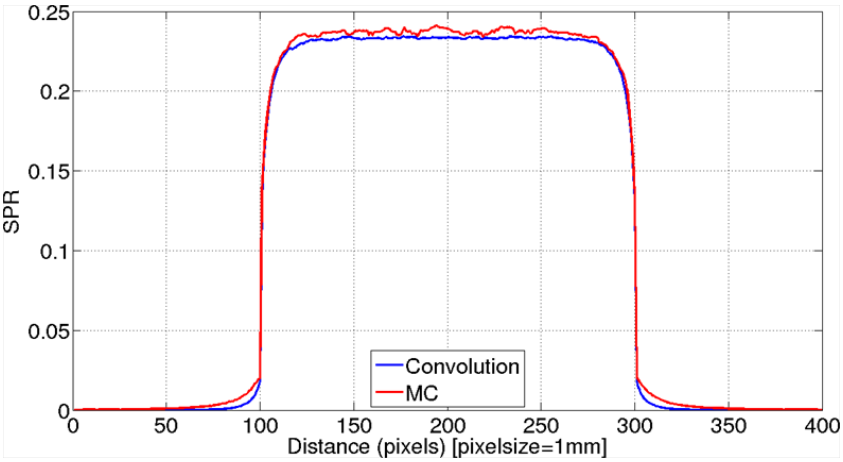

(c) Scatter Profile

Figure 6.8: Uniform phantom experiment: side and top views of the geometry of this experiment are shown in (a) and (b) respectively. (c) represents a SPR profile across the centre of the image receptor. The estimated SPR from the convolution and SPR from MC simulations are illustrated as a blue and red line respectively.

It was observed that both methodologies agree and similar SPR values were found along the SPR profile as illustrated in Figure 6.8(c).

Trapezoidal phantom: In a second approach to explore the thickness-dependent scatter kernels, a trapezoidal phantom made of 100% glandular tissue was used. This phantom illustrated, like in compressed breasts, a region with constant thickness ($3cm$) at the centre and a region where the thickness decreases towards the edge of the phantom. Side and top views of the setup are shown in Figure 6.9(a) and 6.9(b) respectively. For this experiment, the average SEM for the direct MC SPR values was 1.3%.

As observed in Figure 6.9(c), good correlation was found once more in the SPR profiles from both MC and convolution-based approach.

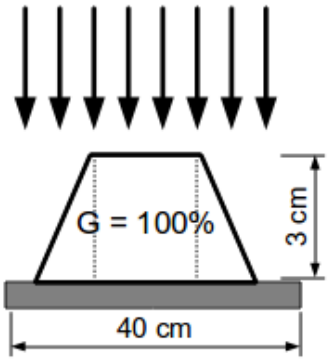

(a) Side View

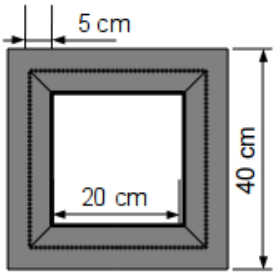

(b) Top View

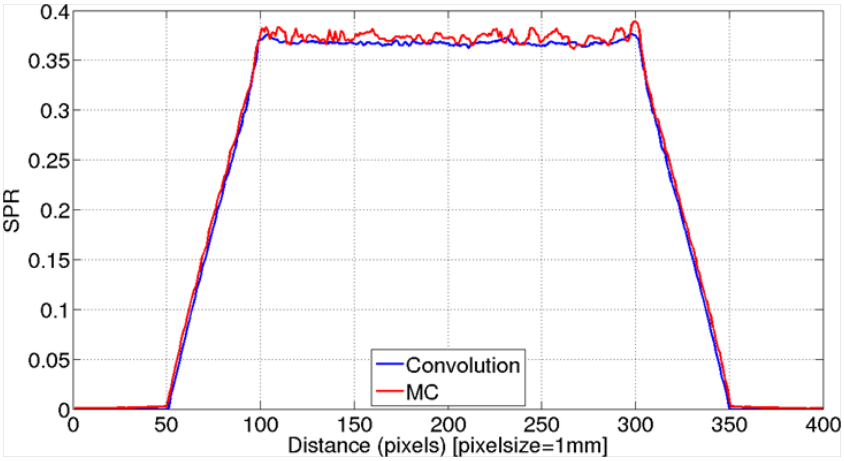

(c) Scatter Profile

Figure 6.9: Trapezoidal phantom experiment: side and top views of the geometry of this experiment are shown in (a) and (b) respectively. (c) represents a SPR profile across the centre of the image receptor. The estimated SPR from the convolution and SPR from MC simulations are illustrated as a blue and red line respectively.

Hexagonal phantom: Finally, moving towards a more realistic phantom shape, a hexagonal phantom of 100% glandular tissue was designed. As the phantom is thicker, the number of direct MC simulations was increased from 6 to 9, illustrating an average SEM of 2% for the SPR. This experiment represented a closer geometry when comparing with a compressed breast, where a constant thickness region ($5cm$) is observed as well as a region where the thickness decreases simulating certain degrees of curvature. This is observed in the side and top views of the geometry shown in Figure 6.10(a) and 6.10(b) respectively.

The SPR profiles observed in Figure 6.10(c) illustrate similar performance in SPR of both methodologies in the region of constant thickness. However, larger discrepancies (overestimation) are observed at the edges of the phantom, where an air gap under the phantom is observed. Therefore, the overestimation of scattered radiation

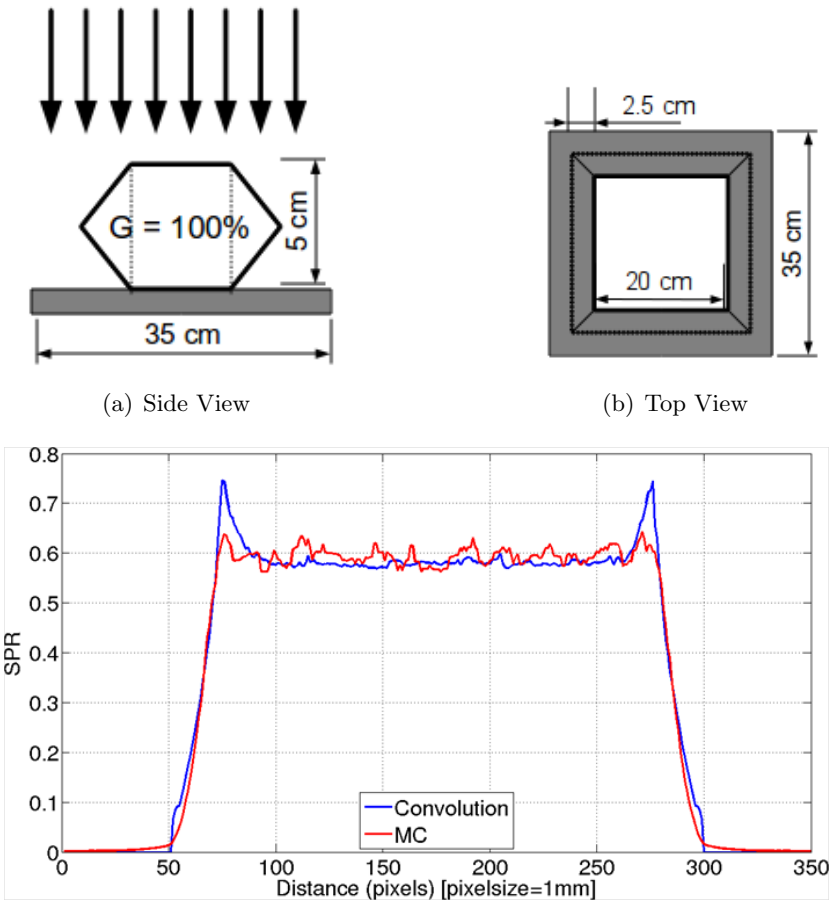

(a) Side View

(b) Top View

(c) Scatter Profile

Figure 6.10: Hexagonal phantom experiment: side and top views of the geometry of this experiment are shown in (a) and (b) respectively. (c) represents a SPR profile across the centre of the image receptor. The estimated SPR from the convolution and SPR from MC simulations are illustrated as a blue and red line respectively..

by the convolution-based method could be due to this air gap which was not initially considered. This type of behaviour was previously seen when applying the thickness-dependent scatter kernels in the breast models in section 6.1.2.2; large discrepancies were found at the edges of the breast phantom, where an air gap between the lower curvature of the breast phantom and the image receptor is located.

For this reason, a modification of the thickness-dependent scatter kernels suggested in the literature is proposed in the next section for scattered radiation estimation.

6.1.3 Scatter estimation: air gap inclusion

It has been demonstrated in the previous section that spatially invariant scatter kernels, which only account for breast thickness and projection angle, have some limitations

when estimating scatter fields using realistic breast geometries in DBT geometries, where anti-scatter grids are not used. This produces underestimation of scatter in regions where an air gap between the lower surface of the compressed breast and the image receptor is found. Furthermore, it was observed that such discrepancies increase with projection angle as the air gap increases.

In this section, the effect of the projected air gap AG traversed by photons exiting the curved edge of the breast phantom before impinging on the image receptor has been considered when applying the scatter kernel in the convolution-based methodology.

In order to calculate the proposed scatter kernel $K_{\phi,t,G,AG}$, a new set of pencil beam experiments were conducted. The SPSFs have been calculated for a series of uniform phantoms of several thickness (1 to 100 mm), glandularities (0 and 100%), projection angles (perpendicular to the detector surface) (0, 7.5 and 25^o) and, as mentioned above, air gaps between the lower surface of the uniform phantom. The air gaps were simulated using several idealised image receptors separated $2mm$ between them as illustrated in Figure 6.11. In other words, the air gaps AG were simulated from $0mm$ up to $50mm$ in steps of $2mm$.

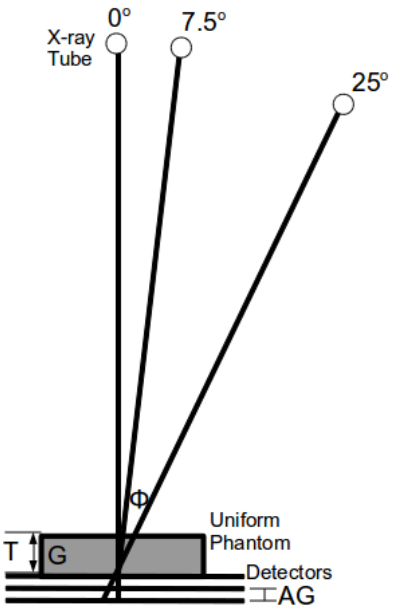

Figure 6.11: Side-views of three pencil beam experiments for a uniform slab phantom of thickness T, glandularity G and different air gaps AG. Note that several (idealised) detectors are used to simulate the air gaps AG.

Once the new SPSFs were calculated, these were stored in a look-up table. Then, the scatter $S_\phi(x,y)$ was estimated as described in Equation 6.5, where the proposed scatter kernel $K_{\phi,t,G,AG}$ was inserted.

$$S_\phi(x,y) = \sum_{k_1=-a}^{a} \sum_{k_2=-b}^{b} P(k_1,k_2) K_{\phi,t,G,AG}(x-k_1, y-k_2) \qquad [eV]. \qquad (6.5)$$

Refer to Figure 3.13 to observe the scatter PSF behaviour when the air gap is increased.

6.1.3.1 Results using breast phantom

As described previously, scatter images from MC simulations were compared with the results from the convolution-based methodology. In this section, breast phantom thickness and air gap dependent scatter kernels were used. The comparison was undertaken using the relative error scatter map mentioned in Section 6.1.2.1. As stated before, the average SEM calculated in the direct MC simulations when using the $5cm$ thick anthropomorphic breast phantom and $0.5\text{x}0.5mm^2$ pixel size was 1.6 and 2.1% for the primary and scattered radiation respectively.

The relative error scatter map $\epsilon_S(x, y)$ when using a $5cm$ thick breast phantom and a projection angle of 0^o is shown in Figure 6.12. In order to compare the performance of the previously discussed thickness-dependent scatter kernel (Th. kernel) with the proposed thickness and air gap dependent scatter kernel (Th.-AG kernel), profiles of the relative error $\epsilon_S(x, y)$ when using both scatter kernels are plotted.

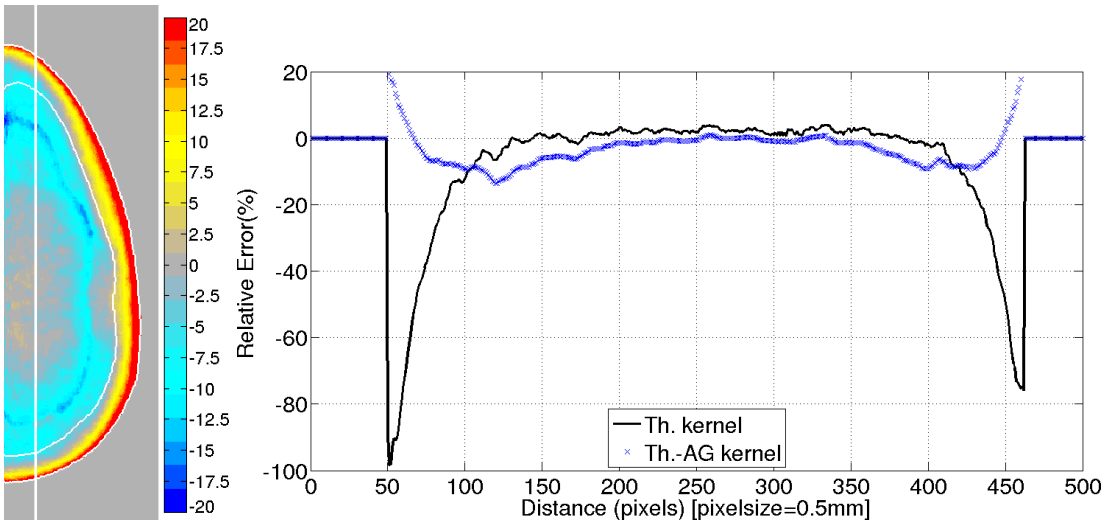

(a) Error map (%) (b) Vertical profile

Figure 6.12: (a) Relative error scatter map $\epsilon_S(x, y)$ observed within a $5cm$ thick breast phantom and ϕ=0^o for estimated scatter using the thickness and air gap dependent scatter kernels. Note that errors are illustrated using a bipolar colourmap, in %, showing errors between lower than -20% and greater than 20%. Edges where the air gap starts as well as the edge region of the breast phantom are highlighted in white. The profile along the vertical white line for the thickness-dependent (Th. kernel) and thickness and air gap dependent (Th.-AG kernel) scatter kernels is shown in (b).

It can be observed from Figure 6.12(b) that the large errors seen previously at the edges of the breast phantom have been strongly reduced by a factor of 4.5, when taking into account the effects of the air gaps.

Similar performance was found when using the same $5cm$ breast phantom and a projection angle of 25^o as shown in Figure 6.13. Previously, when employing the thickness-dependent scatter kernel, an overestimation of scattered radiation of more than 150%

were observed. However, these discrepancies were reduced to no more than 30% (underestimation) in the worst case when using the proposed new scatter kernels for this geometry.

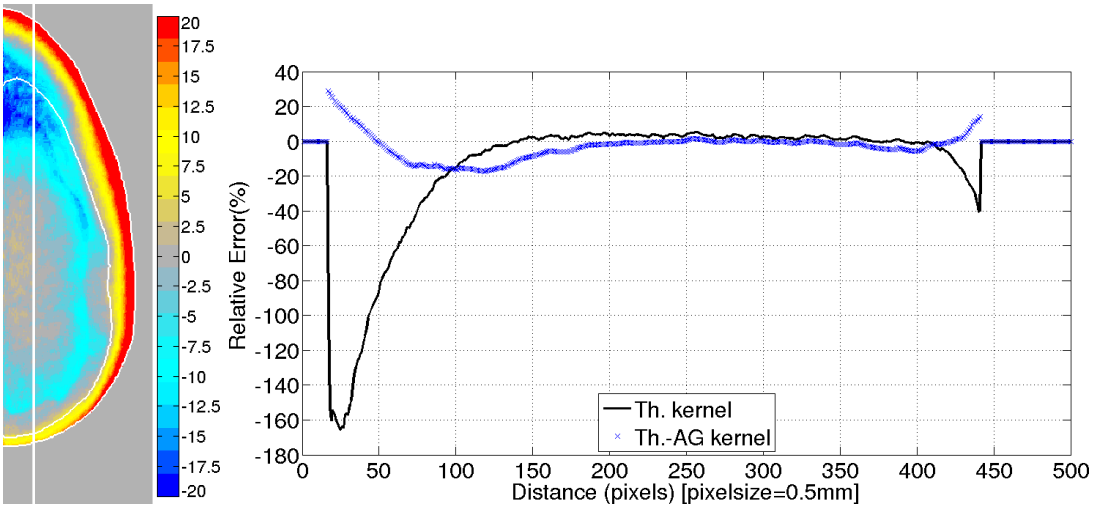

(a) Error map (%) (b) Vertical profile

Figure 6.13: (a) Relative error scatter map $\epsilon_S(x, y)$ observed within a $5cm$ thick breast phantom and ϕ=25^o for estimated scatter using the thickness and air gap dependent scatter kernels. Note that errors are illustrated using a bipolar colourmap, in %, showing errors between lower than -20% and greater than 20%. Edges where the air gap starts as well as the edge region of the breast phantom are highlighted in white. The profile along the vertical white line for the thickness-dependent (Th. kernel) and thickness and air gap dependent (Th.-AG kernel) scatter kernels is shown in (b).

Scattered radiation results from the convolution-based approach using the $5cm$ thick breast phantom and projection angle of 25^o showed an overall discrepancy with MC simulations-based scatter field of 20%. However, for the purposes of this work, discrepancies of less than 10% for $\epsilon_S(x, y)$ are desirable. As the scattered radiation is typically lower than the primary, the error in the total image (primary+scatter) is expected to be smaller than 10%. In order to improve results keeping the execution time low, simple correction factors were proposed as explained in the next section.

6.1.4 Residual correction factor for scatter image

As has been seen in the previous section, although accounting for the physics processes at the breast edge produces an improvement over the proposed thickness-dependent scatter kernel, a further improvement is also required to achieve a maximum discrepancy of 10%. This is because at the edge of the breast phantom, the scatter response performs differently in the area towards the inner part of the breast phantom and outside the breast phantom, where less scattering material is found.

The MC simulations account for the exact geometry of the breast phantom, whereas the

convolution-based approach uses scatter response functions assuming uniform thickness in all directions. When calculating the scatter response functions, it was previously described that the pencil beam experiment employed phantoms with uniform thicknesses. Therefore, when applying the convolution in a given point within the breast phantom, uniform thickness of the breast phantom in all directions is assumed. This assumption can be used in the centre of the breast phantom where the thickness decreases slowly. However, at the edges of the breast phantom, the breast thickness changes rapidly and the scatter kernels used in this work do not take this fact into account.

Sun et al. [111] suggested to use adaptive scatter kernels near the edges of an object to reduce this problem. However, in this work, a simple way to address this issue was proposed using a residual correction factor, which depends on the distance to the edge of the breast (r).

This correction factor $CF_\phi(r)$ was calculated pixel-by-pixel based for each projection of the breast phantoms as explained in Equation 6.6.

$$CF_\phi(r) = \frac{S_{MC}(x,y)}{S_\phi(x,y)}. \tag{6.6}$$

The residual correction factors calculated for the aforementioned $5cm$ thick breast phantom and the two projections angles studied in this chapter are illustrated in Figure 6.14.

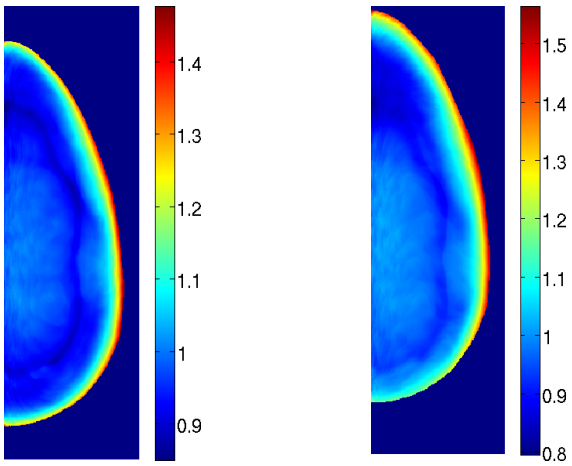

(a) 0^o (b) 25^o

Figure 6.14: Correction factor calculated pixel-by-pixel for a $5cm$ thick breast phantom using a projection angle of (a) 0^o and (b) 25^o.

As the CF is distance to the edge of the breast phantom dependent (r), the minimum distance from each pixel to the edge of the breast phantom was computed. Then, the the average CF value for each of the distances was calculated. Figure 6.15 represents the average CF value for all distances computed corresponding to the cases illustrated in Figure 6.14. It can be observed that the major correction is applied near the edge of the breast phantom, where the aforementioned underestimation of scatter is compensated

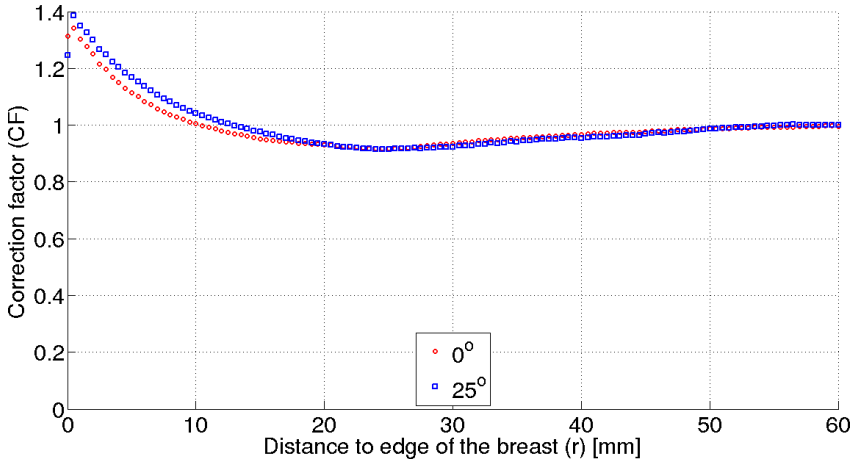

Figure 6.15: Average correction factor values calculated for a breast phantom of thickness $5cm$ and incident angles of 0^o (red) and 25^o (blue).

with CF values greater than one. On the other hand, no correction (CF = 1) is needed as distance r increases towards the centre of the breast phantom.

The scatter image produced after applying the correction factor $S_{CF}(x, y)$ was calculated by multiplying $CF_\phi(r)$ and the scatter calculated after the convolution stage $S_\phi(x, y)$ when using the proposed thickness and air gap dependent scatter kernels. This is illustrated in Equation 6.7.

$$S_{CF}(x, y) = S_\phi(x, y) \times CF(r) \tag{6.7}$$

6.1.4.1 Results using breast phantom

In this section, the discrepancies between the scattered radiation from MC results and from the convolution method using thickness-dependent kernels, thickness and air gap dependent kernels and thickness and air gap dependent kernels with correction factors are shown.

The $\epsilon_S(x, y)$ results corresponding to a projection angle of 0^o imaging a breast phantom of $5cm$ are shown in Figure 6.16. It is observed that the proposed correction factors have reduced most of the large errors leaving an overall error of less than 5%. Profiles shown in Figure 6.16(d) describe the improvement in scatter estimation after modifying the thickness-dependent scatter kernel using the distance to the edge of the phantom dependent correction factor.

Figure 6.17 illustrates similar improvement in the performance of the suggested scatter kernels and correction factor when simulating a projection angle of 25^o. The large errors of more than 100% have been strongly reduced when accounting for the aforementioned air gap. Moreover, those errors have been kept within the 10% limit of this work with the aid of residual correction factors.

It is arguable that the improved performance when using the correction factors is due to their calculation using the actual breast phantom. However, it was demonstrated

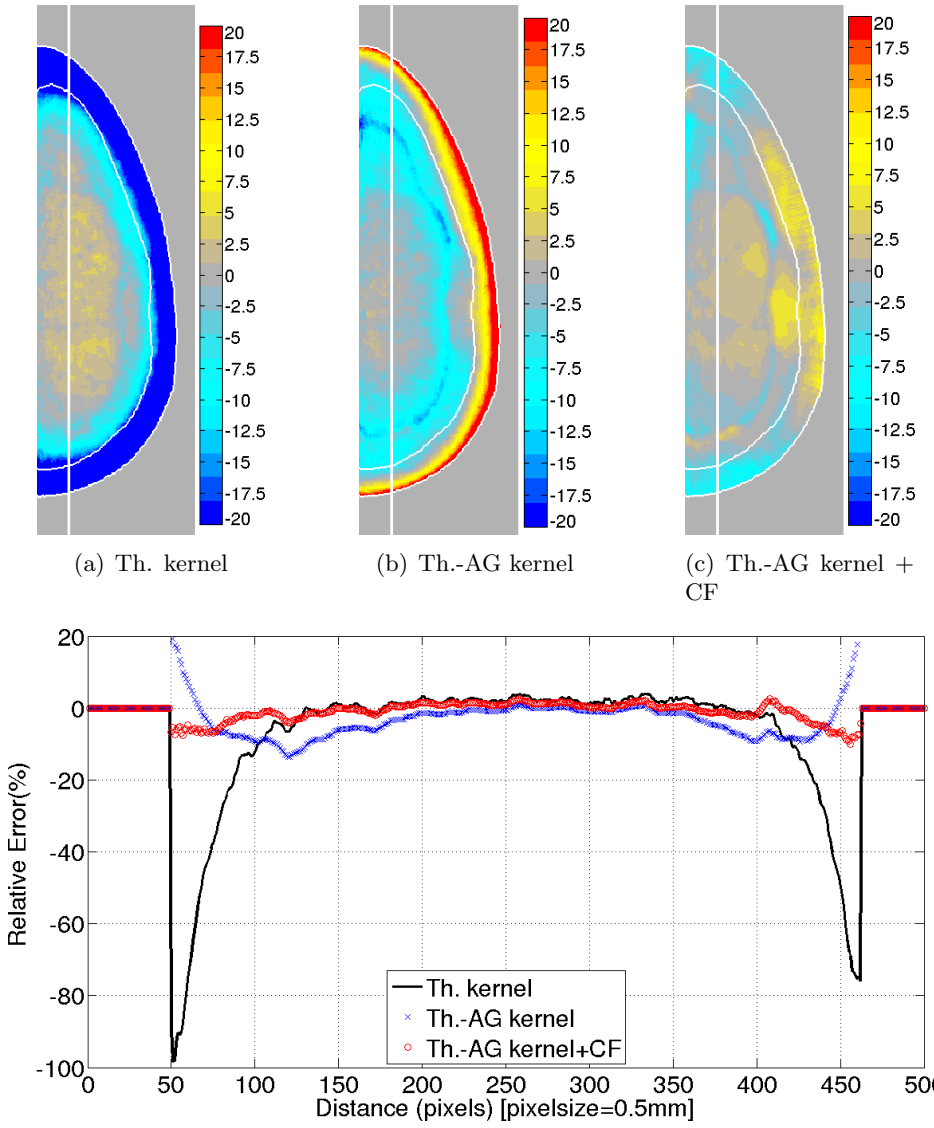

(a) Th. kernel (b) Th.-AG kernel (c) Th.-AG kernel + CF

(d) Vertical profile

Figure 6.16: Relative error scatter map $\epsilon_S(x, y)$ observed within a $5cm$ thick breast phantom and ϕ=0^o for estimated scatter using the (a) thickness-dependent, (b) thickness and air gap dependent scatter kernels and (c) thickness and air gap dependent scatter kernels and CF. Note that errors are illustrated using a bipolar colourmap, in %, showing errors between lower than -20% and greater than 20%. Edges where the air gap starts as well as the edge region of the breast phantom are highlighted in white. The profile along the vertical white line for the thickness-dependent (Th. kernel), thickness and air gap dependent (Th.-AG kernel) and Th.-AG kernel with correction factors (Th.-AG kernel+CF) scatter kernels are shown in (d).

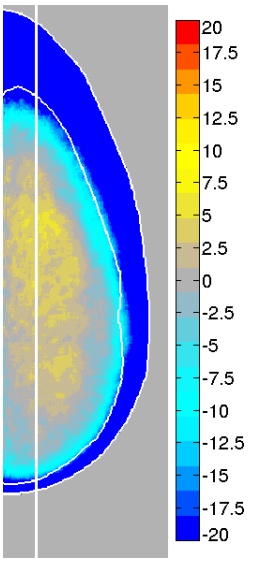

(a) Th. kernel

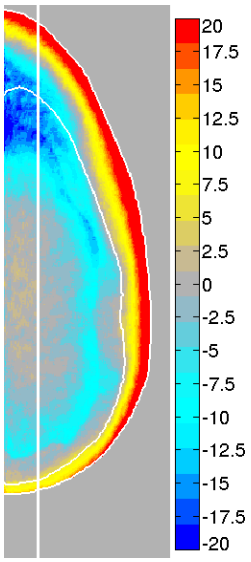

(b) Th.-AG kernel

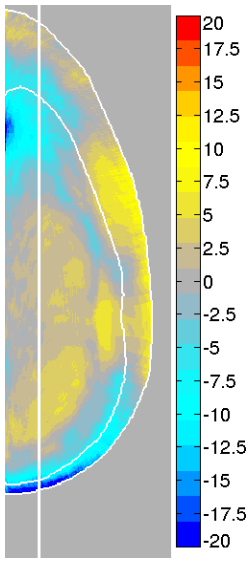

(c) Th.-AG kernel + CF

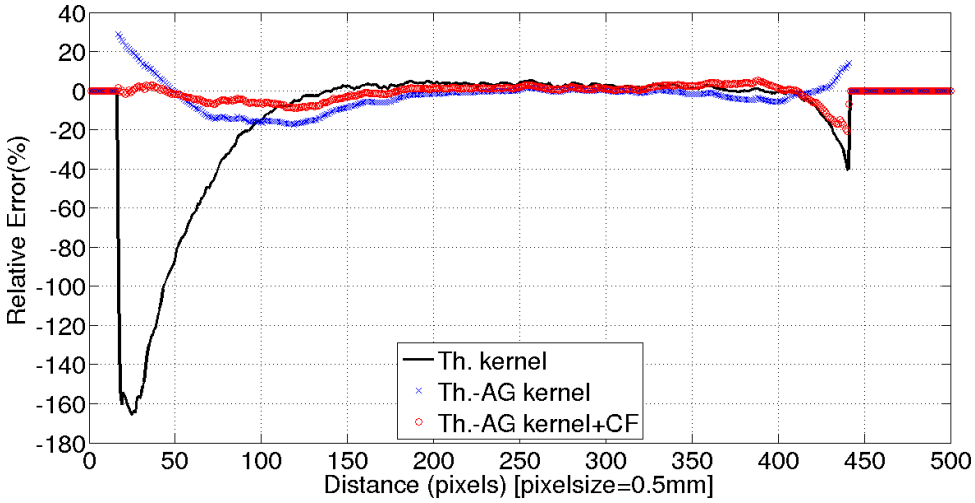

(d) Vertical profile

Figure 6.17: Relative error scatter map $\epsilon_S(x, y)$ observed within a $5cm$ thick breast phantom and ϕ=25^o for estimated scatter using the (a) thickness-dependent, (b) thickness and air gap dependent scatter kernels and (c) thickness and air gap dependent scatter kernels and CF. Note that errors are illustrated using a bipolar colourmap, in %, showing errors between lower than -20% and greater than 20%. Edges where the air gap starts as well as the edge region of the breast phantom are highlighted in white. The profile along the vertical white line for the thickness-dependent (Th. kernel), thickness and air gap dependent (Th.-AG kernel) and Th.-AG kernel with correction factors (Th.-AG kernel+CF) scatter kernels are shown in (d).

that a correction method which account for the distance to the edge of the phantom could be used for optimal results.

Despite the success demonstrated with the simplified geometry shown above, a significant limitations of this work so far was the use of an idealised DBT geometry. In real DBT units, there is further geometry to consider that may influence the observed scatter distribution: the compression paddle and breast support represent a potentially significant source of scatter in the image as described by [82, 107]. This motivates the need to move to a more complex geometry, which is described in the next section.

6.2 Realistic DBT geometry

The DBT geometry used in this section approximately corresponds to the Hologic Selenia Dimensions commercial system as illustrated in Figure 6.18. The X-ray tube was placed at $700mm$ from the detector surface for the 0^o X-ray tube position and the rotation axis was located across the middle of the image receptor.

The configuration used also contains, from top to bottom, a $2.8mm$ thick compression paddle of polycarbonate, an anthropomorphic breast model, a carbon-fibre breast support plate with a thickness of $1mm$ and a $200\mu m$ thick Se detector with its corresponding cover (127μm thick aluminised polyester). Note that there is an air gap of $24mm$ between the bottom of the breast support and the detector cover. Despite the fact that the widest projection angle of this commercial system is 7.5^o in screening mode, in this work projection angles up to 25^o have been studied as observed in Figure 6.18(a). This is in order to consider the effects of wider angle sweep employed by other manufacturers [74, 75].

The imaging configuration described above was modelled in the MC code and 10 runs of 10^9 X-ray photons were simulated, irradiating the entire image receptor using a pixel size of 1mm^2. As described in Chapter 4, a 7x7 median filter was applied five times in order to smooth the images, showing a maximum statistical error of 0.25% for the scatter images. As the primary images were not median filtered, the average SEM was measured to be 1.5% for the $9.3cm$ thick breast phantom and projection angle of 25^o, which corresponds to the largest SEM observed. In order to calculate the SEM of the scatter kernels, the pencil beam was run 5 times and the SPR value was calculated after integrating the Scatter PSF using a circular FOV of radius $100mm$. The SEM observed was smaller than 0.1%.

Regarding the anthropomorphic breast models, three breast phantoms were used in this study, whose parameters, along with the clinically relevant energy spectrum used for each, are presented in Table 6.3.

As explained for the ideal system shown in the previous section, this geometry was used to calculate ground truth data using MC simulation, with which results from the proposed convolution-based methodology will be compared.

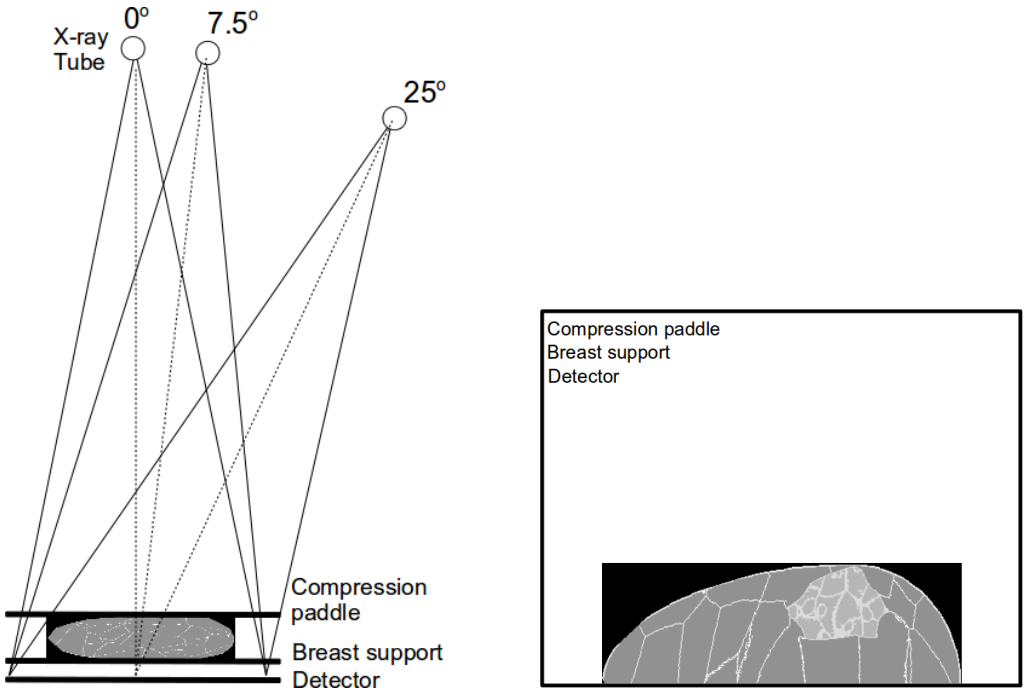

(a) Side View (b) Top View

Figure 6.18: DBT geometry used in this study for a real DBT system. Side and top view are illustrated in (a) and (b) respectively.

Table 6.3: Parameters of the breast phantoms and energy spectra used in the realistic DBT study.

Energy spectrum	HVL (mm Al)	Thickness(mm)	Glandularity(%)	Voxelsize(mm^3)
26kVp W/Al	0.44	22	30.0	
31kVp W/Al	0.54	50	20.0	0.5x0.5x0.5
40kVp W/Al	0.70	93	9.6	

6.2.1 Primary image calculation

When using the idealised DBT geometry in Section 6.1, the primary transmission image from MC simulations were inserted in the convolution-based scatter prediction. However, for the case of a realistic DBT geometry, the image generated from the primary (i.e. unscattered) beam $P(x, y)$ observed across each pixel (x, y) at the image receptor was calculated analytically using the Beer-Lambert's law. The development of an tool to fully generate the primary and scattered radiation motivated this change. Thus in this work, the primary radiation within the detector is calculated as

$$P(x,y) = \sum_x \sum_y \sum_{E=E_{min}}^{E_{max}} \epsilon(E) \cdot w(E) \cdot E \cdot e^{\sum_i -\mu_i(E) \cdot t_i(x,y)} dE \qquad [eV], \tag{6.8}$$

where $\mu_i(E)$ represents the linear attenuation coefficients of the different i tissues found along the photon path $t_i(x, y)$. Each pixel at the image receptor is evaluated at energy

intervals, dE, across the complete energy spectrum $w(E)$ emitted from the X-ray tube. The energy-dependent absorption efficiency of the image receptor, which was calculated using MC simulations separately, is denoted as $\epsilon(E)$.

Moreover, $t_i(x, y)$ within the voxelised breast phantom was computed at each location at the image receptor using the ray tracing methodology described by Siddon [194], which determines the distance traversed across each tissue/material along a ray cast from the X-ray tube (infinitesimal point) to the centre of each pixel at the image detector. This code for this ray tracing method was created by Dr. Premkumar Elangovan and was previously validated with X-ray photons paths calculated in MC simulations.

The average error found between the analytically calculated primary $P(x, y)$ and primary from MC simulations was 0.2% and the largest disagreement was 0.5%.

6.2.2 Scatter PSFs using realistic geometry

As shown in Figure 6.18, the revised setup used in this section was different from the idealised geometry studied in Section 6.1, so SPSFs were re-calculated matching the new configuration. Therefore, new pencil beam experiments for 0, 7.5 and 25^o were run as previously explained using the geometry shown in Figure 6.19(a), where new layers such as the compression paddle and breast support were included.

In addition, the SPSF intrinsic to the system (SPSF_{sys}) was also calculated. In order to do so, the geometry illustrated in Figure 6.19(b) was simulated. This setup did not contain any scattering material, i.e. phantom, and thus all the scattered radiation recorded within the image receptor was due to the different layers included in the X-ray mammography system. Primary incident angles from 0 to 35^o were calculated in steps of 5^o. This SPSF_{sys} will be proposed below to account for the scattered radiation beneath the breast phantom generated by the overlying system layers.

SPSFs for such realistic DBT systems cannot be found in the literature. Therefore, to ensure these are properly understood, they are studied in further detail below.

Sample SPSF from idealised and realistic geometries are shown in Figure 6.20(a). They correspond to a $2cm$ thick phantom of 0% glandularity and no air gap between the phantom bottom surface and the breast support (AG=$0mm$). When the idealised geometry is used (blue), a smooth SPSF is observed. However, the real geometry (in red) has produced a sharp peak within the first $1mm$ followed by a much flatter response.

This abrupt change is produced by the new layers (compression paddle, breast support and detector's cover) added for the realistic geometry, that were omitted in the idealised geometry. Furthermore, when the phantom is removed from the realistic geometry, the SPSF also exhibits this sharp peak as illustrated in Figure 6.20(b). Note that in this latter figure, the phantom thickness was 4cm, while the other parameters were kept unchanged.

In a further study, the scatter contribution from each of the simulated layers was calculated using MC simulations. The SPSF for each of the materials is shown in Figure 6.21. This has demonstrated that this increase of scatter within the first millimeter of the

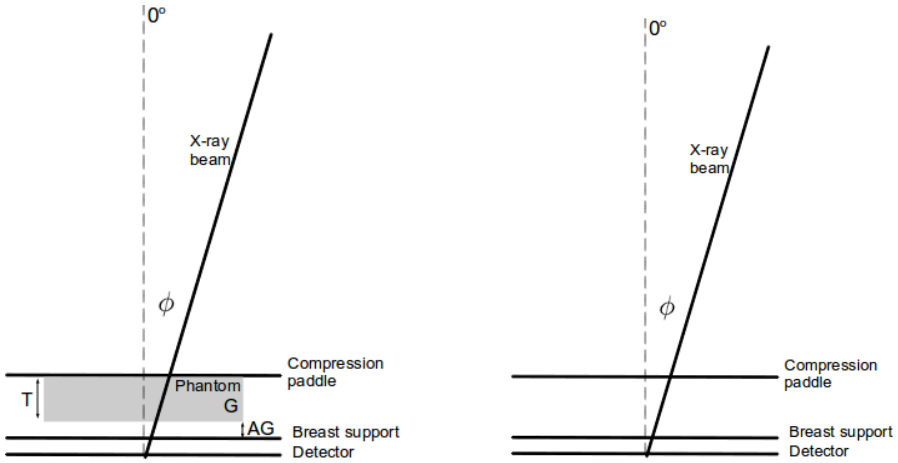

Figure 6.19: (a) shows the pencil beam geometry used when calculating the SPSF for a real DBT geometry. The scatter response from the system SPSF_{sys} (without scattering material) was calculated as illustrated in (b).

SPSF is due to the forward scattered photons from the detector's cover (light blue), which corresponds to a 127μm thick aluminised polyester in direct contact with the image receptor. In the idealised geometry, the breast phantom was in direct contact with the detector. However, the detector's cover used for the realistic geometry had a higher density material which produced this increment of scattered photons at low scattering angles (forward scatter). Despite this increment, the contribution of scatter from this thin cover layer is dramatically reduced with radial distance from the X-ray photon beam.

Using results from the above experiment, the SPR contribution from all the layers included in the realistic simulations have been studied for different radial distances (i.e. circular field of view FOV) as presented in Table 6.4. These values were calculated after integrating the SPSFs illustrated in Figure 6.21 over a given radial distance r.

Table 6.4: SPR values calculated after integrating the SPSF curves shown in Figure 6.21 over several radial distances, r.

Source	r=0.10mm	r=1mm	r=116mm
Total	136.86e-5	381.37e-5	0.530
Paddle	0.04e-5 (0.0%)	3.74e-5 (1.0%)	0.022 (4.1%)
Phantom	1.19e-5 (0.9%)	114.08e-5 (29.9%)	0.447 (84.4%)
Breast support	0.12e-5 (0.1%)	13.37e-5 (3.5%)	0.022 (4.2%))
Detector cover	135.28e-5 (98.9%)	244.11e-5 (64.0%)	0.003 (0.5%)
Multiple layers	0.24e-5 (0.2%)	6.06e-5 (1.6%)	0.037 (6.9%)

It can be observed that the SPR contribution from the detector's cover is reduced as the radial distance increases. Thus, for a radial distance of 0.10mm, the SPR from the detector's cover represents 98% of the total SPR. However, after integrating the SPSF over the entire circular phantom (r=116mm), the contribution of the detector's cover is drastically reduced to 0.5% of the overall SPR.

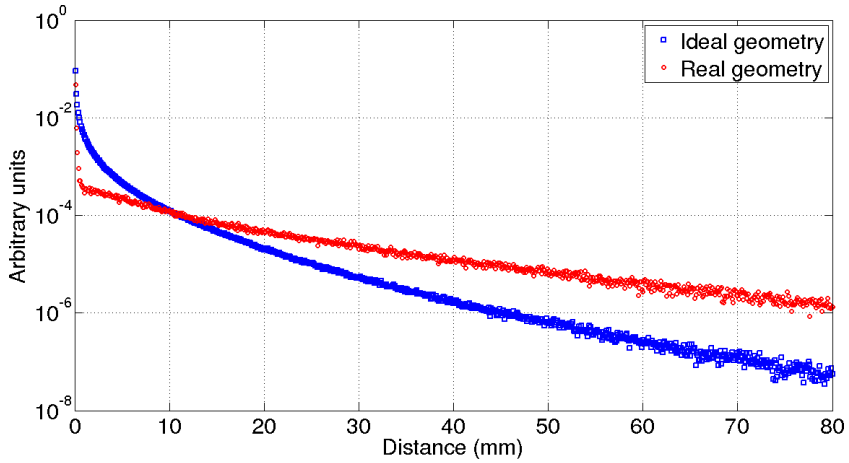

(a)

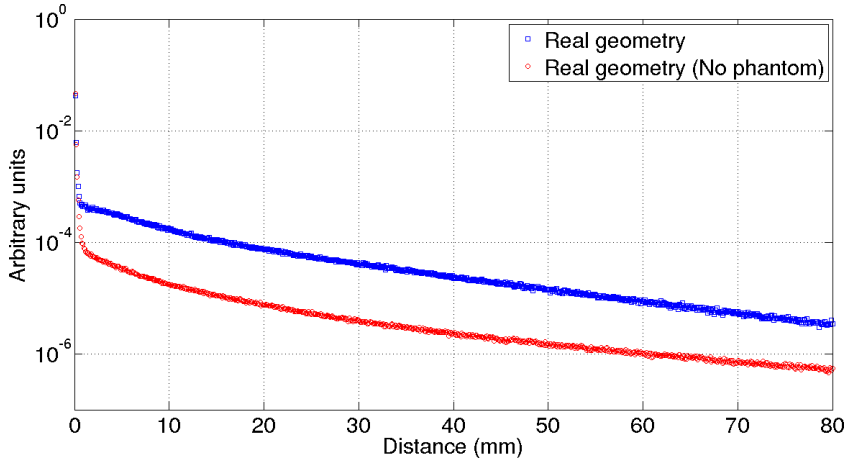

(b)

Figure 6.20: (a) illustrates the SPSF for a $2cm$ thick phantom, glandularity G=0% and AG=$0mm$ using an idealised and realistic geometry. The SPSFs for a real geometry with and without a $4cm$ phantom (G=0%) are shown in (b).

As expected, the major contribution of scattered photons comes from the uniform phantom (84% contribution in the total SPF for a radius of $116mm$) as it represents the thickest layer simulated.

6.2.3 Scatter estimation

As described in the previous section, SPSFs were calculated using a geometry with and without uniform phantoms, corresponding to SPSF (which includes a phantom of particular thickness and glandularity) and SPSF_{sys} respectively. Therefore, a set of scatter kernels based on SPSF was used within the breast phantom region and a different set (based on SPSF_{sys}) outside during the convolution process. A binary

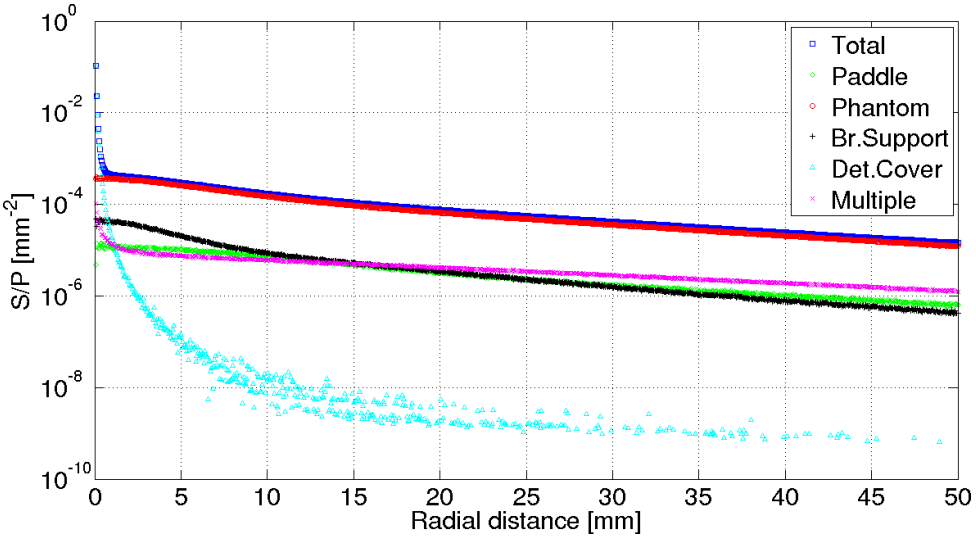

Figure 6.21: SPSF contribution for each of the layers included in the system using a $4cm$ thick breast phantom of glandularity 0% and AG = $0mm$. When the scattered radiation recorded within the detector comes from more than one layer, this has been labeled as 'multiple'.

template was used to calculate all the pixels inside and outside the breast phantom projection.

The total scatter image $S_{T,\phi}(x,y)$ for a projection angle ϕ was estimated as a combination of the scatter image within the breast area $S_{bre,\phi}(x,y)$ and the scatter outside the breast region $S_{sys,\phi}(x,y)$:

$$S_{T,\phi}(x,y) = S_{bre,\phi}(x,y) + S_{sys,\phi}(x,y) \qquad [eV]. \tag{6.9}$$

$S_{bre}(x,y)$ was estimated as previously illustrated in Equation 6.5, where $K_{\phi,t,G,AG}$ was calculated using the SPSF for the realistic geometry. Note that SPSFs calculated for a single projection (at either 0, 7.5 or 25^o) was used across the entire breast phantom area. Therefore, it was assumed parallel X-ray beam within the breast phantom region.

The scatter contribution from the system $S_{sys,\phi}(x,y)$ was estimated after convolving the primary image at the image receptor $P(x,y)$ with a scatter kernel $K_{sys,\phi,T}$ in the region outside the phantom.

$$S_{sys,\phi}(x,y) = \sum_{k_1=-a}^{a} \sum_{k_2=-b}^{b} P(k_1,k_2) K_{sys,\phi,T}(x-k_1, y-k_2) \qquad [eV]. \tag{6.10}$$

$K_{sys,\phi,T}$ depends only on the distance from the compression paddle to the breast support, i.e. breast thickness T, as the air gap distance between the breast support and image receptor is constant.

As previously described, $K_{sys,\phi,T}$ was calculated in the absence of any scattering material (see Figure 6.19(b)). However in reality, the scatter from the system is attenuated

by the breast tissue in the region near the breast phantom edge. Therefore, the calculated SPSF_{sys} needs to be attenuated by the corresponding breast tissue thickness.

Figure 6.22 represents a diagram to understand this process, where two cases of scattered X-ray photons within the compression paddle are shown. In the case O-B, an X-ray photon is recorded within the image receptor at point (x_1',y_1') after a scattering interaction within the paddle (corresponding to point (x,y) at the receptor) without being attenuated by any other tissue. Thus, the results agree with the previously calculated SPSF_{sys}. In contrast, the scattered photon O-A is attenuated along the path that the X-ray photon traverses until it reaches the image receptor at (x_2',y_2').

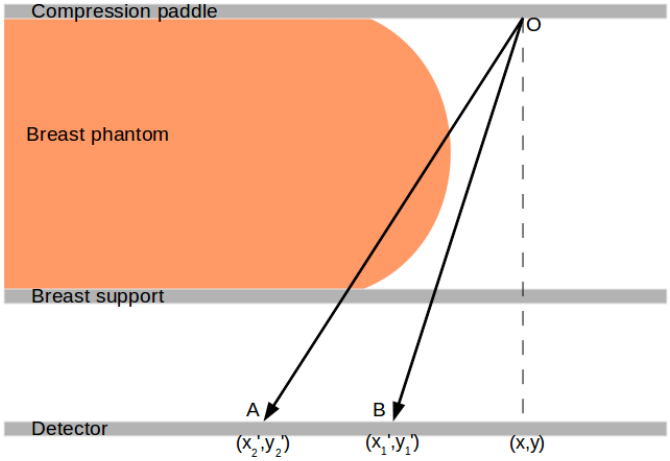

Figure 6.22: Systematic diagram showing two cases of scattered photons from the compression paddle. The ray O-B shows an unattenuated X-ray photon which reach the image receptor at (x_1',y_1'). The X-ray photon scattered from the paddle following O-A path, recorded at (x_2',y_2'), should be attenuated due to the path traversed within the breast phantom.

Previously when the methodology for the idealised DBT geometry was described, it was introduced the idea of a distance-to-the-edge of the breast phantom correction factor. This option was explored here to account for the attenuation of the X-ray photons as they traverse through the breast phantom. In order to avoid using the breast phantom to calculate the correction factor, a series of D-shape phantoms were used. However, it was found that due to the non-symmetry curvature of the breast phantom models, this methodology did not show good performance and was discarded, motivating the exploration of an alternative method.

In this alternative method, $K_{sys,\phi,T}$ was weighted accordingly to account for the path traversed by the X-ray photons from the compression paddle to the image receptor. This weight map $\alpha(x, y, x', y')$ compensates for the lack of scattering material outside the breast phantom ($\alpha = 1$) and for the attenuation due to the breast tissue ($\alpha < 1$) and was calculated as the ratio of the energy deposited within the image receptor with and without the breast phantom as follows:

$$\alpha(x,y,x',y') = \frac{\sum_{E=E_{min}}^{E_{max}} \epsilon(E)\cdot w(E)\cdot E\cdot e^{\sum_i -\mu_i(E)\cdot t_i(x,y,x',y')}dE}{\sum_{E=E_{min}}^{E_{max}} \epsilon(E)\cdot w(E)\cdot E\cdot e^{\sum_j -\mu_j(E)\cdot t_j(x,y,x',y')}dE}, \tag{6.11}$$

where $\epsilon(E)$ and $w(E)$ correspond to the energy efficiency of the detector and the energy spectrum (normalised to an area of 1) observed after the compression paddle respectively. The linear attenuation coefficients $\mu(E)$ and distances from the compression paddle to the image receptor $t(x, y, x', y')$ along the X-ray photon beam were also included. The subscripts i and j correspond to the number of tissues found along the X-ray beam in the presence and absence of the breast phantom respectively. When breast tissue was found, the $\mu(E)$ was set to the average glandularity of the breast phantom G (see Table 6.3). The distances $t(x, y, x', y')$ were calculated using the Siddon X-ray tracing methodology [194].

The task of calculating the distances from every point in the compression paddle to each pixel in the detector was very time consuming. Thus, in order to reduce the computation time, the evaluated points in the compression paddle were separated by $3mm$. Furthermore, only the pixels within the projected breast phantom shadow were evaluated.

Once $\alpha(x, y, x', y')$ was calculated for each point within the compression paddle, S_{sys} was estimated as follows

$$S_{sys}(x,y) = \sum_{k_1=-a}^{a} \sum_{k_2=-b}^{b} P(k_1,k_2) K_{sys,\phi,T}(x-k_1, y-k_2) \alpha(x,y,x',y') \qquad [eV]. \quad (6.12)$$

In order to account for the X-ray incident angle at each evaluated point in the compression paddle, the X-ray incident angle and the direction of the primary X-ray photons were taken into account. For a given point in the compression paddle (outside the breast phantom area), the closest simulated incident angle (previously calculated from 0 to 35^o in steps of 5^o) was used.

An example of these incident (white circular lines) and direction angles (yellow lines) are shown in Figure 6.23 for a projection angle of 0^o and a 5cm thick breast phantom (red contour).

6.2.4 Results using anthropomorphic breast phantoms

Using the methodology described above, the total scatter image $S_T(x, y)$ was calculated for the anthropomorphic breast phantoms described in Table 6.3. These scatter images were compared with results from direct MC simulations $S_{MC}(x, y)$ as illustrated in Equation 6.4. Furthermore, as shown for the idealised DBT geometry, results employing the conventional convolution approach, which uses thickness dependent scatter kernels $K_{\phi,t,G}$, were compared with results using the approach suggested in this work, $K_{\phi,t,G,AG}$, for a realistic DBT geometry.

Figure 6.24 illustrates the error maps for the $22mm$ thick breast phantom. A bipolar colourmap was used to illustrated the change in signs across the breast phantom projection. Results from the conventional convolution approach (top row), which uses thickness dependent scatter kernels, were compared with the scatter images when using the convolution approach suggested in this work (bottom row).

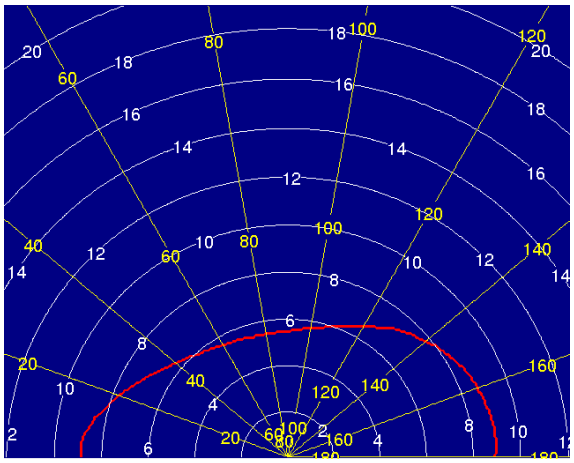

Figure 6.23: X-ray incident angles (white circular lines, in degrees) and incident direction (yellow lines, in degrees) calculated for a projection angle of 0^o. Note that the X-ray source is located where all the yellow lines converge. The contour of the 5cm thick breast phantom is shown in red.

In order to understand the magnitude of the errors observed in Figure 6.24, the histogram of the errors for each of the images is shown in Figure 6.25. In this figure, the histogram of the errors from the conventional convolution approach (left column) can be compared with the histogram of the errors from the convolution approach suggested in this work (right column), where a thickness and air gap dependent scatter kernel is used. Each of the rows corresponds, from top to bottom, to the projection angles of 0, 7.5 and 25^o.

The scattered radiation estimated from both the conventional and the proposed convolution illustrated similar performance, and no large reduction of errors is observed when accounting for the air gap (proposed in this work). This is observed in Table 6.5, where the percentages of the projected breast area with errors less than 10% for both methodologies are presented. The reason of this behaviour was the very thin breast phantom used ($22mm$), where the air gaps between the breast phantom and the breast support were small. Thus, the improvement observed when accounting for the air gap was minimum.

Table 6.5: Percentage of the projected breast phantom area with errors equal or less than 10% (target) when using the conventional scatter kernels and the scatter kernels proposed in this work. Results for the $22mm$ thick breast phantom and the projection angles studied are shown. Last row corresponds to the difference between both methodologies.

Method	0^o	7.5^o	25^o
Conventional	97%	100%	95%
This work	98%	100%	97%
Difference	0%	0%	2%

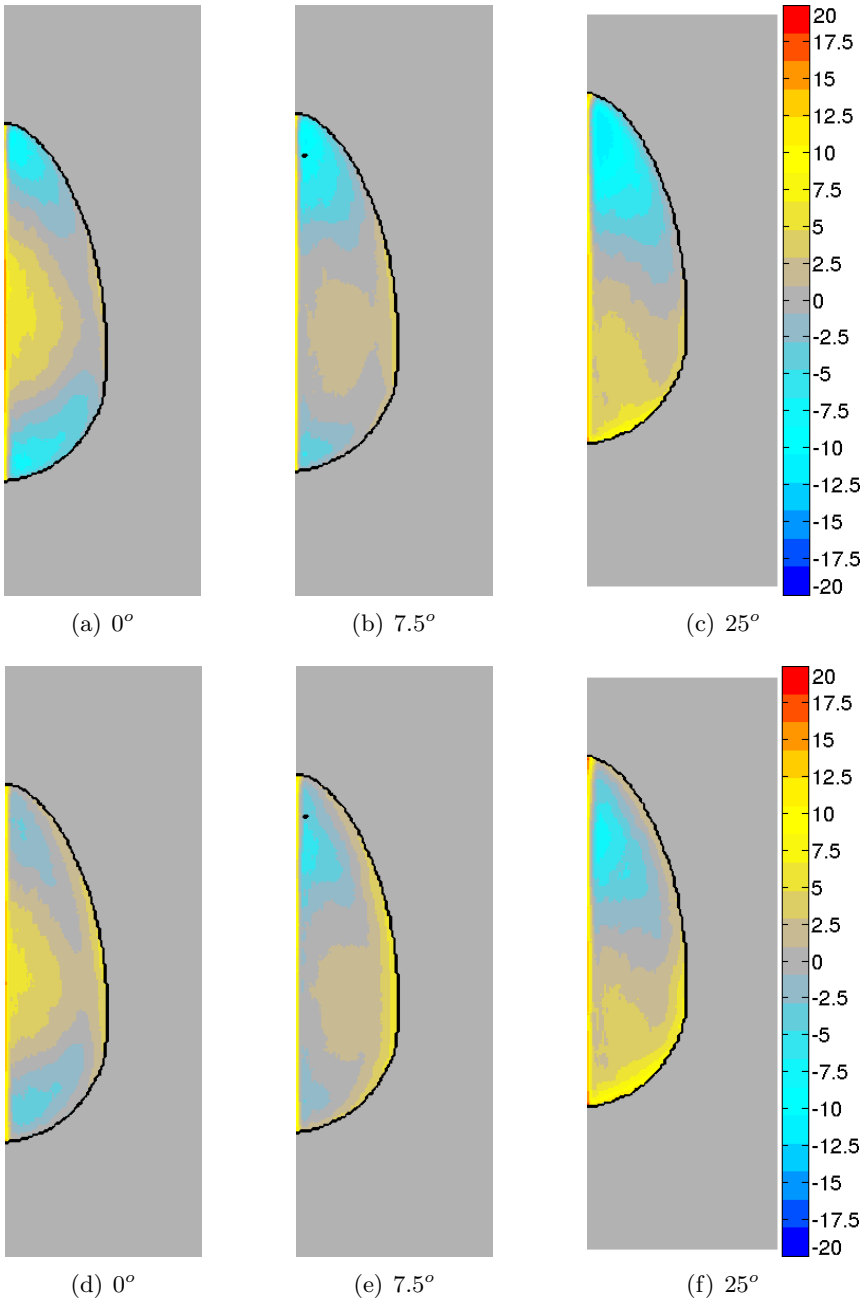

(a) 0^o (b) 7.5^o (c) 25^o

(d) 0^o (e) 7.5^o (f) 25^o

Figure 6.24: Relative error scatter map $\epsilon_S(x, y)$ observed for the 22mm thick breast phantoms (G=30%) and projection angles of 0, 7.5 and 25^o. Top row illustrates results using the conventional approach of breast thickness (Th) dependent scatter kernels. The results using the approach proposed in this work (Th and AG dependent kernels) are illustrated in the bottom row. A colourmap, in %, shows errors between less than -20 and greater than 20%. The edge of the breast phantoms is highlighted in black.

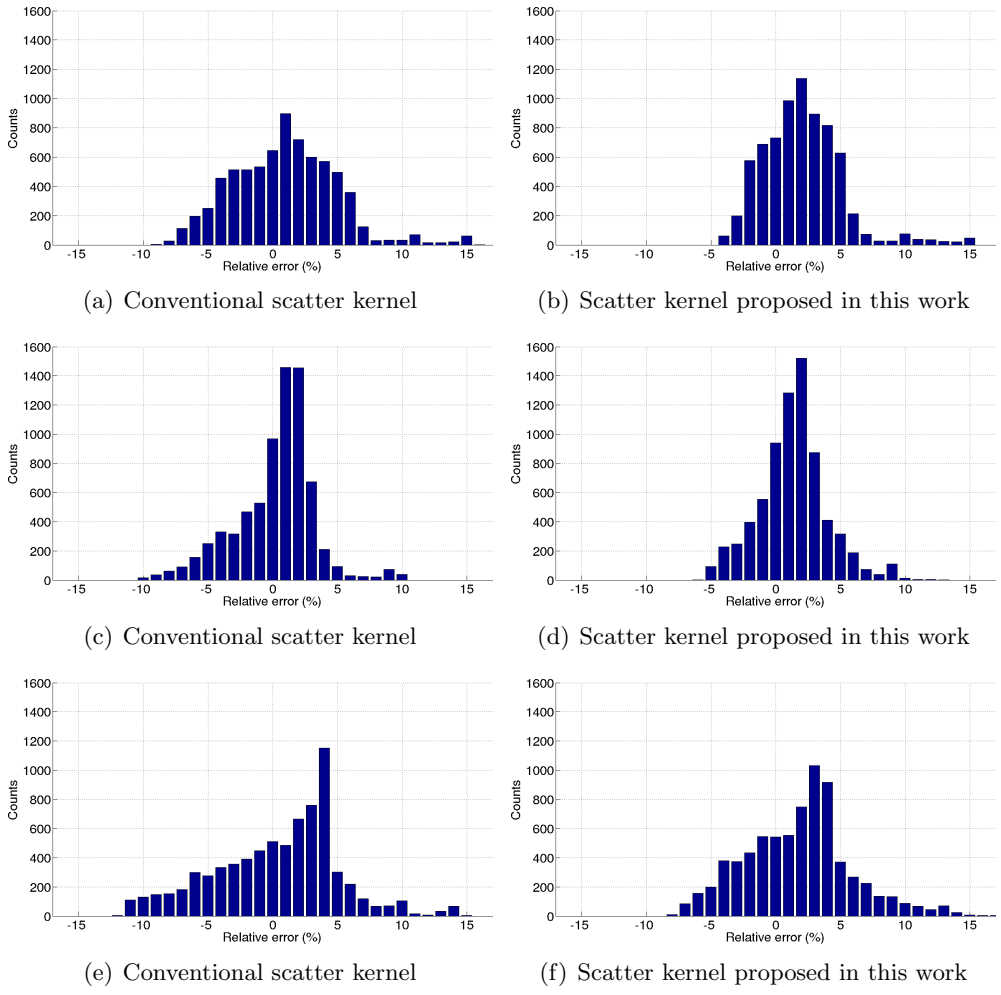

(a) Conventional scatter kernel (b) Scatter kernel proposed in this work

(c) Conventional scatter kernel (d) Scatter kernel proposed in this work

(e) Conventional scatter kernel (f) Scatter kernel proposed in this work

Figure 6.25: Histograms of the relative error scatter maps $\epsilon_S(x, y)$ observed for the 22mm thick breast phantoms (G=30%) shown in Figure 6.24. Top, middle and bottom row illustrate results for 0^o, 7.5^o and 25^o. The left column represents the histogram for the conventional approach of breast thickness (Th) dependent scatter kernels, whereas the right column shows the histogram using the approach proposed in this work (Th and AG dependent kernels).

Scatter error maps for the $50mm$ thick breast phantom are shown in Figure 6.26 and the corresponding histograms of the errors are illustrated in Figure 6.27. In this case, the conventional convolution starts to show large overestimation of scatter (dark blue area) as the air gap increases. As shown previously for the idealised DBT geometry, when the air gap distance between the breast phantom and the breast support is taken into account, these errors are largely reduced as observed in the bottom row of Figure 6.26. In the histograms is observed how errors as large as 30% are reduced to no more than 15% approximately.

Furthermore, this is reflected in the increase of the breast phantom area with errors

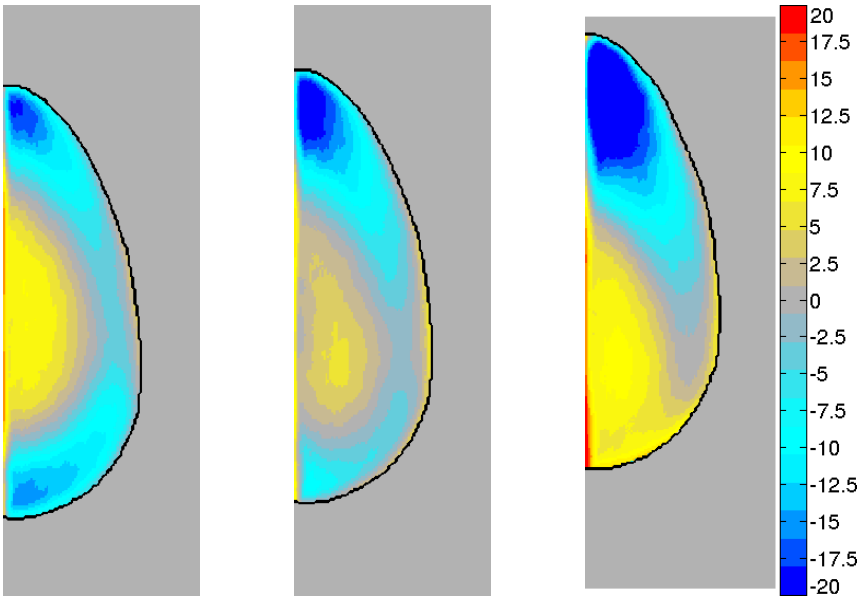

(a) 0^o (b) 7.5^o (c) 25^o

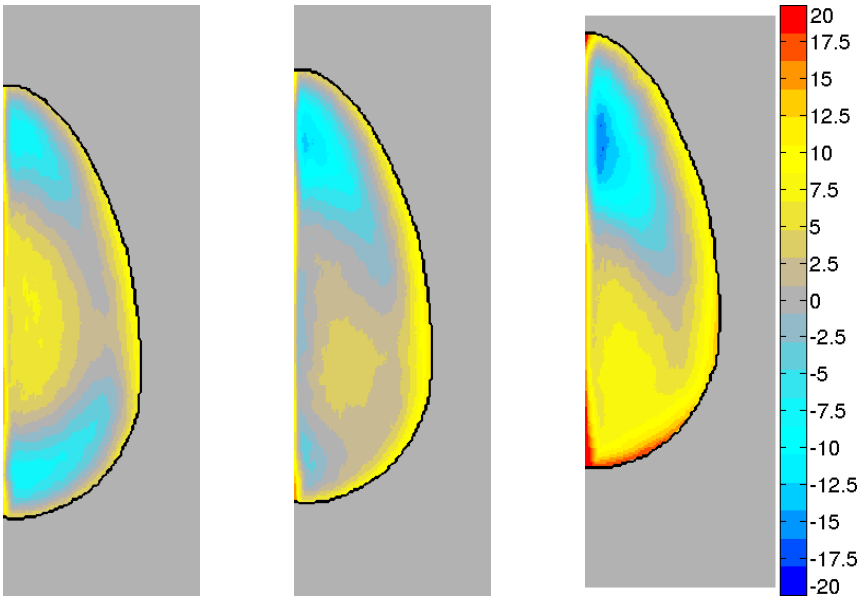

(d) 0^o (e) 7.5^o (f) 25^o

Figure 6.26: Relative error scatter map $\epsilon_S(x, y)$ observed for the 50mm thick breast phantoms (G=20%) and projection angles of 0, 7.5 and 25^o. Top row illustrates results using the conventional approach of breast thickness (Th) dependent scatter kernels. The results using the approach proposed in this work (Th and AG dependent kernels) are illustrated in the bottom row. A colourmap, in %, shows errors between less than -20 and greater than 20%. The edge of the breast phantoms is highlighted in black.

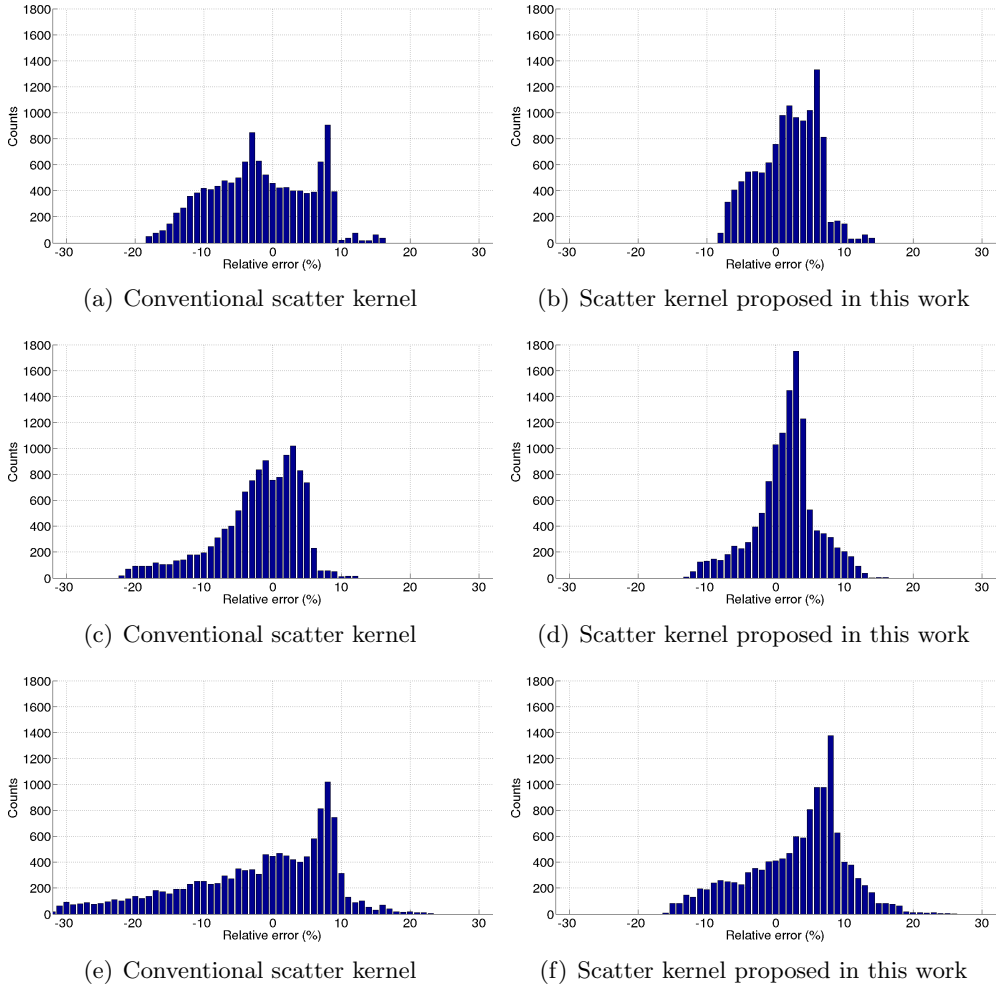

(a) Conventional scatter kernel (b) Scatter kernel proposed in this work

(c) Conventional scatter kernel (d) Scatter kernel proposed in this work

(e) Conventional scatter kernel (f) Scatter kernel proposed in this work

Figure 6.27: Histograms of the relative error scatter maps $\epsilon_S(x, y)$ observed for the 50mm thick breast phantoms (G=20%) shown in Figure 6.26. Top, middle and bottom row illustrate results for 0^o, 7.5^o and 25^o. The left column represents the histogram for the conventional approach of breast thickness (Th) dependent scatter kernels, whereas the right column shows the histogram using the approach proposed in this work (Th and AG dependent kernels).

equal or less than the target of 10% as illustrated in Table 6.6. It is observed that such area is increased by 18, 8 and 11% when imaging the $50mm$ thick breast phantom at 0, 7.5 and 25^o respectively.

The relative error maps for the $93mm$ thick breast phantom are illustrated in Figure 6.28 and their associated histograms are presented in Figure 6.29. This breast phantom represents the thickest phantom studied in this work, therefore the aforementioned air gaps are the largest of all the breast phantoms.

The thickness dependent scatter kernels (conventional convolution approach) show large errors (up to 60%) at the edges of the breast phantom (dark blue), where the air gap is

Table 6.6: Percentage of the projected breast phantom area with errors equal or less than 10% (target) when using the conventional scatter kernels and the scatter kernels proposed in this work. Results for the $50mm$ thick breast phantom and the projection angles studied are shown. Last row corresponds to the difference between both methodologies.

Method	0^o	7.5^o	25^o
Conventional	81%	87%	71%
This work	99%	95%	82%
Difference	18%	8%	11%

larger. These errors increase with projection angle as the air gap also increases. These air gaps allow the X-ray photons to travel further distances before being absorbed within the image receptor. Thus, scatter kernels which do not account for the air gaps produce more scattered radiation in the regions where the air gaps exits. However, the proposed thickness and air gap dependent scatter kernels, reduce the errors in these regions considerably.

This reduction is observed in Table 6.7, where an increase in the area of the projected breast phantom with errors equal or less than 10% is shown when accounting for this air gap.

Table 6.7: Percentage of the projected breast phantom area with errors equal or less than 10% (target) when using the conventional scatter kernels and the scatter kernels proposed in this work. Results for the $93mm$ thick breast phantom and the projection angles studied are shown. Last row corresponds to the difference between both methodologies.

Method	0^o	7.5^o	25^o
Conventional	48%	37%	45%
This work	95%	89%	63%
Difference	47%	52%	18%

As mentioned at the beginning of the chapter, the convolution methodology was investigated in the search of a faster approach than MC simulations to estimate scattered radiation. MC simulations needed between 8 to 10 hours per projection to estimate the scatter field using a 2.2 GHz Intel Quad-Core E5520 processor. On the other hand, the convolution-based methodology described in this work took between 30 to 45 minutes per projection, depending on the size of the breast phantom, using the previously described processor. It was found that most of the computational time was spent in calculating the weighting map α (Equation 6.11). This reduction in time (compared with MC) was achieved after the pre-calculation of the scatter kernels and grouping regions of similar thickness and air gap during the convolution as explained previously.

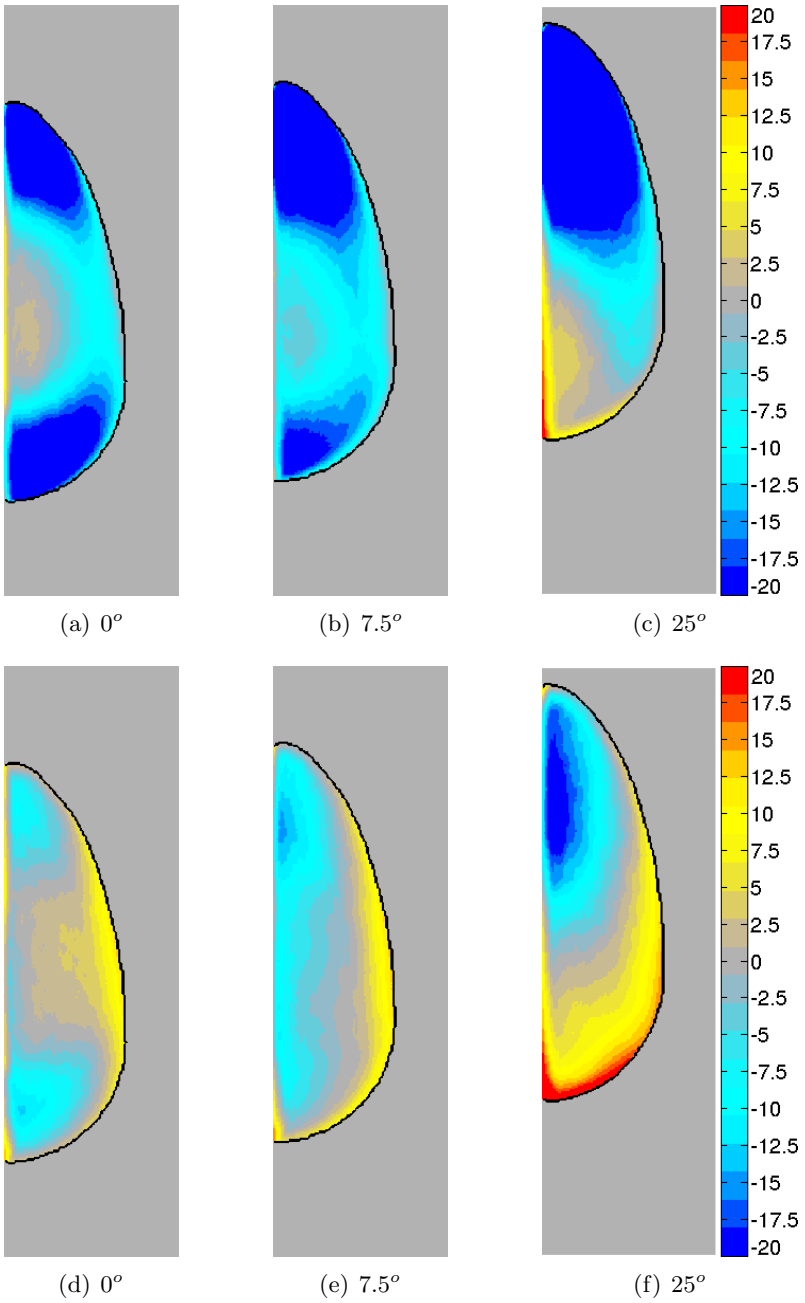

(a) 0^o (b) 7.5^o (c) 25^o

(d) 0^o (e) 7.5^o (f) 25^o

Figure 6.28: Relative error scatter map $\epsilon_S(x, y)$ observed for the 93mm thick breast phantoms (G=9.6%) and projection angles of 0, 7.5 and 25^o. Top row illustrates results using the conventional approach of breast thickness (Th) dependent scatter kernels. The results using the approach proposed in this work (Th and AG dependent kernels) are illustrated in the bottom row. A colourmap, in %, shows errors between less than -20 and greater than 20%. The edge of the breast phantoms is highlighted in black.

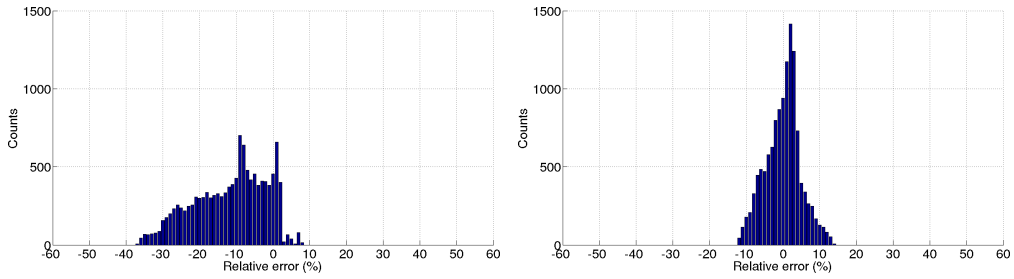

(a) Conventional scatter kernel (b) Scatter kernel proposed in this work

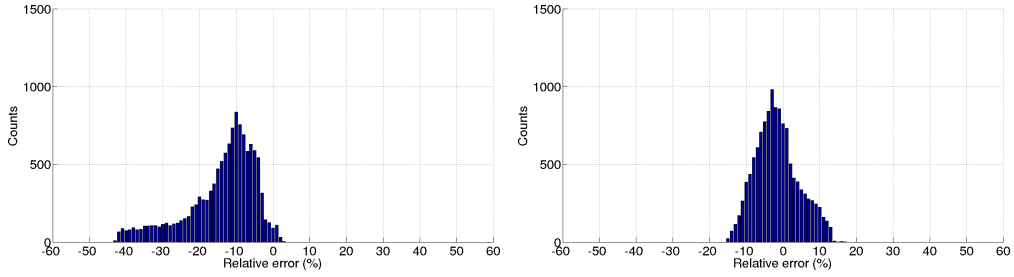

(c) Conventional scatter kernel (d) Scatter kernel proposed in this work

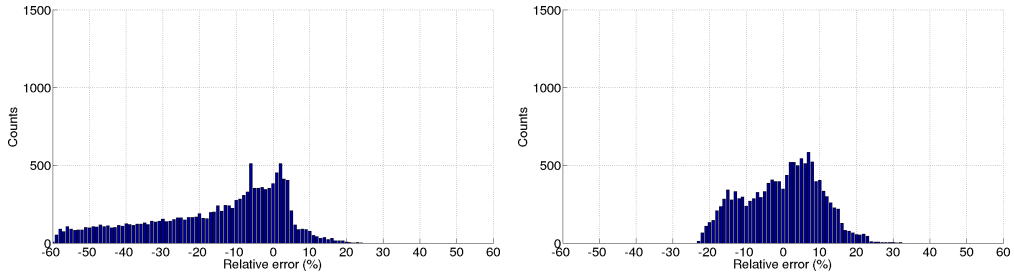

(e) Conventional scatter kernel (f) Scatter kernel proposed in this work

Figure 6.29: Histograms of the relative error scatter maps $\epsilon_S(x, y)$ observed for the 93mm thick breast phantoms (G=9.6%) shown in Figure 6.28. Top, middle and bottom row illustrate results for 0^o, 7.5^o and 25^o. The left column represents the histogram for the conventional approach of breast thickness (Th) dependent scatter kernels, whereas the right column shows the histogram using the approach proposed in this work (Th and AG dependent kernels).

6.3 Summary and discussion

Most DBT systems do not employ an anti-scatter grid, thus the levels of scattered radiation in the detector are higher than those observed in FFDM. This fact requires a good understanding of the scatter signal for each of the projections, which can be used to estimate the appropriate amount of scatter in the projected images.

MC simulations have represented the conventional approach to study scattered radiation in this work. However, it was found these are very time consuming and several hours will be needed to estimate the appropriate scatter field for each of the projections.

As a consequence, a faster approach to estimate scattered radiation is desired.

The convolution-based approach is widely used in the literature to calculate the scatter field in X-ray mammography. It estimates the scatter by convolving the primary image with the appropriate scatter kernel, which varies across the images based on the thickness of the breast.

One of the principal limitations of the convolution-based approach found in the literature has been the highly idealised objects used. When this 'conventional' approach was studied for a series of anthropomorphic breast phantoms using an idealised geometry, it was found that it overestimates the scattered radiation at the edges of the breast phantom. This effect gets worse with increasing projection angle. A further examination using simple phantoms (uniform, trapezoidal and hexagonal) demonstrated that this overestimation of scattered radiation is mainly due to the air gap between the lower surface of the object and the detector.

For this reason, the convolution approach was modified in order to account for this air gap, demonstrating an improvement in the scatter estimation when using realistic breast phantoms.

Then, the proposed convolution-based approach was adapted for a realistic DBT geometry, which include the compression paddle and breast support. In this new geometry, the scatter from the system was also taken in to account. Results showed that the convolution-based approach suggested in this work, can estimate the scattered radiation within a 10% error across most of the breast area. Furthermore, the computation time was reduced from the 8 to 10 hours observed in MC simulations to less than 1 hour per projection when using the proposed convolution approach [1].

[1] Using a 2.2GHz Intel Quad-Core E5520 processor.

Chapter 7

Conclusions and Further Work

As was mentioned at the start of this thesis, X-ray mammography technologies are in constant development and, as such, manufacturers release new systems faster than the rate at which these can be reliably assessed using conventional clinical trials. To address this, image simulation framework might be developed, that would facilitate a faster rate of assessment, thus representing a powerful approach to test such systems without the radiation burden associated with using human subjects. However, in order to simulate such images, or imaging systems, the scatter field must be accurately modelled as this radiation might influence breast cancer detection performance. As such, this has been the main focus of the work contained in this thesis. Furthermore, accurate modelling of the scatter field, particularly where no anti-scatter grid exists, would help to understand the specific distribution of this type of radiation and its effect on image quality, and so, can be used to improve the design in future imaging systems. Moreover, knowledge of this scatter field distribution can also be employed in clinical imaging in the development of post-processing algorithms for scatter correction.

Thus, the main conclusions of this work after modelling scatter fields in several planar X-ray mammography and DBT systems are drawn together and presented in this chapter. These are followed by a summary of proposed further work based on the conclusions of this thesis.

7.1 Conclusions

Although GEANT4 was originally designed to simulate interaction of particles with matter at high energies, it has also been proposed that it may usefully be applied in the X-ray mammography energy range using its low energy packages [78, 82, 153, 154]. Therefore, GEANT4 was validated against experimental and published data with a maximum discrepancy of 4% and thus represents a suitable MC simulation toolkit to use in X-ray mammography, in accord with the findings published elsewhere.

In Chapter 5, GEANT4 was used to generate SPR maps using a CDMAM phantom geometry for three planar X-ray mammography systems currently available: Hologic Selenia Dimensions, GE Essential and Siemens Mammomat 3000. It can be concluded,

perhaps unsurprisingly, that, as they all include anti-scatter grids, SPR values of less than 0.2 were observed across the CDMAM phantom area. For a $40mm$ thick PMMA block and the CDMAM phantom, the amount of scatter recorded within the image receptor ranged from 6% to 17%, depending on the particular anti-scatter grid design employed by each manufacturer. As expected, the cellular anti-scatter grid design used by the Hologic Selenia system illustrated higher CIF (1.60) compared with linear designs (1.50). This is attributed to the low density material employed (air for interspace and copper for the septa) which increases the primary transmission, as well as its cellular design which reduces the scatter transmission. This suggests that further investigation can be undertaken to explore the use of other materials and designs of the anti-scatter grid geometry as will be described in the next section.

In the same chapter, a CDMAM image simulation tool [18], which assumed constant scatter across the image, was modified to account for a more accurate scatter distribution calculated from MC simulations, using the X-ray mammography systems described above. This new design also attempted to reduce the dependency on clinical measurements as the scatter field was previously measured experimentally. These results demonstrated that the scatter field does not vary significantly across the CDMAM phantom area as the anti-scatter grid absorbs most of the scattered radiation. However, when linear anti-scatter grids are used, scatter increases up to 10% in the first few millimetre within the phantom due to the increase of scattered X-photons from the compression paddle and breast support. For the cellular grid design, no increase in scatter due to the system was observed. It can be concluded that when an object of uniform thickness, such as a PMMA block, is imaged in planar X-ray mammography systems (using the anti-scatter grid), a simple constant offset value to account for the scatter field can be safely assumed in regions far from the edge of the object, the value of which depends on particular system geometry.

In DBT, as anti-scatter grids are not typically employed, the SPR values observed within the image receptor were expected to be larger and vary more rapidly across the field of view than in planar X-ray mammography. For thick breasts, SPR values of 1 or larger have been reported in the literature, especially as the projection angle increases. Furthermore, the contribution of the scattered radiation from the system has been reported to be as large as a third of the total scattered radiation at the edges of the breast [82].

Despite excellent performance can be achieved in modelling physical processes using MC simulations, this approach has been shown to be very extremely consuming. As single projection simulations may take up to 10 hours to execute with a SEM in scatter of 0.25%, and DBT systems require a large number of such projections of the breast (15 for Hologic Selenia), a faster kernel-based alternative was explored in Chapter 6 to more effectively estimate such scattered radiation distribution. Although the DBT system studied here approximates the Hologic Selenia system, it is anticipated that the methodology proposed in Chapter 6 could be extrapolated to other DBT systems.

The fixed convolution-based approached described in the literature [19, 20, 21, 22, 23, 24, 25] was evaluated using a range of simulated breast phantoms. Despite good agreement found between the convolution-based and MC-based results in the central region of the breast phantom, where the phantom thickness is constant, large discrepancies

(approximately 60%) were observed at the edges of these breast phantoms. An exhaustive study revealed, for the first time, that the air gap between the lower curvature of the breast phantom and the detector was the main source of the aforementioned discrepancies. Surprisingly, this effect has not been previously investigated in the literature. This phenomena is due to the limitations of the idealised objects previously used by other authors, where D-shape phantoms with perpendicular boundaries were typically employed to approximate the female breast. Furthermore, this is the first time the convolution-based approach is proposed for use in DBT geometries. In such situations the distribution of scattered radiation can have greater variation across the image receptor compared to FFDM and thus requires more detailed analysis.

In order to account for the aforementioned thickness-dependent errors, new scatter kernels, which account for both breast thickness and air gap distances, were proposed for three different breast phantoms representative of the range of breast thicknesses and glandularities found in breast screening populations. Furthermore, scattered radiation emanating from the imaging system itself was also considered in order to improve the overall performance. Thus, the approach proposed here has shown good agreement with MC-based calculations of scattered radiation distributions: the projected breast area with errors less than 10% error improved by up to 39% using this new approach of the thickness dependent-only kernel-based approach. Therefore, it is proposed that to accurately model the scattered radiation in X-ray systems where anti-scatter grids are absent (i.e. DBT or dedicated breast CT), a realistic geometry of both the system and the imaging object is required to account for all the major scattering processes (previously been neglected in the literature).

Thus, following detailed validation on the use of GEANT4 for X-ray mammography, the main achievements contained in this thesis are:

- An examination of different anti-scatter geometries employed by three conventional X-ray mammography systems demonstrated that the use of cellular anti-scatter grids reduces the scattered radiation by almost a factor of three, improving the contrast in the image by 6% and that such an approach might guide future development in this area.
- Confirmation by MC simulation that a simple scatter offset value was sufficient to account for scatter effects in imaging the CDMAM phantom when using anti-scatter grids. Results illustrated an overall average error of 1% in the associated contrast detailed curves when compared with experimental data.
- The discovery of air gap dependent scatter effects towards the edge of the breast, and the subsequent development of a kernel-based method to produce a fast non-MC method of scatter field estimation. This has also included, for the first time in a kernel-based method, the separation of system-based and breast-based scatter components, and demonstrates that although system-based scatter produces approximately 10% of the total scatter, in regions close to the curved breast edge, the contribution from the system-based scatter can increase up to 30%. This approach can produce scatter maps with less than 10% error in the majority of the projected breast phantom area (63-100%) 10 times faster than the time needed to conduct a MC simulation.

7.2 Further Work

Having modelled the scattered distribution in planar X-ray mammography and DBT, several interesting aspects may be explored further that directly arise from the assumptions used in this work, and moreover, present themselves as arising from the results produced here.

In this work, MC simulations were used to study the scatter rejection performance of three commercially available anti-scatter grids for planar X-ray mammography systems. Results were presented for a particular energy spectrum per imaging system and one breast thickness. It would be interesting to extend this to a wider range of breast (or PMMA) thicknesses and energy spectra as this may reveal if cellular anti-scatter grids outperform the linear designs in a larger number of cases. It would also be of interest to investigate other anti-scatter grid materials and geometries to reduce the scattered radiation even further. These may include an optimisation of the size of the interspace in the cellular grid, the septa thickness or even a revolutionary cellular grid where the septa increases towards the breast edge.

With respect to DBT systems, there is a large interest in accurate scatter field estimation [82, 123, 129]. The scatter kernel approach proposed in this work for a realistic DBT geometry was tested using three representative anthropomorphic breast phantoms developed by Bakic et al. [52]. Although other breast phantom models are available [49, 51, 195], it has been seen in this work that the scattered radiation is highly dependent on the breast curvature shape, which is associated to the breast composition: denser breast will have more symmetrical curvature than adipose breasts. For this reason, it would be useful to quantify actual compressed breast curvatures in clinical scenarios. This can be undertaken using recently developed low cost 3D depth camera technology, such as the Microsoft Kinect [196, 197].

One of the assumptions made in this work when estimating the scattered radiation using the convolution-based methodology, was that the incidence angle of all X-ray photons within the breast phantom area were the same (i.e. projection angle). This assumption can be true for a 0^o projections angle as described by Boone and Cooper [19]. However, variations of the X-ray photon incident angles up to 30% are seen for large projection angles (25^o). Thus, examining the effects of this assumption on the propagated errors in the resulting scatter field estimates would be useful. Furthermore, it would be also interesting to modify the methodology describe here to independently calculate the scatter response function from the breast phantom, compression paddle and breast support, and combine these together to produce the overall scatter field estimation. However, introducing further complexity inevitably impacts on execution time, so that at some point the run-time advantage of a kernel-based approach will become marginal compared to using a MC-based approach.

Appendix A

Abbreviations and Acronyms

- **2D**: two dimensional
- **3D**: three dimensional
- **μm**: micrometer
- **ACRIN**: American College of Radiology Imaging Network
- **AEC**: automatic exposure control
- **AG**: air gap
- **BF**: Bucky factor
- **CD** contrast-detail
- **CDMAM**: Contrast Detail MAMmography
- **CERN**: European Organization for Nuclear Research
- **CIF**: contrast improvement factor
- **cm**: centimeter
- **CNR**: contrast-to-noise ratio
- **CR**: computerised radiography
- **CRUK**: Cancer Research UK
- **CT**: computed tomography
- **CW**: chest wall
- **DAVID**: DAWN-based Visual Volume Intersection Debugger
- **DAWN**: Drawer for Academic WritiNgs
- **DBT**: digital breast tomosynthesis

- **DMIST**: Digital Mammography Imaging Screening Trial
- **DR**: digital radiography
- **ESD**: edge spread device
- **ESF**: edge spread function
- **FDA**: Food and Drug Administration
- **FFDM**: full-field digital mammography
- **FFT**: fast Fourier transform
- **FOV**: field of view
- **FPD**: flat panel detector
- **G**: glandularity
- **GE**: General Electric
- **GATE**: GEANT4 Application for Tomographic Emission
- **HTC**: high transmission cellular
- **HVL**: half value layer
- **IARC**: International Agency for Research in Cancer
- **ID**: indirect radiography
- **keV**: kilo electron volts
- **kVp**: kilo voltage peak
- **LSF**: line spread function
- **mm**: millimeter
- **MC**: Monte Carlo
- **MGD**: mean glandular dose
- **MTF**: modulation transfer function
- **NHS**: National Health Service
- **NHSBSP**: NHS Breast Screening Programme
- **NIST**: National Institute of Standards and Technology
- **NNPS**: normalised noise power spectrum
- **PET**: positron emission tomography
- **PMMA**: polymethyl methacrylate

- **PRNG**: pseudo-random number generator
- **PSF**: point spread function
- **ROI**: region of interest
- **SDD**: source-to-detector distance
- **SEM**: standard error of the mean
- **SF**: scatter fraction
- **SFR**: screen-film receptor
- **SNR**: signal-to-noise ratio
- **SNR**$_d$: differential SNR
- **SPECT**: single-photon emission computed tomography
- **SPR**: scatter-to-primary ratio
- **SPSF**: scatter point spread function
- **T**: thickness
- **T**$_p$: transmission of primary
- **T**$_s$: transmission of scatter
- **TFT**: thin-film transistor
- **VRML**: virtual reality modeling language
- **Z**: atomic number

Appendix B

Anatomy of the female breast

A mature female breast has a hemispheric shape and its tissue is composed mainly of variable proportions of glandular and adipose (or fatty) tissue. This distribution is maintained by hormonal influences of menstrual cycles until the menopause, where the glandular tissue decreases and is replaced by adipose tissue [198]. The breast has no muscle and is covered by a thin layer of skin. Furthermore, suspensory ligaments (Cooper's ligaments) are found to support the breast between the skin and the chest wall.

In terms of glandular tissue, each breast contains a mammary gland with between 15 to 20 lobes [4], each of which contains hundreds of tiny lobules where milk is produces when a woman is breast-feeding. During lactation, the breast can increased 3 or 4 times its normal weight [198] and milk flows from the lobules through the lactiferous ducts and lactiferous sinus ending at the centre of the areola, the nipple.

Figure B.1 illustrates a sagittal view of the breast described above in schematic form, where the most important components of the breast are highlighted.

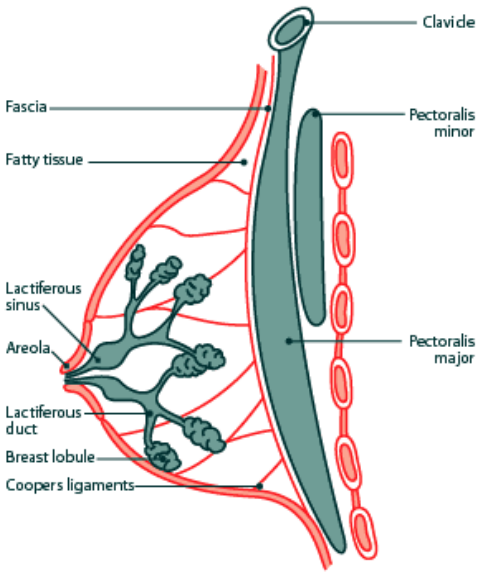

Figure B.1: Anatomy of a typical female breast. Image taken from [199].

Appendix C

Relative error maps using an idealised DBT geometry

In this appendix, results for the experiments described in Section 6.1 are illustrated for a $5cm$ thick breast phantom and projection angle of 7.5°; and $7.5cm$ thick breast phantom and projection angles of 0°, 7.5° and 25°.

C.1 5cm thick beast phantom and projection angle 7.5^o

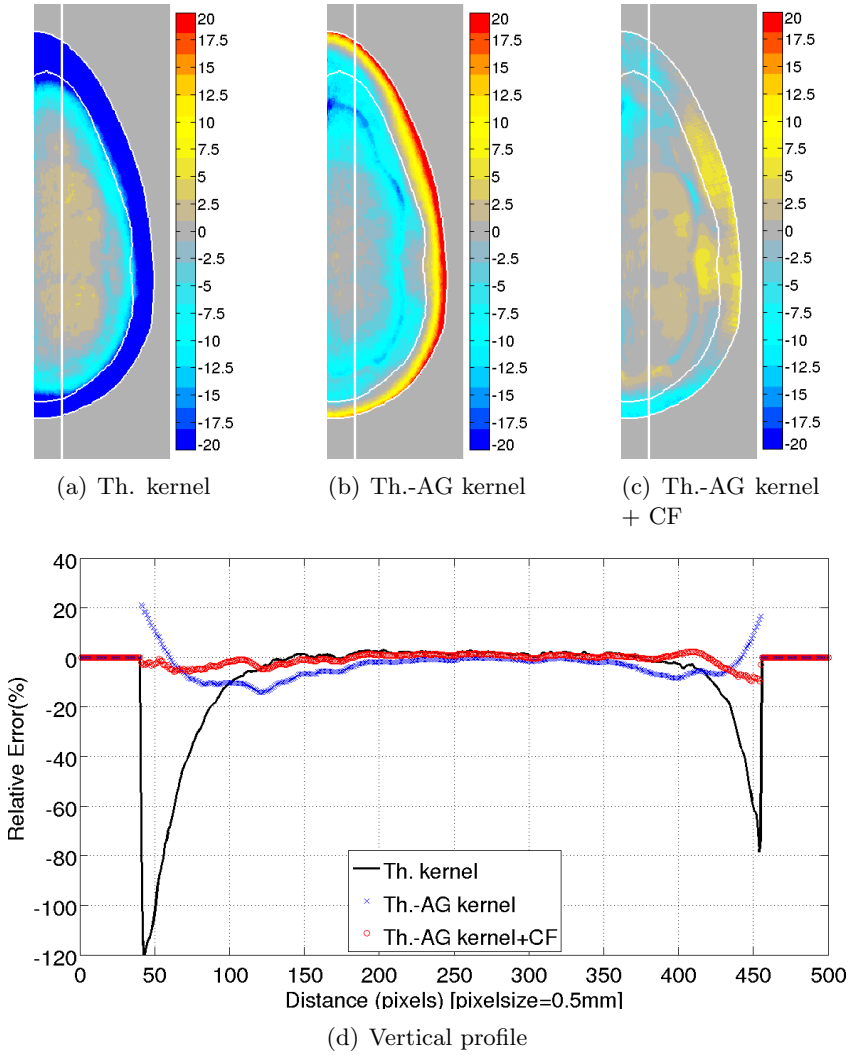

(a) Th. kernel (b) Th.-AG kernel (c) Th.-AG kernel + CF

(d) Vertical profile

Figure C.1: Relative error scatter map $\epsilon_S(x, y)$ observed within a $5cm$ thick breast phantom and ϕ=7.5^o for estimated scatter using the (a) thickness-dependent, (b) thickness and air gap dependent scatter kernels and (c) thickness and air gap dependent scatter kernels and CF. Note that errors are illustrated using a bipolar colormap, in %, showing errors between lower than -20% and greater than 20%. Edges where the air gap starts as well as the edge region of the breast phantom are highlighted in white. The profile along the vertical white line for the thickness-dependent (Th. kernel), thickness and air gap dependent (Th.-AG kernel) and Th.-AG kernel with correction factors (Th.-AG kernel+CF) scatter kernels are shown in (d).

C.2 7.5cm thick beast phantom and projection angle 0^o

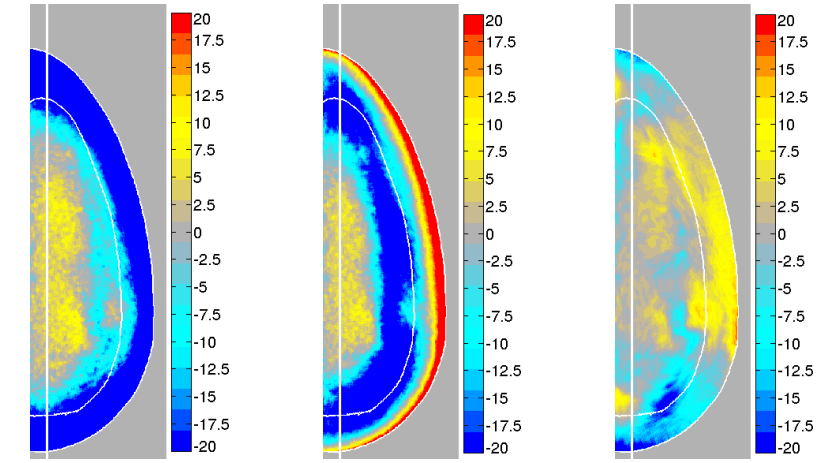

(a) Th. kernel (b) Th.-AG kernel (c) Th.-AG kernel + CF

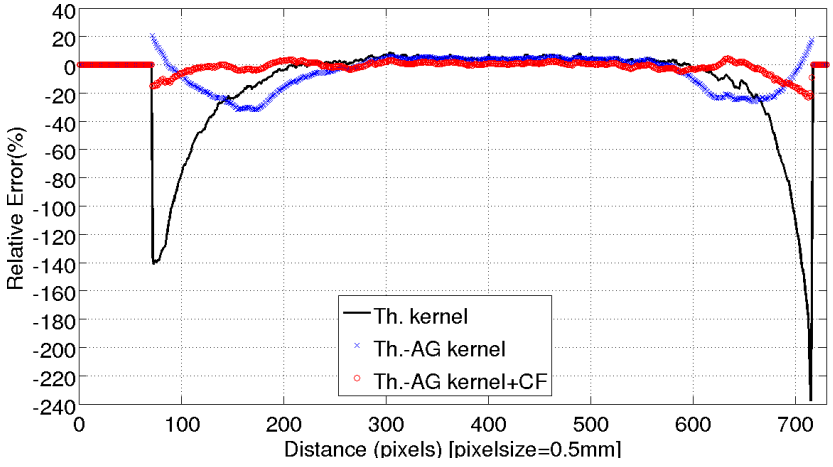

(d) Vertical profile

Figure C.2: Relative error scatter map $\epsilon_S(x, y)$ observed within a 7.5cm thick breast phantom and ϕ=0^o for estimated scatter using the (a) thickness-dependent, (b) thickness and air gap dependent scatter kernels and (c) thickness and air gap dependent scatter kernels and CF. Note that errors are illustrated using a bipolar colormap, in %, showing errors between lower than -20% and greater than 20%. Edges where the air gap starts as well as the edge region of the breast phantom are highlighted in white. The profile along the vertical white line for the thickness-dependent (Th. kernel), thickness and air gap dependent (Th.-AG kernel) and Th.-AG kernel with correction factors (Th.-AG kernel+CF) scatter kernels are shown in (d).

C.3 7.5cm thick beast phantom and projection angle 7.5^o

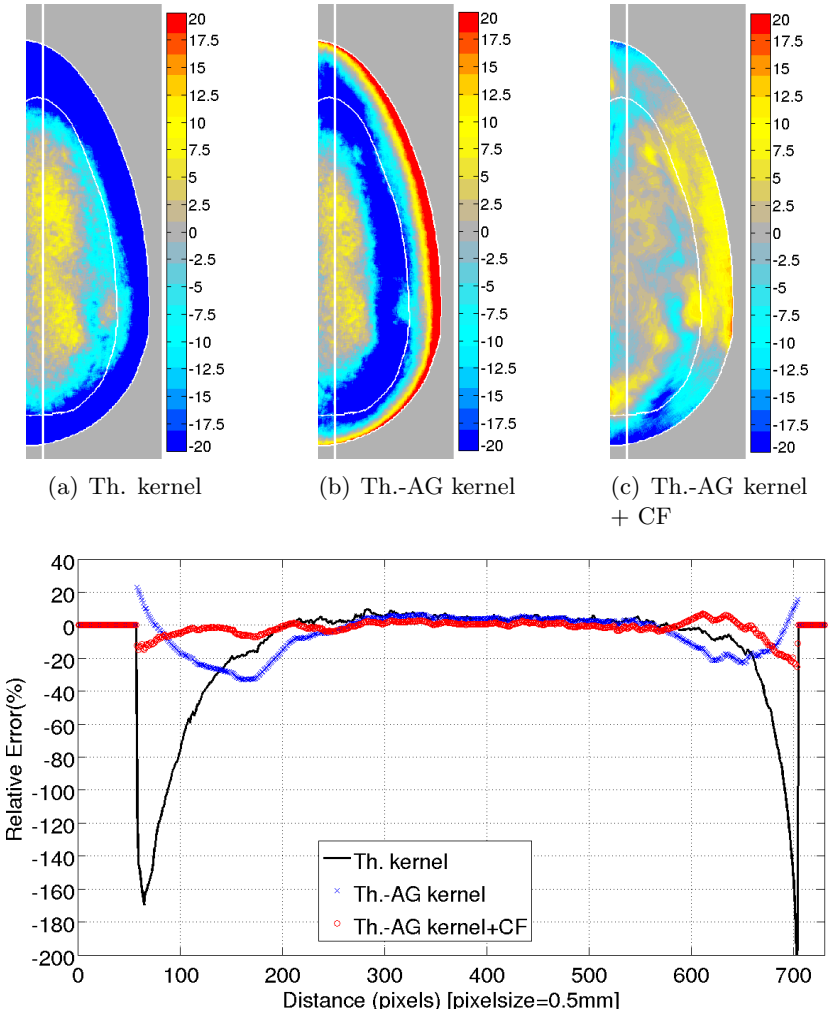

(a) Th. kernel (b) Th.-AG kernel (c) Th.-AG kernel + CF

(d) Vertical profile

Figure C.3: Relative error scatter map $\epsilon_S(x, y)$ observed within a $7.5cm$ thick breast phantom and ϕ=7.5^o for estimated scatter using the (a) thickness-dependent, (b) thickness and air gap dependent scatter kernels and (c) thickness and air gap dependent scatter kernels and CF. Note that errors are illustrated using a bipolar colormap, in %, showing errors between lower than -20% and greater than 20%. Edges where the air gap starts as well as the edge region of the breast phantom are highlighted in white. The profile along the vertical white line for the thickness-dependent (Th. kernel), thickness and air gap dependent (Th.-AG kernel) and Th.-AG kernel with correction factors (Th.-AG kernel+CF) scatter kernels are shown in (d).

C.4 7.5cm thick beast phantom and projection angle 25^o

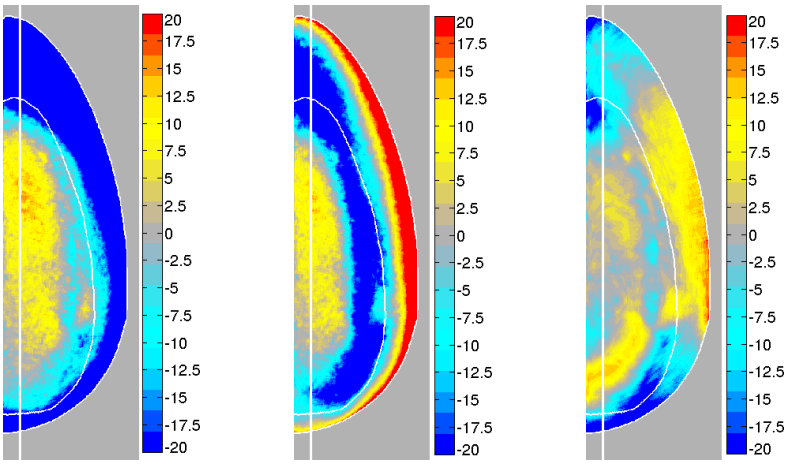

(a) Th. kernel (b) Th.-AG kernel (c) Th.-AG kernel + CF

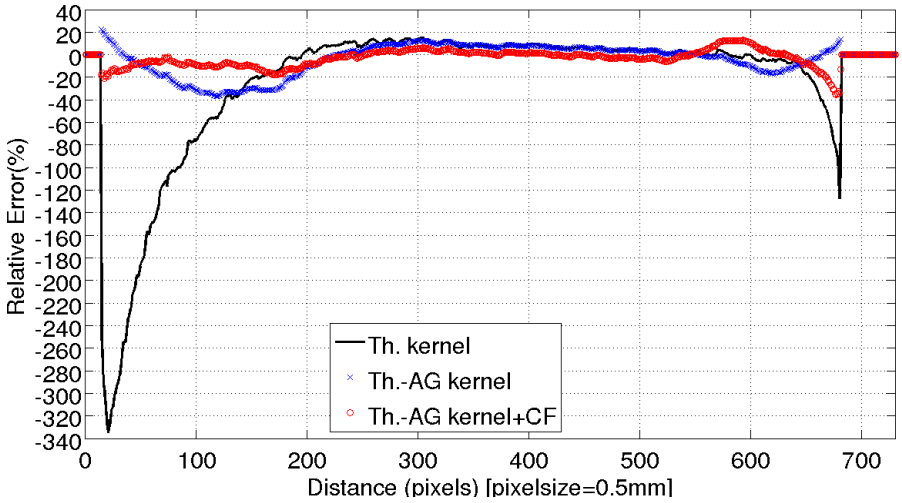

(d) Vertical profile

Figure C.4: Relative error scatter map $\epsilon_S(x, y)$ observed within a 7.5cm thick breast phantom and ϕ=25^o for estimated scatter using the (a) thickness-dependent, (b) thickness and air gap dependent scatter kernels and (c) thickness and air gap dependent scatter kernels and CF. Note that errors are illustrated using a bipolar colormap, in %, showing errors between lower than -20% and greater than 20%. Edges where the air gap starts as well as the edge region of the breast phantom are highlighted in white. The profile along the vertical white line for the thickness-dependent (Th. kernel), thickness and air gap dependent (Th.-AG kernel) and Th.-AG kernel with correction factors (Th.-AG kernel+CF) scatter kernels are shown in (d).

Appendix D

List of Publications:

The following publications have resulted from the work documented in this thesis:

Journal publications:

1. R. W. Bouwman, **O. Diaz**, R.E. van Engen, K.C. Young, G.J. den Heeten, M.J.M Broeders, W.J.H. Veldkamp and D.R. Dance. Phantoms for quality control procedures in digital breast tomosynthesis: dose assessment. *Physics in Medicine and Biology* 58 (13), pp 4423-4438, 2013.

2. A. Rashidnasab, P. Elangovan, M. Yip, **O. Diaz**, D. R. Dance, K.C. Young and K. Wells. Simulation and assessment of realistic breast lesions using fractal growth models. *Physics in Medicine and Biology* 58 (16), pp 5613-5627, 2013.

Conference publications:

1. A. Rashidnasab, P. Elangovana, **O. Diaz**, A. Mackenzie, K.C. Young, D.R. Dance and K. Wells. Simulation of 3D DLA masses in digital breast tomosynthesis. *In Proc. of SPIE Medical Imaging* 8668, 86680Y-1-9, 2013.

2. R. Bouwman, **O. Diaz**, K.C. Young, R. van Engen , W. Veldkamp, D.R. Dance. Phantoms for quality control procedures of digital breast tomosynthesis. *IWDM 2012, Lecture Notes in Computer Science* 7361, pp 322-329, 2012.

3. P. Elangovan, A. Mackenzie, **O. Diaz**, A. Rashidnasab, D.R. Dance, K.C. Young, L. M. Warren, E. Shaheen, H. Bosmans, P.R. Bakic, K. Wells. A Modelling Framework for Evaluation of 2D-Mammography and Breast Tomosynthesis systems. *IWDM 2012, Lecture Notes in Computer Science* 7361, pp 338-345, 2012.

4. A. Mackenzie, D.R. Dance, **O. Diaz**, A. Barnard, K.C. Young. Converting One Set of Mammograms to Simulate a Range of Detector Imaging Characteristics for Observer Studies. *IWDM 2012, Lecture Notes in Computer Science* 7361, pp 394-401, 2012.

5. **O. Diaz**, D.R. Dance, K.C. Young, P. Elangovan, P.R. Bakic and K. Wells. A fast scatter field estimator for digital breast tomosynthesis. *In Proc. SPIE Medical Imaging* 8313, 831305. 2012.

6. A. Rashidnasab, P. Elangovan, D.R. Dance, K.C. Young, M. Yip, **O. Diaz** and K. Wells. Realistic simulation of breast mass appearance using random walk. *In Proc. SPIE Medical Imaging* 8313, 83130L. 2012.

7. A. Rashidnasab, P. Elangovan, D.R. Dance, K.C. Young, **O. Diaz** and K. Wells. Modelling realistic breast lesions using diffusion limited aggregation. *In Proc. Medical Imaging SPIE* 8313, 83134L. 2012.

8. **O. Diaz**, M. Yip, J. Cabello, D.R. Dance, K.C. Young and K. Wells. Monte Carlo simulation of scatter field for calculation of contrast of discs in synthetic CDMAM images. *In 10^{th} International Workshop on Digital Mammography*, volume 6136, pages 628–635, Jun 2010.

Bibliography

[1] International Agency for Research on Cancer. GLOBOCAN 2008. [Online] Available: http://globocan.iarc.fr/. IARC, Lyon, France, mar 2013.

[2] Cancer Research UK. Breast cancer statistics. [Online] Available: http://www.cancerresearchuk.org/cancer-info/cancerstats/types/breast/. CRUK, London, UK, mar 2013.

[3] Office for National Statistics. Cancer incidence and mortality in the United Kingdom, 2008-10. [online] available: http://www.ons.gov.uk/ons/rel/cancer-unit/cancer-incidence-and-mortality/2008-2010/index.html. Technical report, December 2012.

[4] G.J. Tortora and B. Derrickson. *Principles of Anatomy and Physiology*. John Wiley and Sons, eleventh edition, 2006.

[5] Virtual Medical Centre. [Online] Available: http://www.virtualmedicalcentre.com., aug 2009.

[6] L. Nyström, I. Andersson, M. Bjurstam, J. Frisell, B. Nordenskjöld, and L.E. Rutqvist. Long-term effects of mammography screening: updated overview of the swedish randomised trials. *The Lancet*, 359:909–919, 2002.

[7] P. Forrest. Breast Cancer Screening. Technical report, Department of Health and Social Security, 1986.

[8] National Health Service Cancer Screening Programmes. Breast screening program for England. [Online] Available: http://www.cancerscreening.nhs.uk/breastscreen/index.html. Public Health England, mar 2013.

[9] E.D. Pisano, C. Gatsonis, E. Hendrick, M.J. Yaffe, J.K. Baum, S. Acharyya, E.F. Conant, L.L. Fajardo, L. Bassett, C. DOrsi, R. Jong, and M. Rebner. Diagnostic performance of digital versus film mammography for breast-cancer screening. *The New England Journal of Medicine*, 353(17):1773–1783, 2005.

[10] E.D. Pisano, C. Gatsonis, M.J. Yaffe, E. Hendrick, A.N.A. Tosteson, D.G. Fryback, L.W. Bassett, E.F. Baum, J.K. Conant, R.A. Jong, M. Rebner, and C.J. DOrsi. American college of radiology imaging network digital mammographic imaging screening trial: Objectives and methodology. *Radiology*, 236(2):404–412, 2005.

[11] V. Beral, S. Cush, I.O. Ellis, J. Emery, K. Faulkner, R. Given-Wilson, M Law, J. Loughlin, M.J. Michell, S.M. Moss, M. Noblet, J. Patnick, M. Reed, C. Rubin, K. Toward, and D. Winstone. Screening for breast cancer in England: Past and future. *NHSBSP Publication*, (61), 2006.

[12] J. Beutel, H.L. Kundel, and Van Metter R.L. *Handbook of Medical Imaging: Physics and Psychophysics*. SPIE Society of Photo-Optical Instrumentation Eng., Bellingham, Washington, 2000.

[13] M.R. Patel and G.J. Whitman. Negative mammographm in symptomatic patients with breast cancer. *Academic Radiology*, 5(1):26–33, 1998.

[14] N.F. Boyd, H. Guo, L.J. Martin, L. Sun, J. Stone, E. Fishell, R.A. Jong, G. Hislop, A. Chiarelli, S. Minkin, and M.J. Yaffe. Mammographic density and the risk and detection of breast cancer. *The New England Journal of Medicine*, 356:227–236, 2007.

[15] John M. et al Lewin. Clinical compararison of full-field digital mammography and screen-film mammography for detection of breast cancer. *American Roentgen Ray Society*, 179:671–677, 2002.

[16] P. Skaane, K. Young, and A. Skjennald. Population-based mammography screening: Comparison of screen-film and full-field digital mammography with soft-copy readingoslo i study. *Radiology*, 229:877–884, 2003.

[17] P. Skaane and A. Skjennald. Screen-film mammography versus full-field digital mammography with soft-copy reading: Randomized trial in a population-based screening programthe oslo ii study. *Radiology*, 232:197–204, 2004.

[18] M. Yip, A Alsager, E. Lewis, K. Wells, and K.C. Young. Validation of a digital mammography image simulation chain with automated scoring of CDMAM images. In *International Workshop on Digital Mammography*, volume 5116, pages 409–416. Springer, 2008.

[19] J.M. Boone and V.N. Cooper. Scatter/primary in mammography: Monte Carlo validation. *Medical Physics*, 27(8):1818–1831, 2000.

[20] L.A. Love and R.A. Kruger. Scatter estimation for a digital radiographic system using convolution filtering. *Medical Physics*, 14(2):178–185, 1987.

[21] J. Boone, B.A. Arnold, and J.A. Seibert. Characterization of the point spread function and modulation transfer function of scattered radiation using a digital imaging system. *Medical Physics*, 13(2):254–256, 1986.

[22] J.A. Seibert and J. Boone. X-ray scatter removal by deconvolution. *Medical Physics*, 15(4):567–575, 1988.

[23] A.H. Baydush and C.E. Floyd. Improved image quality in digital mammography with image processing. *Medical Physics*, 27(7):1503–1508, 2000.

[24] G. Wu, J.G. Mainprize, J.M. Boone, and M.J. Yaffe. Evaluation of scatter effects on image quality for breast tomosynthesis. *Medical Physics*, 36(10):4425–4432, 2009.

[25] J.L. Ducote and S. Molloi. Scatter correction in digital mammography based on image deconvolution. *Physics in Medicine and Biology*, 55:1295–1309, 2010.

[26] M.J. Berger, J.H. Hubbell, S.M. Seltzer, J. Chang, J.S. Coursey, R. Sukumar, D.S. Zucker, and K. Olsen. XCOM: Photon Cross Section Database (version 1.4). [Online] Available: `http://physics.nist.gov/xcom`. National Institute of Standards and Technology, Gaithersburg, MD, oct 2009.

[27] D.R. Dance, S.H. Evans, C.L. Skinner, and A.G. Bradley. *The Physics of Medical Imaging*, chapter Diagnostic Radiology with X-Rays. IOP Publishing Ltd, Bristol (England), 1988.

[28] M.J. Berger, J.S. Coursey, M.A. Zucker, and J. Chang. ESTAR, PSTAR, and ASTAR: Computer programs for calculating stopping-power and range tables for electrons, protons, and helium ions (version 1.2.3, 2005). [Online] Available: `http://physics.nist.gov/Star`. National Institure of Standards and Techonology, Gaithersburg, MD, USA, apr 2013.

[29] M.O. Krause, C.W. Nestor, C.J. Sparks, and E. Ricci. X-ray fluorescence cross sections for K and L X-rays of the elements. Technical Report ORNL-5399, OAK Ridge National Laboratory, 1978.

[30] J. Hsieh. *Computed Tomography. Principles, design, artifacts and recent advances*. SPIE and John Wiley and sons, Inc., second edition, 2009.

[31] J.R. Cunningham and D.R. Dance. *Diagnostic Radiology Physics: A Handbook for Teachers and Students*, chapter Interaction of radiation with matter. International Atomic Energy Agency, Viena, 2013 in press.

[32] Kaye and Laby. Tables of Physical and Chemical Constants. version 1.0. (2005). 4.2.1 x-ray absorption edges, characteristic x-ray lines and fluorescence yields. [Online] Available: `http://www.kayelaby.npl.co.uk/atomic_and_nuclear_physics/4_2/4_2_1.html`. The National Physical Laboratory, Middlesex, UK, mar 2013.

[33] J.H. Hubbell. Review of photon interaction cross section data in medical and biological context. *Physics in Medicine and Biology*, 44:R1–R22, 1999.

[34] J.H. Hubbell, Wm.J. Veigele, E.A. Briggs, R.T. Brown, D.T. Cromer, and R.J. Howerton. Atomic form factors, incoherent scattering functions, and photon scattering cross sections. *Journal of Physical and Chemical Reference Data*, 4(3):471–505, 1975.

[35] J.H. Hubbell. Summary of existing information on the incoherent scattering of photons, particularly on the validity of the use of the incoherent scattering function. *Radiation Physics and Chemistry*, 50(1):113–124, 1997.

[36] D.R. Dance. *Physics for Medical Imaging Applications*, volume 240, chapter Physical principles of mammography. Springer, 2007.

[37] P.C. Johns and M.J. Yaffe. X-ray characterisation of normal and neoplastic breast tissue. *Physics in Medicine and Biology*, 32(6):675–695, 1987.

[38] M. Sandborg, D.R. Dance, J. Persliden, and G. Alm Carlsson. A monte carlo program for the calculation of contrast, noise and absorbed dose in diagnostic radiology. *Computer Methods and Programs in Biomedicine*, 42(3):167 – 180, 1994.

[39] D.R. Dance, A. Thilander Klang, M. Sandborg, C.L. Skinner, I.A. Castellano Smith, and G. Alm Carlsson. Influence of anode/filter material and tube potential on contrast, signal-to-noise ratio and average absorbed dose in mammography: a Monte Carlo study. *The British Journal of Radiology*, 73:1056–1067, 2000.

[40] J.M. Boone, T. Fewell, and J. Jennings. Molybdenum, rhodium and tungsten anode spectral models using interpolating polynomials with applications to mammography. *Medical Physics*, 24(2):1863–1874, 1997.

[41] J.M. Boone and A. Seibert. An accurate method for computer-generating tungsten anode X-ray spectra from 30 to 140kv. *Medical Physics*, 24(11):1661–1670, 1997.

[42] K.P. Ng, C.S. Kwok, and F.H. Tang. Monte Carlo simulatino of x-ray spectra in mammography. *Physics in Medicine and Biology*, 45:1309–1318, 2000.

[43] J.W. Byng, J.G. Mainprize, and M.J. Yaffe. X-ray characterization of breast phantom materials. *Physics in Medicine and Biology*, 43:1367–1377, 1998.

[44] D.R. Dance, C.L. Skinner, K.C. Young, J.R. Beckett, and C.J. Kotre. Additional factors for estimation of mean glandular breast dose using the uk mammography dosimetry protocol. *Physics in Medicine and Biology*, 45:3225–3240, 2000.

[45] D.R. Dance, J. Persliden, and Alm Carlsson G. Calculation of dose and contrast for two mammographic grids. *Physics in Medicine and Biology*, 37(1):235–248, 1992.

[46] J.M. Boone, K.K Lindfors, V.N. Cooper, and J.A. Seibert. Scatter/primary in mammography: Comprehensive results. *Medical Physics*, 27(10):2408–2416, 2000.

[47] D.M. Cunha, A. Tomal, and M.E. Poletti. Evaluation of scatter-to-primary ratio, grid performance and normalized average glandular dose in mammography by Monte Carlo simulation including interference and energy broadening effects. *Physics in Medicine and Biology*, 55:4335–4359, 2010.

[48] M.J. Yaffe, J.M. Boone, N. Packard, O. Alonso-Proulx, S.Y. Huang, C.L. Peressotti, A. Al-Mayah, and K. Brock. The myth of the 50-50 breast. *Medical Physics*, 36(12):5437–5443, 2009.

[49] K. Bliznakova, Z. Bliznakov, V. Bravou, Z. Kolitsi, and N. Pallikarakis. A three-dimensional breast software phantom for mammography simulation. *Physics in Medicine and Biology*, 48:3699–3719, 2003.

[50] A.K.W. Ma, S. Gunn, and D.G. Darambara. Introducing DeBRa: a detailed breast model for radiological studies. *Physics in Medicine and Biology*, 54:4533–4545, 2009.

[51] K. Bliznakova, S. Suryanarayanan, A. Karellas, and N. Pallikarakis. Evaluation of an improved algorithm for producing realistic 3D breast software phantoms: Applications for mammography. *Medical Physics*, 37(11):5604–5617, 2010.

[52] P.R. Bakic, C. Zhang, and A.D.A. Maidment. Development and characterization of an antropomorphic breast software phantom based upon region-growing algorithm. *Medical Physics*, 38(6):3165–3176, 2011.

[53] B.A. Lau, I. Reiser, R.M. Noshikawa, and P.R. Bakic. A statistically defined anthropomorphic software breast phantom. *Medical Physics*, 39(6):3375–3385, 2012.

[54] G.R. Hammerstein, D.W. Miller, D.R. White, M.E. Masterson, H.Q. Woodard, and J.S. Laughlin. Absorbed radiation dose in mammography. *Radiology*, 130:485–491, 1979.

[55] ICRU. Photon, electron, proton and neutron interaction data for body tissues. Technical Report 46, International Commission on Radiation Units and Measurements, 1992.

[56] G. Ullman, M. Sandborg, R. Hunt, D.R. Dance, and Alm Carlsson G. Implementation of pathologies in the Monte Carlo model in chest and breast imaging. Technical Report 94, Institutionen för radiologi, Universitetet i Linköping, December 2003.

[57] G.T. Barnes. Contrast and Scatter in X-ray Imaging. *RadioGraphics*, 11:307–323, 1991.

[58] P.S. Rezentes, A. de Almeida, and G.T. Barnes. Mammography grid performance. *Radiology*, 210:227–232, 1999.

[59] J.E. Gray and J.A. Princehorn. HTC grids improve mammography contrast. Technical report, Hologic, Inc., 2004.

[60] A Krol, D.A. Bassano, C.C. Chamberlain, and S.C Prasad. Scatter reduction in mammography with air gap. *Medical Physics*, 23(7):1263–1270, 1996.

[61] J.M. Boone, J.A. Sibert, C-M. Tang, and S.M. Lane. Grid and slot scan scatter reduction in mammography: Comparison by using Monte Carlo techquines. *Radiology*, 222:519–527, 2002.

[62] G.F. Knoll. *Radiation detection and measurement*. John Wiley and Sons, Inc, fourth edition, 2010.

[63] M.J. Yaffe and J.G. Mainprize. Detectors for digital mammography. *Technology in Cancer Research and Treatment*, 3(4):309–324, 2004.

[64] U. Bick and F. Diekmann, editors. *Digital Mammography*. Springer, 2010.

[65] E.D. Pisano and M.J. Yaffe. Digital mammography. *Radiology*, 234:353–362, 2005.

[66] K.C Young. Recent developments in digital mammography. *Imaging*, 18:68–74, 2006.

[67] P.M. Shikhaliev, T. Xu, and S. Molloi. Photon counting computed tomography: concept and initial results. *Medical Physics*, 32(2):427–436, 2005.

[68] M. Åslund, B. Cederström, M. Lundqvist, and M. Danielsson. Physical characterization of a scanning photon counting digital mammography system based on si-strip detectors. *Medical Physics*, 34(6):1918–1925, 2007.

[69] M. Lundqvist, M. Danielsson, and B. Cederström. Measurements on a full-field digital mammography system with a photon counting crystalline silicon detector. In *Physics of Medical Imaging*, volume 5030, pages 547–552. Proc. of SPIE, 2003.

[70] P.M. Shikhaliev. Energy-resolved computed tomography: first experimental results. *Physics of Medical Imaging*, 53:5595–5613, 2008.

[71] J.T. Dobbins and D.J Godfrey. Digital x-ray tomosynthesis: current state of the art and clinical potential. *Physics in Medicine and Biology*, 48:R65–R106, 2003.

[72] Z. Kolitsi, G. Panayiotakis, V. Anastassopoulos, A. Scodras, and N. Pallikarakis. A multiple projection method for digital tomosynthesis. *Medical Physics*, 19(4):1045–1050, 1992.

[73] L T. Niklason, B T. Christian, L E. Niklason, D B. Kopans, D E. Castleberry, B H. Opsahl-Ong, and C E. Landberg. Digital Tomosynthesis in Breast Imaging. *Radiology*, 205:399–406, 1997.

[74] J.A. Baker and J.Y. Lo. Breast tomosynthesis: State-of-the-art and review of the literature. *Academic Radiology*, 18:1298–1310, 2011.

[75] I. Sechopoulos. A review of breast tomosynthesis. part i. the image acquisition process. *Medical Physics*, 40(1):014301–1, 2013.

[76] I. Andersson, D.M. Ikeda, S. Zackrisson, M. Ruschin, T. Svahn, P. Timberg, and A. Tingberg. Breast tomosynthesis and digital mammography: a comparison of breast cancer visibility and birads classification in a population of cancers with subtle mammographic findings. *European Radiology*, 18:2817–2825, 2008.

[77] G. Gennaro, A. Toledano, C. di Maggio, E. Baldan, E. Bezzon, M. La Grassa, L. Pescarini, I. Polico, A. Proietti, A. Toffoli, and P.C. Muzzio. Digital breast tomosynthesis versus digital mammography: a clinical performance study. *European Radiology*, 20:1545–1553, 2010.

[78] I. Sechopoulos, S. Suryanarayanan, S. Vedantham, C. D'Orsi, and A. Karellas. Computation of the glandular radiation dose in digital tomosynthesis of the breast. *Medical Physics*, 34(1):221–232, 2007.

[79] D.R. Dance, K.C. Young, and R.E. van Engen. Estimation of mean glandular dose for breast tomosynthesis: factors for use with the UK, European and IAEA breast dosimetry protocols. *Physics in Medicine and Biology*, 56(2):453–471, 2011.

[80] X. Qian, A. Tucker, E. Gidcumb, J. Shan, G. Yang, X. Calderon-Colon, S. Sultana, J. Lu, O. Zhoue, D. Spronk, F. Sprenger, Y. Zhang, D. Kennedy, T. Farbizio, and Z. Jing. High resolution stationary digital breast tomosynthesis using distributed carbon nanotube x-ray source array. *Medical Physics*, 39(4):2090–2099, 2012.

[81] R.J. Acciavatti and A.D.A. Maidment. Observation of super-resolution in digital breast tomosynthesis. *Medical Physics*, 39(12):7518–7538, 2012.

[82] I. Sechopoulos, S. Suryanarayanan, S. Vedantham, C. D'Orsi, and A. Karellas. Scatter radiation in digital tomosynthesis of the breast. *Medical Physics*, 34(2):564–576, 2007.

[83] B. Liu, T. Wu, R.H. Moore, and D.B. Kopans. Monte Carlo simulation of x-ray scater based on patient model from digital breast tomosynthesis. In *Physics of Medical Imaging*, volume 6142, page 61421N. Proc. of SPIE, 2006.

[84] R.S. Saunders, E. Samei, J.Y. Lo, and J.A. Baker. Can compression be reduced for breast tomosynthesis? monte carlo study on mass and microcalcification conspicuity in tomosynthesis. *Radiology*, 251(3), 2009.

[85] D. Förnvik, I. Andersson, T. Svahn, P. Timberg, S. Zackrisson, and A. Tingberg. The effect of reduced breast compression in breast tomosynthesis: human observer study using clinical cases. *Radiation Protection Dosimetry*, 139(1–3):118–123, 2010.

[86] A. Tingberg. X-ray tomosynthesis: A review of its use for breast and chest imaging. *Radiation Protection Dosimetry*, 139(1–3):100–107, 2010.

[87] B. Chen and R. Ning. Cone-beam volume CT breas imaging: Feasibility study. *Medical Physics*, 29(5):755–770, 2002.

[88] J.M. Boone, A.L.C. Kwan, K. Yang, G.W. Burkett, K.K. Lindfors, and T.R. Nelson. Computed Tomography for imaging the breast. *Journal of Mammary Gland Biology and Neoplasia*, 11:103–111, 2006.

[89] S.J. Glick. Breast CT. *Annual Review of Biomedical Engineering*, 9(1):501–526, 2007.

[90] A. Karellas, J.Y. Lo, and C.G. Orton. Cone beam x-ray CT will be superior to digital x-ray tomosynthesis in imaging the breast and delineating cancer. *Medical Physics*, 35(2):409–411, 2008.

[91] A.L.C. Kwan, J.M. Boone, and N. Shah. Evaluation of x-ray scatter properties in a dedicated cone-beam breast ct scanner. *Medical Physics*, 32(9):2967–2975, 2005.

[92] W.A. Kalender, M. Beister, J.M. Boone, D. Kolditz, S.V. Vollmar, and M.C.C. Weigel. High-resolution spiral CT of the breast at very low dose: concept and feasibility considerations. *European Radiology*, 22:1–8, 2012.

[93] Koning Corporation. [Online] Available: `http://www.koningcorporation.com/`. Koning Corporation, West Henrietta, NY, USA, jun 2013.

[94] Y. Chen, B. Liu, J.M. O'Connor, C.S. Didier, and S.J. Glick. Characterization of scatter in cone-beam CT breast imaging: Comparison of experimental measurements and Monte Carlo simulation. *Medical Physics*, 36(3):857–869, 2009.

[95] A. O'Connell, D.L. Conover, Y. Zhang, P. Seifert, W. Logan-Young, C.F.L. Lin, L. Sahler, and R. Ning. Cone-beam CT for breast imaging: Radiation dose, breast coverage, and image quality. *American Journal of Roentgenology*, 195:496–509, 2010.

[96] A. Rashidnasab, P. Elangovan, D.R. Dance, K.C. Young, O. Diaz, and K. Wells. Modeling realistic breast lesions using diffusion limited aggregation. In *SPIE Medical Imaging*, page 8313 83134L, 2012.

[97] A. Rashidnasab, P. Elangovan, D.R. Dance, K.C. Young, M. Yip, O. Diaz, and K. Wells. Realistic simulation of breast mass appearance using random walk. In *SPIE Medical Imaging*, page 8313 83130L, 2012.

[98] E. Shaheen, C. van Ongeval, F. Zanca, L. Cockmartin, N. Marshall, J. Jacobs, K.C. Young, D.R. Dance, and H. Bosmans. The simulation of 3D microcalcification clusters in 2D digital mammography and breast tomosynthesis. *Medical Physics*, 38(12):6659–6671, 2011.

[99] P. Elangovan, A. Mackenzie, O. Diaz, A. Rashidnasab, D.R. Dance, K C. Young, L.C. Warren, H. Shaheen, P.R. Bosmans, P.R. Bakic, and K. Wells. A modelling framework for evaluation of 2d-mammography and breast tomosynthesis systems. In *International Workshop on Breast Imaging*, 2012.

[100] X. Gong, S.J. Glick, B. Liu, A.A. Vedula, and S. Thacker. A computer simulation study comparing lesion detection accuracy with digital mammography, breast tomosynthesis, and cone-beam CT breast imaging. *Medical Physics*, 33:1041–1052, 2006.

[101] H.P. Chan, K.L. Lam, and Y. Wu. Studies of performance of antiscatter grids in digital radiography: effects on signal-to-noise ratio. *Medical Physics*, 17(4):655–664, 1990.

[102] U. Neitzel. Grids or airgaps for scatter reduction in digital radiography: a model calculation. *Medical Physics*, 19(2):475–481, 1992.

[103] W.J.H. Veldkamp, M.A.O. Thijssen, and N. Karssemeijer. The value of scatter removal by a grid in full field digital mammography. *Medical Physics*, 30(7):1712–1718, 2003.

[104] R. Fahrig, J.G. Mainprize, N. Robert, A. Rogers, and M.J. Yaffe. Performance of glass fiber antiscatter device at mammographic energies. *Medical Physics*, 21(8):1277–1282, 1994.

[105] G.T. Barnes and I.A. Brezovich. The intensity of scattered radiation in mammography. *Radiology*, 126:243–247, 1978.

[106] V.N. Cooper, J.M. Boone, J.A. Seibert, and C.J. Pellot-Barakat. An edge spread technique for measurement of the scatter-to-primary ratio in mammorgaphy. *Medical Physics*, 27(5):845–853, 2000.

[107] D.R. Dance and G.J. Day. The computation of scatter in mammography by Monte Carlo methods. *Physics in Medicine and Biology*, 29(3):237–247, 1984.

[108] K. Nykanen and S. Siltanen. X-ray scattering in full-field digital mammography. *Medical Physics*, 30(7):1864–1873, 2003.

[109] D.G. Kruger, F. Zink, W.W. Peppler, Ergun D.L, and C.A. Mistretta. A regional convolution kernel algorithm for scatter correction in dual-energy images: Comparison to sigle-kernel algorithms. *Medical Physics*, 21(2):175–184, 1994.

[110] J. Star-Lack, M. Sun, A. Kaestner, R. Hassanein, G. Virshup, T. Berkus, and M. Oelhafen. Efficient scatter correction using asymmetric kernels. In *Physics of Medical Imaging*, volume 7258, page 72581ZI. Proc. of SPIE, 2009.

[111] M. Sun and J.M. Star-Lack. Improved scatter correction using adaptative scatter kernel superposition. *Physics in Medicine and Biology*, 55:6695–6720, 2010.

[112] S. Park, A. Badal, S. Young, and K.J. Myers. A mathematical framework for including various sources of variability in a task-based assessment of digital breast tomosynthesis. In *SPIE Medical Imaging*, 2012.

[113] C.E. Tromans, M.R. Cocker, and M. Brady. A model of primary and scattered photons fluence for mammographic x-ray image quantification. *Physics in Medicine and Biology*, 57:6541–6570, 2012.

[114] M. Åslund, Lundqvist M. Cederström, B., and M. Danielsson. Scatter rejection in multislit digital mammography. *Medical Physics*, 33(4):933–940, 2006.

[115] B. Liu and X. Li. Effects of scatter radiation on reconstructed images in digital breast tomosynthesis. In *Physics of Medical Imaging*, volume 7258, page 72585Y. Proc. of SPIE, 2009.

[116] E. Salvagnini, H. Bosmans, L. Struelens, and N.W. Marshall. Quantification of scattered radiation in projection mammography: Four practical methods compared. *Medical Physics*, 39(6):3167–3180, 2012.

[117] R. Ning, T. Xiangyang, and D. Conover. X-ray scatter correction algorithm for cone beam ct imaging. *Medical Physics*, 31(5):1195–1202, 2004.

[118] S.Z. Shen, A.K. Bloomquist, G.E Mawdsley, and M.J. Yaffe. Effect of scatter and an antiscatter grid on the performance of a slot-scanning digital mammography system. *Medical Physics*, 33(4):1108–1115, 2006.

[119] H.P. Chan and K. Doi. The validity of Monte Carlo simulations in studies of scattered radiation in diagnostic radiology. *Physics in Medicine and Biology*, 28(2):109–129, 1983.

[120] H.P. Chan and K. Doi. Physical characteristics of scattered radiation in diagnostic radiology: Monte Carlo simulation studies. *Physics in Medicine and Biology*, 12(2):152–165, 1985.

[121] J. Boone and J.A. Seibert. Monte Carlo simulation of the scattered radiation distribution in diagnostic radiology. *Medical Physics*, 15(5):713–720, 1988.

[122] S.K. Ahn, G. Cho, and H. Jeon. A scatter correction using thickness iteration in dual-energy radiography. *IEEE Transaction on nuclear science*, 53(1):133–138, 2006.

[123] O. Diaz, D R. Dance, K C. Young, P. Elangovan, P R. Bakic, and K. Wells. A fast scatter field estimator for Digital Breast Tomosynthesis. In *SPIE Medical Imaging*, page 8313 831305, 2012.

[124] M.E. Poletti, O.D. Gonçalves, I. Mazzaro, and H. Schechter. Evaluation of the influence of scattering profiles on the resolution, scatter/primary ratio, and grid performance in mammography. *Radiation Physics and Chemistry*, 61:607–610, 2001.

[125] R.A. Hunt, D.R. Dance, P.R. Bakic, A.D.A. Maidment, M. Sandborg, and G. Ullman. Calculation of the properties of digital mammograms using a computer simulation. *Radiation Protection Dosimetry*, 114(1-3):395–398, 2005.

[126] M.A. Al Kafi, N Maalej, and A.A. Naqvi. Scatter dose calculation for anti-scatter linear grids in mammography. *Applied Radiation and Isotopes*, 67:1837–1841, 2009.

[127] G. Mettivier, P. Russo, N. Lanconelli, and S. Lo Meo. Evaluation of scattering in Cone-Beam breast Computed Tomography: a Monte Carlo and experimental phantom study. *IEEE Transactions on Nuclear Science*, 57(5):2510–2517, 2010.

[128] O. Diaz, M. Yip, J. Cabello, D.R. Dance, K.C. Young, and K. Wells. Monte Carlo simulation of scatter field for calculation of contrast of discs in synthetic CDMAM images. In *Lecture Notes in Computer Science (Digital Mammography)*, volume 6136, pages LNCS 628–635. Springer, 2010.

[129] S. Feng and I. Sechopoulos. A software-based x-ray scatter correction method for breast tomosynthesis. *Medical Physics*, 38(21):6643–6653, 2011.

[130] J. Boone and J.A. Seibert. An analytical model of the scattered radiation distribution in diagnostic radiology. *Medical Physics*, 15(5):721–725, 1988.

[131] J.T. Bushberg, J.A. Seibert, E.M. Leidholdt Jr, and J.M. Boone. *The Essential Physics of Medical Imaging*. Lippincott Williams and Wilkins, Philadelphia, second edition, 2012.

[132] R. Moeckli, F.R. Verdun, S. Fidler, M. Pachoud, S. Bulling, P. Schnyder, and J.F. Valley. Influence of scatter reduction method and monochromatic beams on image quality and dose in mammography. *Medical Physics*, 30(12):3156–3164, 2003.

[133] J.H. Siewerdsen, M.J. Daly, B. Bakhtiar, D.J. Moseley, S. Richard, H. Keller, and D.A. Jaffray. A simple, direct method for x-ray scatter estimation and correction in digital radiography and cone-beam ct. *Medical Physics*, 33(1):187–197, 2006.

[134] W.H. Press, S.A. Teokolsky, W.T. Vetterling, and B.P. Flannery. *Numerical Recipes in C*. Cambridge Press University, UK, second edition, 1992.

[135] R.C. Gonzalez and R.E. Woods. *Digital Image Processing*. Pearson Education, Inc., Upper Saddle River, New Jersey, third edition, 2008.

[136] G. Spyrou, G. Panayiotakis, and G. Tzanakos. Mastos: Mammography simulation tool for design optimization studies. *Medical Informatics and The Internet in Medicine*, 25(4):275–293, 2000.

[137] D.R. Dance. Monte Carlo calculation of conversion factors for the estimation of mean glandular breast dose. *Physics in Medicine and Biology*, 35(9):1211–1219, 1990.

[138] T. Sakellaris, G. Spyrou, G. Tzanakos, and G. Panayiotakis. Monte Carlo simulation of primary electron production inside an a-selenium detector for x-ray mammpgraphy: physics. *Physics in Medicine and Biology*, 50:3717–3738, 2005.

[139] M. Ljungberg, S-E. Strand, and M.A. King, editors. *Monte Carlo calculations in nuclear medicine: applications in diagnostic imaging*. Institute of Physics Publishing, 1998.

[140] R.L. Ford and W.R. Nelson. The EGS code system: computer programs for the Monte Carlo simulation of electromagnetic cascade showers (version 3). Technical Report SLAC–210, UC–32, Stanford Linear Accelerator Center, 1978.

[141] J.F. Briesmeister. *MCNP - A General Monte Carlo N-Particle Transport Code*, 2000.

[142] J. Baro, J. Sempau, J.M Fernandez-Varea, and F. Salvat. PENELOPE: An algorithm for Monte Carlo simulation of the penetration and energy loss of electrons and positrons in matter. *Nuclear Instrumenrs and Methods in Physics Research*, B(100):31–46, 1995.

[143] S. Agostinelli, J. Allison, K. Amako, J. Apostolakis, H. Araujo, P. Arce, M. Asai, D. Axen, S. Banerjee, and G. Barrand. Geant4 – a simulation toolkit. *Nuclear Instruments and Methods in Physics Research*, 506(3):250–303, 2003.

[144] J. Allison, K. Amako, J. Apostolakis, H. Araujo, P. Arce, M. Asai, G. Barrand, R. Capra, and S. Chauvie. Geant4 developments and applications. *IEEE Transactions on Nuclear Science*, 53(1):270–278, 2006.

[145] A. Ferrari, P.R. Sala, A. Fasso, and J. Ranft. FLUKA: a multi-particle transport code. Technical report, CERN-2005-10 (2005), INFN/TC_05/11, SLAC-R-773, 2005.

[146] G. Battistoni, S. Muraro, P.R. Sala, F. Cerutti, and A. Ferrari. The FLUKA code: Description and bechmarking. In *AIP conference proceeding*, volume 896, pages 31–49, 2007.

[147] D.W.O. Rogers. Review: Fifty years of Monte Carlo simulations for medical physics. *Physics in Medicine and Biology*, 51:R287–R301, 2006.

[148] Geant4 Collaboration. *Geant4 Physics Reference Manual, Version: Geant4 9.3*, December 2009.

[149] D.E. Raeside. Monte Carlo principles and applications. *Physics in Medicine and Biology*, 21(2):181–197, 1976.

[150] L. Archambault, L. Beaulie, J.F. Carrier, F. Castrovillari, S. Chauvie, F. Foppiano, G. Ghiso, S. Guatelli, S. Incerti, E. Lamanna, S. Larsson, M.C. Lopes, L. Peralta, M.G. Pia, P. Rodrigues, V.H. Tremblay, and A. Trindade. Overview of Geant4 applications in medical physics. In *IEEE Nuclear Science Symposium Conference*, volume 3, pages 1743–1745, 2003.

[151] G. Barca, F. Castrovillari, S. Chauvie, D. Cuce, F. Foppiano, G. Ghiso, S. Guatelli, E. Lamanna, M.C. Lopes, L. Peralta, M.G. Pia, P. Rodrigues, A. Trindade, and M. Veltri. A powerful simulation tool for medical physics applications: Geant4. *Nuclear Physics B - Proceedings Supplements*, 125(0):80 – 84, 2003.

[152] P. Rodrigues, R. Moura, C. Ortigao, L. Peralta, M.G. Pia, A. Trindade, and J. Varela. Geant4 applications and developments for medical physics experiments. *Nuclear Science, IEEE Transactions on*, 51(4):1412 – 1419, aug. 2004.

[153] I. Sechopoulos. *Investigation of physical processes in digital X-ray tomosynthesis*. PhD thesis, Georgia Institute of Technology, May 2007.

[154] Feijo Pery Vidal and Hoff Gabriela. Geant4 validation on mammography applications. In *Nuclear Science Symposium Conference Record, 2008. NSS '08. IEEE*, pages 3497 –3498, oct. 2008.

[155] J. Perez-Calatayud, D. Granero, and F. Ballester. Phantom size in brachytherapy source dosimetric studies. *Medical Physics*, 31(7):2075–2081, 2004.

[156] G.A.P. Cirrone, G. Cuttone, S. Guatelli, S.L. Nigro, B. Mascialino, M.G. Pia, L. Raffacle, G. Russo, and M.G. Sabini. Implementation of a new monte carlo simulation tool for the development of a proton therapy beam line and verification of the related dose distributions. In *Nuclear Science Symposium Conference Record, 2003 IEEE*, volume 3, pages 1756 – 1758 Vol.3, oct. 2003.

[157] P. Rodrigues, A. Trindade, L. Peralta, C. Alves, A. Chaves, and M.C. Lopes. Application of GEANT4 radiation transport toolkit to dose calculations in anthropomorphic phantoms. *Applied Radiation and Isotopes*, 61(6):1451 – 1461, 2004.

[158] S. Jan, G. Santin, D. Strul, S. Staelens, K. Assie, D. Autret, S. Avner, R. Barbier, and M. Bardies. GATE: a simulation toolkit for PET and SPECT. *Physics in Medicine and Biology*, 49:4543–4561, 2004.

[159] Geant4 website: `http://geant4.cern.ch/`.

[160] Geant4 General Particle Source : `http://reat.space.qinetiq.com/gps/`.

[161] J. Perl. Geant4 workshop visualization tutorial using the OpenGL event display. http://conferences.fnal.gov/g4tutorial/g4cd/Documentation/Visualization/G4OpenGLTutorial/G4OpenGLTutorial.html, oct 2012.

[162] HyperNews Geant4. Geant4 at Hypernews. `http://hypernews.slac.stanford.edu/HyperNews/geant4/cindex`, oct 2012.

[163] F. James. A review of pseudorandom number generators. *Computer Physics Communications*, 60:329–344, 1990.

[164] V. Demchik. Pseudo-random number generators for Monte Ccarlo simulations on ATI Graphics Processing Units. *Computer Physics Communications*, 182:692–705, 2011.

[165] D.E. Cullen, J.H. Hubbell, and L. Kissel. EPDL97: The evaluated photon data library'97 version. Technical Report UCLR–50400, Vol.6, Rev.5, Lawrence Livermore National Laboratory, 1997.

[166] S.T. Perkins, D.E. Cullen, and S.M. Seltzer. Tables and grahs of electron-interaction cross sections for 10ev to 100gev derived from the LLNL evaluated electron data library (EEDL), z = 1–100. Technical Report UCLR–50400, Vol.31, Lawrence Livermore National Laboratory, 1991.

[167] S.T. Perkins, D.E. Cullen, M.H. Chen, J. Rathkopf, J. Scofield, and J.H. Hubbell. Tables and graphs of atomic subshell and relaxation data derived from the LLNL evaluated atomic data library (EADL), z = 1–100. Technical Report UCLR–50400, Vol.30, Lawrence Livermore National Laboratory, 1991.

[168] F. Salvat, J.M. Fernandez-Varea, E. Acosta, and J. Sempau. Penelope - a code system for Monte Carlo simulation of electron and photon transport. In *Workshop Proceedings Issy-les-Moulineaux, France*, 2001.

[169] S. Guatelli, B. Mascialino, M.G. Pia, M. Piergentili, L. Pandola, S. Parlati, K. Amako, T. Murakami, K. amd Sasaki, L. Urban, M. Maire, and V. Ivanchenko. Precision validation of Geant4 electromagnetic physics. American Nuclear Society Topical Meeting in Monte Carlo, April 2005.

[170] K. Amako, S. Guatelly, V.N. Ivachenko, M. Maire, B. Mascialino, K. Murakami, P. Nieminen, L. Pandola, S. Parlati, and M. Grazia Pia. Comparison of Geant4 electromagnetic physics models against the NIST regerence data. *IEEE Transactions on Nuclear Science*, 52(4):910–918, 2005.

[171] G.A.P. Cirrone, G. Cuttone, F. Di Rosa, L. Pandola, F. Romano, and Q. Zhang. Validation of the Geant4 electromagnetic photons cross-sections for elements and compounds. *Nuclear Instruments and Methods in Physics Research A*, 618:315–322, 2010.

[172] J.H. Hubbell and I. Overbó. Relativistic atom form factors and photon coherent scattering cross sections. *Journal of Physical and Chemical Reference Data*, 8(1):69–105, 1979.

[173] D.E. Cullen. A simple model of photon transport. *Nuclear Instruments and Methods in Physics Research Section B*, 101(4):499–510, 1995.

[174] R. Bouwman, K.C. Young, B. Lazzari, V. Ravaglia, M. Broeders, and R. van Engen. An alternative method for noise analysis using pixel variance as part of quality control procedures on digital mammography systems. *Physics in Medicine and Biology*, 54:6809–6822, 2009.

[175] R.W. Bouwman, Diaz. O., R.E. van Engen, K.C. Young, G.J. den Heeten, M.J.M. Broeders, W.J.H. Veldkamp, and D.R. Dance. Phantoms for quality control procedures in digital breast tomosynthesis: dose assessment. *Physics in Medicine and Biology*, 58(13):4423–4438, 2013.

[176] H. Zaidi. Comparative evaluation of photons cross-section libraries for materials of interest in PET Monte Carlo simulations. *IEEE Transactions on Nuclear Science*, 47(6):2722–2735, 2000.

[177] B. Ren, C. Ruth, T. Wu, Y. Zhang, A. Smith, and L. Niklason. A new generation FFDM/tomosynthesys fusion system with selenium detector. In *SPIE Medical Imaging*, volume 7622 76220B-11, 2010.

[178] A. Mackenzie, A. Workman, D.R. Dance, M. Yip, K. Wells, and K.C. Young. Validation of a method to convert an image to appear as if acquired using a different digital detector. pages 79614F–79614F–12, 2011.

[179] H. Bosmans, A.K. Carton, F. Rogge, F. Zanca, J. Jacobs, C. Van Ongenval, K. Nijs, A. Van Steen, and G. Marchal. Image quality measurements and metrics in full field digital mammography: an overview. *Radiation Protection Dosimetry*, 117(1-3):120–130, 2005.

[180] J.A. Thomas, K. Chakrabarti, R. Kaczmarek, and A. Romanyukha. Contrast-detail phantom scoring methodology. *Medical Physics*, 32(3):807–814, 2005.

[181] R. Rico, S.L. Muller, G. Peter, A. Noel, and J. Stines. Automated scoring of CDMAM: a dose study. In *SPIE Medical Imaging: Image Perception, Observer Performance, and Technology Assessment*, volume 5034, pages 164–173, 2003.

[182] K.C. Young, J.J.H. Cook, J.M. Oduko, and H. Bosmans. Comparison of software and human observers in reading images of the CDMAM test object to assess digital mammography systems. In *Physics of Medical Imaging*, volume 6142, pages 6142061–13. Proc. of SPIE, 2006.

[183] M. Yip, W. Chukwu, E. Kottis, E. Lewis, J.M. Oduko, O. Gundogdu, K.C. Young, and K. Wells. Automated scoring method for the CDMAM phantom. In *Physics of Medical Imaging*, volume 7263, pages 72631A–72631A–10. Proc. of SPIE, 2009.

[184] M. Visser and N. Karssemeijer. *Manual CDCOM version 1.5: software for automated readout of CDMAM 3.4 images.*

[185] M. Yip, F. Zanca, A. Mackenzie, A. Workman, K.C. Young, D.R. Dance, H. Bosmans, E. Lewis, and K. Wells. Validation of a simulated dose reduction methodology using digital mammography CDMAM images and mastectomy images. In *Lecture Notes in Computer Science (Digital Mammography)*, volume LNCS 6136, pages 78–85. Springer, 2010.

[186] M. Yip, A. Mackenzie, E. Lewis, D.R. Dance, K.C. Young, W. Christmas, and K. Wells. Image resampling effects in mammographic image simulation. *Physics in Medicine and Biology*, 56:N275–N286, 2011.

[187] J.T. Bushberg, J.A. Seibert, E.M. Leidholdt (Jr), and J.M. Boone. *The Essential Physics of Medical Imaging.* Lippincott Williams and Wilkins, Philadelphia, USA, second edition, 2002.

[188] J.M. Oduko, K.C. Young, and A. Burch. A survey of patient dose from digital mammography systems in the UK in 2007 to 2009. In *Lecture Notes in Computer Science (Digital Mammography)*, volume LNCS 6136, pages 365–370. Springer, 2010.

[189] K.C. Young, J.J.H Cook, J. Oduko, and H. Bosmans. Automated and human determination of threshold contrast for digital mammography systems. In *International Workshop on Digital Mammography*, volume 4046, pages 266–272. Springer, 2006.

[190] G. Prieto, M. Chevalier, and E. Guibelalde. Automatic scoring of CDMAM using a model of the recognition threshold of the human visual system: R*. In *Image Processing ICIP*, pages 2489–2492, 2009.

[191] H.P. Chan and K. Doi. Investigation of the performance of antiscatter grids: Monte Carlo simulations studies. *Physics in Medicine and Biology*, 27(6):785–803, 1982.

[192] R.A. Hunt, D.R. Dance, M. Pachoud, G. Alm Carlsson, M. Sandborg, G. Ullman, and F.R. Verdun. Monte Carlo simulations of a mammographic test phantom. *Radiation Protection Dosimetry*, 114(1-3):432–435, 2005.

[193] K. Smans, J. Zoetelief, B. Verbrugge, W. Haeck, L. Struelens, F. Vanhavere, and H. Bosmans. Simulation of image detectors in radiology for determination of scatter-to-primary ratios using Monte Carlo radiation transport code MCNP/MCNPX. *Medical Physics*, 37(5):2082–2091, 2010.

[194] R.L. Siddon. Fast calculation of the exact radiological path for a three-dimensional CT array. *Medical Physics*, 12(2):252–255, 1985.

[195] C.M. Li, W.P. Segars, G.D. Tourassi, J.M. Boone, and J.T. Dobbins. Methodology for generating a 3d computerized breast phantom from empirical data. *Medical Physics*, 36(7):3122–3131, 2009.

[196] J. Smisek, M. Jancosek, and T. Pajdla. 3D with Kinect. In *Computer Vision Workshops (ICCV Workshops), 2011 IEEE International Conference on*, pages 1154–1160, 2011.

[197] K. Khoshelham and S. O. Elberink. Accuracy and resolution of Kinect depth data for indoor mapping applications. *Sensors*, 12(2):1437–1454, 2012.

[198] Helmuth Vorherr. *The Breast: Morphology, Physiology and Lactation*. Academic Press, London(England), 1974.

[199] NursingCrib. [Online] Available: `http://nursingcrib.com/anatomy-and-physiology/anatomy-and-physiology-of-mammary-glands-breast/`., aug 2009.